MODELING AND EXPERIMENTAL ANALYSIS OF PIEZOELECTRIC AUGMENTED SYSTEMS FOR STRUCTURAL HEALTH AND STRESS MONITORING APPLICATIONS

MOHAMMAD I. ALBAKRI

Dissertation submitted to the faculty of the Virginia Polytechnic Institute and State University in partial fulfillment of the requirements for the degree of

DOCTOR OF PHILOSOPHY

IN

ENGINEERING MECHANICS

PABLO A. TARAZAGA, CHAIR

DANIEL J. INMAN

MEHDI AHMADIAN

MUHAMMAD R. HAJJ

SCOTT W. CASE

November 15, 2016

Blacksburg, Virginia

Keywords: Structural Health Monitoring, Electromechanical Impedance, Acoustoelasticity, Piezoelectric Materials, Spectral Element Method, High Frequency, Damage Characterization.

MODELING AND EXPERIMENTAL ANALYSIS OF PIEZOELECTRIC AUGMENTED SYSTEMS FOR STRUCTURAL HEALTH AND STRESS MONITORING APPLICATIONS

MOHAMMAD ISMAIL ALBAKRI

ABSTRACT

Detection, characterization, and prognosis of damage in civil, aerospace and mechanical structures, known as structural health monitoring (SHM), have been a growing area of research over the last few decades. As several in-service civil, mechanical and aerospace structures are approaching or even exceeding their design life, the implementation of SHM systems is becoming a necessity. SHM is the key for transforming schedule-driven inspection and maintenance into condition-based maintenance, which promises enhanced safety and overall life-cycle cost reduction. While damage detection and characterization can be achieved, among other techniques, by analyzing the dynamic response of the structure under test, damage prognosis requires the additional knowledge of loading patterns acting on the structure. Accurate, nondestructive, and reference-free measurement of the state-of-stress in structural components has been a long-standing challenge without a fully satisfactory outcome.

In light of this, the main goal of this research effort is to advance the current state-of-the-art of structural health and loading monitoring, with the focus being cast on impedance-based SHM and acoustoelastic-based stress measurement techniques. While impedance-based SHM has been successfully implemented as a damage detection technique, the utilization of electromechanical impedance measurements for damage characterization imposes several challenges. These challenges are mainly stemming from the high-frequency nature of impedance measurements. Current acoustoelastic-based practices, on the other hand, are hindered by their poor sensitivity and the need for calibration at a known state-of-stress. Addressing these challenges by developing and integrating theoretical models, numerical algorithms, and experimental techniques defines the main objectives of this work.

A key enabler for both health and loading monitoring techniques is the utilization of piezoelectric transducers to excite the structure and measure its response. For this purpose, a new three-layer spectral element for piezoelectric-structure interaction has been developed in this work, where the adhesive bonding layer has been explicitly modeled. Using this model, the dynamic response of piezoelectric-augmented structures has been investigated. A thorough parametric study has been conducted to provide a better understanding of bonding layer impact on the response of the coupled structure. A procedure for piezoelectric material characterization utilizing its free electromechanical impedance signature has also been developed. Furthermore, impedance-based damage characterization has been investigated, where a novel optimization-based damage identification approach has been developed. This approach exploits the capabilities of spectral element method, along with the periodic nature of impedance peaks shifts with respect to damage location, to solve the ill-posed damage identification problem in a computationally efficient manner.

The second part of this work investigates acoustoelastic-based stress measurements, where a model-based technique that is capable of analyzing dispersive waves to calculate the state-of-stress has been developed. A criterion for optimal excitation waveform selection has been proposed in this work, taking into consideration the sensitivity to the state-of-stress, the robustness against material and geometric uncertainties, and the ability to obtain a reflection-free response at desired measurement locations. The impact of material- and geometry-related uncertainties on the performance of the stress measurement algorithm has also been investigated through a comprehensive sensitivity analysis. The developed technique has been experimentally validated, where true reference-free, uncalibrated, acoustoelastic-based stress measurements have been successfully conducted.

Finally, the applicability of the aforementioned health and loading monitoring techniques to railroad track components has been investigated. Extensive in-lab experiments have been carried out to evaluate the performance of these techniques on lab-scale and full-scale rail joints. Furthermore, in-field experiments have been conducted, in collaboration with Norfolk Southern and the Transportation Technology Center Inc., to further investigate the performance of these techniques under real life operating and environmental conditions.

Modeling and Experimental Analysis of Piezoelectric Augmented Systems for Structural Health and Stress Monitoring Applications

Mohammad Ismail Albakri

GENERAL AUDIENCE ABSTRACT

Structural health monitoring (SHM) addresses the problem of damage detection and identification in civil, aerospace and mechanical structures. As several in-service structures are approaching or even exceeding their design life, the implementation of SHM systems is becoming a necessity. Besides Damage identification, a complete assessment of the structure under test requires the knowledge of loading patterns acting on it. Accurate, nondestructive, and reference-free measurement of the state-of-stress in structural components has been a long-standing challenge without a fully satisfactory outcome.

This research effort aims to advance the current state-of-the-art of structural health and loading monitoring with the focus being cast on impedance-based SHM and acoustoelastic-based stress measurement techniques. Theoretical models and numerical algorithms have been developed as a part of this wok to facilitate impedance-based damage identification and provide a better understanding of a number of factors affecting the performance of this technique. A new acoustoelastic-based stress measurement technique has also been developed and experimentally validated. Using this technique, true reference-free, uncalibrated stress measurements have been successfully conducted for the first time. The applicability of the aforementioned techniques to the railroad industry has been investigated, where their performance is evaluated under real-life operating and environmental conditions.

To my soulmate, Sameha

To my little princess, Nahla

To my parents

ACKNOWLEDGMENTS

unforgettable experience. Lots of thanks to all of you for all the discussions we had, for your delightful comments, and most importantly, for your friendship.

Last but not least, I would like to thank my wife and my best friend, Sameha, along with my lovely daughter, Nahla, for their support, encouragement and unconditional love. They have sacrificed a lot for me to accomplish this work. Indeed, without them by my side, this could not have been possible. My deepest gratitude is also due to my beloved parents for all the support and encouragement. They have always believed in me and provided me with emotional and spiritual support. For that, and countless other things, thank you.

Mohammad I. Albakri,
Blacksburg, VA, USA. November. 2016

TABLE OF CONTENTS

Chapter Three   The Effects of Piezoelectric Wafer and Bonding Layer Characteristics on the Dynamic Response of Smart Structures

Chapter Four   Electromechanical Impedance-based Damage Identification

Table of Contents

LIST OF FIGURES

LIST OF TABLES

CHAPTER ONE

INTRODUCTION

1.1   Background and Motivation

Motivated by safety and economic benefits, the field of structural health monitoring (SHM) has been a growing area of research over the last few decades (Farrar and Worden, 2007; Sohn et al., 2004). SHM addresses the problem of damage detection and identification of civil, mechanical, and aerospace components and structures. Unlike non-destructive evaluation (NDE), which is normally performed in an off-line and local manner, SHM is an online condition screening process that aims to assess the integrity of the structure in near real-time. The implementation and use of SHM systems are becoming increasingly important as many civil, mechanical and aerospace structures are approaching or even exceeding their design life, but still in use due to economic reasons. Furthermore, SHM has the potential to perform post-extreme-events damage assessment, such as after earthquakes or blast loadings, which in turn can be used to guide maintenance and reinstating efforts (Brownjohn, 2007). SHM is the key for transforming schedule-driven inspection and maintenance into condition-based maintenance, which promises enhanced safety and overall life-cycle cost reduction.

In the context of SHM, damage is defined as any change in the structure that adversely affects its performance, including material degradation, changes in geometry, boundary conditions and connectivity (Farrar and Worden, 2007). The damage identification process, in general, includes several levels of complexity: (i) detecting the existence of damage, (ii) determining damage type, (iii) determining the

1

locations of damage, and (iv) assessing damage severity (Worden et al., 2007). To achieve these objectives, the damage identification process involves the measurement of the structure's response to certain excitations over time, the extraction of damage-sensitive features from the measured response and the analysis of these features to identify the current state of structure's health.

The fundamental basis of most damage identification methods is that the presence and evolution of damage will alter the mass, stiffness and damping characteristics of the structure, which in turn reflect on its dynamic response. Among the different SHM techniques, impedance-based SHM has emerged as a promising, non-intrusive, cost-effective, highly-sensitive solution for real-time damage assessment (Park et al., 2003). This technique utilizes piezoelectric materials, lead zirconate titanate (PZT) wafers in particular, as collocated sensors and actuators (Giurgiutiu and Zagrai, 2000; Park and Inman, 2007). Due to the coupled electromechanical behavior of piezoelectric materials, the electrical impedance of piezoelectric wafers is directly related to the mechanical impedance of the host structure (Liang et al., 1994a). Therefore, changes in the host structure, induced by cracks, material degradation, loose connections, and other structural defects, are reflected on the electrical impedance of the piezoelectric wafer, and can readily be detected.

Besides damage detection and characterization, which are the main objectives of current SHM practices, monitoring the state-of-stress in structural and mechanical components is of significant importance. Accurate, nondestructive, and reference-free measurement of stress state in structural components has been a long-standing challenge without a fully satisfactory outcome. Besides externally applied loads, stresses arise in structures from two main sources: environmental conditions and manufacturing processes. Among the different types of stresses induced by environmental conditions, thermal stresses are the most critical. Temperature variations of a constrained structural component, e.g. a continuously welded rail, result in excessive tensile or compressive stresses. This, in turn, may lead to failure, with buckling, fatigue, and breakage being the most common manifestations.

Knowledge of the state-of-stress in structural components provides an insight into the health of that component and the integrity of the surrounding structure. This information can then be utilized to guide maintenance scheduling and operations planning efforts. For instance, an abrupt drop or increase in the load carried by a certain member in the structure indicates, respectively, failure in that element or in the surrounding structural components. In railroad tracks, compressive thermal loads increase the threat of buckling that, if not identified, can result in catastrophic derailments with potential loss of lives (Andrew Kish et al., 2013). Furthermore, a continuous monitoring of the evolution of the state-of-stress in structural

components provides valuable information regarding loading patterns and material degradation. Such information is pivotal for damage identification and remaining life predictions, which are the ultimate goals of SHM. A nondestructive, reliable, stand-alone, and reference-free solution for monitoring the state-of-stress in structural components has the potential to advance SHM practices, reduce life-cycle cost, and enhance safety and reliability.

Several theories and techniques have been developed over the last few decades to tackle the problem of stress state measurement, many of them are destructive in nature (Rossini et al., 2012). Nondestructive techniques, on the other hand, exploit the dependence of mechanical, acoustic, electrical, and magnetic characteristics of the material on the internal state-of-stress (Hsu, 1974; Blitz and Simpson, 1996; Kamminga et al., 2000; Skrzypek et al., 2001; Vangi, 2001; Hutchings et al., 2005; Żurek, 2005; Wilson et al., 2007). One particular theory that attracted most of the attention is the acoustoelastic theory, which describes the dependence of propagating waves characteristics on the state-of-stress (Green et al., 1952; Biot, 1965; Willson, 1977). It has been established in the literature that dispersion relations depend on the initial state-of-stress in the structure. Theories describing such dependence have been developed for one, two and three-dimensional cases. These theories have laid the basis for stress measurement ultrasonic techniques, each has its own merits and limitations. In general, most of the techniques currently available share one or more of the following limiting factors: the need for extremely accurate time-of-flight measurements, the need for calibration at a known reference state-of-stress, measurement complexity, and high sensitivity to material uncertainties. These limitations hinder the in-field applicability of such techniques, especially for already in service structures where a reference state-of-stress is hardly attainable.

The development of a stress measurement solution that mitigates the limitations of the currently available techniques has been a long-standing challenge. Furthermore, being compatible with SHM techniques, such stress measurement solution will lead to an integrated health and loading monitoring systems capable of providing a more complete assessment of the state of the structure.

1.2   Review of Literature

This section highlights major research efforts that lead to the development of impedance-based SHM, vibration-based damage identification, and acoustoelastic-based stress measurement. A number of challenges facing the advancement of these fields have been identified. These challenges will serve as

guiding landmarks of this research effort and will identify its contributions to the current body of knowledge.

1.2.1   Impedance-based Structural Health Monitoring

Liang and Rogers (1994b) were the first to develop the impedance approach to study the dynamic response of smart structures. They derived a simple closed-form solution for the actuator current and force output, taking into consideration the effects of actuator-structure interaction. With the impedance approach, the dependence of transducers electrical impedance on the mechanical impedance of the host structure was established, which later on formed the basis for impedance-based SHM. Sun et al. (Sun et al., 1995) were among the first to utilize the impedance signature for SHM purposes, where they used piezoelectric patches to detect damage in an assembled truss structure.

The basic concept of impedance-based SHM is to monitor changes in the mechanical impedance of the structure being tested to detect the presence of damage and track its progression. Making use of the coupled electromechanical behavior of piezoelectric materials, the problem of measuring the mechanical impedance of the host structure is significantly simplified, as it is directly related to the electrical impedance of the piezoelectric wafer. Therefore, changes in the host structure, induced by cracks, material degradation, loose connections, and other structural defects, are reflected on the electrical impedance of the piezoelectric wafer, and thus can readily be detected.

Liang's model was developed for a one-dimensional piezoelectric wafer perfectly bonded to a structure of impedance Z_{St}. The electrical impedance of the piezoelectric wafer can be described as (Liang et al., 1994b)

$$Z(\omega) = \frac{V(\omega)}{I(\omega)} = -i\omega \frac{h}{wl}\left[e_{33}^{\sigma} + d_{31}^{2}s_{11}^{E}\left(\frac{Z_{PZT}}{Z_{St} + Z_{PZT}}\frac{\tan(kl_{a})}{kl_{a}} - 1\right)\right]^{-1} \tag{1.1}$$

where $Z_{PZT} = -iwhs_{11}^{E}k/\omega tan(kl)$ is the short circuit impedance of the piezoelectric wafer, $k = (\omega^{2}\rho_{PZT}/s_{11}^{E})^{1/2}$ is the wave number, ρ_{PZT} is the density of the piezoelectric material, w, h, and $2l$ are the piezoelectric wafer's width, thickness and length, respectively. d_{13} is the piezoelectric coupling coefficient, s_{11}^{E} is the mechanical compliance of the material measured at zero electric field, and e_{33}^{σ} is the electric permittivity measured at zero stress.

In later studies, analytical, semi-analytical, and numerical electromechanical impedance models for one, two, and three-dimensional cases have been developed. These models are briefly reviewed in the following sections, with the focus on high-frequency applications.

Bhalla and Soh (Bhalla and Soh, 2004a) extended Liang's model to the two-dimensional case by introducing the concept of effective impedance. They defined the effective impedance as the ratio of the planner force exerted on the piezoelectric wafer to the change in its perimeter-normalized surface area. In later studies, Annamdas and Soh (Annamdas and Soh, 2007) introduced the concept of directional sum impedance and used it to develop a semi-analytical impedance model for the three-dimensional case.

Park et al. (Park et al., 2000a) successfully implemented Impedance-based SHM technique for real-time damage detection in composite reinforced concrete walls, a bridge section, and a pipe joint. Bhalla et al. (Bhalla et al., 2002) investigated a number of practical issues pertaining to the technique's implementation including multiplexing and sensor protection. They conducted a repeatability study over a period of two months and found that piezoelectric wafers performance was repeatable and reliable enough to be used in real-life structures. Park et al. (2003) studied several parameters affecting the impedance method, including measurement frequency range, sensing region, and excitation levels. Several application areas of impedance-based SHM were also reviewed and presented. In later studies, impedance-based SHM has been successfully applied to detect damage in numerous civil, aerospace, and mechanical components and structures, both in the lab and under real operating conditions. This included composite structures (Annamdas and Radhika, 2013; Saravanos and Heyliger, 1995; Wang and Zou, 2013; Xu and Liu, 2002a; ZOU et al., 2000), reinforced concrete (Han et al., 2015; Talakokula and Bhalla, 2014; Zou et al., 2015), bridges (Ko and Ni, 2005; Park et al., 2006), wind turbine blades (Pitchford et al., 2007; Taylor et al., 2014), space structures (Annamdas and Soh, 2010; Zagrai et al., 2010), and railroad track components (Bouteiller et al., 2006; Park et al., 2008).

As discussed earlier, impedance-based SHM is a vibration-based damage identification technique. Thus, its sensitivity depends on the frequency range at which the structure is excited and the response is measured. It has been shown that the wavelength of the excitation signal has to be smaller than the characteristic length of the damage in order for it to be successfully detected (Nokes and Cloud, 1993). Therefore, for enhanced sensitivity to incipient type damages, impedance-based SHM is carried out at high frequency, typically in the range of 30–400 kHz (Park et al., 2003). Peairs et al. (2007) studied the possibility of preselecting preferred frequency ranges based on the free transducer characteristics. They concluded that the characteristics of both the transducer and the host structure determine optimal monitoring frequency ranges.

Compared to other health monitoring and nondestructive evaluation techniques, impedance-based SHM has the advantage of being non-intrusive, highly sensitive to incipient damages, unaffected by changes in boundary conditions, model independent, suitable for autonomous continuous health monitoring, and readily applicable to complex structures. This makes the technique an attractive choice for damage detection purposes. However, the utilization of electromechanical impedance measurements for more than damage detection remains an active area of research. This can be ascribed to the high-frequency nature of impedance measurements and its accompanying challenges to damage identification efforts. This is discussed in more detail in the following sections.

1.2.2   High-Frequency Modeling

Chee et al. reviewed the main approaches developed for modeling piezoelectric transducers used in intelligent structures (Chee et al., 1998). They classified models into two main groups; analytical exact solutions, or finite element based solutions. Analytical solutions are only available for simple geometries with many simplifying assumptions regarding displacement fields, constitutive equations and perfect bonding between the piezoelectric patch and the structure. Finite element modeling, on the other hand, allows addressing more complex structures, but at the cost of increased computational requirements. In such early studies, high-frequency dynamic responses of smart structures have not been considered, and the discussions were limited to low-frequency applications.

Since then, the Finite Element Method (FEM) has been widely adopted to model the piezoelectric-structure interaction for a wide variety of applications. Linear and quadratic beam, shell, plate and solid piezoelectric elements have been formulated for this purpose, some were reviewed by Benjeddou (2000). Jiang and Li (2007) formulated a piezoelectric composite beam finite element taking into account high-order displacement fields, high-order electric fields, and a linear temperature field. Ha and Chang (2010a) developed a hybrid spectral finite element for modeling piezoelectric induced wave propagation in thin plates. In their work, 6th order elements (known as time domain spectral finite elements) were used in the in-plane direction, while 1st order elements were used in the thickness direction. This formulation led to a reduction in computational cost, compared to solid high-order elements, while maintaining a comparable accuracy. In spite of their superior accuracy compared to lower order finite elements, the computational cost associated with time domain spectral finite elements is relatively high, especially when used for high-frequency dynamic problems.

The frequency domain spectral element method, which will be referred to as Spectral Element Method (SEM) from now on, provides an efficient solution for modeling high-frequency structural vibrations. Unlike conventional finite element methods, SEM uses the homogeneous solutions of the governing equations in the frequency domain as basis functions. This eliminates the need for mesh refinement, and thus, the structure can be accurately represented by a small number of elements (James F Doyle, 1997; Lee et al., 2000; Lee, 2009). This has attracted several researchers to implement the SEM to study the high-frequency piezoelectric-structure interaction for SHM, active control of structural vibration and noise suppression applications.

Lee and Kim (2000) developed a two-layer elastic-piezoelectric beam model using the SEM. They adopted the Euler-Bernoulli and elementary rod assumptions for both layers, which adversely affected the accuracy of their model at high-frequency ranges. However, the superiority of this approach over the conventional FEM was evident. In a later study, they developed a three-layer elastic-viscoelastic-piezoelectric element to account for the effects of the bonding layer (Lee and Kim, 2001).

Park et al. (2010a) employed the Mindlin-Hermann rod and the Timoshenko beam theories for the base beam only while modeling the piezoelectric wafer following Euler-Bernoulli theory. In their work, the coupled equations of motion and boundary conditions were derived by applying Hamilton's principle assuming perfect bonding between the piezoelectric wafers and the structure. A similar model was developed by Park et al. (2013), where Lagrange multipliers were used to investigate the constraint forces at the piezoelectric-beam interface. In later studies, Lee et al. (2013) relaxed the assumption of negligible shear deformation in the piezoelectric wafer, and applied the Timoshenko beam theory for both layers, resulting in more accurate solutions at high-frequency ranges. All of the aforementioned models neglect the existence of the adhesive bonding layer between the piezoelectric and the host structure with the underlying assumption of perfect bonding. The effects of bonding layer characteristics on the dynamic behavior of smart structures are discussed in the following section.

1.2.3   Bonding Layer Effects

Piezoelectric-based SHM techniques, such as impedance, wave-propagation, and acoustic emission methods, normally utilize piezoelectric wafers that are surface bonded to the host structure through a layer of adhesive material. This layer provides a medium for stress transfer between the piezoelectric wafer and the structure. The effects of bonding layer on piezoelectric-structure interaction have been the focus of several analytical (Sirohi and Chopra, 2000; Han et al., 2008a; Dugnani, 2009; Ha and Chang, 2010b;

Agrahari and Kapuria, 2016; Islam and Huang, 2016; Willberg, 2016) and experimental (Reaves and Horta, n.d.; Qing et al., 2006; Islam and Huang, 2014) studies. These studies showed that the characteristics of the bonding layer, thickness and rigidity in particular, have a significant impact on the effectiveness of sensing and actuation achieved by piezoelectric transducers, the amplitude of waves propagating into the structure, and the measured electromechanical impedance. These effects are found to be more profound at high-frequency ranges (Qing et al., 2006).

Crawley and De Luis (1987) developed what is believed to be the first analytical model for piezoelectric-structure interaction that accounts for bonding layer effects. In their model, pure one-dimensional shear is assumed to exist in the bonding layer and pure extensional strain is assumed to exist in the piezoelectric patch and the base structure. They introduced a non-dimensional shear-lag parameter that quantifies the effectiveness of shear transfer through the bonding layer. They reported that the shear-lag effect becomes less significant as the shear modulus of the bonding layer increases or the layer's thickness decreases. Sirohi and Chopra (2000) followed Crawley and De Luis approach and derived a closed-form solution for the shear lag effect due to a finitely thick bonding layer. They found that the ratio of actuation strain of the piezoelectric transducer and the transferred strain in the beam surface, $(\zeta \equiv \varepsilon_{PZT}/\varepsilon_{Beam} - 1)$, is governed by the following equation

$$\frac{\partial^2 \zeta}{\partial x^2} - \Gamma^2 \zeta = 0 \qquad (1.2)$$

where $\Gamma^2 \equiv \frac{G}{E_{PZT}\, h_{PZT}\, h_{Bond}} + \frac{3G}{E_{Beam}\, h_{Beam}\, h_{Bond}}$ is the shear-lag correction factor, G is the shear modulus of the bonding layer, and h_i and E_i are the thickness and the Young's modulus of the ith layer, respectively. Based on this analysis, the effect of shear lag appears as a reduction in the effective dimensions of the piezoelectric patch. The fact that these models are based on the static approach, where the equivalent forces induced by the piezoelectric actuator is determined based on strain compatibility and static equilibrium in a frequency independent fashion, hinders their applicability to dynamic problems.

The impedance approach, first presented by Liang et al. (Liang et al., 1994a), was expanded by Xu and Liu (2002b) to include the effect of the bonding layer. In this approach, an effective structural impedance was calculated as the resultant of two impedances in series, the mechanical impedance of the host structure (Z_{St}), and that of the bonding layer (Z_{BL})

$$Z_{Eff} = \frac{Z_{St} Z_{BL}}{Z_{St} + Z_{BL}} = \xi Z_{St} \tag{1.3}$$

$$\xi = \frac{1}{1 + K_{St}/K_{BL}} \tag{1.4}$$

where K_{St} and K_{BL} are the dynamic stiffness of the structure and the bonding layer, respectively. For a perfectly bonded piezoelectric patch, $K_{BL} \to \infty$, and $Z_{Eff} = Z_{St}$. For the case of no coupling between the structure and the patch, $K_{BL} = 0$, and hence $Z_{Eff} = 0$.

Bhalla and Soh (2004b) studied the mechanism of force transfer through the bonding layer and its effect on the electromechanical impedance for one and two-dimensional cases. In their model, it was assumed that the beam is actuated in pure bending, the piezoelectric wafer is in a state of pure one-dimensional axial strain, and the bonding layer is in pure thickness-unvarying shear. For the one-dimensional case, they derived a closed form solution for the parameter ξ, which was introduced by Xu and Liu (2002b). A parametric study on the effects of bonding layer thickness and shear modulus on the electromechanical impedance response was also conducted. They found that a compliant, thick bonding layer can result in an overestimation of peak frequencies or the dominance of the piezoelectric patch own response.

The effects of bonding layer characteristics on the amplitude of the fundamental lamb wave modes were investigated by Ha and Chang (2010b). in this study, time domain spectral elements were utilized to model a piezoelectric actuated plate including the adhesive bonding layer. They found that the characteristics of the bonding layer along with the thickness and diameter of the piezoelectric transducers determine the amplitude of the generated lamb waves. Except for thin piezoelectric transducer, a thin adhesive layer with high rigidity was found to be advantageous for waves generation. A similar study was conducted by Islam and Huang (2016), however, they reported that an optimal value for adhesive thickness exists for a given system. This optimal value was found to be dependent on bonding layer rigidity and the characteristics of the piezoelectric transducers.

Qing et al. (2006) experimentally investigated the effect of bonding layer thickness and shear modulus on the performance of surface bonded piezoelectric patches. Three types of adhesives were investigated in their study, Hysol EA 9395, Hysol EA 9396, and Hysol EA 9361, with 4940 MPa, 2750 MPa, and 723 MPa elasticity moduli, respectively. Bonding thicknesses were varied from 10 μm to 120 μm. Experimental results showed that bonding layer properties impact the electromechanical impedance signature and the

amplitude of the measured signal. The effects are more profound at high-frequency ranges. Dugnani (2009) developed a dynamic model for a disk piezoelectric patch attached to a structure via a thin adhesive layer. The study found that the effect of the adhesive layer is frequency dependent, and the electromechanical impedance peaks shift to the lower frequency range as the thickness of the bonding layer increases.

Detailed numerical models for high-frequency piezoelectric-adhesive-structure interaction are very few in literature. Lee and Kim (2001) were the first to use spectral element method to model a three layered piezoelectric-viscoelastic-beam system. They modeled shear stress in the viscoelastic layer in terms of a stress relaxation function represented in Stieltjes integral form. Ritdumrongkul et al. (2004) modified Lee and Kim model and used elastic properties for the adhesive layer. However, both studies ignored rotary inertia and shear deformations for the beam and the piezoelectric wafer. Hence, the accuracy of such models is questionable at high-frequency ranges.

In this work, the high-frequency dynamic response of a coupled piezoelectric-beam system is modeled including the adhesive bonding layer. A new three-layer spectral element is formulated for this purpose. Elementary rod theory and Timoshenko beam theory are employed to model the base beam, the adhesive bonding layer, and the PZT wafer. Hence, the current model accounts for axial and shear deformations, in addition to rotary inertia for all three layers. This is the first model of piezoelectric-adhesive-structure interaction that takes such effects into consideration. The details of model development and validation are discussed in Chapter 2, whereas the effects of bonding layer characteristics on the high-frequency dynamic response of smart structures are addressed in detail in Chapter 3.

1.2.4   Vibration-based Damage Detection and Identification

Detection, localization, and characterization of damage in civil, aerospace, and mechanical structures and components have been the main objectives of all SHM practices. Vibration-based damage identification methods have been extensively studied over the last few decades. Detailed reviews of such methods have been presented by Doebling et. al (1996), Farrar et al. (2001), and Sohn et. al (2004), and more recently by Carden and Fanning (2004), Yan et al. (2007), and Fan and Qiao (2011). Global and local model-based damage identification techniques in time, frequency, and modal domains have been developed. Optimization algorithms, finite element model updating, and sensitivity-based methods have been also used to solve the inverse problem of damage identification. Changes in natural frequencies, mode shapes, modal parameters, mode shape curvature, and flexibility matrices are the most common damage-sensitive features that have been utilized for damage identification. Impedance signature can be added to the list as an

attractive choice to guide damage identification methods due to the ease and convenience with which it can be measured. This is especially true when incipient-type damages are to be located and characterized.

Due to the massive amount of literature related to this subject, the focus of this section is limited to those techniques utilizing natural frequencies, frequency response functions and impedance signatures for damage identification. Compared to other damage sensitive features, these are the easiest to measure, quantities are determined with high accuracy, and a single measurement location is sufficient in many applications.

Adams et al. (1978) were the first to propose the use of vibration measurements for damage location and magnitude assessment. In their study, a damage in a bar was modeled as a spring of stiffness (K) connecting the two undamaged sections. They found that the ratio of frequency variation of different modes is a function of damage location only

$$\frac{\Delta\omega_{n,p}}{\Delta\omega_{n,q}} = \frac{\left[\frac{x}{l}cosec^2\left(\frac{p\pi x}{l}\right) + \left(1 - \frac{x}{l}\right)cosec^2\left(p\pi\left(1 - \frac{x}{l}\right)\right)\right]q}{\left[\frac{x}{l}cosec^2\left(\frac{q\pi x}{l}\right) + \left(1 - \frac{x}{l}\right)cosec^2\left(q\pi\left(1 - \frac{x}{l}\right)\right)\right]p} \tag{1.5}$$

where x is the location of the damage, l is the length of the bar, and $\Delta\omega_{n,i}$ is the change in natural frequency of the ith mode. This derivation is valid only for bar like structures where axial modes of vibration are considered. Moreover, the analysis assumes that damage severity affects different modes in the same manner, which is not always valid.

Gudmundson (1982) developed a method based on first-order perturbation theory to predict changes in natural frequencies due to cracks and notches. He found that the change in the natural frequency of the nth mode induced by the presence of a crack depends on the strain energy of the static solution

$$\omega_{crack}^2 = \omega_n^2\left[1 - \frac{W_1}{W_0}\right] \tag{1.6}$$

where ω_n is the undisturbed natural frequency of the nth mode, W_1 is the strain energy change due to the crack, and W_0 is the total strain energy of the nth mode.

Since then, several studies have been published utilizing shifts in natural frequencies as a damage identification parameter. These were first reviewed by Salawu (1997). In this review, a number of factors limiting the successful application of such approaches were discussed. The study found that poor sensitivity to local damages and the dependence on boundary conditions, which are both associated with the dependence on low order natural frequencies, to be the main limitations of natural frequency-based damage identification algorithms.

Cerri and Vestroni (2000) studied analytically the impact of location and intensity of a diffused crack on the frequency variations of the first three modes of a beam. In their study, cracks were modeled as rotational springs, whose normalized stiffness (k) is a function of crack width and severity

$$k \equiv \frac{K}{EI_0/l} = \frac{1-\beta}{b\beta} \tag{1.7}$$

where EI_0 is the flexural rigidity of the undamaged beam, l is the total length of the beam, b is the damaged section width normalized by the length l, and β is ratio of the flexural rigidity of the damaged section to that of the pristine part. Solving the characteristic equation for a beam with a torsional spring allows the determination of natural frequencies as a function of crack location and intensity. Two approaches where proposed to solve the inverse problem of damage identification. The first is based on finding damage parameters that satisfy the characteristic equation for at least three measured frequencies. The second approach minimizes an objective function quantifying the difference between measured and simulated natural frequencies. A similar study was conducted by Chinchalkar (2001), but the problem was approached numerically using FEM. These studies found that the accuracy of the proposed approaches is strongly dependent on the characteristics of the damage being identified, especially its location.

Lee and Chung (2000) used the lowest four natural frequencies of a cracked beam to get a first approximation of crack location using a mode ordering technique. For this approximate location, crack size is determined by the FEM. The crack location is then updated using the determined crack size and natural frequencies following Equation 1.6. With this method, a maximum error of 25% in damage severity was reported. Furthermore, due to the limitations of the mode ordering technique, the approach is only applicable to a single crack.

Kim et al. presented a finite element based damage-localization algorithm. This algorithm requires the evaluation of a modal energy matrix, F_{ij}, for the ith mode that is concentrated in the jth element

$$F_{ij} = \frac{\{\phi_i\}^T [C_j] \{\phi_i\}}{\{\phi_i\}^T [C] \{\phi_i\}}$$ (1.8)

where $\{\phi_i\}$ is the ith mode shape, $[C]$ is the global stiffness matrix of the system, and $[C_j]$ is the contribution of the jth element to the global stiffness matrix. Damage location is then determined by solving for an element damage index vector, α_j, as follows

$$\left(\frac{\Delta\omega_i}{\omega_i}\right)^2 = \sum_{j=1}^{NE} F_{ij}\alpha_j$$ (1.9)

They also developed a damage severity algorithm based on modal strain energy defined for Euler-Bernoulli beams. Both algorithms were successful in characterizing cracks located near the center of the beam; however, the accuracy severely degraded as the cracks were shifted towards the edges.

Yang and Wang (2010) used the concept of natural frequency vector assurance criterion for damage detection. With this approach, several damage configurations were simulated using a finite element model of the structure. The resulting natural frequency vectors were used to build damage feature database. Measured natural frequencies of an unknown damaged structure were then compared to this database to detect and characterize damages.

For all the aforementioned studies, one common limitation is that the low-frequency dynamic response of the structure is utilized for damage characterization. Therefore, such techniques are not sensitive to local and incipient type damages where the damage-induced change in the global dynamic response is insignificant (Farrar et al., 2001). Furthermore, these techniques are sensitive to boundary conditions variations, which hinders their applicability to real structures.

Frequency Response Function (FRF) based damage identification techniques have also been extensively studied over the last few decades. Thyagarajan et al. (1998) developed an FRF assignment method for damage identification. The technique is, in fact, an optimization-based FE model updating technique that uses FRFs of damaged and pristine structures to solve for stiffness and damping scale factors. The optimization problem is solved using QNSTR subroutine, which is part of Matlab optimization toolbox. The technique is computationally inefficient, as the optimization technique is brute force in nature, and a large number of objective function evaluations were needed for convergence.

Lee and Shin (2002) developed an FRF-based structural damage identification method by evaluating a damage identification matrix. The technique was applied to beams modeled following Euler-Bernoulli theory. The evaluation of this damage identification matrix requires the knowledge of mode shapes and natural frequencies of the pristine structures along with the FRF of the damaged structure. For this technique to work, FRFs of the damaged structure need to be measured at several locations, which is not always feasible. Furthermore, the proposed technique relies on the first few modes, which are global in nature. Therefore, it is expected to be insensitive to incipient-type damages.

Few studies utilized the impedance signature for damage characterization. In these studies, the SEM is utilized to simulate the high-frequency dynamic response of the structure under consideration, which is then compared to the measured response. Park et al. developed a technique to detect and locate structural damages in rods by monitoring impedance measurements and tracking changes in the FRF data (Park et al., 2000b). Similar work was presented by Guo et al. (2011), where they utilized SEM, optimization techniques, and impedance measurements for damage characterization. In these studies, the structure under consideration was discretized to a finite number of spectral elements. Damage is then characterized by solving for changes in the local wave number in each individual element. Such approaches increase the number of elements required to model the structure and hamper the advantages offered by the SEM. Furthermore, the accuracy to which the damage can be identified is limited by the resolution of the spectral element mesh.

1.2.5   Acoustoelastic-based Stress Measurement

Ultrasonic waves have been used in the field of nondestructive testing since 1929 (Hauk, 1997). This technique involves introducing low-energy, high-frequency stress wave in the material and analyzing its propagation and reflections to evaluate structural integrity. The use of ultrasonic waves for material characterization and stress measurement dates back to 1953 when Hughes and Kelly laid the basis for the theory of acoustoelasticity (Hughes and Kelly, 1953). They studied the propagation of bulk elastic waves in a pre-stressed solid by adopting Murnaghan theory of finite deformations along with third-order elasticity theory, and described the dependence of longitudinal and shear wave speeds on the state-of-stress. Bulk waves are in general nondispersive, and their dependence on the state-of-stress can be simply described in terms of the third order elastic constants. The nondispersive nature of such waves allows the utilization of time-of-flight measurements to determine changes in wave speed. This has laid the foundation for material characterization and stress measurement applications via waves birefringence.

The extension of this theory to wave propagation in semi-infinite and bounded materials has been thoroughly investigated in the literature. Hayes and Rivlin (1961) studied the propagation of Rayleigh surface waves in a uniformly deformed isotropic material. Under such deformation, surface waves are nondispersive, and the change in wave speed is proportional to principle strains. If the initial state-of-stress is nonuniform, Rayleigh waves become dispersive (Hirao et al., 1981). Duquennoy et al. (1999) theoretically determined Rayleigh wave acoustoelastic coefficients for orthotropic materials based on its intrinsic characteristics; its density and the second- and third-order elastic constants. Husson (1985) theoretically investigated the acoustoelastic effect for Lamb waves. He showed that the dispersive nature of symmetric and anti-symmetric Lamb waves is reflected on their corresponding acoustoelastic constants, and these constants are strongly dependent on frequency. Numerous theoretical, numerical, and experimental studies have been conducted to further investigate the acoustoelastic effect and demonstrate its potential applications (Chen and Wilcox, 2007a; Chaki and Bourse, 2009; Loveday and Wilcox, 2010; Frikha et al., 2011). Gandhi et al. (2012) theoretically and experimentally studied the propagation of lamb waves in biaxially-stressed plates. They found that the change in wave speed, for both symmetric and anti-symmetric modes, is strongly dependent on propagation direction and excitation frequency. Similar results were reported by Shi et al. (2013), where they estimated arbitrary biaxial loads acting on aluminum plates based on changes in phase velocity along multiple propagation directions. For the plate shown in Figure 1.a, the change in ultrasonic plane wave velocity with the application of stress can be expressed as (Hauk, 1997; Shi et al., 2013)

$$\frac{\Delta C_p(\theta)}{C_p^0(\theta)} = (K_1\sigma_{11} + K_2\sigma_{22})cos^2(\theta) + (K_3\sigma_{11} + K_4\sigma_{22})sin^2(\theta) \qquad (1.10)$$

where ΔC_p is the change in phase velocity due to the application of stress, C_p^0 is the stress-free phase velocity, θ is the direction of wave propagation in the principal coordinate system, and σ_{11} and σ_{22} are the principal stresses. The constants $K_1, \dots, K_4$, are the acoustoelastic constants for the particular wave mode, which are functions of second and third order elastic constants. Third order constants are known for their sensitivity to microstructural changes in the material being tested. Therefore, calibration is required to calculate the values of the acoustoelastic constants, which requires a known reference state-of-stress. Such a reference state is not always available, especially if the structure of interest is already in service.
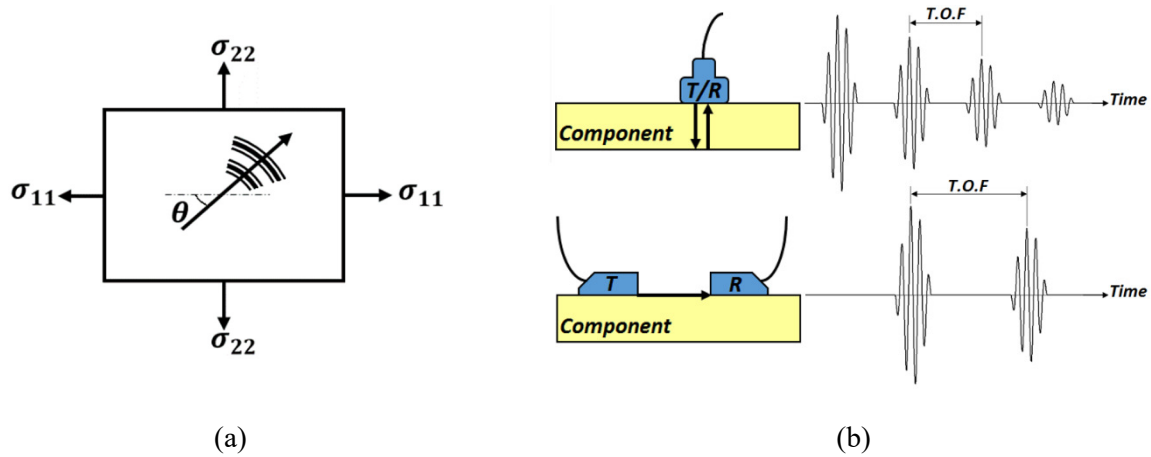
Figure 1.1. (a) a plane wave propagating in a plate under biaxial stress, and (b) Time-Of-Flight (T.O.F) measurement configurations of ultrasonic waves. Reproduced and modified from (Withers and Bhadeshia, 2001).

Changes in phase velocity are determined based on time-of-flight measurements, some configurations for conducting such measurements are shown in Figure 1.b. Since changes in ultrasonic wave velocity are in the order of 10^{-6} per MPa (Hauk, 1997), time-of-flight has to be measured with nanosecond accuracy. Hence, extremely high sampling rates are needed. Furthermore, uncertainties associated with noise contamination, ultrasonic attenuation, along with dispersion effects adversely affect the accuracy within which time-of-flight can be determined, which in turn results in high uncertainty in the measured state-of-stress.

The effects of excitation frequency on the sensitivity of the acoustoelastic effect have been addressed by a number of researchers. Rizzo and di Scalea (2003) studied the acoustoelastic effect in axially loaded steel bars. They reported that the acoustoelastic sensitivity is frequency-dependent, and low excitation frequencies result in the largest sensitivity. Albakri and Tarazaga (2016) theoretically showed, based on approximate beam theories, that the sensitivity and robustness of stress measurements are enhanced when low-frequency first anti-symmetric lamb wave mode (A_0) is utilized. However, at low frequencies, A_0 mode is strongly dispersive (Graff, 1975; James F Doyle, 1997). Due to their highly dispersive nature, the original waveform distorts as it propagates through the structure rendering time-of-flight-based wave speed measurements impractical. Therefore, advanced analysis techniques are required to tackle the problem of wave propagation of highly dispersive modes. Few studies can be found in the literature describing methods and algorithms designed to compensate for the effects of dispersion in propagating waves (De

Marchi et al., 2010, 2009; Fromme et al., 2006; Perelli et al., 2012; Wilcox, 2003; Zhai et al., 2010). These methods utilize dispersion curves, group velocity, in particular, to backtrack dispersion effects and reconstruct a "dispersion-free" signal in the space domain. Dispersion compensation techniques have mainly been developed for events localization purposes, where propagating waves are utilized to determine impact or structural defect locations. The utilization of such algorithms for material characterization and stress measurement is yet to be investigated. Furthermore, successful implementation of dispersion compensation algorithms requires the measured response to be free of reflections, which imposes a lower limit on the frequency range that can be utilized.

1.3   Research Goals and Objectives

The main goal of this research effort is to advance the current state of the art of impedance-based SHM and acoustoelastic-based stress measurements, and lay the foundation for an integrated structural health and loading monitoring system capable of providing more a complete assessment of the state of the structure. The literature survey presented in the previous section identified a number of challenges facing the achievement of this goal. Addressing these challenges by developing and integrating theoretical models, numerical algorithms, and experimental techniques define the main objectives of this work. These objectives can be summarized as follows

- **Development and validation of high-frequency piezoelectric-structure interaction model**
  The sensitivity of vibration-based damage detection techniques to incipient type damages increases at higher frequencies. Therefore, developing a computationally efficient model for piezoelectric-structure interaction that retains its accuracy at high-frequency ranges is crucial for model-based damage characterization efforts.

  To assure the accuracy of the underlying assumptions adopted in the model development along with its numerical implementation, the results have to be validated against high-fidelity models developed using commercial finite element packages.

- **Study the effects of adhesive bonding layer on the dynamic behavior of piezoelectric augmented structures**
  Piezoelectric-based SHM techniques normally utilize surface bonded piezoelectric wafers, where the characteristics of the adhesive bonding layer have a significant impact on piezoelectric-structure

interaction. A detailed parametric study of the adhesive bonding layer effects on the dynamic response of smart structures including transfer functions, impedance signature, wave propagation and sensitivity to structural damages will help better understand these effects, and improve the accuracy of model-based damage characterization efforts.

- **Development of computationally efficient impedance-based damage characterization method**
  Impedance signatures are known to be highly sensitive to structural defects and can be easily and conveniently measured. Developing a computationally efficient algorithm that utilizes impedance measurements for damage identification purposes will extend the capabilities of impedance-based SHM beyond mere damage detection, and provide a more complete assessment of structures' integrity.

- **Development of robust, reference-free acoustoelastic-based stress measurement technique**
  In order to enhance the sensitivity of acoustoelastic-based measurements to the state-of-stress in the structure, low-frequency anti-symmetric lamb wave modes have to be utilized, with dispersion and reflections being the main challenges. Developing a stress measurement technique capable of dealing with these challenges is crucial for the utilization of such highly stress sensitive waves.

- **In-field implementation of structural health and loading monitoring system for railroad track components**
  The Railroad industry is considered as a potential customer that will significantly benefit from the developed structural health and loading monitoring systems. To evaluate the performance, robustness, and reliability of these techniques under real-life operating and environmental conditions, in-field implementation and testing on operating railroad tracks have to be conducted.

1.4   Dissertation Layout

The structure of this dissertation follows the order by which the previously discussed challenges have been raised. In Chapter 2, the high-frequency piezoelectric-structure interaction model is developed including the adhesive bonding layer. A new three-layer spectral element is formulated for this purpose. Elementary rod theory and Timoshenko beam theory are employed to model the base beam, the adhesive bonding layer, and the piezoelectric wafer. The effects of bonding layer characteristics on the high-frequency dynamic

response of smart structures are discussed in detail in Chapter 3. A parametric study is conducted to evaluate the effects of bonding layer thickness and modulus of rigidity on the transient and steady-state response of the coupled system, including frequency response functions and electromechanical impedance.

An optimization-based damage characterization approach that utilizes the high-frequency impedance signature is developed in Chapter 4. This approach overcomes the limitations addressed in Section 1.2.4 by introducing two new features: adaptive spectral element discretization, and sine-fit damage localization. The former minimizes the total number of elements required to discretize the system along with the number of damage characterization parameters, while the later solves the ill-posed inverse problem of damage characterization in a computationally efficient manner. These features are integrated into a two-stage optimization algorithm to fully characterize open cracks in one-dimensional structures.

Chapter 5 addresses the problem of low-frequency acoustoelastic-based stress measurements. A new model-based stress measurement technique is developed, where the acoustoelastic theory is integrated with a numerical optimization algorithm to calculate the state-of-stress in one-dimensional structures of arbitrary cross-sections. The details of the algorithm's development and experimental validation are discussed in the chapter, along with an in-depth analysis of its performance in the presence material and geometry-related uncertainties.

Practical applications of the developed structural health and loading monitoring systems are presented in Chapter 6. The major contributions of this work along with future research directions are highlighted in Chapter 7.

Chapter Two

Piezoelectric-structure Interaction Model

2.1 Introduction

For SHM applications, transient and steady-state electromechanical responses of piezoelectric wafers are utilized for incipient damage detection and identification. Impedance-based SHM, for instance, measures the steady-state impedance signature of a piezoelectric wafer attached to a host structure. Changes in the electrical impedance of the piezoelectric wafer reflect changes in the mechanical impedance of the host structure, and hence, structural damage can be detected (Liang et al., 1994a; Park et al., 2003, 2000b; Albakri and Tarazaga, 2014). The transient dynamic response, on the other hand, is the focus of wave-propagation-based SHM techniques. In such techniques, piezoelectric wafers are used to excite the structure generating progressive elastic waves. Transmitted and reflected waves along with dispersion relations and time-of-flight are then analyzed to detect and locate structural defects (Krawczuk et al., 2004; Raghavan and Cesnik, 2007). Accurate modeling of the high-frequency piezoelectric-structure interaction is extremely important to further develop the capabilities of such SHM techniques and optimize their performance.

In this chapter, the high-frequency dynamic response of a coupled piezoelectric-beam system is modeled including the adhesive bonding layer in between. The chapter starts with exploring the fundamental theories for modeling the dynamic response of decoupled beam and piezoelectric components and builds on that to formulate a new comprehensive three-layer piezoelectric-adhesive-beam element. Elementary and Mindlin-

Herrmann approximate rod theories, along with Euler-Bernoulli and Timoshenko approximate beam theories are employed to model each of the aforementioned components, and the results are validated against the commercial FE package, Abaqus.

2.2   Fundamental Beam Theories

This section discusses a number of approximate theories for longitudinal and flexural deformations in one-dimensional structures. These theories include the Elementary rod theory, Mindlin-Herrmann rod theory, Euler-Bernoulli beam theory, and Timoshenko beam theory. The underlying assumptions of each theory are discussed in detail. Spectral element formulation following each of the aforementioned theories is presented, and the results are compared to the FEM predictions, where plane-stress second-order elements are used to discretize the structure. Furthermore, dispersion relations predicted by each theory are compared to the exact solution given by Pochhammer-Chree frequency equation. Concluding remarks regarding the frequency range within which each approximate theory is valid are presented at the end of the section.

2.2.1   Euler-Bernoulli Beam and Elementary Rod Theories

Consider a linear elastic, homogeneous beam undergoing axial and lateral deformations. Let axial deformations be approximated by the Elementary (classical) rod theory, while lateral deformations be described by the Euler-Bernoulli beam theory. For this system, the displacement field can be expressed as

$$u(x, z, t) = u_0(x, t) - z \frac{\partial w_0}{\partial x}(x, t)$$
$$w(x, z, t) = w_0(x, t)$$

(2.1)

where u_0 and w_0 are the axial and lateral displacements of the beam's neutral axis, respectively. With the assumption of small strains and deflections, and upon the application of Hamilton's principle, the equations of motion in u and w directions are found to be

$$\rho A \frac{\partial^2 u_0}{\partial t^2} - EA \frac{\partial^2 u_0}{\partial x^2} = 0$$
$$\rho A \frac{\partial^2 w_0}{\partial t^2} + \frac{\partial^2}{\partial x^2} \left(EI \frac{\partial^2 w_0}{\partial x^2} \right) = 0$$

(2.2)

where E, ρ, A and I are the beam's modulus of elasticity, mass density, cross sectional area and second moment of area, respectively. Boundary conditions are also obtained following the application of Hamilton's principle as follows

$$F_x = EA\frac{\partial u_0}{\partial x}$$

$$F_z = -EI\frac{\partial^3 w_0}{\partial x^3} \tag{2.3}$$

$$M = EI\frac{\partial^2 w_0}{\partial x^2}$$

Due to geometric and material symmetry around the neutral axis, axial and flexural displacements, u_0 and w_0, are fully decoupled. Since no geometric nor material nonlinearities are considered, the principle of superposition is applicable, and the response of the system to a generalized excitation can be obtained by independently solving for the responses to the x- and z-components of that excitation.

Following the procedure outlined in Appendix A, a spectral Euler-Bernoulli-Elementary-Rod (EBER) element is formulated. In frequency domain, response variables, u_0 and w_0, are expressed as

$$\begin{Bmatrix} u_0 \\ w_0 \end{Bmatrix}(x,t) = \frac{1}{N}\sum_{n=0}^{N-1}\begin{Bmatrix} U \\ W \end{Bmatrix}_n(x,\omega_n)e^{i\omega_n t} = \frac{1}{N}\sum_{n=0}^{N-1}\sum_m\left(\begin{Bmatrix} A_m \\ B_m \end{Bmatrix}e^{-ik_{mn}x}\right)e^{i\omega_n t} \tag{2.4}$$

Since the two equations are fully decoupled and can be solved independently, the scaling matrix r_m, appearing in Eq. A.3, is not necessary and the formulation can proceed taking only the amplitude vector A, into consideration. Substituting the spectral solution in the governing equations yields

$$\begin{bmatrix} -\rho A\omega^2 + EAk^2 & 0 \\ 0 & -\rho A\omega^2 + EIk^4 \end{bmatrix}A = 0 \tag{2.5}$$

For a nontrivial solution, the above matrix has to be singular, which leads to the characteristic equation

$$(-\rho A\omega^2 + EAk^2)(-\rho A\omega^2 + EIk^4) = 0 \tag{2.6}$$

This results in a 6th order polynomial in k, with the following solutions

$$k_{1,2} = \pm\alpha\omega, \; k_{3,4} = \pm\beta\omega^{1/2}, \; k_{5,6} = \pm i\beta\omega^{1/2} \tag{2.7}$$

where $\alpha = (\rho/E)^{1/2}$ and $\beta = (\rho A/EI)^{1/4}$. Thus, EBER theory predicts three wave modes, these are a propagating axial wave, a propagating flexural wave and an evanescent flexural mode. For the beam shown in Figure 2.1, the non-dimensional real and imaginary components of the wavenumbers predicted by EBER theory are depicted in Figure 2.2.

Material Properties

$E = 69 \; GPa, v = 0.33$

$\rho = 2700 \; Kgm^{-3}$

Dimensions

$L_b = 400 \; mm, h_b = 2 \; mm$

$width = 20 \; mm$
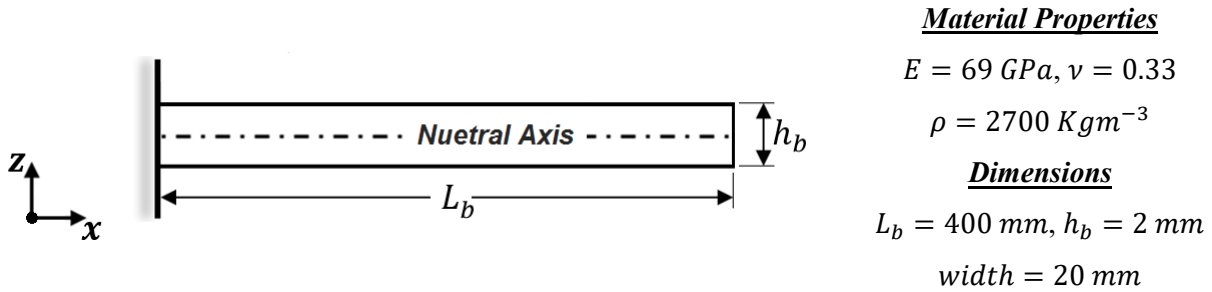
Figure 2.1 Dimensions and material properties for a simple beam considered in this section.
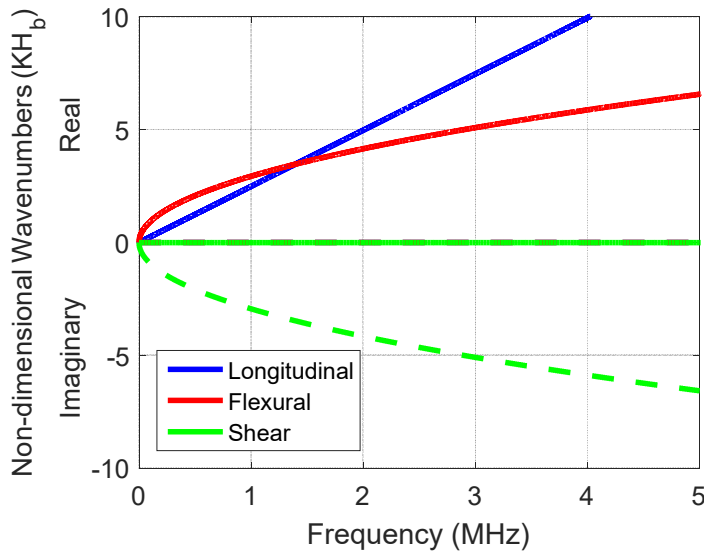
Figure 2.2. Non-dimensional wavenumbers predicted by EBER theory.
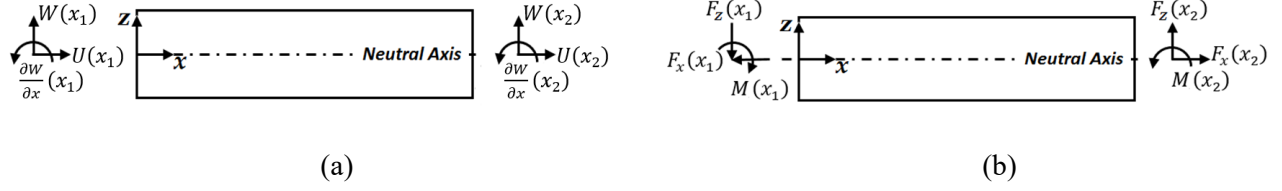
Figure 2.3. Beam element showing (a) nodal displacements, and (b) nodal forces

For a two-node spectral element, shown in Figure 2.3, spectral nodal degrees of freedom are defined as follows

$$
\boldsymbol{d} = \begin{Bmatrix} u_0(0) \\ w_0(0) \\ \dot{w}_0(0) \\ u_0(L) \\ w_0(L) \\ \dot{w}_0(L) \end{Bmatrix}
$$

$$
= \underbrace{\begin{bmatrix} 1 & 1 & 0 & 0 & 0 & 0 \\ 0 & 0 & 1 & 1 & 1 & 1 \\ 0 & 0 & -ik_3 & -ik_4 & -ik_5 & -ik_6 \\ e^{-ik_1 L} & e^{-ik_2 L} & 0 & 0 & 0 & 0 \\ 0 & 0 & e^{-ik_3 L} & e^{-ik_4 L} & e^{-ik_5 L} & e^{-ik_6 L} \\ 0 & 0 & -ik_3 e^{-ik_3 L} & -ik_4 e^{-ik_4 L} & -ik_5 e^{-ik_5 L} & -ik_6 e^{-ik_6 L} \end{bmatrix}}_{H(\omega)} \boldsymbol{A}
\tag{2.8}
$$

Nodal forces and moments, shown in Figure 2.3.b, are given by

$$
\boldsymbol{F} = \begin{Bmatrix} F_x(0) \\ F_z(0) \\ M(0) \\ F_x(L) \\ F_z(L) \\ M(L) \end{Bmatrix} = \underbrace{\begin{bmatrix} ik_1 EA & ik_2 EA & 0 & 0 \\ 0 & 0 & iEIk_3^3 & iEIk_6^3 \\ 0 & 0 & EIk_3^2 & \ldots & EIk_6^2 \\ -ik_1 EA e^{-ik_1 L} & -ik_2 EA e^{-ik_2 L} & 0 & 0 \\ 0 & 0 & -iEIk_3^3 e^{-ik_3 L} & -iEIk_6^3 e^{-ik_6 L} \\ 0 & 0 & -EIk_3^2 e^{-ik_3 L} & -EIk_6^2 e^{-ik_6 L} \end{bmatrix}}_{G(\omega)} \boldsymbol{A}
\tag{2.9}
$$

From which the dynamic stiffness matrix, $\boldsymbol{K}(\omega)$, is obtained as follows

$$
\boldsymbol{F} = \boldsymbol{G}(\omega)\boldsymbol{H}^{-1}(\omega)\boldsymbol{d} = \boldsymbol{K}(\omega)\boldsymbol{d}
\tag{2.10}
$$

Receptance Frequency Response Function (FRF) obtained by a single EBER spectral element is compared to that predicted by the commercial finite element package, Abaqus, for the beam shown in Figure 2.1. Quadratic, plane-stress elements with a reduced integration rule are selected to spatially discretize the structure. The FE mesh was refined until convergence was achieved at the frequency range of interest. For 0-10 kHz frequency range, 2 layers of plane stress elements with 75 elements in each layer are sufficient for mesh convergence. Figure 2.4 shows the driving point receptance FRF for the beam tip when the beam is excited in x- and z- directions. It could be noticed that both models are in a good agreement up to the 16th mode (~6.9 KHz), beyond which the responses start to deviate with more than 1% error in natural frequencies. Both models predict the exact same natural frequency for the 19th mode (9479 Hz), which is the 2nd longitudinal mode.

2.2.2   Timoshenko Beam and Elementary Rod Theories

For the beam described in Section 2.2.1, the assumptions of negligible shear strain and rotary inertia are relaxed by adopting Timoshenko beam theory to describe the lateral deformations. This leads to the following displacement field
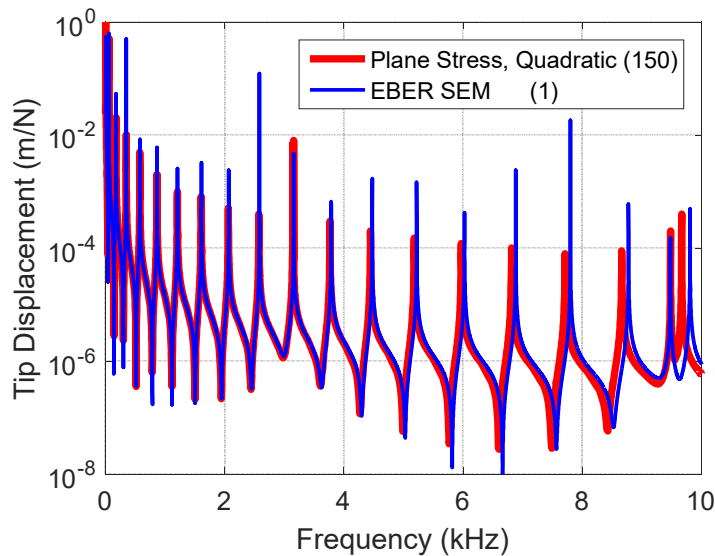
Figure 2.4. Driving point receptance FRF of the beam tip. In the figure, SEM predictions are shown in thin blue lines, while those of plane-stress finite elements are shown in thick red lines.

$$u(x,z,t) = u_0(x,t) - z\phi(x,t)$$
$$w(x,z,t) = w_0(x,t)$$

(2.11)

where ϕ denotes the angle of rotation of the beam's neutral axis normal. Applying Hamilton's principle, the equations of motion and boundary conditions are found to be

$$\rho A \frac{\partial^2 u_0}{\partial t^2} - EA \frac{\partial^2 u_0}{\partial x^2} = 0$$

$$\rho A \frac{\partial^2 w_0}{\partial t^2} - GA\bar{K}\left(\frac{\partial^2 w_0}{\partial x^2} - \frac{\partial \phi}{\partial x}\right) = 0$$

(2.12)

$$\rho I \frac{\partial^2 \phi}{\partial t^2} - EI \frac{\partial^2 \phi}{\partial x^2} - GA\bar{K}\left(\frac{\partial w_0}{\partial x} - \phi\right)$$

and

$$F_x = EA \frac{\partial u_0}{\partial x}$$

$$F_z = GA\bar{K}\left(\frac{\partial w_0}{\partial x} - \phi\right)$$

(2.13)

$$M = EI \frac{\partial \phi}{\partial x}$$

where $\bar{K}$ is the Timoshenko correction factor, which will be calculated later in this section. As it is the case for EBER theory, axial and flexural displacements, u_0 and w_0, are fully decoupled due to the geometric and material symmetry around the neutral axis. Following the procedure outlined in Appendix A, a spectral Timoshenko Beam Elementary Rod (TBER) element is formulated as follows

$$\begin{Bmatrix} u_0 \\ w_0 \\ \phi \end{Bmatrix}(x,t) = \frac{1}{N}\sum_{n=0}^{N-1}\begin{Bmatrix} U \\ W \\ \Phi \end{Bmatrix}_n (x,\omega_n)e^{i\omega_n t} = \frac{1}{N}\sum_{n=0}^{N-1}\sum_m \left(\begin{Bmatrix} A_m \\ B_m \\ r_{2m}B_m \end{Bmatrix}e^{-ik_{mn}x}\right)e^{i\omega_n t}$$

(2.14)

where the transverse displacement Fourier coefficient is chosen to be the reference with respect to which the in-plane rotation Fourier coefficient is scaled. Substituting the assumed spectral form in the governing equations and seeking a non-trivial solution yield the following characteristic equation

$$det\left(\begin{bmatrix} -\rho A\omega^2 + EAk^2 & 0 & 0 \\ 0 & -\rho A\omega^2 + GA\overline{K}k^2 & -iGA\overline{K}k \\ 0 & iGA\overline{K}k & -\rho I\omega^2 + EIk^2 + GA\overline{K} \end{bmatrix}\right) = 0 \qquad (2.15)$$

This results in a 6th order polynomial in k, representing three wave modes. Two of these modes are always propagating modes, representing axial and flexural waves, while the third (which represents a shear mode) starts as an evanescent mode and transfers to a propagating mode upon passing through the cut-off frequency $\omega_c = (GA\overline{K}/\rho I)^{1/2}$. The correction factor $\overline{K}$ can be determined by either matching the cut-off frequency to that of lamb waves, or by matching the high-frequency flexural mode wave speed to that of Rayleigh wave speed (Doyle, 1997). Following the later criterion, Timoshenko correction factor is found to be:

$$\overline{K} = \frac{C_R^2}{C_S^2} = \left(\frac{0.87 + 1.12\nu}{1 + \nu}\right)^2 \qquad (2.16)$$

which yields $\overline{K} = 0.869$ for $\nu = 0.33$. Figure 2.5 shows the non-dimensional wavenumbers predicted by this theory for the beam shown in Figure 2.1 and a 0.869 correction factor. Once wave numbers are calculated for a given frequency, the amplitude ratio, $r_{2m} \ni m = 3, \dots, 6$, in Eq. 2.14 is obtained as follows
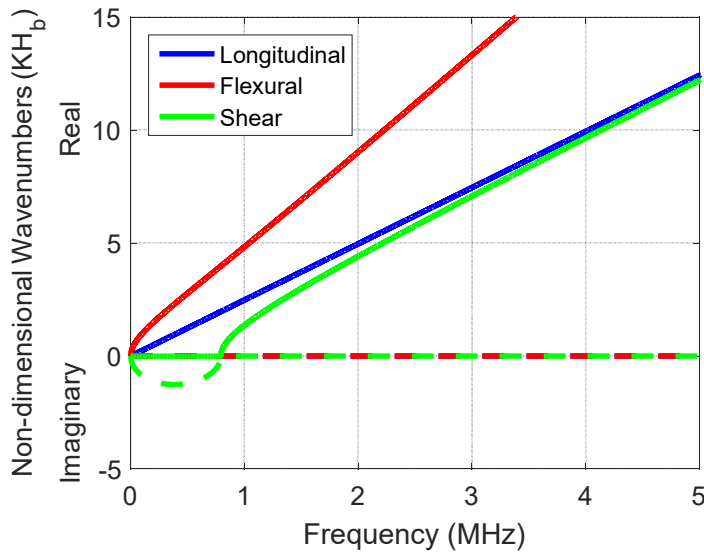
Figure 2.5. Non-dimensional wavenumbers predicted by TBER theory.

$$r_{2m} \equiv \frac{|\Phi|}{|W|} = -i\frac{\rho A\omega^2 - GA\overline{K}k_m^2}{GA\overline{K}k_m} \tag{2.17}$$

For a two-node spectral element, Figure B.1, spectral nodal degrees of freedom and spectral nodal forces and moments vectors are defined as

$$\boldsymbol{d} = \{U_1 \quad W_1 \quad \Phi_1 \quad U_2 \quad W_2 \quad \Phi_2\}^T = \boldsymbol{H}(\omega)\boldsymbol{A}$$
$$\boldsymbol{F} = \{F_{x1} \quad F_{z1} \quad M_1 \quad F_{x2} \quad F_{z2} \quad M_2\}^T = \boldsymbol{G}(\omega)\boldsymbol{A} \tag{2.18}$$

where $\boldsymbol{H}(\omega)$ and $\boldsymbol{G}(\omega)$ are defined in Appendix B. The dynamic stiffness matrix, relating nodal displacements and nodal forces in frequency domain, is then obtained following Eq. 2.10.

Figure 2.6 shows the driving point receptance FRF for the beam tip obtained with a single TBER spectral element as compared to the FEM predictions with the mesh described in Section 2.2.1. It could be noticed that both models are in a very good agreement over the entire frequency range. Error in natural frequencies at the 20th mode (at 9665 Hz) is 0.01%, which is of the same order of magnitude of the frequency resolution used to calculate the FRFs. Although the beam selected for this study is considered to be slender, with $h_b/L_b = 0.05$, the improvement that Timoshenko beam theory provides over Euler-Bernoulli beam theory is evident, as a comparison between figures 2.4 and 2.6 would suggest. Hence, Timoshenko beam theory will be adopted to describe the transverse vibration for the piezoelectric-structure interaction model. As for longitudinal vibration, Mindlin-Herrmann higher order rod theory is investigated in the upcoming section.

2.2.3   Timoshenko Beam and Mindlin-Herrmann Rod Theories

For the beam described in Section 2.2.1, the assumption of negligible lateral contractions induced by Poisson's effect is relaxed by adopting the Mindlin-Hermann rod theory to describe the axial deformations of the beam. This leads to the following displacement field

$$u(x,z,t) = u_0(x,t) - z\phi(x,t)$$
$$w(x,z,t) = w_0(x,t) + z\varphi(x,t) \tag{2.19}$$

where φ denotes the lateral contraction due to Poisson's effect. Applying Hamilton's principle, the equations of motion and boundary conditions are found to be
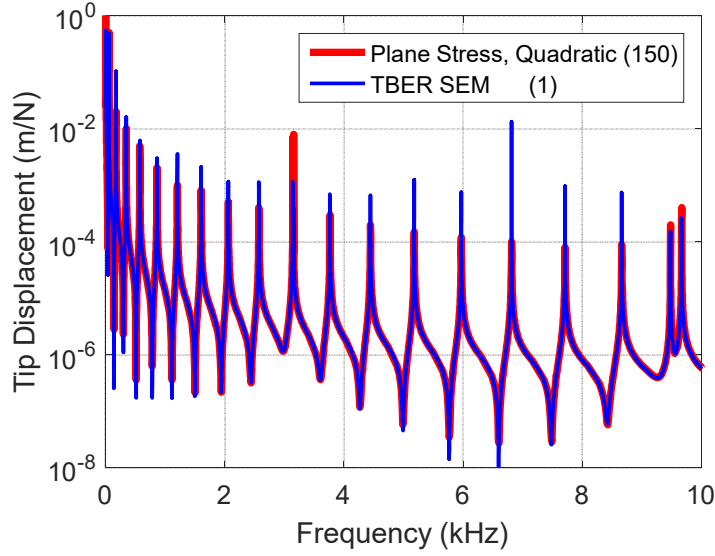
Figure 2.6. Driving point FRF of the beam tip. TBER SEM predictions are shown in thin, blue lines, while plane-stress FEM predictions are shown in thick, red lines.

$$\rho A \frac{\partial^2 u_0}{\partial t^2} - Q_{11}A \frac{\partial^2 u_0}{\partial x^2} - Q_{13}A \frac{\partial \varphi}{\partial x} = 0$$

$$\rho I \frac{\partial^2 \varphi}{\partial t^2} + Q_{13}A \frac{\partial u_0}{\partial x} - Q_{55}\overline{K}I \frac{\partial^2 \varphi}{\partial x^2} + Q_{33}A\varphi = 0$$

$$\rho A \frac{\partial^2 w_0}{\partial t^2} - Q_{55}A\overline{K} \left(\frac{\partial^2 w_0}{\partial x^2} - \frac{\partial \phi}{\partial x} \right) = 0$$

$$\rho I \frac{\partial^2 \phi}{\partial t^2} - Q_{11}I \frac{\partial^2 \phi}{\partial x^2} - Q_{55}A\overline{K} \left(\frac{\partial w_0}{\partial x} - \phi \right) = 0$$

(2.20)

and

$$F_x = Q_{11}A \frac{\partial u_0}{\partial x} + Q_{13}A\varphi$$

$$F_z = Q_{55}A\overline{K} \left(\frac{\partial w_0}{\partial x} - \phi \right)$$

$$M = Q_{11}I \frac{\partial \phi}{\partial x}$$

$$0 = Q_{55}I \frac{\partial \varphi}{\partial x}$$

(2.21)

29

As it is the case for EBEB and TBER theories, axial and flexural displacements, u_0 and w_0, are fully decoupled due to the symmetry around the neutral axis. Following the procedure outlined in Appendix A, a spectral Timoshenko Beam Mindlin Rod (TBMR) element is formulated as follows

$$\begin{Bmatrix} u_0 \\ \varphi \\ w_0 \\ \phi \end{Bmatrix}(x,t) = \frac{1}{N}\sum_{n=0}^{N-1}\begin{Bmatrix} U \\ \Psi \\ W \\ \Phi \end{Bmatrix}_n (x,\omega_n)e^{i\omega_n t} = \frac{1}{N}\sum_{n=0}^{N-1}\sum_m \left(\begin{Bmatrix} A_m \\ r_{1m}A_m \\ B_m \\ r_{2m}B_m \end{Bmatrix} e^{-ik_{mn}x} \right) e^{i\omega_n t} \tag{2.22}$$

where the longitudinal displacement Fourier coefficient is chosen to be the reference with respect to which the lateral contraction Fourier coefficient is scaled, and the transverse displacement Fourier coefficient is chosen to be the reference with respect to which the in-plane rotation Fourier coefficient is scaled. Substituting the assumed spectral solution in the governing equation and seeking a non-trivial solution yields the following characteristic equation

$$det\left(\begin{bmatrix} \rho A\omega^2 - Q_{11}Ak^2 & -ikQ_{13}A & 0 & 0 \\ ikQ_{13}A & \rho I\omega^2 - GI\bar{K}k^2 - Q_{33}A & 0 & 0 \\ 0 & 0 & \rho A\omega^2 - GA\bar{K}k^2 & -iGA\bar{K}k \\ 0 & 0 & iGA\bar{K}k & \rho I\omega^2 - Q_{11}Ik^2 - GA\bar{K} \end{bmatrix} \right) = 0$$

$$\tag{2.23}$$

This results in an 8th order polynomial in k, representing four wave modes. Two of these modes are always propagating modes, representing longitudinal and flexural waves. The third (which represents a shear wave mode) starts as an evanescent mode that transfers to a propagating mode at a cut-off frequency $\omega_c = (GA\bar{K}/\rho I)^{1/2}$, while the forth mode (corresponding to lateral contractions) has a cut-off frequency $\omega_c = (EA/\rho I(1-v^2))^{1/2}$. Figure 2.7 shows the non-dimensional wavenumbers predicted by this theory for the beam shown in Figure 2.1.

Once wave numbers are calculated for a given frequency, the amplitude ratios, $r_{1m} \ni m = 1,\dots,4$ and $r_{2m} \ni m = 5,\dots,8$, appearing in Eq. 2.22, are calculated as follows

$$r_{1m} \equiv \frac{|\Psi|}{|U|} = -i\frac{\rho A\omega^2 - Q_{11}Ak^2}{kQ_{13}A}$$

$$r_{2m} \equiv \frac{|\Phi|}{|W|} = -i\frac{\rho A\omega^2 - GA\bar{K}k_m^2}{GA\bar{K}k_m} \tag{2.24}$$
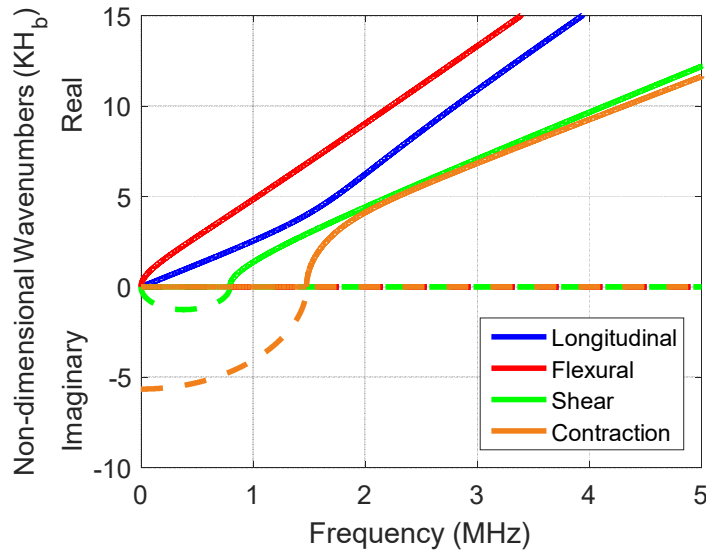
Figure 2.7. Non-dimensional wavenumbers predicted by TBMR theory.

For a two-node spectral element, spectral nodal degrees of freedom and spectral nodal forces and moments vectors, shown in Figure B.2, are defined as

$$\boldsymbol{d} = \{U_1 \quad \Psi_1 \quad W_1 \quad \Phi_1 \quad U_2 \quad \Psi_2 \quad W_2 \quad \Phi_2\}^T = \boldsymbol{H}(\omega)\boldsymbol{A}$$

$$\boldsymbol{F} = \{F_{x1} \quad 0 \quad F_{z1} \quad M_1 \quad F_{x2} \quad 0 \quad F_{z2} \quad M_2\}^T = \boldsymbol{G}(\omega)\boldsymbol{A}$$

(2.25)

where $\boldsymbol{H}(\omega)$ and $\boldsymbol{G}(\omega)$ are defined in Appendix B. The dynamic stiffness matrix, relating nodal displacements and nodal forces in frequency domain, is then obtained following Eq. 2.10.

Figure 2.8.a shows the driving point receptance FRFs predicted by TBER and TBMR spectral elements at $(x, z) = (L_b, 0)$. It could be noted that flexural modes are perfectly matching, since both models have the same underlying theory and assumptions. Longitudinal modes, on the other hand, show some minor discrepancies, with a $\sim$0.1% maximum error in natural frequencies occurring at the 16[th] longitudinal mode ($\sim$97.95 kHz). Experimentally, displacement, velocity, or acceleration are usually measured at the beam surface, i.e. $z = \pm h_b/2$. At such points, the effects of lateral contractions, introduced by the Mindlin-Herrmann theory, on transverse displacement become more prominent, which in turn reflects on the measured dynamic response, as shown in Figure 2.8.b. In the figure, the driving point receptance FRF for the transverse displacement at the point $(x, z) = (L_b, h_b/2)$ is plotted following TBER and TBMR theories. The effects of lateral contraction on the transverse displacement FRF appear as additional peaks coinciding

31

with longitudinal modes natural frequencies. For the current numerical studies, the amplitude of these peaks is only limited by the frequency resolution with which FRFs are calculated. In the presence of damping, these effects are expected be less significant.
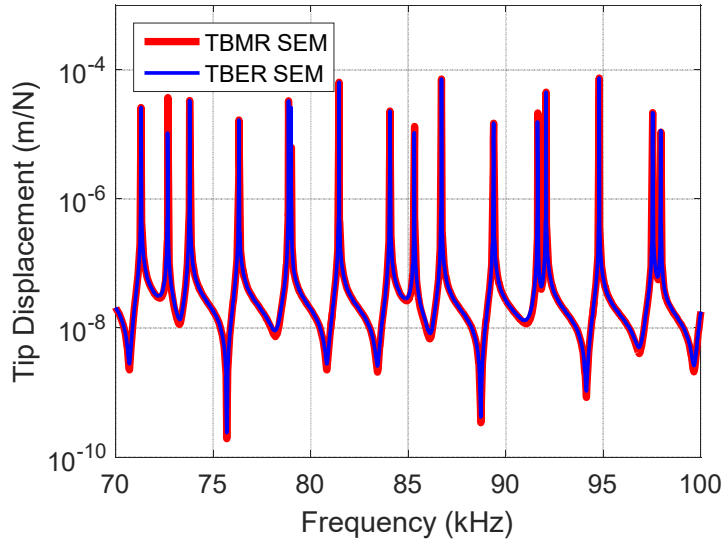
(a)
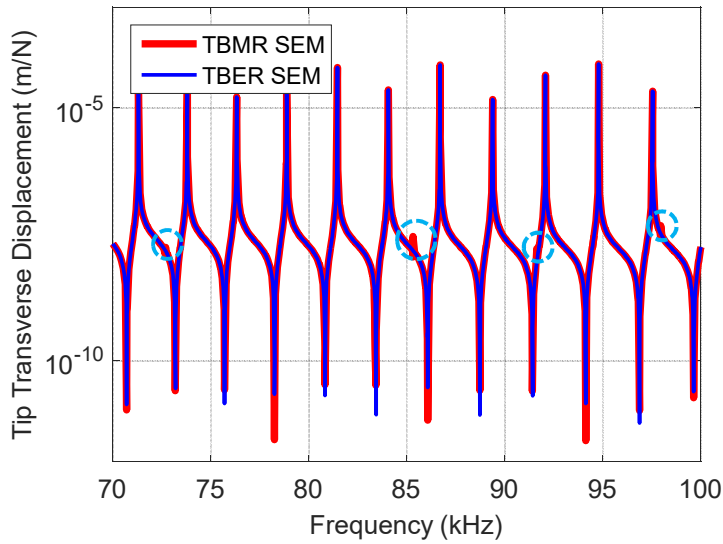
(b)

Figure 2.8. Driving point receptance FRFs, (a) displacement magnitude at $(x , z) = (L_b , 0)$, and (b) transverse displacement at $(x , z) = (L_b , h_b/2)$.

Thus, for slender structures, which are the main focus of this work, Mindlin-Herrmann theory does not provide a significant added accuracy compared to the elementary (classical) rod theory. Although this statement is not accurate at very high-frequency ranges, the fact that beam assumption itself may not hold true at such high frequencies (due to the width-direction modes coming to the picture) makes the additional information carried by the Mindlin-Herrmann theory of little practical value.

2.2.4 Pochhammer-Chree Exact Solution

For a linear elastic isotropic material, and in the absence of body forces, the equation of motion describing the propagation of infinitesimal elastic waves can be expressed as

$$\rho \ddot{\boldsymbol{u}} = (\lambda + \mu)\nabla(\nabla.\boldsymbol{u}) - \nabla \times (\nabla \times \boldsymbol{u}) \qquad (2.26)$$

where $\boldsymbol{u}$ is the displacement field vector, λ and μ are Lamé elastic constants, ρ is the volumetric mass density and $(\dot{\ })$ denotes partial derivatives with respect to time. For cylindrical wave guides, such as rods, a generalized solution of the following form is obtained using Helmholtz decomposition (Graff, 1975)

$$\boldsymbol{u}(r,\theta,x,t) = \boldsymbol{u}(r)e^{-in\theta}e^{-i(kx-\omega t)} \qquad (2.27)$$

where $\boldsymbol{u}(r) = \{u_r(r) \quad u_\theta(r) \quad u_x(r)\}^T$, and n is the circumferential order integer. Dispersion relations describing longitudinal, flexural and torsional wave modes in cylindrical rods are given by the Pochhammer-Chree frequency solution. Based on the value of the circumferential order integer n, the solution can be divided into two classes of modes:

- Symmetric Modes ($n = 0$): these modes have no dependence on θ. They represent longitudinal wave modes which propagate symmetrically along the wave guide. Dispersion relation for these modes can be expressed as

$$\frac{2\alpha}{R}(\beta^2 + k^2)J_1(R\alpha)J_1(R\beta) - (\beta^2 - k^2)^2(R\alpha)J_0(R\alpha)J_1(R\beta) - 4k^2\alpha\beta J_1(R\alpha)J_0(R\beta) = 0 \quad (2.28)$$

where $\alpha^2 = \omega^2/c_p^2 - k^2$, $\beta^2 = \omega^2/c_s^2 - k^2$, $J_n(x)$ is an nth order Bessel function of the first kind, $c_p = \sqrt{(\lambda + 2\mu)/\rho}$ and $c_s = \sqrt{\mu/\rho}$ are the pressure and shear bulk velocities in the rod material, respectively.

- Anti-symmetric Modes ($n \neq 0$): these modes represent flexural wave modes. Dispersion relation for these modes can be expressed as

$$J_1(R\alpha)J_1^2(R\beta)\left(f_1\mathcal{J}_\beta^2 + f_2\mathcal{J}_\alpha\mathcal{J}_\beta + f_3\mathcal{J}_\beta + f_4\mathcal{J}_\alpha + f_5\right) = 0 \tag{2.29}$$

where $\mathcal{J}_x = x\frac{J_0(x)}{J_1(x)}$, and $f_1, \cdots, f_5$ are polynomials in α, β and k defined in (Graff, 1975).

Seco and Jimenez (2012) developed a Matlab algorithm to numerically solve Pochhammer-Chree dispersion relations. This algorithm is used in this work to generate the so-called "Exact dispersion curves", shown in figures 2.9 and 2.10, which provide a reference to which approximate theories are compared. Figure 2.9 depicts dispersion curves, in the form of phase and group velocities, for the longitudinal wave modes in circular rods. The predictions of the Elemental and the Mindlin-Herrmann approximate theories are plotted against the first three modes predicted by the exact theory (Pochhammer-Chree frequency solution). As previously discussed, the Elementary (Classical) rod theory predicts a single nondispersive mode, while the Mindlin-Herrmann theory predicts the existence of an additional mode that transforms from evanescent to propagating upon crossing a cut-off frequency. Both theories fail to predict the very high-frequency behavior of wave modes, and their applicability is limited to relatively lower frequency ranges. This range of applicability depends on material properties and geometric characteristics of the structure of interest, and it is determined in this work with respect to the cut-off frequency of the evanescent modes.

Flexural wave modes phase and group velocities are shown in Figure 2.10. The results from Euler-Bernoulli and Timoshenko beam theories are plotted against the first three modes predicted by the exact theory. Euler-Bernoulli theory predicts a single propagating wave mode that is accurate only at very low frequencies. Timoshenko beam theory, on the other hand, very well predicts the first flexural wave mode. It also captures the cut-off frequency for the second flexural mode, however, the predicted phase and group velocities for this mode quickly deviates from the exact solution. As it is the case for longitudinal wave modes, the frequency range within which approximate theories are applicable depends on the characteristics of the structure of interest. In general, Timoshenko beam theory provides an accurate approximation up till the cut-off frequency of the second flexural wave mode $\left(\omega_c = (GA\overline{K}/\rho I)^{1/2}\right)$.
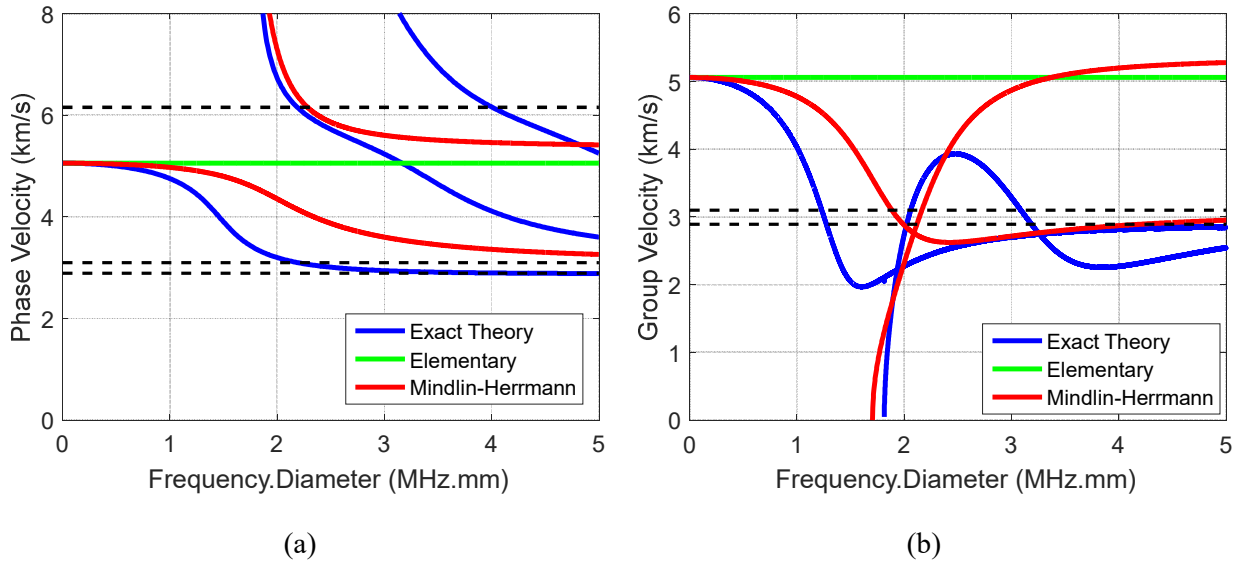
Figure 2.9. Longitudinal modes (a) phase velocities and (b) group velocities for circular rods, as predicted by the Elementary, Mindlin-Herrmann, and exact theories. Dashed lines represent C_P, C_S and C_R values (from up to down, respectively).
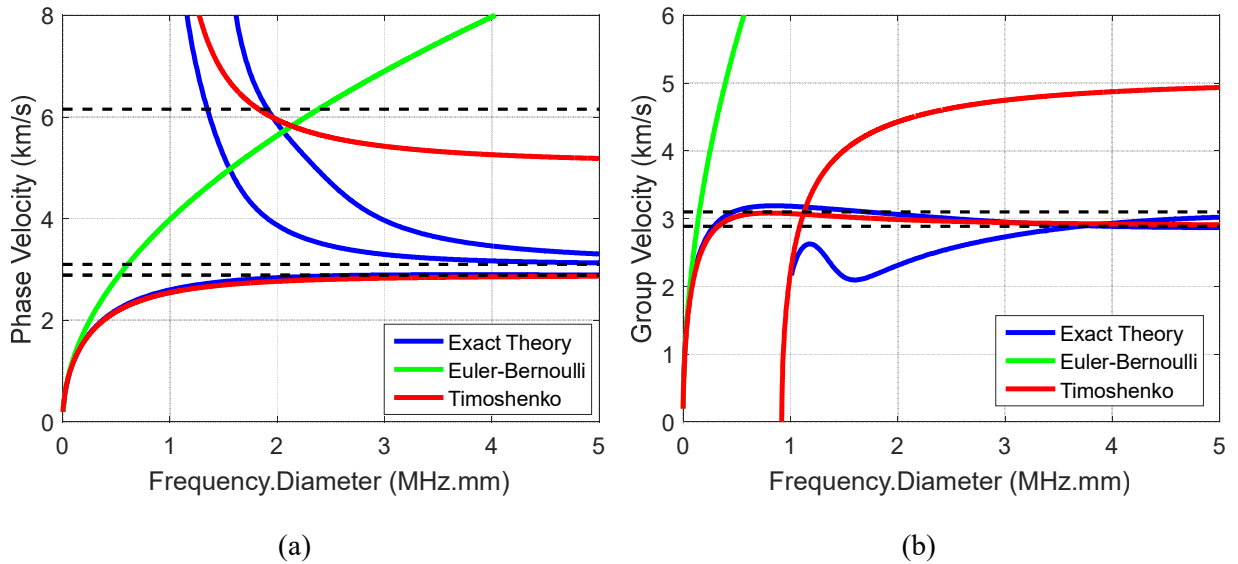
Figure 2.10. Flexural modes (a) phase velocities and (b) group velocities for circular rods, as predicted by Euler-Bernoulli, Timoshenko, and exact theories. Dashed lines represent C_P, C_S and C_R values (from up to down, respectively).

To further investigate the range of applicability of the aforementioned approximate theories, the relative error in phase and group velocities predicted by approximate theories are calculated for the first flexural and longitudinal modes. The results are depicted in Figure 2.11. In the figure, the frequency axis is normalized by the cut-off frequency of the second flexural mode (denoted by ω_c). Beyond this frequency, both beam approximate theories considered in this work fail as a result of higher order modes becoming progressive, as shown in figure 2.10. Therefore, ω_c provides the first constraint on the frequency range within which approximate beam theories are applicable.
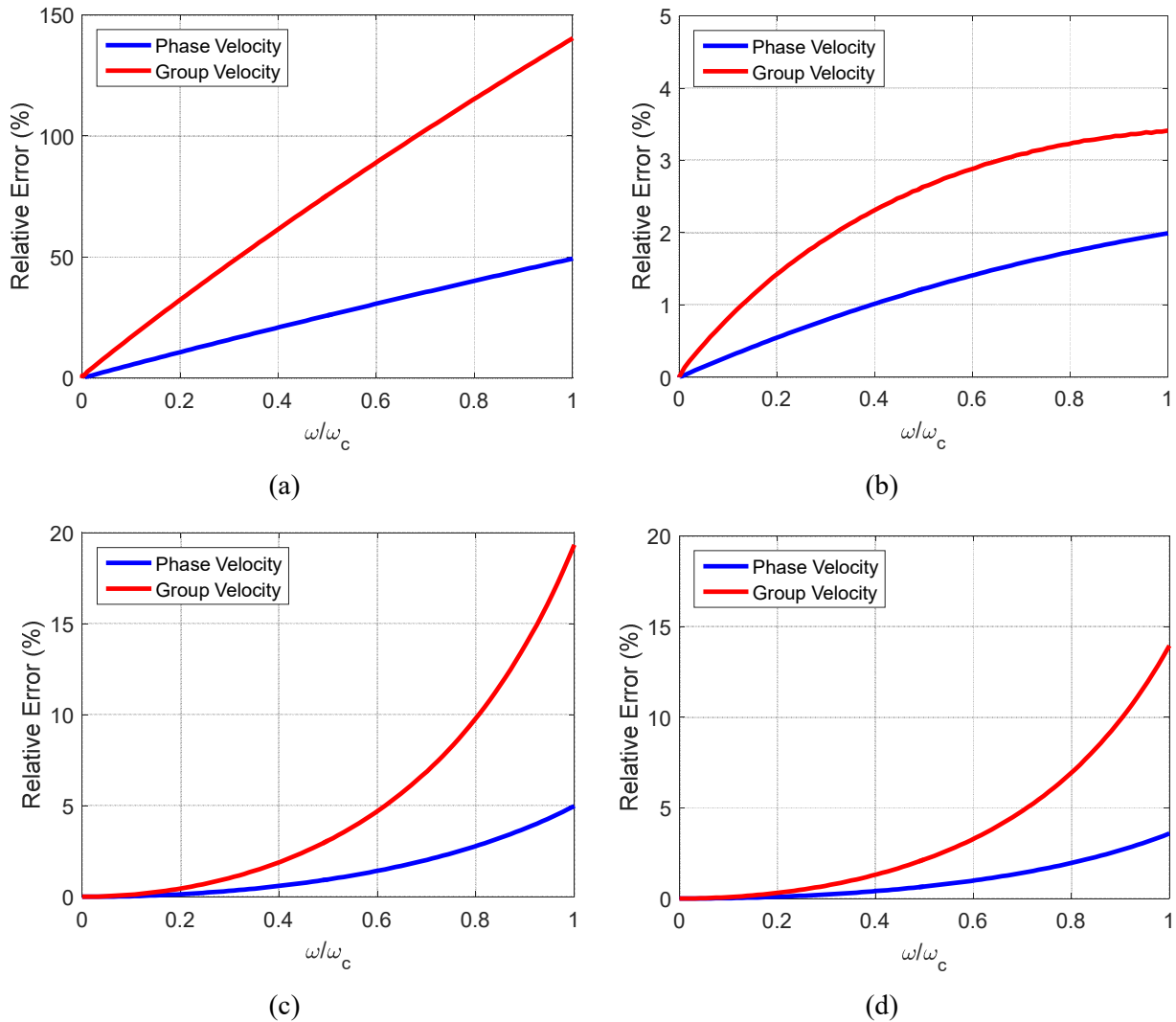
Figure 2.11. Relative error in phase and group velocities for the first mode predicted by (a) Euler-Bernoulli beam theory, (b) Timoshenko beam theory, (c) Elementary rod theory, and (d) Mindlin-Herrmann rod theory. Results are calculated for a 1-mm-diameter Aluminum rod.

Within this frequency range, Euler-Bernoulli beam theory clearly fails to capture phase and group velocities of the first flexural mode. Predictions are acceptable only at the very low-frequency range, $0.025\omega_c$ for a maximum error of 5%. Therefore, Euler-Bernoulli beam theory will not be considered for the high-frequency piezoelectric-structure interaction model. Timoshenko beam theory, on the other hand, accurately predicts the first flexural mode, with a maximum error of 3.4% at $\omega = \omega_c$. As for longitudinal modes, Mindlin-Herrmann rod theory is found to provide a more accurate estimate of phase and group velocities. However, for the frequency range of interest ($\omega < \omega_c$), the performance of both approximate theories is comparable, as shown in figures 2.11.c and 2.11.d. Due to its simplicity, especially when multi-layer structures are considered, the Elementary rod theory is favored over the Mindlin-Hermann theory in this work. Hence, the Timoshenko beam and the Elementary rod approximate theories are adopted in later sections for the piezoelectric-structure interaction model.

2.3   Piezoelectric Transducers and Electromechanical Impedance

Consider a piezoelectric wafer in its free-free configuration, i.e. the wafer is not attached to a host structure, as shown in Figure 2.12. Assuming linear piezoelectricity and a 31 operating mode, the constitutive equations describing the coupled electromechanical behavior of the piezoelectric wafer are (Donald J. Leo, 2007)

$$\begin{Bmatrix} \sigma_1 \\ D_3 \end{Bmatrix} = \begin{bmatrix} \bar{c}_{11}^E & -e_{13} \\ e_{31} & \bar{\epsilon}_{33}^S \end{bmatrix} \begin{Bmatrix} \varepsilon_1 \\ E_3 \end{Bmatrix} \tag{2.30}$$

where ε_1 is the green strain tenor component in x-direction, σ_1 is the Cauchy stress tensor component in the x-direction, D_3 is the electric displacement in z-direction, E_3 is the electric field in z-direction, e_{13} is the piezoelectric coupling coefficient, $\bar{c}_{11}^E = c_{11}^E(1 - i\eta)$ is the complex mechanical stiffness of the material measured at zero electric field. For the simplified one-dimensional plane-stress problem at hand, c_{11}^E reduces to the Young's modulus of elasticity of the piezoelectric material. $\bar{\epsilon}_{33}^S = \epsilon_{33}^S(1 - i\gamma)$ is the complex permittivity measured at zero strain, η and γ are the mechanical and dielectric loss factors, respectively.
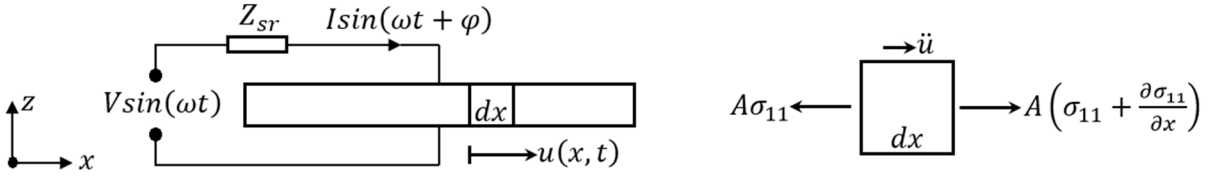
Figure 2.12. Schematic of a piezoelectric wafer in free-free configuration. Also shown is a differential element with the forces acting on it.

For the differential element shown in Figure 2.12, and upon substituting the constitutive relations, equilibrium requires

$$\rho \frac{\partial^2 u}{\partial t^2} = \frac{\partial \sigma_1}{\partial x} = \frac{\partial}{\partial x}(\bar{c}_{11}^E \varepsilon_1 - e_{13}E_3) \tag{2.31}$$

For small strains and deformations, and assuming that the piezoelectric wafer electrodes are highly conductive, i.e. the electric field all over the wafer surface is constant, Eq. 2.31 reduces to

$$\rho \frac{\partial^2 u}{\partial t^2} = \bar{c}_{11}^E \frac{\partial^2 u}{\partial x^2} \tag{2.32}$$

This is the classical one-dimensional wave equation. Similar results can be obtained using the energy method. Starting with the kinetic energy functional for the piezoelectric wafer

$$T = \frac{1}{2}\int_V \rho \dot{u}^2 dV = \frac{1}{2}\int_0^L \rho A \dot{u}^2 dx \tag{2.33}$$

Following the Electric Gibbs energy definition for piezoelectric materials (Donald J. Leo, 2007), the potential energy functional for the system is given by

$$U = \frac{1}{2}\int_V \left(\bar{c}_{11}^E \varepsilon_1^2 - 2e_{31}\varepsilon_1 E_3 - \bar{\epsilon}_{33}^S E_3^2\right)dV = \frac{A}{2}\int_0^L \left(\bar{c}_{11}^E \dot{u}^2 - 2e_{31}\dot{u}E_3 - \bar{\epsilon}_{33}^S E_3^2\right)dx \tag{2.34}$$

where dots indicate temporal partial derivatives and primes indicate spatial partial derivatives. The work done on the system by the applied voltage and external forces is given by

$$W = \int_0^L AE_3 D_3 \, dx + F_x u|_0^L, \tag{2.35}$$

where F_x is the external force acting on the wafer's edges. Applying Hamilton's Principle, the coupled electromechanical governing equation is derived as follows

$$\delta \int_{t_0}^{t_1} \frac{A}{2} \int_0^L \rho(\dot{u} + \epsilon\dot{\eta})^2 - \bar{c}_{11}^E (\dot{u} + \epsilon\dot{\eta})^2 + 2e_{31}(\dot{u} + \epsilon\dot{\eta})E_3 \, dx + F_x(u + \epsilon\dot{\eta})|_0^l \, dt = 0 \tag{2.36}$$

where η is a piecewise smooth function satisfying the condition $\eta(t_0) = \eta(t_1) = 0$. Since the above equation has to be satisfied for any arbitrary piecewise smooth function η, the following equation should always be true

$$\rho \frac{\partial^2 u}{\partial t^2} = \bar{c}_{11}^E \frac{\partial^2 u}{\partial x^2} \tag{2.37}$$

with the following boundary conditions

$$F_x = A\bar{c}_{11}^E \dot{u} - Ae_{31}E_3 \tag{2.38}$$

Equation 2.37 agrees with that obtained by applying equilibrium conditions, while the boundary conditions follow directly from the first equation of the piezoelectric material constitutive relations.

Following the procedure outlined in Appendix A, a spectral piezoelectric element is formulated. Starting with the assumed solution

$$u(x,t) = \frac{1}{N} \sum_{n=0}^{N-1} U_n(x, \omega_n) e^{i\omega_n t} = \frac{1}{N} \sum_{n=0}^{N-1} \sum_m \left(B_m e^{-ik_{mn}x}\right) e^{i\omega_n t} \tag{2.39}$$

Substituting the assumed spectral solution in the governing equation and seeking a non-trivial solution yield the following characteristic equation

$$-\rho\omega^2 + \bar{c}_{11}^E k^2 = 0 \tag{2.40}$$

Which predicts one wave mode with forward and backward propagating modes. For a two-node piezoelectric spectral element, nodal displacements and nodal forces vectors are defined as

$$d = \begin{Bmatrix} U(0) \\ U(L) \end{Bmatrix} = \underbrace{\begin{bmatrix} 1 & 1 \\ e^{-ikL} & e^{ikL} \end{bmatrix}}_{H(\omega)} B$$

(2.41)

$$F = \begin{Bmatrix} -F_x(0) \\ F_x(L) \end{Bmatrix} = \underbrace{A\bar{c}_{11}^E \begin{bmatrix} ik & -ik \\ -ike^{-ikL} & ike^{ikL} \end{bmatrix}}_{G(\omega)} B + \frac{Ae_{31}}{h_p} \begin{Bmatrix} 1 \\ -1 \end{Bmatrix} V$$

where h_p is the piezoelectric wafer thickness, and $V = E_3 h_p$ is the voltage difference across the terminals of the piezoelectric wafer. For a piezoelectric wafer operating as an actuator, the applied voltage is known, and the dynamic behavior of the system is described by the following equation

$$F = K(\omega)d + \frac{Ae_{31}}{h_p} \begin{Bmatrix} 1 \\ -1 \end{Bmatrix} V$$

(2.42)

where $K(\omega) = G(\omega)H^{-1}(\omega)$ is the dynamic stiffness matrix. The current passing through the actuator can be calculated as follows

$$I = \frac{A}{h_p} \int_0^L \dot{D}_3 dx$$

(2.43)

Upon substituting the second part of Eq.2.30 into Eq. 2.43

$$I = i\omega \frac{A}{h_p} \left(e_{31} \big(u(L) - u(0) \big) + \frac{\bar{\epsilon}_{33}^S L}{h_p} V \right)$$

(2.44)

From which the electromechanical impedance is calculated as follows

$$Z = \frac{V}{I} = V \left[i\omega \frac{A}{h_p} \left(e_{31} \big(u(L) - u(0) \big) + \frac{\bar{\epsilon}_{33}^S L}{h_p} V \right) \right]^{-1}$$

(2.45)

When the piezoelectric wafer operates as a sensor, the voltage term is unknown, and an additional constraint is required. This constraint is obtained from the condition that the total electric displacement on a piezoelectric sensor is negligible due to the large input impedance of the data acquisition system (Park et al., 2010b). Thus

$$\int_A D_3 \, dA = 0 \tag{2.46}$$

which yields, upon the substitution of Eq. 2.30 and solving for $V(t)$

$$V(t) = \frac{-e_{31} h_p}{\bar{\epsilon}_{33}^S L} \big(u(L) - u(0) \big) \tag{2.47}$$

Substituting Eq. 2.47 in Eq. 2.41 and simplifying the result yields

$$\boldsymbol{F} = \boldsymbol{K_{Sen.}}(\omega)\boldsymbol{d} = \left(\boldsymbol{G}(\omega)\boldsymbol{H}^{-1}(\omega) + \alpha_s \begin{Bmatrix} -1 \\ 1 \end{Bmatrix} \{-1 \quad 1\} \right) \boldsymbol{d} \tag{2.48}$$

where $\alpha_s = A e_{31}^2 / \bar{\epsilon}_{33}^S L$.

For the piezoelectric wafer described in Table 2.1, the axial displacement of the wafer's tip is calculated as a function of the voltage applied across the wafer, the results are shown in Figure 2.13. The predictions obtained with the spectral elements formulated in this section are compared to those obtained from the commercial FE package, Abaqus. A single spectral element is used to model the piezoelectric wafer, whereas 272 quadrilateral plane stress elements with second-order shape functions are used for the FE model. The predictions obtained with both approaches are perfectly matching for the selected frequency range, 0-100 kHz. At zero frequency excitation, the tip displacement is found to be 6.74×10^{-10} m/volt, which is equivalent to the free deflection of the piezoelectric wafer given by $e_{31} V / 2 h_p \bar{c}_{11}^E$.

Table 2.1. Geometric and material properties of the piezoelectric wafer.

Geometric Characteristics		
$l_{pzt} = 17 \, mm$	$b_{pzt} = 6 \, mm$	$h_{pzt} = 1 \, mm$
Material Properties (Leo, 2007)		
$E = 63 \, GPa$	$v = 0.33 \qquad \eta = 0.02$	$\gamma = 0.01$
$\rho = 7600 kgm^{-3}$	$\bar{\epsilon}_{33}^S = 5.7 \times 10^{-9} Fm^{-1}$	$e_{31} = -5 \, Cm^{-2}$
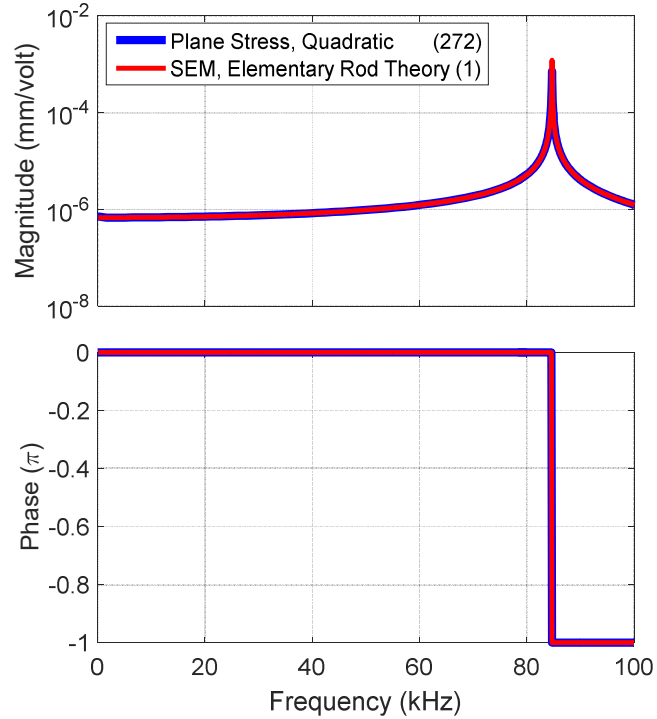
Figure 2.13. Receptance FRF of the piezoelectric wafer's tip as a function of the applied voltage. The number of elements used to discretize the piezoelectric wafer is given in the parentheses.

2.4   Piezoelectric Augmented Structures

For most practical applications, piezoelectric wafers are either embedded in the structure or bonded to its surface. The basis for all of these applications is the energy transfer between the piezoelectric wafer and the host structure, which takes place through the adhesive bonding layer. In this section, the high-frequency dynamic response of an elastic beam coupled with a piezoelectric wafer is investigated, including the bonding layer in between.

2.4.1   Model Development

Figure 2.14 shows a schematic of the piezoelectric augmented beam system considered in this study. The model consists of three main parts, the base beam, the piezoelectric wafer, and the adhesive bonding layer between them. Longitudinal deformations of the base beam, the adhesive layer, and the piezoelectric wafer are approximated by the elementary rod theory. Lateral deformations, on the other hand, are approximated
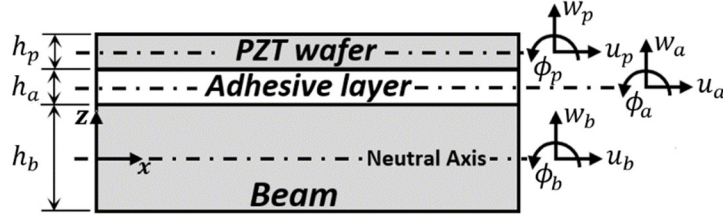
Figure 2.14. Schematic of the piezoelectric-adhesive-beam system.

by the Timoshenko beam theory, where rotary inertia and shear effects are taken into consideration. Based on the aforementioned assumptions, displacement fields in each of the three domains are defined as follows

$$u_{Beam}(x,z,t) = u_b(x,t) - z\phi_b(x,t)$$
$$w_{Beam}(x,z,t) = w_b(x,t)$$

$$u_{Adh}(x,z,t) = u_a(x,t) - \left[z - \frac{h_b+h_a}{2}\right]\phi_a(x,t)$$
$$w_{Adh}(x,z,t) = w_a(x,t)$$

$$u_{PZT}(x,z,t) = u_p(x,t) - \left[z - \frac{h_b+2h_a+h_p}{2}\right]\phi_p(x,t)$$
$$w_{PZT}(x,z,t) = w_p(x,t)$$

(2.49)

where u_r , and w_r are the axial and lateral displacements of the rth neutral axis, respectively. h_r is the thickness of the rth layer, where r takes the values b, a, and p for the base beam, the adhesive bonding layer and the piezoelectric wafer, respectively. ϕ_b, ϕ_a, and ϕ_p are the angles of rotation of the neutral axes normal vectors.

Displacement continuity, i.e. no-slip assumption, at the beam-adhesive interface $\left(z = \frac{h_b}{2}\right)$, and the adhesive-piezoelectric interface $\left(z = \frac{h_b}{2} + h_a\right)$ adds four constraints on the displacement field. Imposing these constraints on Eq. 2.49 results in

$$u_{Beam}(x,z,t) = u_b(x,t) - z\phi_b(x,t)$$

$$u_{Adh}(x,z,t) = u_b(x,t) - \frac{h_b}{2}\phi_b(x,t) - \left(z - \frac{h_b}{2}\right)\phi_a(x,t)$$

(2.50)

43

$$u_{PZT}(x,z,t) = u_b(x,t) - \frac{h_b}{2}\phi_b(x,t) - h_a\phi_a(x,t) - \left(z - \frac{h_b+2h_a}{2}\right)\phi_p(x,t)$$

$$w_{Beam}(x,z,t) = w_{Adh}(x,z,t) = w_{PZT}(x,z,t) = w_b(x,t)$$

With small strains and deformations assumption, the normal and shear strains in each of the three layers are given as follows

$$\varepsilon_1 = \acute{u}_b - z\acute{\phi}_b$$
$$\varepsilon_{13} = \frac{1}{2}(\acute{w}_b - \phi_b)$$
$$-\frac{h_b}{2} \leq z \leq \frac{h_b}{2}$$

$$\varepsilon_1 = \acute{u}_b - \frac{h_b}{2}\acute{\phi}_b - \left(z - \frac{h_b}{2}\right)\acute{\phi}_a$$
$$\varepsilon_{13} = \frac{1}{2}(\acute{w}_b - \phi_a)$$
$$\frac{h_b}{2} \leq z \leq \frac{h_b}{2} + h_a \qquad (2.51)$$

$$\varepsilon_1 = \acute{u}_b - \frac{h_b}{2}\acute{\phi}_b - h_a\acute{\phi}_a - \left(z - \frac{h_b+2h_a}{2}\right)\acute{\phi}_p$$
$$\varepsilon_{13} = \frac{1}{2}(\acute{w}_b - \phi_p)$$
$$\frac{h_b}{2} + h_a \leq z \leq \frac{h_b}{2} + h_a + h_p$$

where the primes indicate spatial partial derivatives. Assuming linear piezoelectricity, the constitutive equations of the piezoelectric wafer operating in 31-mode are (Donald J. Leo, 2007)

$$\begin{Bmatrix} \sigma_1 \\ \tau_{13} \\ E_3 \end{Bmatrix} = \begin{bmatrix} \bar{c}_{11}^D & 0 & -h_{31} \\ 0 & \bar{c}_{55}^D & 0 \\ -h_{31} & 0 & \bar{\beta}_{33}^S \end{bmatrix} \begin{Bmatrix} \varepsilon_1 \\ \gamma_{13} \\ D_3 \end{Bmatrix} \qquad (2.52)$$

where h_{31} is the piezoelectric coupling coefficient, $\bar{c}_{11}^D = c_{11}^D(1 - i\eta)$ is the complex mechanical stiffness of the material measured at zero electric displacement, $\bar{\beta}_{33}^S = \beta_{33}^S(1 - i\gamma)$ is the complex inverse permittivity measured at zero strain. All other symbols are as defined for Eq. 2.30. Unlike the piezoelectric constitutive relations defined in Eq. 2.30, the independent variables in the previous equation are strain and electric charge. These variables are chosen for the piezoelectric-adhesive-beam model in order to facilitate the comparison with the most relevant models published in the literature (Lee et al., 2013; Jang et al., 2014). Transformation rules from the form defined by Eq. 2.30 to that used in Eq. 2.52 are given in Appendix C.

The beam and the adhesive layer are assumed to be isotropic, linear-elastic materials with the following constitutive relations

$$\left\{ \begin{matrix} \sigma_1 \\ \tau_{13} \end{matrix} \right\} = \begin{bmatrix} c_{11} & 0 \\ 0 & c_{55} \end{bmatrix} \left\{ \begin{matrix} \varepsilon_1 \\ \gamma_{13} \end{matrix} \right\} \tag{2.53}$$

where c_{ij} is the elements of the reduced stiffness matrix obtained with plane-stress assumption.

Based on the assumed displacement field, the kinetic energy of the piezoelectric-adhesive-beam system can be expressed as follows

$$T = \frac{1}{2} \int_{V_B} \rho_b (\dot{u}_B^2 + \dot{w}_B^2) dV + \frac{1}{2} \int_{V_A} \rho_a (\dot{u}_A^2 + \dot{w}_A^2) dV + \frac{1}{2} \int_{V_{PZT}} \rho_p (\dot{u}_{PZT}^2 + \dot{w}_{PZT}^2) dV \tag{2.54}$$

where ρ_r is the density of the rth layer. Following Helmholtz free energy definition for piezoelectric materials, the potential energy for the system is calculated as follows

$$U = \frac{1}{2} \int_{V_B} (c_{11}\varepsilon_1^2 + c_{55}\gamma_{13}^2) dV + \frac{1}{2} \int_{V_A} (c_{11}\varepsilon_1^2 + c_{55}\gamma_{13}^2) dV$$
$$+ \frac{1}{2} \int_{V_{PZT}} (c_{11}\varepsilon_1^2 + c_{55}\gamma_{13}^2 - 2h_{31}\varepsilon_1 D_3 + \beta_{33}D_3^2) dV \tag{2.55}$$

The work done on the system by the applied voltage, external forces and moments is given by

$$W = \int_0^L \frac{A_p}{h_p} V(t) D_3 \, dx + F_x u_b|_0^L + F_z w_b|_0^L + M_b \phi_b|_0^L \tag{2.56}$$

where $F_x, F_z,$ and M_b are the external forces and moments associated with u_b , w_b, and ϕ_b, respectively. Applying Hamilton's Principle, the electric displacement is found to be

$$D_3 = \beta_{33}^{-1} h_{13} \left(\dot{u}_b - \frac{h_b}{2}\dot{\phi}_b - h_a\dot{\phi}_a - \frac{h_p}{2}\dot{\phi}_p \right) + \left(h_p \beta_{33} \right)^{-1} V(t) \tag{2.57}$$

The coupled electromechanical governing equations are also found by applying Hamilton's Principle and substituting Eq. 2.57 in the resulting set of equations

$$\rho A_1 \ddot{u}_b - \rho A_2 \ddot{\phi}_b - \rho A_3 \ddot{\phi}_a - \rho A_4 \ddot{\phi}_p - EA_1 \ddot{u}_b + EA_2 \ddot{\phi}_b + EA_3 \ddot{\phi}_a + EA_4 \ddot{\phi}_p = 0$$

$$\rho A_1 \ddot{w}_b - GA_1 \ddot{w}_b + GA_2 \dot{\phi}_b + GA_3 \dot{\phi}_a + GA_4 \dot{\phi}_p = 0$$

$$-\rho A_2 \ddot{u}_b + \rho I_1 \ddot{\phi}_b + \rho I_2 \ddot{\phi}_a + \rho I_3 \ddot{\phi}_p + EA_2 \dot{u}_b - EI_1 \ddot{\phi}_b - EI_2 \ddot{\phi}_a - EI_3 \ddot{\phi}_p - GA_2(\dot{w}_b - \phi_b) = 0$$

$$-\rho A_3 \ddot{u}_b + \rho I_2 \ddot{\phi}_b + \rho I_4 \ddot{\phi}_a + \rho I_5 \ddot{\phi}_p + EA_3 \dot{u}_b - EI_2 \ddot{\phi}_b - EI_4 \ddot{\phi}_a - EI_5 \ddot{\phi}_p - GA_3(\dot{w}_b - \phi_a) = 0$$

$$-\rho A_4 \ddot{u}_b + \rho I_3 \ddot{\phi}_b + \rho I_5 \ddot{\phi}_a + \rho I_6 \ddot{\phi}_p + EA_4 \dot{u}_b - EI_3 \ddot{\phi}_b - EI_5 \ddot{\phi}_a - EI_6 \ddot{\phi}_p - GA_4(\dot{w}_b - \phi_p) = 0$$

$$(2.58)$$

Similarly, force and moment boundary conditions are found to be

$$EA_1 \dot{u}_b - EA_2 \dot{\phi}_b - EA_3 \dot{\phi}_a - EA_4 \dot{\phi}_p - \bar{\alpha} V(t) = F_x$$

$$GA_1 \dot{w}_b - GA_2 \phi_b - GA_3 \phi_a - GA_4 \phi_p = F_z$$

$$-EA_2 \dot{u}_b + EI_1 \dot{\phi}_b + EI_2 \dot{\phi}_a + EI_3 \dot{\phi}_p + \frac{h_b}{2} \bar{\alpha} V(t) = M_b$$

$$\qquad (2.59)$$

$$-EA_3 \dot{u}_b + EI_2 \dot{\phi}_b + EI_4 \dot{\phi}_a + EI_5 \dot{\phi}_p + h_a \bar{\alpha} V(t) = 0$$

$$-EA_4 \dot{u}_b + EI_3 \dot{\phi}_b + EI_5 \dot{\phi}_a + EI_6 \dot{\phi}_p + \frac{h_p}{2} \bar{\alpha} V(t) = 0$$

where dots indicate temporal partial derivatives and primes indicate spatial partial derivatives. All other symbols used in Eq. 2.58 and Eq. 2.59 are listed in Appendix D. In the limit of vanishing bonding layer thickness, the current three-layer model reduces to the perfect bonding case. The resulting reduced model agrees with that proposed by (Jang et al., 2014), which provides an initial validation of the developed model.

As is the case for the free piezoelectric wafer model, voltage terms appearing in Eq. 2.59 are determined depending on the mode of operation of the piezoelectric wafer. When operating as an actuator, $V(t)$ is known, and it is the prescribed voltage acting across the piezoelectric wafer. In this case, the current passing through the sensor can be calculated as follows

$$I = \frac{i\omega b}{\beta_{33}} \left(h_{13} \left(\Delta u_b - \frac{h_b}{2} \Delta \phi_b - h_a \Delta \phi_a - \frac{h_p}{2} \Delta \phi_p \right) + \frac{L}{h_p} V(t) \right) \qquad (2.60)$$

where $\Delta U = U(L) - U(0)$.

On the other hand, when acting as a sensor, the total electric displacement across the piezoelectric wafer is negligible. This yields, upon substituting in Eq. 2.57 and solving for $V(t)$

$$V(t) = -\frac{h_p h_{13}}{L}\left[u_b - \frac{h_b}{2}\phi_b - h_a\phi_a - \frac{h_p}{2}\phi_p\right]_0^L \tag{2.61}$$

Equations 2.58 along with 2.60 or 2.61 fully describe the coupled electromechanical behavior of the system, with boundary conditions given by Eq. 2.59.

2.4.2   Numerical Implementation

The coupled partial differential equations representing the dynamics of the piezoelectric-adhesive-beam system have to be solved numerically. Two solution techniques are adopted and presented in this section. The spectral element method is first implemented following the procedure outlined in Appendix A. An alternative formulation based on the conventional finite element method is then presented. The later method aims to provide means to verify the spectral element formulation.

Spectral element formulation

With the spectral element method, all response variables and external forces appearing in the governing equations and boundary conditions, Eq. 2.58 and Eq. 2.59, are first transformed to frequency domain by applying discrete Fourier transform as follows

$$\boldsymbol{u}(x,t) = \frac{1}{N}\sum_{n=0}^{N-1}\boldsymbol{U_n}(x,\omega_n)e^{i\omega_n t} \tag{2.62}$$

where: $\boldsymbol{u}(x,t) = \{u_b(x,t)\ w_b(x,t)\ \phi_b(x,t)\ \phi_a(x,t)\ \phi_p(x,t)\}^T$ is the response variables vector in time domain.

$\boldsymbol{U_n}(x,\omega_n) = \{\hat{u}_{bn}(x,\omega_n)\ \hat{w}_{bn}(x,\omega_n)\ \hat{\phi}_{bn}(x,\omega_n)\ \hat{\phi}_{an}(x,\omega_n)\ \hat{\phi}_{pn}(x,\omega_n)\}^T$ is the vector of the corresponding Fourier coefficients at the nth angular frequency ω_n.

N is the number of spectral components considered in the discrete Fourier transform, with $N/2$ being the Nyquist frequency.

The Fourier coefficients are assumed to have a general solution of the form

$$\hat{u}_{bn}(x, \omega_n) = \sum_m r_{1m} A_m \, e^{-ik_{mn}x}$$

$$\widehat{w}_{bn}(x, \omega_n) = \sum_m r_{2m} A_m \, e^{-ik_{mn}x}$$

$$\hat{\phi}_{bn}(x, \omega_n) = \sum_m r_{3m} A_m \, e^{-ik_{mn}x} \qquad (2.63)$$

$$\hat{\phi}_{an}(x, \omega_n) = \sum_m r_{4m} A_m \, e^{-ik_{mn}x}$$

$$\hat{\phi}_{pn}(x, \omega_n) = \sum_m r_{5m} A_m \, e^{-ik_{mn}x}$$

where k_{mn} is the wavenumber corresponding to the mth mode at the nth angular frequency, $\boldsymbol{r}$ and $\boldsymbol{A}$ are respectively the scaling matrix and amplitude vector for the Fourier coefficients in the frequency domain. Fourier coefficients can be scaled relative to any one of them. In this work, $\hat{u}_{bn}$ is selected to be the scaling coefficient, thus, $r_{1m} = 1 \ \forall \ m$, and all other coefficients are calculated with respect to $\hat{u}_{bn}$. Substituting the spectral solution in the governing equations, Eq. 2.58, yields

$$\boldsymbol{Q} \begin{Bmatrix} 1 \\ r_2 \\ r_3 \\ r_4 \\ r_5 \end{Bmatrix} A = 0 \qquad (2.64)$$

where the elements of $\boldsymbol{Q}$ are defined in Appendix D. To get a nontrivial solution, the matrix $\boldsymbol{Q}$ should be singular, which leads to the characteristic equation

$$det(\boldsymbol{Q}) = 0 \qquad (2.65)$$

This results in a 10th order polynomial in k, with only even order terms appearing in the characteristic equation. Therefore, five wave modes exist at each frequency, corresponding to forward and backward propagating waves along with evanescent modes. Since there is no closed form solution for this high-order polynomial, the characteristic equation is solved numerically.

Once wavenumbers are calculated, the components of the scaling matrix r, appearing in Eq. 2.63, are obtained by solving the following system of linear algebraic equations for each wavenumber k_{mn} as follows

$$\begin{bmatrix} Q_{22} & Q_{23} & Q_{24} & Q_{25} \\ Q_{32} & Q_{33} & Q_{34} & Q_{35} \\ Q_{42} & Q_{43} & Q_{44} & Q_{45} \\ Q_{52} & Q_{53} & Q_{54} & Q_{55} \end{bmatrix} \begin{Bmatrix} r_2 \\ r_3 \\ r_4 \\ r_5 \end{Bmatrix} = - \begin{Bmatrix} Q_{21} \\ Q_{31} \\ Q_{41} \\ Q_{51} \end{Bmatrix} \tag{2.66}$$

A more accurate and computationally efficient approach for solving the characteristic equation and obtaining the scaling matrix r is to recast the problem as a quadratic eigenvalue problem. The matrix $\boldsymbol{Q}$, appearing in Eq. 2.64, can be rearranged as follows

$$\boldsymbol{Q} = \boldsymbol{Q_1}\omega^2 + \boldsymbol{Q_2} + \boldsymbol{Q_3}k + \boldsymbol{Q_4}k^2 \tag{2.67}$$

where $\boldsymbol{Q_i}$, $i = 1, \ldots, 4$, are defined in Appendix D. Therefore, obtaining a nontrivial solution for Eq. 2.64 at a given frequency is equivalent to solving the quadratic eigenvalue problem for wavenumbers k. The scaling matrix, r, automatically follows as the eigenvectors matrix.

Fourier coefficients can be determined in terms of the unknown vector $\boldsymbol{A}$. These unknowns are found by applying force and moment boundary conditions at each node. For the two-node spectral finite element, shown in Figure 2.15, the spectral nodal degrees of freedom are defined as follows

$$\boldsymbol{d} = \boldsymbol{H}(\omega)\boldsymbol{A} \tag{2.68}$$

where $\boldsymbol{d} = \left\{ \hat{u}_b(x_1)\ \hat{w}_b(x_1)\ \hat{\phi}_b(x_1)\ \hat{\phi}_a(x_1)\ \hat{\phi}_p(x_1)\ \hat{u}_b(x_2)\ \hat{w}_b(x_2)\ \hat{\phi}_b(x_2)\ \hat{\phi}_a(x_2)\ \hat{\phi}_p(x_2) \right\}^T$, x_1, and x_2 are the coordinates of the element's left and right nodes, respectively, and the subscript n is dropped for brevity. The matrix $\boldsymbol{H}(\omega)$ represents the shape functions matrix, and it has the following structure

$$\boldsymbol{H}(\omega) = \begin{bmatrix} r_{11}\xi_1(x_1) & r_{12}\xi_2(x_1) & \cdots & r_{110}\xi_{10}(x_1) \\ & \vdots & \ddots & \vdots \\ r_{51}\xi_1(x_1) & r_{52}\xi_2(x_1) & \cdots & r_{510}\xi_{10}(x_1) \\ r_{11}\xi_1(x_2) & r_{12}\xi_2(x_2) & \cdots & r_{110}\xi_{10}(x_2) \\ & \vdots & \ddots & \vdots \\ r_{51}\xi_1(x_2) & r_{52}\xi_2(x_5) & \cdots & r_{510}\xi_{10}(x_2) \end{bmatrix} \tag{2.69}$$

(a)

(b)
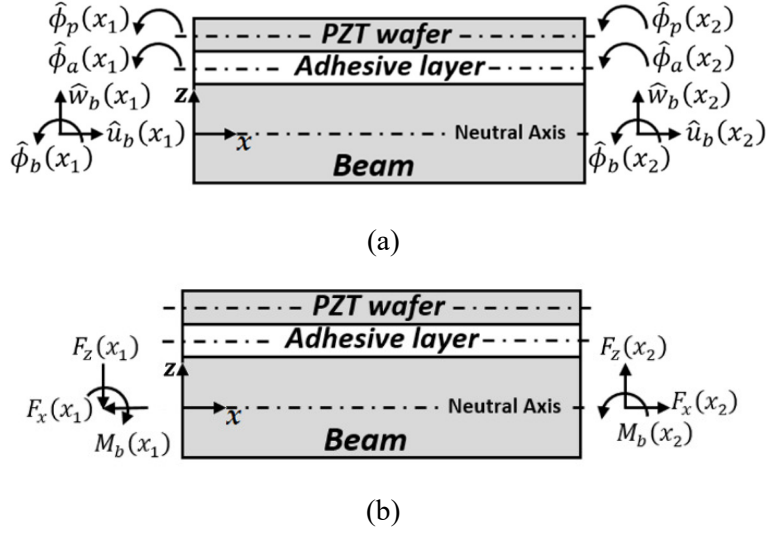
Figure 2.15. Three-layer piezoelectric-adhesive-beam spectral element, showing (a) nodal displacements, and (b) nodal forces.

where $\xi_m(x_j) = e^{-ik_m x_j}$, $m = 1, \dots, 10$, and $j = 1,2$.

Nodal forces and moments, shown in Figure 2.15.b, are obtained by substituting the spectral solution of response variables into Eq. 2.59

$$\boldsymbol{F} = \boldsymbol{G}(\omega)\boldsymbol{A} + \boldsymbol{F}_{PZT} \tag{2.70}$$

where $\boldsymbol{F}$ is the nodal forces and moments vector defined as

$$\boldsymbol{F} = [-F_x(x_1) \quad -F_z(x_1) \quad -M_b(x_1) \quad 0 \quad 0 \quad F_x(x_2) \quad F_z(x_2) \quad M_b(x_2) \quad 0 \quad 0]^T \tag{2.71}$$

The boundary conditions matrix, $\boldsymbol{G}(\omega)$, is defined in Appendix D.

Force and moment components induced by the voltage applied across the piezoelectric wafer when operating as an actuator are denoted by $\boldsymbol{F}_{PZT}$, and are defined as

$$\boldsymbol{F}_{PZT} = \alpha_a \left[1 \quad 0 \quad -\frac{h_b}{2} \quad -h_a \quad -\frac{h_p}{2} \quad -1 \quad 0 \quad \frac{h_b}{2} \quad h_a \quad \frac{h_p}{2}\right]^T \hat{V}_n \tag{2.72}$$

where $\hat{V}_n$ is the Fourier coefficients of the applied voltage at the nth angular frequency.

Substituting Eq. 2.68 into Eq. 2.70, the dynamic stiffness matrix relating nodal forces and nodal displacements vectors in frequency domain is calculated as follows

$$F - F_{PZT} = K_{Act.}(\omega)d \qquad (2.73)$$

where the dynamic stiffness matrix for an actuator piezoelectric wafer, $K_{Act.}(\omega)$, is defined in terms of the shape functions matrix and the boundary conditions matrix as follows

$$K_{Act.}(\omega) = G(\omega)H^{-1}(\omega) \qquad (2.74)$$

When piezoelectric wafers act as sensors, F_{PZT} in Eq. 73 vanishes, and the voltage effects are included in the dynamic stiffness matrix according to Eq. 2.61 as follows

$$K_{Sen.}(\omega) = G(\omega)H^{-1}(\omega) + \alpha_s \gamma^T \gamma \qquad (2.75)$$

where $\alpha_s = \alpha_a h_p h_{13}/L$, and $\gamma \epsilon \mathbb{R}^{1\times10}$ is defined in Appendix D. Nodal forces and moments are then expressed as a function of the nodal displacements vector as follows

$$F = K_{Sen.}(\omega)d \qquad (2.76)$$

where d and F follow the same definitions given by Eq. 2.68 and Eq. 2.71, respectively.

For beams partially covered with piezoelectric wafers, the proposed three-layer element is assembled with beam-only elements following the standard assembly procedure used in the finite element method.

Finite Element Formulation

To verify the proposed spectral element solution and evaluate its accuracy, the conventional finite element method is utilized to solve the coupled piezoelectric-adhesive-beam system derived in Section 2.4.1. In the absence of distributed loads, the weak formulation of the problem stated by equations 2.58 and 2.59 is expressed as

$$\rho A_1 \bar{M}_{ij} \ddot{u}_{bj} - \rho A_2 \bar{M}_{ij} \ddot{\phi}_{bj} - \rho A_3 \bar{M}_{ij} \ddot{\phi}_{aj} - \rho A_4 \bar{M}_{ij} \ddot{\phi}_{pj} + EA_1 \bar{K}_{ij} u_{bj} - EA_2 \bar{K}_{ij} \phi_{bj}$$
$$- EA_3 \bar{K}_{ij} \phi_{aj} - EA_4 \bar{K}_{ij} \phi_{pj} = 0$$

$$\rho A_1 \bar{M}_{ij} \ddot{w}_{bj} + GA_1 \bar{K}_{ij} w_{bj} - GA_2 \bar{P}_{ij} \phi_{bj} - GA_3 \bar{P}_{ij} \phi_{aj} - GA_4 \bar{P}_{ij} \phi_{pj} = 0$$

$$-\rho A_2 \bar{M}_{ij} \ddot{u}_{bj} + \rho I_1 \bar{M}_{ij} \ddot{\phi}_{bj} + \rho I_2 \bar{M}_{ij} \ddot{\phi}_{aj} + \rho I_3 \bar{M}_{ij} \ddot{\phi}_{pj} - EA_2 \bar{K}_{ij} u_{bj} - GA_2 \bar{R}_{ij} w_{bj}$$
$$+ \left(EI_1 \bar{K}_{ij} + GA_2 \bar{M}_{ij} \right) \phi_{bj} + EI_2 \bar{K}_{ij} \phi_{aj} + EI_3 \bar{K}_{ij} \phi_{pj} = 0 \qquad (2.77)$$

$$-\rho A_3 \bar{M}_{ij} \ddot{u}_{bj} + \rho I_2 \bar{M}_{ij} \ddot{\phi}_{bj} + \rho I_4 \bar{M}_{ij} \ddot{\phi}_{aj} + \rho I_5 \bar{M}_{ij} \ddot{\phi}_{pj} - EA_3 \bar{K}_{ij} u_{bj} - GA_3 \bar{R}_{ij} w_{bj}$$
$$+ EI_2 \bar{K}_{ij} \phi_{bj} + \left(EI_4 \bar{K}_{ij} + GA_3 \bar{M}_{ij} \right) \phi_{aj} + EI_5 \bar{K}_{ij} \phi_{pj} = 0$$

$$-\rho A_4 \bar{M}_{ij} \ddot{u}_{bj} + \rho I_3 \bar{M}_{ij} \ddot{\phi}_{bj} + \rho I_5 \bar{M}_{ij} \ddot{\phi}_{aj} + \rho I_6 \bar{M}_{ij} \ddot{\phi}_{pj} - EA_4 \bar{K}_{ij} u_{bj} - GA_4 \bar{R}_{ij} w_{bj}$$
$$+ EI_3 \bar{K}_{ij} \phi_{bj} + EI_5 \bar{K}_{ij} \phi_{aj} + \left(EI_6 \bar{K}_{ij} + GA_4 \bar{M}_{ij} \right) \phi_{pj} = 0$$

For first order two-node elements, the indices (i, j) take the value of *(1, 2)*. The sub-element bared matrices appearing in the weak formulation are

$$\bar{M}_{ij} = \int_{x_e}^{x_{e+1}} N_i N_j dx$$

$$\bar{K}_{ij} = \int_{x_e}^{x_{e+1}} \grave{N}_i \grave{N}_j dx$$

$$\bar{P}_{ij} = \int_{x_e}^{x_{e+1}} \grave{N}_i N_j dx$$

$$\bar{R}_{ij} = \int_{x_e}^{x_{e+1}} N_i \grave{N}_j dx$$

where N_i denotes the shape functions defined as first order Lagrange polynomials, x_e, and x_{e+1} are the left and right nodal global coordinates of the finite element.

Combining the terms associated with temporal derivatives in Eq. 2.77, a 10x10 element mass matrix can be defined as

$$\boldsymbol{M}^e = \begin{bmatrix} \mathbf{Z}\bar{M}_{11} & \mathbf{Z}\bar{M}_{12} \\ \mathbf{Z}\bar{M}_{21} & \mathbf{Z}\bar{M}_{22} \end{bmatrix} \qquad (2.78)$$

$$\text{where } \mathbf{Z} = \begin{bmatrix} \rho A_1 & 0 & -\rho A_2 & -\rho A_3 & -\rho A_4 \\ 0 & \rho A_1 & 0 & 0 & 0 \\ -\rho A_2 & 0 & \rho I_1 & \rho I_2 & \rho I_3 \\ -\rho A_3 & 0 & \rho I_2 & \rho I_4 & \rho I_5 \\ -\rho A_4 & 0 & \rho I_3 & \rho I_5 & \rho I_6 \end{bmatrix}.$$

Similarly, a 10x10 element stiffness matrix can be formulated based on Eq. 2.77 as follows

$$K^e = \begin{bmatrix} \Pi(1,1) & \Pi(1,2) \\ \Pi(2,1) & \Pi(2,2) \end{bmatrix} \tag{2.79}$$

$$\text{where } \Pi(i,j) = \begin{bmatrix} EA_1\bar{K}_{ij} & 0 & -EA_2\bar{K}_{ij} & -EA_3\bar{K}_{ij} & -EA_4\bar{K}_{ij} \\ 0 & GA_1\bar{K}_{ij} & -GA_2\bar{P}_{ij} & -GA_3\bar{P}_{ij} & -GA_4\bar{P}_{ij} \\ -EA_2\bar{K}_{ij} & -GA_2\bar{R}_{ij} & EI_1\bar{K}_{ij} + GA_2\bar{M}_{ij} & EI_2\bar{K}_{ij} & EI_3\bar{K}_{ij} \\ -EA_3\bar{K}_{ij} & -GA_3\bar{R}_{ij} & EI_2\bar{K}_{ij} & EI_4\bar{K}_{ij} + GA_3\bar{M}_{ij} & EI_5\bar{K}_{ij} \\ -EA_4\bar{K}_{ij} & -GA_4\bar{R}_{ij} & EI_3\bar{K}_{ij} & EI_5\bar{K}_{ij} & EI_6\bar{K}_{ij} + GA_4\bar{M}_{ij} \end{bmatrix}.$$

Once element matrices are formulated, global mass and stiffness matrices, denoted by $\mathbf{M}$ and $\mathbf{K}$, are assembled. The coupled piezoelectric-adhesive-beam system can then be described as

$$\mathbf{M\ddot{d}} + \mathbf{Kd} = \mathbf{f} \tag{2.80}$$

where the loading vector $\mathbf{f}$ is assembled from the elemental mechanical and electrical forces defined in Eq. 2.71 and Eq. 2.72.

2.4.3   Model Validation

The accuracy of the proposed spectral element model is evaluated by comparing its results with those obtained using the finite element method. This approached is followed since an analytical solution for such coupled systems of equations is not available. Two systems are considered to verify the proposed spectral element model, a unimorph system, denoted by System I, and a cantilever beam partially covered with a piezoelectric wafer, denoted by System II. Longitudinal and flexural displacement frequency response functions along with the electromechanical impedance signatures obtained by the two solution techniques are compared at different frequency ranges.

Figure 2.16.a shows the unimorph system considered in this study, System I. The unimorph is 150 *mm* long, 20 *mm* wide, and fixed at its left end. The base beam is 2 *mm* thick, while the adhesive bonding layer and piezoelectric wafer thicknesses are 0.1 *mm* and 0.2 *mm*, respectively. The piezoelectric wafer is excited with a sinusoidal voltage signal applied across its terminals. Material properties for each of the three layers are summarized in Table 2.2. Due to its geometric and material uniformity, a single spectral element is sufficient to model the entire unimorph. On the other hand, mesh refinement is required with the conventional FEM. The beam is discretized with uniform elements, the number of which is gradually increased until convergence is achieved in the 0-5 kHz frequency range.

The natural frequencies of System I predicted by a single spectral element are compared to those obtained by the FEM up to the 20th mode. The results are summarized in Table 2.3. It can be noted that the FEM solution converges to that obtained by the SEM as the number of elements is increased. For all cases, natural frequencies obtained by the FEM are greater than SEM predictions, which is typically seen when FEM results are compared to exact solutions.

Table 2.2. Material properties for the augmented piezoelectric-adhesive-beam system (Donald J Leo, 2007; Abaqus 6.12, 2012).

	Base Beam (Al 6061)	
$E = 69\ GPa$	$v = 0.33$	$\rho = 2700\ kgm^{-3}$
	Adhesive Bonding Layer	
$E = 1\ GPa$	$v = 0.36$	$\rho = 1100\ kgm^{-3}$
	PZT Wafer (PZT-5A)	
$E = 63\ GPa$	$v = 0.33$	$\rho = 7600 kgm^{-3}$
$h_{31} = -8.772 \times 10^8\ Vm^{-1}$		$\beta_{33} = 1.754 \times 10^8 mF^{-1}$

Table 2.3. Natural frequencies, in Hz, of System I.

Mode	SEM n=1	FEM n=150	n=300	n=500	n=750
1	74.3	76.7	74.9	74.5	74.4
2	465	480	469	466	465
3	1298	1340	1308	1302	1300
4	2533	2615	2554	2541	2537
5	4167	4303	4201	4179	4172
10	14433	14941	14561	14479	14453
15	29964	31132	30258	30070	30011
20	49792	51971	50339	49989	49879

(a)

(b)
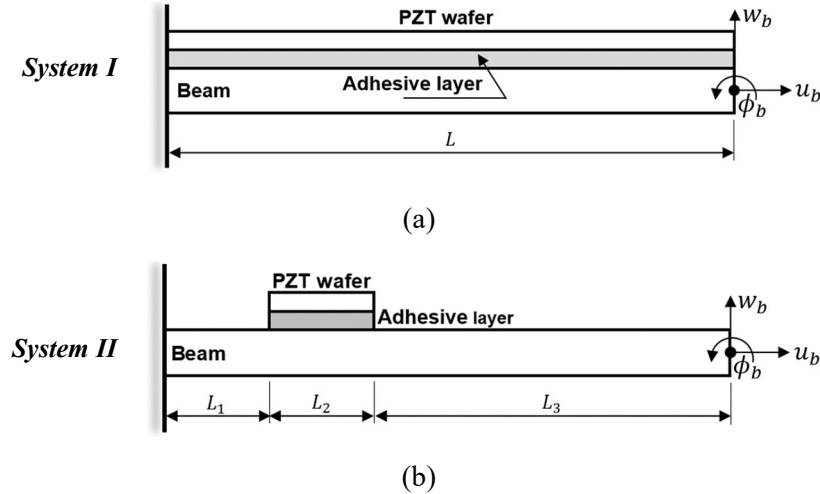
Figure 2.16. Piezoelectric-adhesive-beam systems considered for model validation, (a) System I: a unimorph system of a length $L = 150$ *mm*, and (b) System II: cantilever beam partially covered with a piezoelectric wafer, with $L_1 = 60$ *mm*, $L_2 = 20$ *mm* and $L_3 = 320$ *mm*.

Frequency response functions of the tip longitudinal and lateral displacements and the electromechanical impedance obtained by the two numerical methods, the SEM and the first order FEM, are shown in Figure 2.17 for the 0-5 kHz frequency range. It can be noticed that the FEM results accord well with the SEM predictions. As the number of elements is increased, the FEM results approach SEM predictions from the right until convergence is achieved. The superiority of the SEM over the FEM is evident, especially when high-frequency ranges are of interest.

The study conducted on System I is repeated for the partially covered cantilever beam, System II, shown in Figure 2.16.b. The beam is 400 *mm* long, with a 20 *mm* piezoelectric wafer located 60 *mm* from the fixed end. The width and thicknesses of all three layers are identical to those of System I. Three spectral elements are used to model the partially covered cantilever beam, one three-layer piezoelectric-adhesive-beam element, and two beam-only elements. Several mesh configurations are considered for the conventional FEM, the results of two are presented here. The first mesh configuration, denoted by Mesh 1, consists of 1 *mm* long first order elements for the beam-only sections, and 0.2 *mm* long elements for the piezoelectric-adhesive-beam section. The second mesh configuration, Mesh 2, is further refined with 0.66 *mm* long elements for the beam-only sections, and 0.2 *mm* long elements for the piezoelectric-adhesive-beam section. A sinusoidal voltage signal is applied across the piezoelectric wafer terminals while longitudinal and flexural displacements are measured at the cantilever's tip.
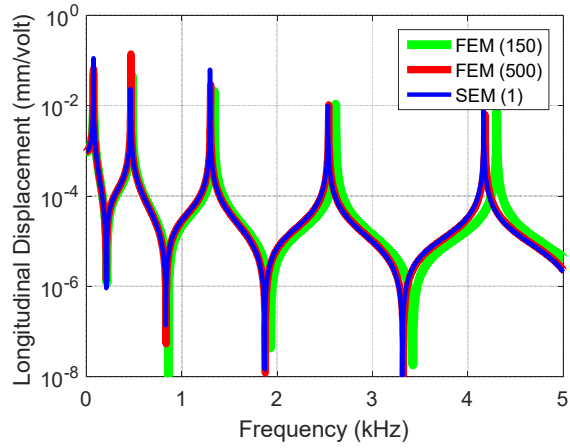
(a)
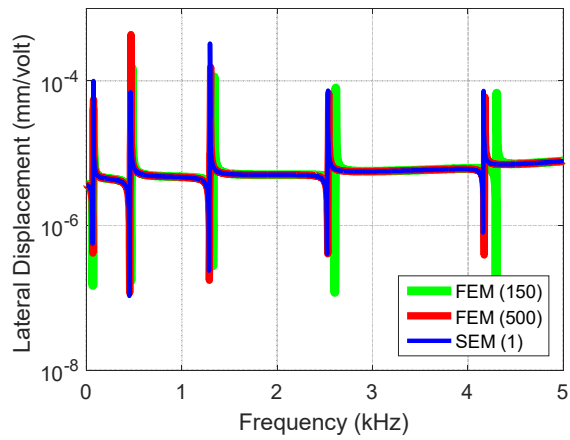
(b)
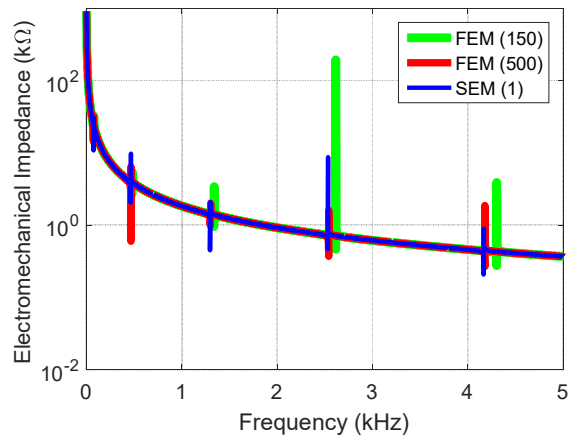
(c)

Figure 2.17. Dynamic response of System I (the cantilever unimorph) excited with a sinusoidal voltage signal in the 0-5 kHz range, (a) lateral displacement FRF, (b) longitudinal displacement FRF, and (c) electromechanical impedance.
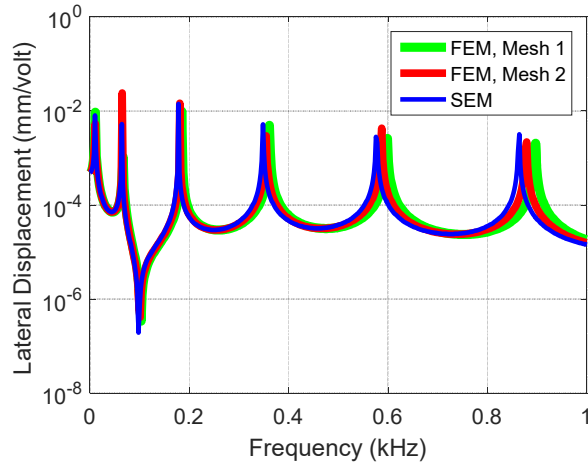
(a)
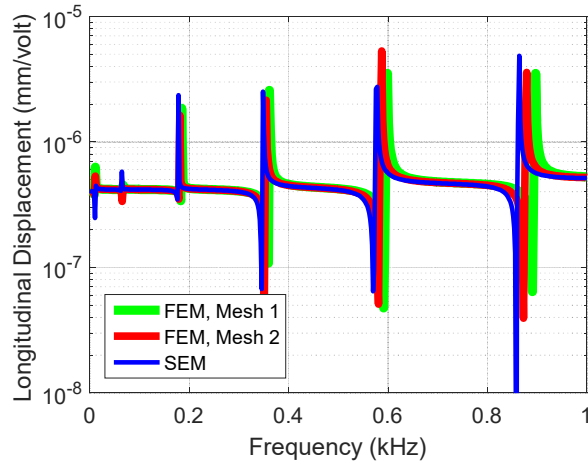
(b)

Figure 2.18. Dynamic response of System II excited with a sinusoidal voltage signal, (a) lateral displacement FRF, and (b) longitudinal displacement FRF in the 0-1 kHz frequency range.

Figure 2.18 shows the frequency response functions for the longitudinal and lateral tip displacements of System II obtained by the SEM and the FEM using the two finite element mesh configurations, Mesh 1 and Mesh 2. To better visualize the results, the frequency range is limited to 1 kHz. As previously noticed, FEM results converge to SEM predictions as the number of elements is increased, and the accuracy of the FEM results obtained with a certain mesh configuration degrades at higher frequencies.

To further validate the developed spectral element model, the dynamic response of System II obtained by the developed spectral and finite element models are compared to those predicted by the commercial finite element package, Abaqus. Quadrilateral, plane stress elements with second-order shape functions are used

to discretize the system. Tie constraints are applied at the interfaces to guarantee displacement continuity. Several layers of elements are used through the thickness of the base beam, the adhesive layer, and the piezoelectric wafer. Figure 2.19 shows the transfer receptance FRF of the tip of System II as obtained by the SEM and the commercial finite element package, Abaqus. Natural frequencies, up to the 20th mode, predicted by these methods are also compared and the results are summarized in Table 2.4. SEM results are found to accord perfectly with those predicted by Abaqus, with a negligible error for the first 20 modes. Both FEM and SEM predictions perfectly match for the 20th mode, as it happens to be an extensional mode.
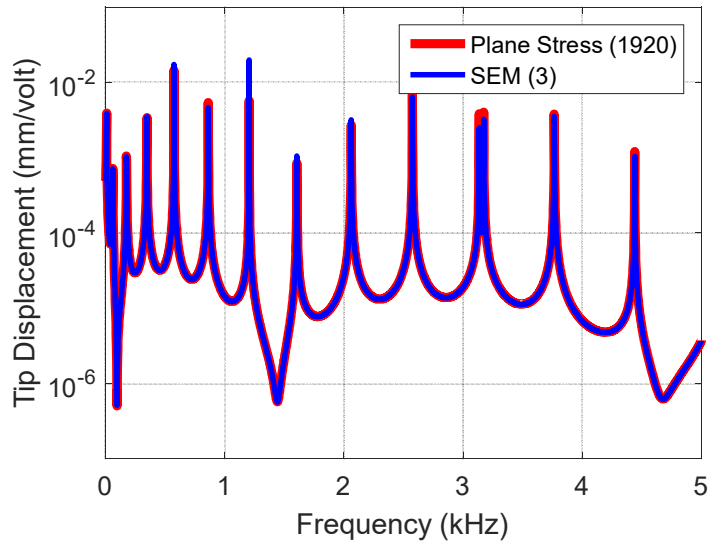
Figure 2.19. Receptance FRF measured at the tip of System II as predated by the SEM and the commercial finite element package, Abaqus. The number of elements used to discretize the system is given in the parentheses.

Table 2.4. Natural frequencies, in Hz, of System II.

Mode	SEM	FEM (1st order elements)		FEM, Abaqus (2nd order, plane stress)
	n=3	Mesh 1	Mesh 2	n=1920
1	10.3	10.7	10.5	10.3
2	63.9	66	65	63.9
3	178	184	181	178
4	348	361	354	349
5	577	598	586	577
10	2575	2671	2618	2576
15	5173	5375	5264	5174
20	9414	9414	9414	9415

2.5   Conclusions

Fundamental rod and beam approximate theories have been briefly reviewed in this chapter. This includes the Elementary rod theory, Mindlin-Herrmann rod theory, Euler-Bernoulli beam theory and Timoshenko beam theory. For each of the aforementioned theories, elastodynamic equations of motion have been derived and numerically implemented using the frequency domain SEM. The capabilities of each approximate theory have been investigated including both transient and steady state dynamic responses. The former has been gauged against the Pochhammer-Chree exact solution, while high-fidelity FEM simulations has been utilized to assess the later. It is found that the elementary rod theory and the Timoshenko beam theory accurately describe the longitudinal and lateral deflections of beams, along with the first symmetric and anti-symmetric wave modes, up to the cut-off frequency of the second anti-symmetric mode, given by $(GA\overline{K}/\rho I)^{1/2}$. The performance of the SEM for solving coupled electromechanical problems has then been evaluated. For this purpose, a free-free piezoelectric transducer operating in 31-mode is considered. The results have been compared to those obtained by second-order, plane-stress, quadrilateral finite elements, and they are found to be in perfect agreement.

For piezoelectric augmented structures, a three-layer element, consisting of a base beam, an adhesive bonding layer, and a piezoelectric wafer, has been developed in this chapter. The formulation of this new element takes into account axial and shear deformations in addition to rotary inertia effects in all three layers. Such effects are known to be significant for the high-frequency dynamic response of piezoelectric augmented structures. Spectral element method has been adopted to numerically solve the coupled governing equations. By relaxing the assumption of perfect bonding and accounting for the presence of the adhesive bonding layer, the proposed model represents an important addition to the piezoelectric-structure interaction models currently available in the literature.

The proposed model has been verified and validated through two numerical examples, a unimorph, and a cantilever beam partially covered with a piezoelectric wafer. Frequency response functions and electromechanical impedance signatures for both systems have been simulated and compared to the FEM predictions. An in-house FE solver has been used for verification purposes, whereas the commercial FE package Abaqus has been used for model validation. FEM results are found to converge to those of SEM as the number of finite elements is increased. The superiority of the SEM over the FEM is evident, especially at high-frequency ranges.

The validated piezoelectric-adhesive-beam model is utilized in Chapter 3 to study the effects of adhesive bonding layer characteristics on the high-frequency dynamic response of piezoelectric augmented structures. In Chapter 4, this model will serve as the core block in the impedance-based damage characterization algorithm.

CHAPTER THREE

THE EFFECTS OF PIEZOELECTRIC WAFER AND BONDING LAYER CHARACTERISTICS ON THE DYNAMIC RESPONSE OF SMART STRUCTURES

3.1 Introduction

Embedded and surface bonded piezoelectric wafers are widely used for control, energy harvesting, and SHM applications. The basis for all of these applications is the energy transfer between the piezoelectric wafer and the host structure, which takes place through the adhesive bonding layer. The characteristics of the bonding layer along with the piezoelectric transducer are found to have an important impact on the sensing and actuation capabilities of piezoelectric-based applications.

In this chapter, the high-frequency dynamic response of an elastic beam coupled with a piezoelectric wafer is investigated. The three-layer spectral element model formulated in Chapter 2 is utilized to study the effects of the piezoelectric wafer and bonding layer characteristics on the dynamic response of the structure. This aims to provide a better understanding of these effects, develop an approach for piezoelectric wafer characterization and bonding layer design. The chapter starts by studying the dynamic response of a free piezoelectric transducer. The equations of motion are non-dimensionalized, and the effects of each non-dimensional parameter on the steady state dynamic response are investigated. A procedure for piezoelectric material characterization based on the measured impedance signature is then proposed. Piezoelectric-augmented structures are then addressed, where a parametric study is conducted to evaluate the effects of

piezoelectric wafer and bonding layer thickness, stiffness and density on the dynamic response of the system. Concluding remarks regarding bonding layer design are finally presented.

3.2   Dynamic Analysis of Free Piezoelectric Transducers

In this section, a piezoelectric transducer in its free configuration is studied following the model developed in Section 2.3. The effects of transducer's geometric and material characteristics on its steady state dynamic response are investigated. As given by equations 2.37, 2.38 and 2.45, for a free piezoelectric wafer operating in the 31-mode, the dynamic response depends on three geometric parameters, four material parameters (two of which are complex), in addition to the excitation frequency. Addressing all seven parameters at the same time is a tedious task with hard-to-generalize results. In order to facilitate the parametric study, a non-dimensional version of these equations is first developed in this section.

Let the dimensionless time, frequency, and displacement, denoted respectively by τ, $\bar{\omega}$, and $\bar{x}$, be defined as follows

$$\tau = \omega^* t$$
$$\bar{\omega} = \frac{\omega}{\omega^*} \tag{3.1}$$
$$\bar{x} = \frac{x}{L}$$

where $\omega^* = \left(c_{11}^E / \rho A \right)^{1/2}$ and L is the piezoelectric wafer's length. The coupled electromechanical equations describing the system can then be expressed as

$$\frac{\partial^2 \bar{u}}{\partial \tau^2} = \beta_1 \frac{\partial^2 \bar{u}}{\partial \bar{x}^2}$$

$$\bar{F}_x = \frac{\partial \bar{u}}{\partial \bar{x}} + \beta_2 \bar{V} \tag{3.2}$$

$$\bar{D}_3 = \frac{\partial \bar{u}}{\partial \bar{x}} + \beta_3 \bar{V}$$

where $\bar{u} = u/L$ is the dimensionless axial deflection of the piezoelectric wafer, $\bar{F}_x = F_x / A\bar{c}_{11}^E$ is the dimensionless axial force, $\bar{D}_3 = D_3 / e_{31}$ is the dimensionless electric displacement, and $\bar{V} = V/V^*$ is the

dimensionless electric potential, with $V^* = 1$ volt being the reference electric potential. The non-dimensional parameters in Eq. 3.2 are defined as follows

$$\beta_1 = A/L^2$$

$$\beta_2 = e_{31}V^*/\bar{c}_{11}^E h_p \tag{3.3}$$

$$\beta_3 = \varepsilon_{33}^S V^*/e_{31}h_p$$

These non-dimensional parameters describe the geometry of the piezoelectric wafer (β_1), the ratio between driving electric force and restoring elastic force (β_2), and the ratio between dielectric charge and that induced by the electromechanical coupling (β_3). With non-zero mechanical and dielectric loss factors, the non-dimensional parameters β_2 and β_3 are complex. For the example shown in Section 2.3, the non-dimensional constants take the values of $\beta_1 = 2.08 \times 10^{-2}$, $\beta_2 = -7.94(1 + i0.01) \times 10^{-8}$, and $\beta_3 = -1.14(1 + i0.1) \times 10^{-6}$.

Following the same procedure, the non-dimensional current, denoted by $\bar{I}$, is defined as follows

$$\bar{I} \equiv \frac{I}{\frac{A}{h_p}Le_{31}\omega^*} = i\bar{\omega}(\bar{u}(1) - \bar{u}(0) + \beta_3\bar{V}) \tag{3.4}$$

Based on which, the non-dimensional electromechanical impedance is defined as

$$\bar{Z} \equiv \frac{\bar{V}}{\bar{I}} = \bar{V}[i\bar{\omega}(\bar{u}(1) - \bar{u}(0) + \beta_3\bar{V})]^{-1} \tag{3.5}$$

Thus, through non-dimensionalization, the overall number of variables reduces from seven to three. This makes the parametric study more manageable with easy to generalize results.

In the context of this work, the steady state dynamic response of the system under consideration is determined by frequency response functions (FRFs) along with the complex electromechanical impedance, represented in the form of magnitude and phase. Merely two non-dimensional parameters are required to describe the FRFs for a piezoelectric actuator in its free configuration. Figure 3.1 shows the dependence of the non-dimensional longitudinal displacement FRF, measured at the wafer's tip, on the non-dimensional parameters β_1 and β_2. For each case, a single non-dimensional parameter is varied while keeping others fixed at their aforementioned nominal values.

Both resonance and anti-resonance frequencies of free piezoelectric actuators are found to increase with the non-dimensional parameter β_1, as shown in Figure 3.1.a. This effect is expected as an increase in β_1 is equivalent to an increase in the wafer's thickness or a decrease in its length, which results in higher fundamental frequencies. The advantages of dimensional analysis are evident in this discussion, where a single non-dimensional parameter successfully captures the net effect of all three geometric parameters of the system.

The effect of β_2 magnitude and phase on FRFs are depicted in Figures 3.1.b and 3.1.c, respectively. The non-dimensional parameter β_2 is defined as the ratio of the driving electric force to the restoring elastic force, thus it can be interpreted as a measure of the electromechanical compliance of the system. The complex part of this parameter stems from the complex stiffness, $\bar{c}_{11}^E$, and represents the mechanical loss factor of the piezoelectric material. A change in β_2 magnitude, for a given loss factor, simply results in a vertical shift in the non-dimensional FRF curves, as shown in Figure 3.1.b for $\beta_1 = 2.08 \times 10^{-2}$, and 0.01 mechanical loss factor. A more compliant system, indicated by a high $|\beta_2|$ value, produces larger deformations for a given excitation voltage. Although a change in β_2 implies a change in $\bar{c}_{11}^E$, which in turn, shall result in fundamental frequency shifts, the fact that FRFs are plotted against the non-dimensional frequency, $\bar{\omega}$, compensates for this effect. Therefore, no shifts in the non-dimensional fundamental frequencies are observed with β_2.

The last non-dimensional parameter affecting FRFs of free piezoelectric actuators is the mechanical loss factor, defined as $\eta \equiv Imag(\beta_2)/Real(\beta_2)$. An increase in mechanical loss factor is equivalent to an increase in damping, which results in wider resonance peaks with smaller amplitude, as shown in Figure 3.1.c. The frequency dependence of damping effects is also shown in the figure, where higher order resonance peaks are found to be more affected by the mechanical loss factor.

The steady state dynamic response of the piezoelectric transducer can also be described by its electromechanical impedance signature. The effects of the non-dimensional parameters β_1 and β_2 on the impedance signature are found to be similar to these on FRFs. An increase in β_1 results in a frequency shift in both magnitude and phase peaks of the impedance signature, as shown in Figure 3.2.

(a)

(b)

(c)
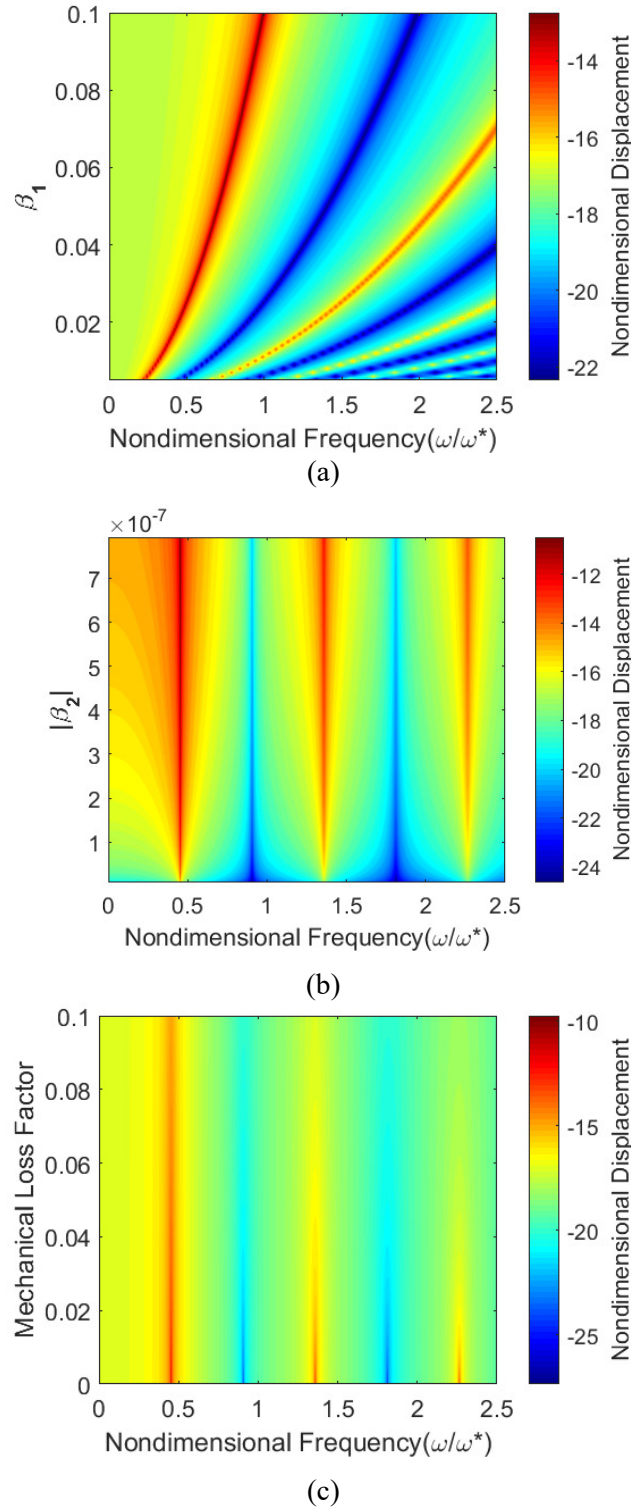
Figure 3.1. Effects of non-dimensional parameters, (a) β_1, (b) β_2 magnitude, and (c) mechanical loss factor, on FRFs of the non-dimensional displacement of the piezoelectric actuator's tip.
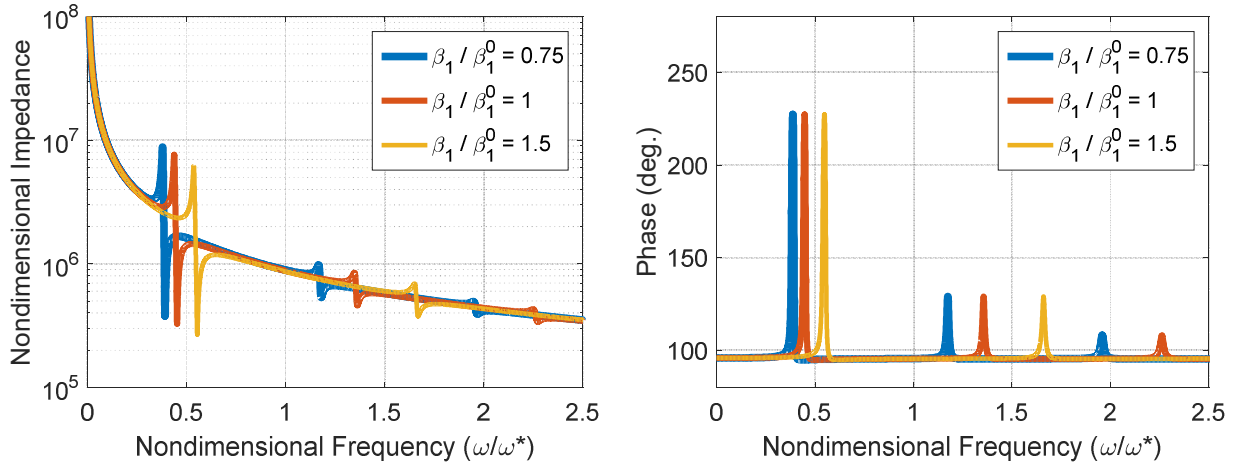
Figure 3.2. Effects of the non-dimensional parameter β_1 on the non-dimensional electromechanical impedance of free piezoelectric transducers.

Away from resonance peaks, impedance signature is not affected by the physical dimensions of the wafer, as the response is dominated by the electrical characteristics of the piezoelectric material. The electromechanical impedance phase is found to be close to 90°, except in the vicinity of resonance peaks, which indicates that the real part of the impedance signature is very small as compared to the overall impedance magnitude, which is a typical characteristic of impedance signatures.

Figure 3.3 depicts the effects of the non-dimensional parameters β_2 on the electromechanical impedance signature of the system. An increase in β_2 magnitude yields an increase in the magnitude and phase of the impedance signature in the vicinity of resonance frequencies. In the limit of $\beta_2 = 0$, corresponding to uncoupled electromechanical characteristics or infinitely stiff material, impedance signature of the piezoelectric transducer reduces to that of an ordinary capacitor. Mechanical loss factor, on the other hand, dampens out impedance peaks resulting in wider and shorter peaks.

The electromechanical impedance of free piezoelectric transducers is also affected by the non-dimensional parameter β_3, which describes the dielectric characteristics of the piezoelectric material. In its most general form, the non-dimensional parameter β_3 is complex with its imaginary part being related to the dielectric loss factor of the material. The effects of this parameter on impedance signature, both magnitude and phase, are shown in Figure 3.4. Unlike the non-dimensional parameters β_1 and β_2, the impact of β_3 on impedance signature is not confined to the vicinity of impedance peaks.
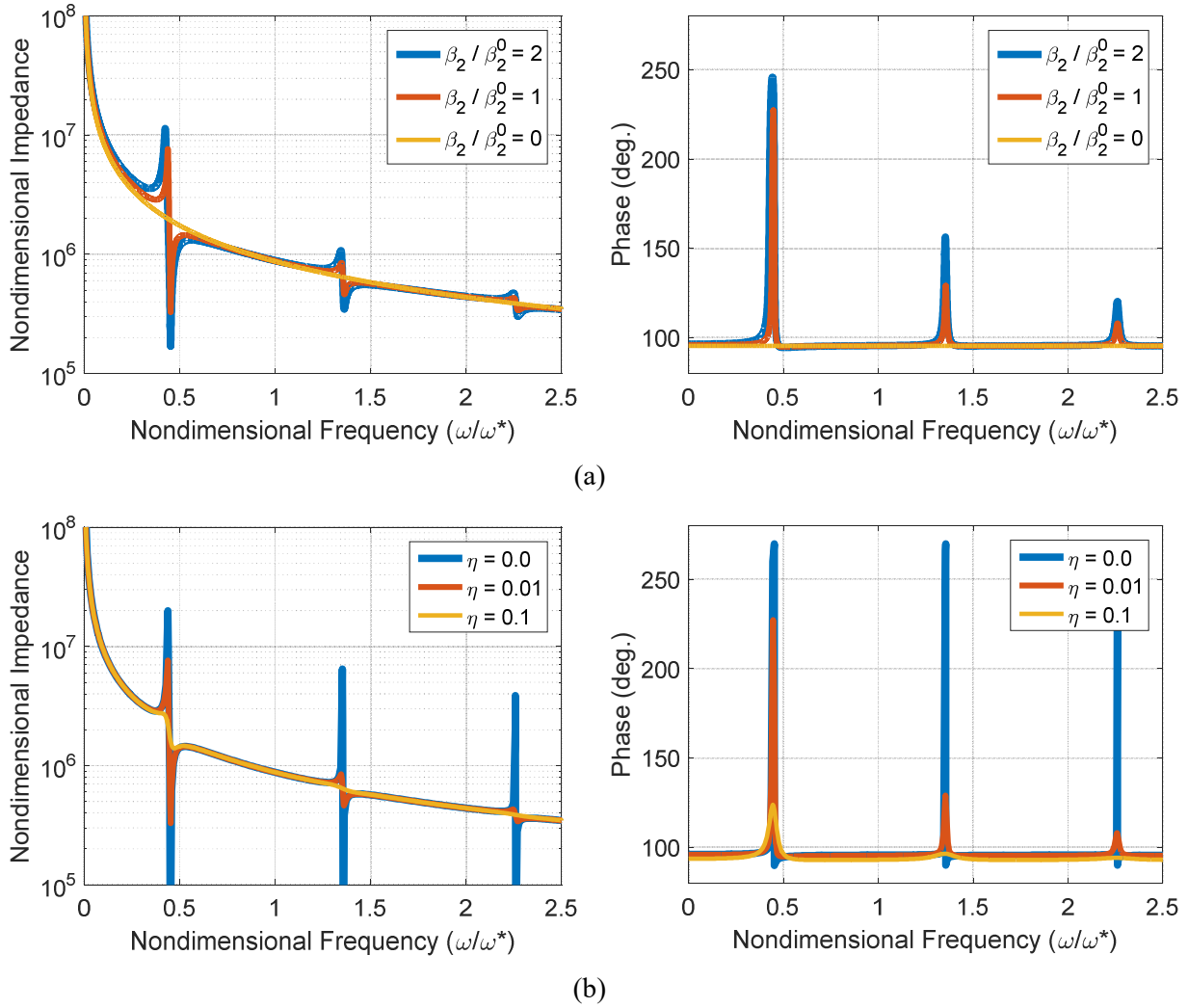
Figure 3.3. Effects of (a) the non-dimensional parameter β_2 magnitude, and (b) mechanical loss factor, on the non-dimensional electromechanical impedance of free piezoelectric transducers.

As the magnitude of β_3 increases, the magnitude of the non-dimensional impedance increases, as shown in Figure 3.4.a. In the limit of $\beta_3 = 0$, not shown in the figure, the impedance signature is completely governed by the electromechanical coupling terms, and it takes the shape of the mechanical impedance FRF. Impedance phase is also dependent on $|\beta_3|$, where phase variations in the vicinity of resonance frequency is found to decrease with larger $|\beta_3|$ values, indicating a more dominant reactance component.
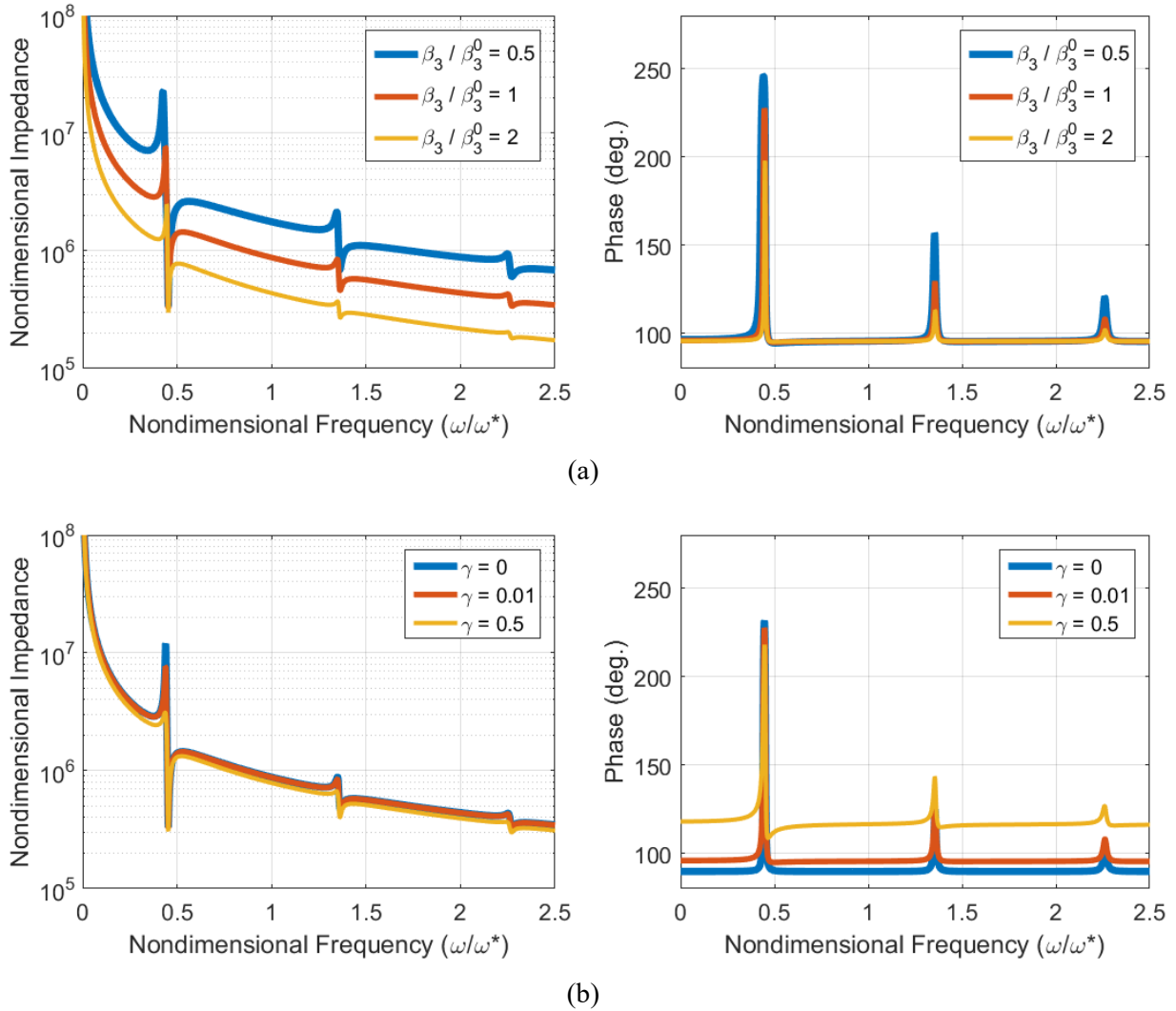
Figure 3.4. Effects of (a) the non-dimensional parameter β_3 magnitude, and (b) dielectric loss factor, on the non-dimensional electromechanical impedance of free piezoelectric transducers.

The effects of the dielectric loss factor, $\gamma = Imag(\beta_3)/Real(\beta_3)$, on impedance signature are shown in Figure 3.4.b. While these effects appear as added damping to impedance magnitude peaks with minimal impact elsewhere, phase curves are significantly affected by this parameter. At $\gamma = 0$, impedance phase is found to be exactly 90°, and thus the real part of the impedance signature is zero, except in the vicinity of impedance peaks. As γ increases, phase curves shift vertically, resulting in larger real components.

The reduction in the number of parameters describing the steady state response of free piezoelectric transducers with the proposed non-dimensional analysis allows efficient characterization of the

piezoelectric material. This can be achieved by model updating techniques, where only three non-dimensional variables need to be specified, rather than seven in the original problem. However, based on the insights provided by the non-dimensional analysis, a more systematic approach can be adopted to facilitate model updating efforts. This approach can be summarized as follows:

Step 1   The non-dimensional parameter β_1 is first determined based on the physical dimensions of the piezoelectric wafer.

Step 2   The non-dimensional frequency of impedance peaks is given by $(2n-1)\pi\sqrt{\beta_1}$, $n = 1,2$, …, from which ω^* is determined.

Step 3   The dielectric loss factor is determined based on the low-frequency phase angle of the impedance signature as follows: $\phi_0 \approx 180 - tan^{-1}(1/\gamma)$.

Step 4   The magnitude of the non-dimensional parameter β_3 is determined based on the low-frequency impedance magnitude as follows: $\beta_3 = 1/\bar{\omega}|\bar{Z}|$.

Step 5   The complex non-dimensional parameter β_2 is finally determined by matching the response at impedance peaks.

It should be pointed out that ω^* and γ are in fact approximated by the calculations presented in step 2 and 3. The quality of these approximations depend on the mechanical loss factor of the piezoelectric material. For most practical scenarios, these approximations hold true. However, for highly damped piezoelectric materials, the aforementioned procedure merely provides an initialization point for model updating algorithms.

3.3   Dynamic Analysis of Piezoelectric Augmented Structures

The effects of piezoelectric and bonding layer characteristics on the dynamic response of piezoelectric augmented structures are investigated in this section. This study is based on the piezoelectric-structure interaction model that has been developed in Section 2.4. For most practical applications, the dynamic response of piezoelectric augmented structures is dominated by the host structure itself. The presence of the piezoelectric wafer and bonding layer merely perturbs the response about that of the host structure. Changes in the dynamic responses across different host structures can be described following a simplified

version of the analysis presented in the previous section. However, this is out of the scope of the current study, as the focus is limited to the impact of the bonding layer and the piezoelectric wafer characteristics on the performance of smart structures. Therefore, material properties and geometric characteristics of the base beam have been preselected, and only those parameters related to the piezoelectric wafer and the bonding layer are included in the parametric study. The dynamic response of the base beam without a piezoelectric wafer being attached is considered as a reference to which all other responses are compared. While different features can be used to identify and quantify the piezoelectric wafer and bonding layer impact on the dynamic response, the focus of the current work has been turned towards resonance frequency shifts and actuation amplitude variations. These features have been selected as they are essential for structural health monitoring, energy harvesting, and control applications.

Let the characteristics of the piezoelectric wafer and the bonding layer, namely their stiffness, density, and thickness, be defined in terms of the following ratios

$$\begin{aligned}
\beta_{E_a} &= E_a/E_b \\
\beta_{E_p} &= E_p/E_b \\
\beta_{\rho_a} &= \rho_a/\rho_b \\
\beta_{\rho_p} &= \rho_p/\rho_b \\
\beta_{h_a} &= h_a/h_b \\
\beta_{h_p} &= h_p/h_b
\end{aligned}$$

(3.6)

where E, ρ, and h respectively denote the modulus of elasticity, density, and thickness of the corresponding layer. Subscripts b, a, and p denote the base beam, the adhesive bonding layer, and the piezoelectric wafer, respectively.

Figure 3.5.a shows the beam that is selected as a benchmark for the current study. The beam is 400-mm-long, 20-mm-wide, and 2-mm-thick, fixed at its left end. Material properties of the beam are summarized in Table 3.1. The beam is excited with two concentrated forces applied at its surface as shown in the figure. This configuration is selected in order to approximate the surface-bonded piezoelectric excitation. The response is calculated at the neutral axis of the beam at its free tip, i.e. $(x, y) = (L, 0)$.

Table 3.1. Material properties for the piezoelectric-adhesive-beam system.

Base Beam (Al 6061)			
$E = 69\ GPa$	$v = 0.33$	$\rho = 2700\ kgm^{-3}$	$\eta = 0.01$
Adhesive Bonding Layer			
$E = 1\ GPa$	$v = 0.35$	$\rho = 1100\ kgm^{-3}$	$\eta = 0.1$
PZT Wafer (PZT-5A)			
$E = 63\ GPa$	$v = 0.33$	$\rho = 7600 kgm^{-3}$	$\eta = 0.025$
$h_{31} = -8.772 \times 10^8\ Vm^{-1}$	$\beta_{33} = 1.754 \times 10^8 mF^{-1}$		$\gamma = 0.05$

(a)

(b)
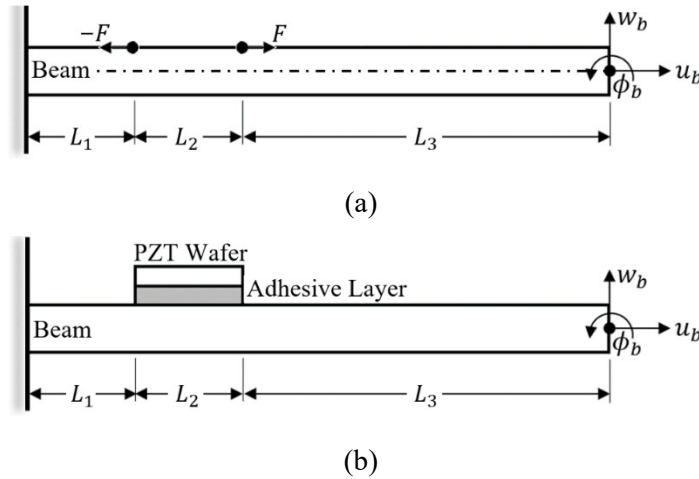
Figure 3.5. Schematics for (a) the simple beam considered as a benchmark, and (b) piezoelectric augmented beam. For both cases with $L_1 = 60\ mm$, $L_2 = 20\ mm$ and $L_3 = 320\ mm$.

Longitudinal and lateral receptance FRFs, in *mm/N*, of the beam's tip are shown in Figure 3.6.a. Three frequency ranges are shown in the figure: 0-5 kHz, 30-40 kHz, and 90-100 kHz. Due to material and geometric symmetry around the neutral axis, longitudinal and lateral displacements are fully decoupled when the response is measured at the neutral axis. Although the response is measured right at the beam's tip, anti-resonances are present in both Longitudinal and lateral FRFs. This is a direct result of the excitation force being applied at the beam's surface, which results in an $Fh_b/2$ bending moment when transferred to the neutral axis.

For the piezoelectric augmented structure, shown in Figure 3.5.b, a 20-mm-long and 0.2-mm-thick piezoelectric wafer is bonded to the beam's surface through a 0.1-mm-thick adhesive layer. Material properties for the piezoelectric wafer and the bonding layer are summarized in Table 3.1. Longitudinal and

lateral displacement FRFs, in *mm/volt*, measured at the tip of the piezoelectric augmented beam are shown in Figure 3.6.b. Unlike the simple beam, there is a clear coupling between the longitudinal and lateral displacements of the piezoelectric augmented structure. This is due to the asymmetry introduced by the surface bonded piezoelectric wafer. A comparison between the FRFs shown in Figure 3.6.a and 3.6.b shows that both responses accord very well at low-frequency. This suggests that the excitation configuration used for the benchmark beam accurately resembles that of surface-bonded piezoelectric transducers. The bonded piezoelectric wafer has a negligible effect on the low-frequency modes of the structure. These effects become more significant at higher frequencies, as shown in the figure. Therefore, the piezoelectric wafer and the bonding layer need to be accounted for when the high-frequency dynamic response is of interest. The following sections discuss in detail the effects of the bonding layer and piezoelectric wafer stiffness, density, and thickness on the dynamic response of the coupled structure.
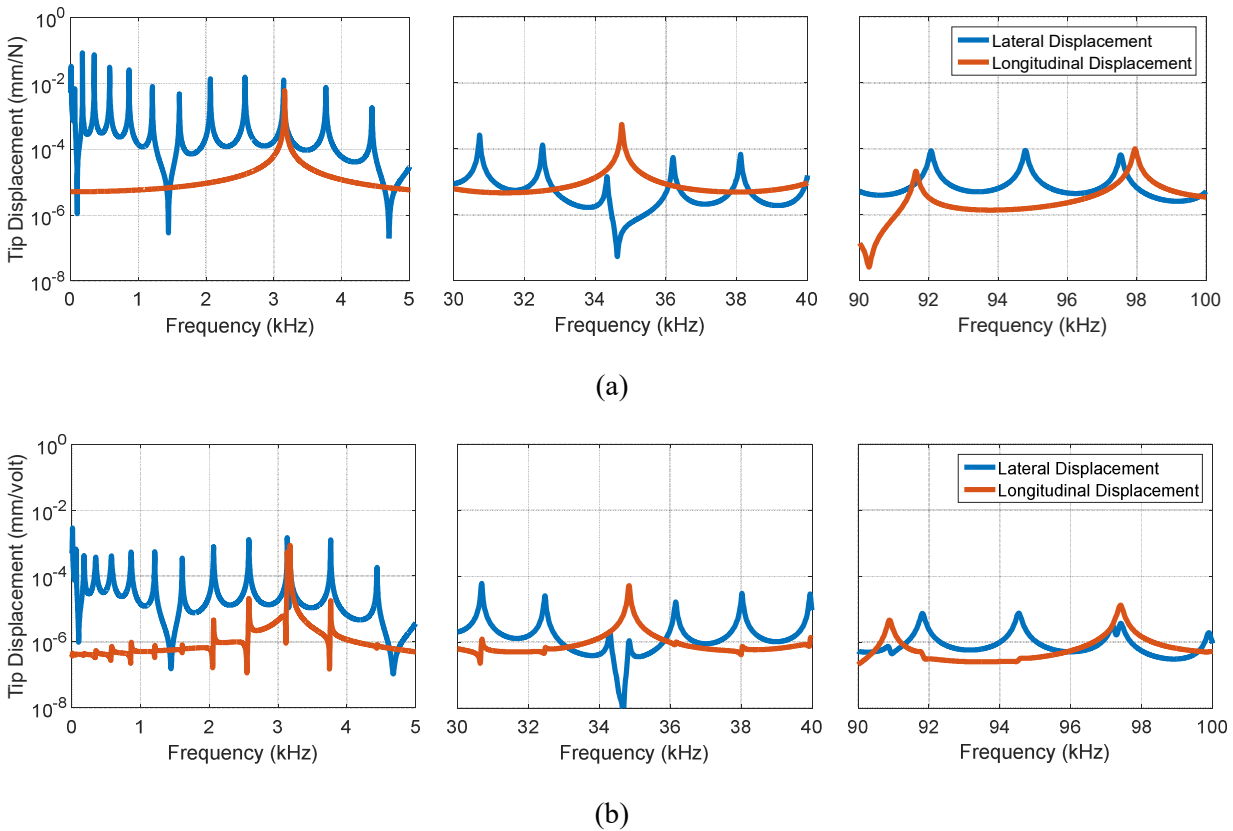
Figure 3.6. Longitudinal and lateral receptance FRFs measured at the beam's tip for (a) the simple benchmark structure, and (b) the piezoelectric augmented structure.

3.3.1   Effects of Piezoelectric and Adhesive Elasticity Moduli

The effects of piezoelectric wafer and bonding layer stiffness, expressed in terms of elasticity moduli, on the dynamic response of the coupled structure are first investigated. For this purpose, the modulus ratio β_{E_a} is varied from $1\text{x}10^{-3}$ to 1, while the ratio β_{E_p} is varied form $1\text{x}10^{-1}$ to 10. All other parameters are kept at their original values as specified in Table 3.1. Changes in resonance frequency associated with the first and the fortieth modes, originally located at 10.2 Hz and 32513 Hz for the benchmark beam, are calculated at different moduli ratio combinations. The results are shown in Figure 3.7 and 3.8. These modes are selected to highlight the frequency dependent nature of the piezoelectric wafer and bonding layer impact on the dynamic response of smart structures.

As a general trend, an increase in the bonding layer and the piezoelectric elasticity moduli results in an increase in all resonance frequencies. The effects are more profound at higher modes, as a comparison between Figure 3.7 and 3.8 suggests. For the cases where the adhesive and the piezoelectric material have comparable elasticity moduli, shown by the close-up view in the figure, both layers have a comparable effect on the dynamic response. The slope of the contour lines in that region reflects the thickness ratio h_a/h_p, which is equal to one half for the structure under consideration.
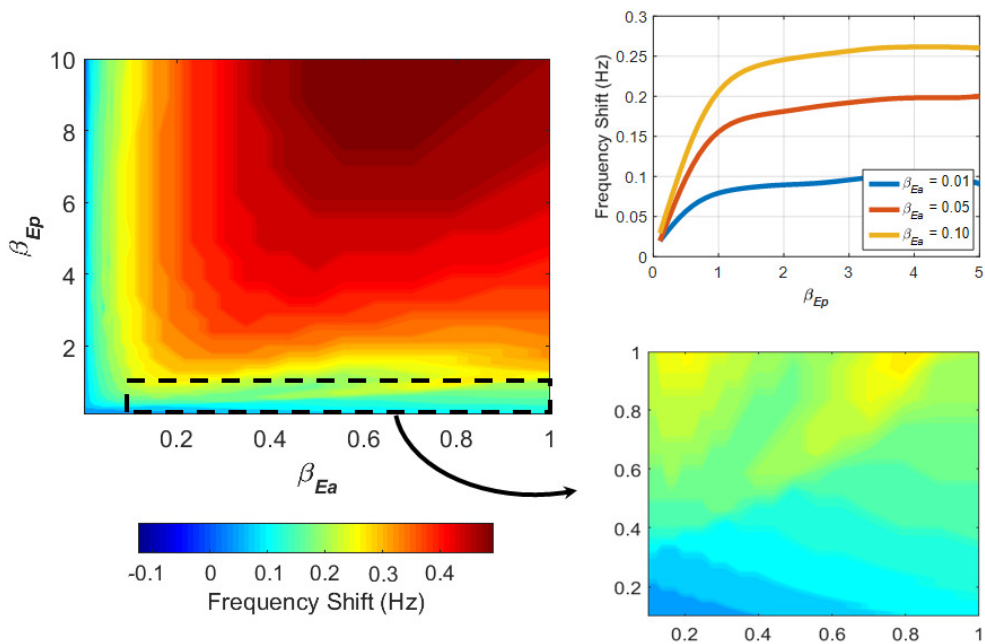
Figure 3.7. Resonance frequency shift for the first mode, originally at 10.2 Hz, as a function of bonding layer and piezoelectric wafer elasticity moduli.

A close examination of the figures reveals important insights on how the dynamic response is affected by bonding layer characteristics. In the limit where the bonding layer stiffness approaches zero, the piezoelectric wafer elasticity modulus is found to have no impact on resonance frequencies, as indicated by contour lines being almost parallel to β_{E_p}-axis. In this case, and due to their inertial effects, the presence of the piezoelectric wafer and bonding layer results in a decrease in resonance frequencies. For high-stiffness adhesives, $E_a \approx E_b$, the shift in resonance frequencies is mostly dominated by the piezoelectric wafer stiffness, as indicated by contour lines being almost parallel to β_{E_a}-axis.

The room temperature elasticity moduli for different types of adhesives commonly used in practical applications have been reported to be in the range of 1-6 GPa (Silva and Adams, 2005; Han et al., 2008b), which corresponds to $\beta_{E_a} \in [0.015 , 0.09]$. For this range, and at a given E_a value, resonance frequencies are found to initially increase with E_p followed by a plateau region. This can be noticed by tracking changes in resonance frequencies for a constant E_a value as shown in Figure 3.7 and Figure 3.8 for $\beta_{E_a} = 0.01$, 0.05, and 0.1. The frequency shift at the plateau strongly depends on the bonding layer stiffness. This behavior can be qualitatively explained by considering the bonding layer and the piezoelectric wafer as a composite structure, where the effective rigidity is capped by the most compliant component.
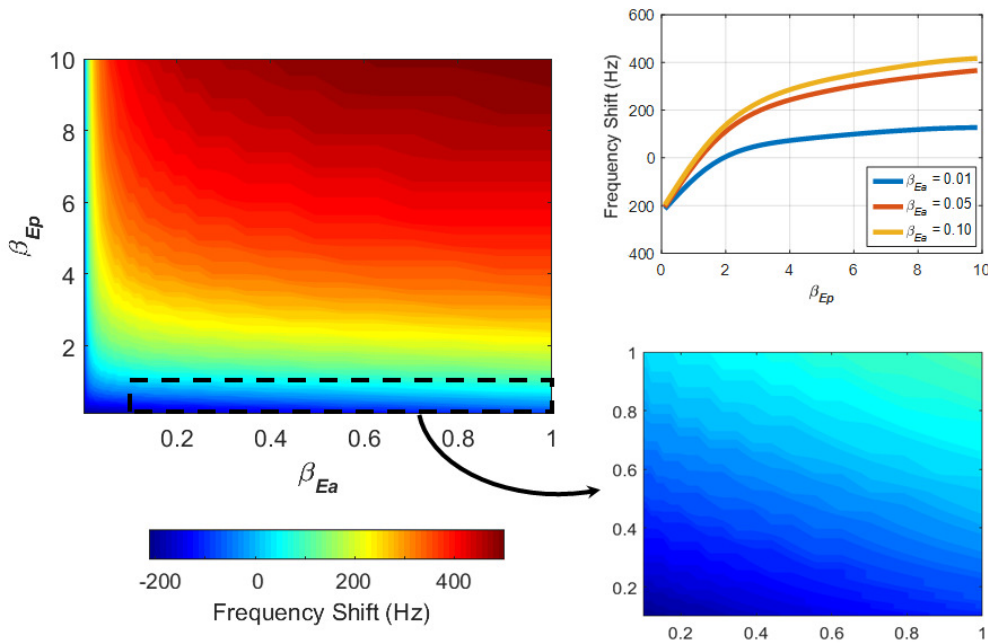
Figure 3.8. Resonance frequency shift for the 40th mode, originally at 32513 Hz, as a function of bonding layer and piezoelectric wafer elasticity moduli.

Figure 3.9 depicts the lateral displacement FRFs measured at the beam's tip at several frequency ranges and several values of β_{E_a}. Although changes in resonance frequencies are negligible at low-frequency ranges, as discussed earlier and shown in the figure, the stiffness of the bonding layer has a significant impact on the actuation authority of the piezoelectric transducer. For a given piezoelectric transducer and excitation amplitude, an increase in bonding layer stiffness results in a monotonic increase in actuation amplitude, indicating a reduction in shear-lag effect. The rate of change of actuation amplitude with respect to bonding layer stiffness decreases as β_{E_a} approaches unity. At this limit, the actuation amplitude is limited by the characteristics of the piezoelectric transducer rather than bonding layer stiffness. As the excitation frequency increases, the impact of bonding layer stiffness on resonance frequencies becomes more significant. Furthermore, the increase in actuation amplitude with adhesive stiffness is no longer monotonic, but it is found to decrease when β_{E_a} exceeds a certain limit. The optimal β_{E_a} value is clearly dependent on frequency, and it is also expected to be a function of bonding layer thickness along with the characteristics of the piezoelectric transducer.

Bonding layer characteristics are also reflected on the electromechanical impedance of piezoelectric augmented structures, as shown in Figure 3.10. The figure depicts the impedance signature of the structure under consideration at two frequency ranges and several values of β_{E_a}. The previously discussed shifts in resonance frequencies are observed in the impedance signature. Furthermore, the sensitivity of impedance measurements to the dynamic behavior of the host structure is significantly affected by bonding layer stiffness. With extremely compliant adhesives, no impedance peaks are observed in the measured signature, and hence, no information about the host structure can be retrieved. As adhesive stiffness increases, impedance peaks become more distinct. Extremely rigid adhesives, on the other hand, adversely affect the amplitude of high-frequency impedance peaks, as is the case for $\beta_{E_a} = 1$ in Figure 3.10.b. This agrees with
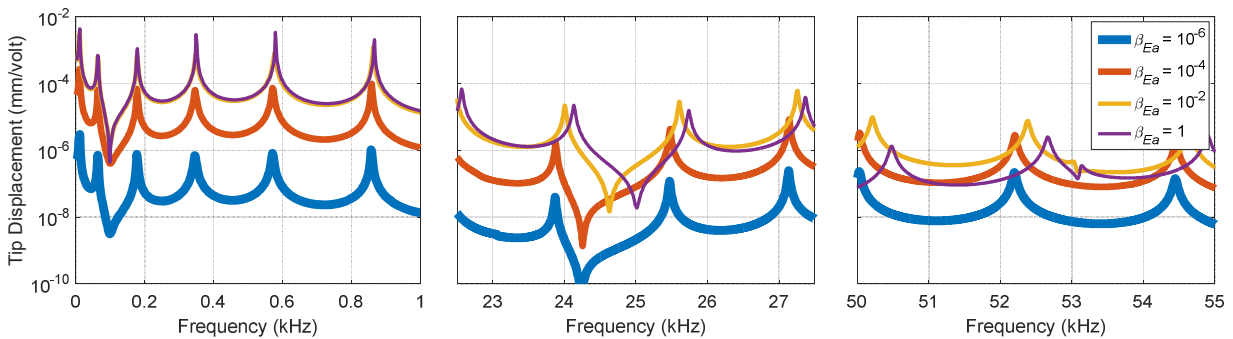
Figure 3.9. Lateral displacement FRFs of the beam's tip with different bonding layer elasticity moduli.

the previously discussed observations regarding the effects of adhesive stiffness on actuation amplitude. The results suggest that there exists an optimal β_{E_a} value for enhanced impedance sensitivity to the underlying structure. This optimal value is a function of frequency over which the structure is interrogated.

3.3.2   Effects of Piezoelectric and Adhesive Density

The effects of piezoelectric wafer and bonding layer densities on the dynamic response of the piezoelectric augmented beam are investigated following the same approach adopted for elasticity moduli. Figure 3.11 depicts the change in the resonance frequency of the beam's fortieth mode, originally at 32513 Hz for the benchmark beam, as the density ratios β_{ρ_a} and β_{ρ_p} are varied from 1x10^{-1} to 10. All other parameters are kept at their original values as specified earlier in this section. The change in resonance frequency of the beam's first mode is found to be negligible, and hence, is not presented.

Unlike elasticity moduli, the effects of the bonding layer and the piezoelectric wafer densities simply appear as monotonic shifts in resonance frequencies. Denser materials result in a drop in all resonance frequencies, and vice versa, with the effects being more profound at higher modes. Both layers, i.e. the adhesive bonding and the piezoelectric wafer, have a comparable impact on the dynamic response, as shown in the figure. The relative effect of density change of these layers is determined by their thickness ratio h_a/h_p, which is equal to one half for the structure under consideration. This ratio is reflected on the slope of the contour lines seen in Figure 3.11.
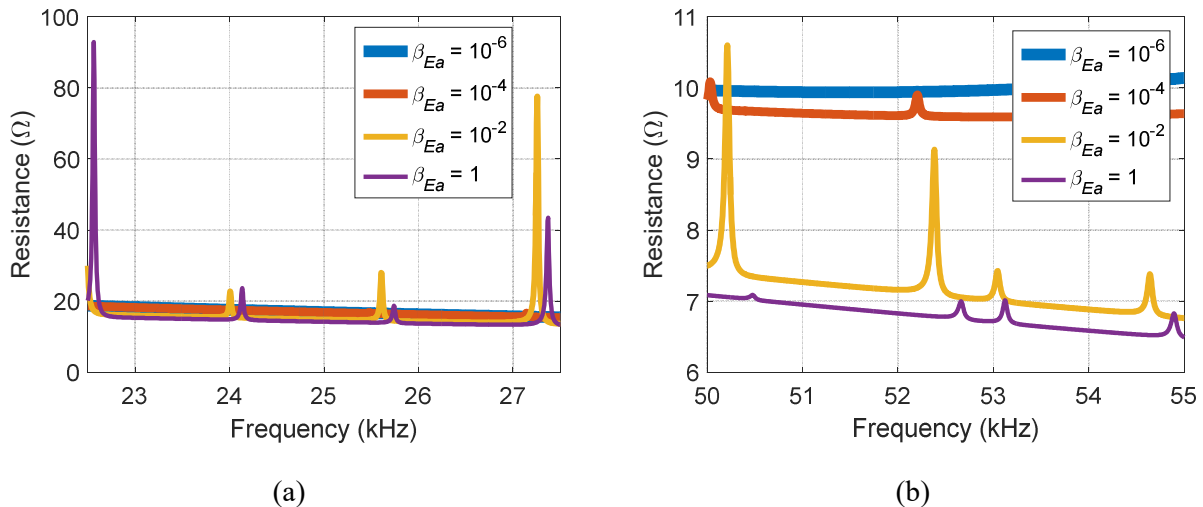
Figure 3.10. Real electromechanical impedance signature of the structure under consideration as a function of β_{Ea} for (a) 22.5-27.5 kHz, and (b) 50-55 kHz frequency ranges.
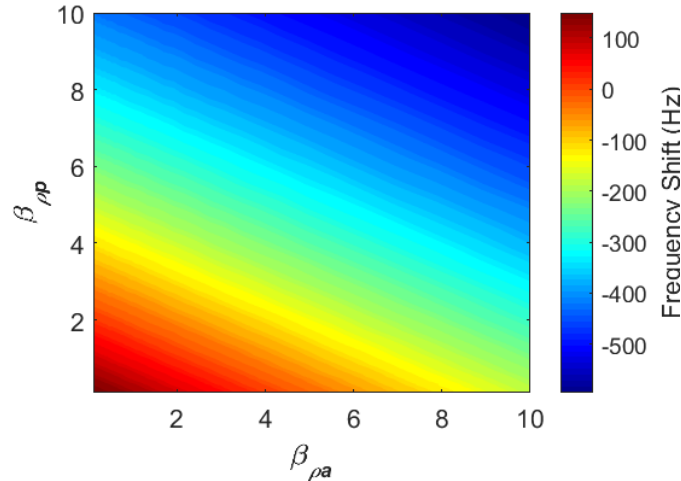
Figure 3.11. Resonance frequency shift for the 40th mode, originally at 32513 Hz, as a function of bonding layer and piezoelectric wafer density.

Figure 3.12 depicts the lateral displacement FRFs measured at the beam's tip at several frequency ranges and several values of β_{ρ_a}. Changes in resonance frequencies are negligible at low-frequency ranges. Frequency shifts become more distinct at higher frequencies, as noticed in the 50-55 kHz response. For all realistic density values, changes in actuation amplitude are negligible. Similar effects are observed on the electromechanical impedance of piezoelectric augmented structure, shown in Figure 3.13, where changes in β_{ρ_a} merely result in impedance peaks shifts.
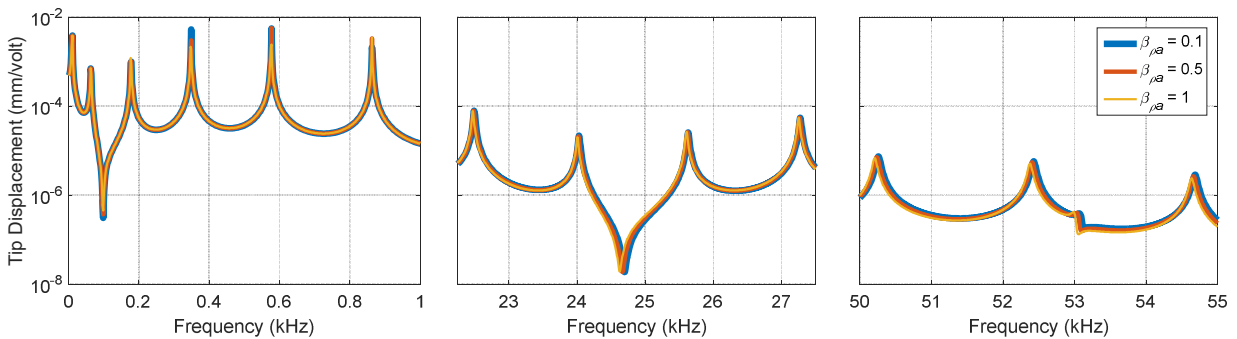
Figure 3.12. Lateral displacement FRFs of the beam's tip with different values of bonding layer density.

3.3.3   Effects of Piezoelectric Wafer and Bonding Layer Thickness

The third set of parameters investigated in this section are piezoelectric wafer and bonding layer thicknesses, defined by the ratios β_{h_a} and β_{h_p}. The effects of these parameters on the dynamic response of piezoelectric augmented structures are investigated following the same approach adopted in the previous sections. Resonance frequency shifts are governed by two counter acting factors related to thickness changes, these are flexural rigidity and inertia. An increase in a given layer's thickness results in an increase in flexural rigidity, which tends to shift resonance frequencies to the right. It also results in an increase in that layer's inertia, which tends to shift resonance frequencies to the left. The overall effect depends on the stifness and density of each layer, in addition to their individual thicknesses. Actaution amplitude, on the other hand, is governed by another two counter acting factors: actuation momnet and shear-lag effect. An increase in a given layer's thickness yields larger bending moment due to the larger offset from the nuetral axis, which in turn results in a larger actaution amplitude. It also causes a more significant shear-lag in the bonding layer, which adversely affects actuation amplitude. The overall effect also depends on the stifness of each layer and the frequency range of interest.

In order to quantify these effects for the structure at hand, the thickness ratio β_{h_a} is varied from 5 x 10^{-3} to 0.5, while the ratio β_{h_p} is varied form 5 x 10^{-2} to 0.5. All other parameters are kept at their original values. Changes in resonance frequency of the first and fortieth modes are calculated at different β_{h_a} and β_{h_p}

(a)   (b)
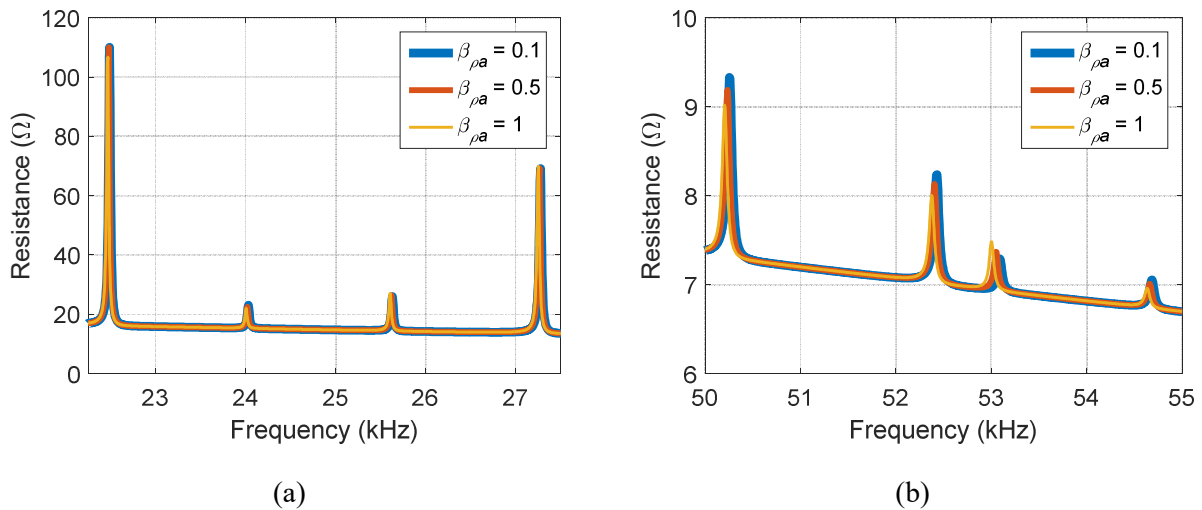
Figure 3.13. Real electromechanical impedance signature of the structure under consideration as a function of $\beta_{\rho a}$ for (a) 22.5-27.5 kHz, and (b) 50-55 kHz frequency ranges.
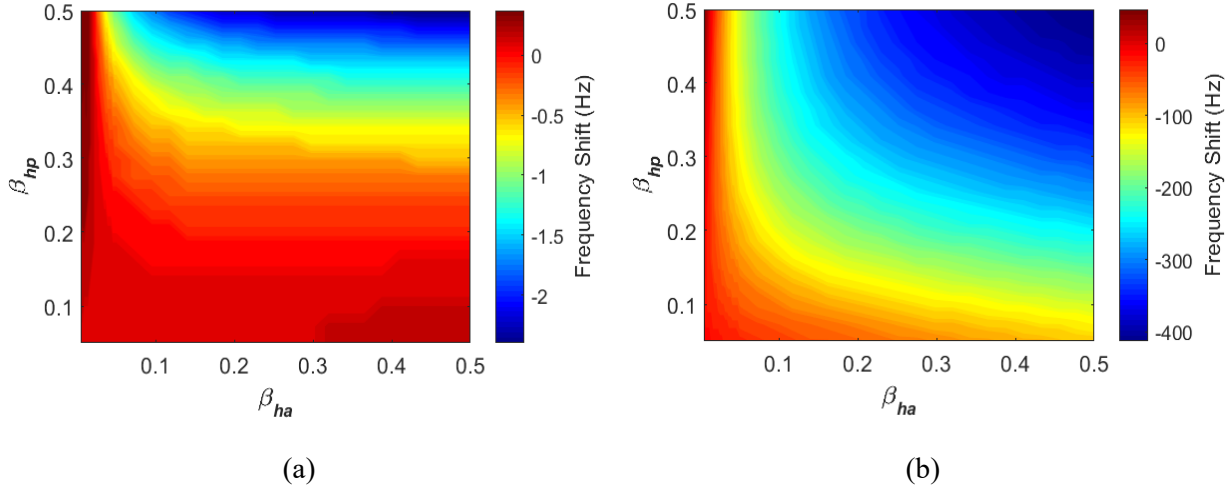
Figure 3.14. Resonance frequency shift for the (a) first mode at 10.2 Hz, and (b) 40th mode at 32513 Hz, as a function of bonding layer and piezoelectric wafer thickness.

combinations. The results are shown in Figure 3.14. For the stiffness and density values, reported in Table 3.1, an increase in either layer thickness results in a reduction in resonance frequencies. This indicates that the effect of the added mass associated with thickness increase outweighs that of the gained flexural rigidity. This is true except for very thin bonding layers, $\beta_{h_a} < 10^{-2}$, where an increase in the piezoelectric wafer thickness results in an increase in resonance frequencies; an indication of more dominant rigidity effects. The thickness threshold beyond which inertial effects dominate, $\beta_{h_a} \approx 10^{-2}$ for the structure under consideration, is strongly dependent on the bonding layer stiffness. This behavior can be ascribed to the fact that the effective rigidity of the piezoelectric wafer and bonding layer is capped by the most compliant component, which is the adhesive bonding in this case. Therefore, an increase in the piezoelectric wafer thickness does not increase the effective rigidity of the composite structure beyond that limit, rendering inertial effects as the only factor affecting the response.

The effect of β_{h_a} on the lateral displacement FRFs measured at the beam's tip at several frequency ranges is shown in Figure 3.15. As discussed earlier, the impact of bonding layer characteristics is more profound at high-frequency ranges. Besides resonance frequency shifts, actuation amplitude is also affected by the bonding layer thickness. At low-frequency excitation, thick bonding layer results in a reduction in actuation amplitude, as shown in the figure, indicating more prominent shear-lag effect. This trend reverses at higher frequency ranges, 50-55 kHz for instance, where an increase in bonding layer thickness yields larger actuation. Therefore, an optimal bonding layer thickness is strongly dependent on the frequency range of interest, and it is also affected by adhesive's rigidity and the characterstics of the piezoelectric wafer.
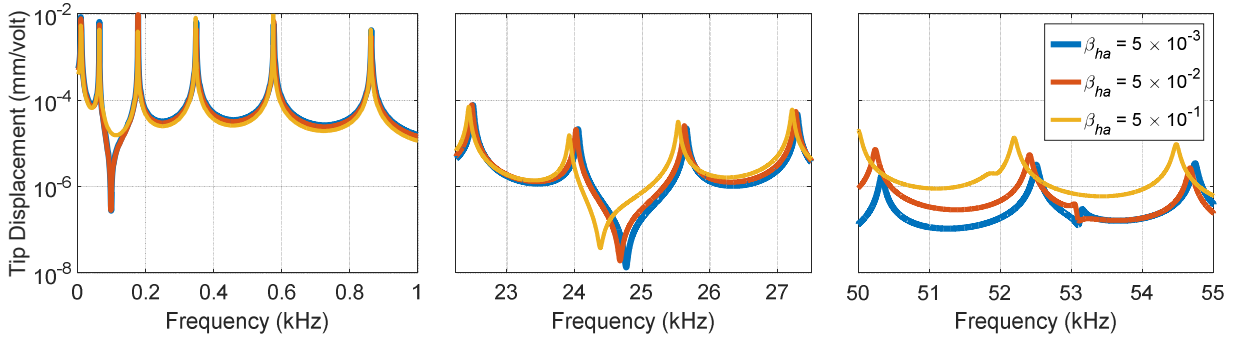
Figure 3.15. Lateral displacement FRFs of the beam's tip with different bonding layer thickness values.

The effects of bonding layer thickness are also reflected on the electromechanical impedance of the coupled structure, as shown in Figure 3.16. Shifts in impedance peaks along with changes in impedance magnitude are observed. These changes have the same underlying origins discussed for the FRFs in Figure 3.15. Unlike adhesive's stiffness, which can degrade over time, bonding layer thickness is time invariant, therefore, its effect can be ignored for impedance-based damage detection applications. This is due to the fact that both baseline and current impedance measurements will be equally affected by bonding layer thickness. Model-based damage characterization efforts, on the other hand, need to accurately account for the adhesive bonding layer. If not accounted for properly, changes in bonding layer characteristic may blur the effects of structural defects, or be misinterpreted as one. This is especially important when high-frequency impedance measurements are utilized for damage characterization, where the effects of the bonding layer on the steady state dynamic response are more profound.

3.4   Conclusions

This chapter investigates the effects of piezoelectric wafer and bonding layer characteristics on the dynamic response of piezoelectric augmented structures. This is achieved utilizing the three-layer spectral element model developed in Chapter 2. The dynamic response of free piezoelectric transducers is first studied by non-dimensionalizing the electromechanically-coupled equations of motion. Three non-dimensional parameters, two of which are complex, fully describe the system. These non-dimensional parameters describe the geometry of the piezoelectric wafer, the ratio between driving electric force and restoring elastic force, and the ratio between dielectric charge and that induced by electromechanical coupling.
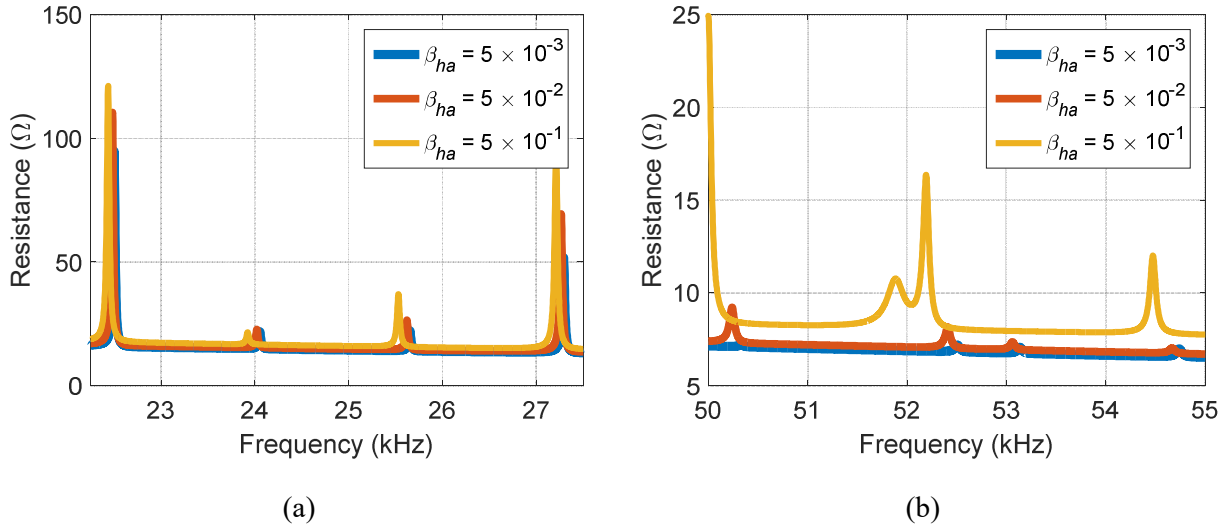
Figure 3.16. Real electromechanical impedance signature of the structure under consideration as a function of β_{ha} for (a) 22.5-27.5 kHz, and (b) 50-55 kHz frequency ranges.

The effects of each non-dimensional parameter on FRFs and electromechanical impedance signatures of the free piezoelectric transducer have been thoroughly studied. A procedure for piezoelectric material characterization based on impedance measurements has also been proposed.

The dynamic response of a piezoelectric-augmented beam has then been studied, where the effects of piezoelectric wafer and bonding layer characteristics, namely thickness, stiffness and density, are investigated. In general, the dynamic response of smart structures is determined by the host structure itself, and the effects of the piezoelectric wafer and bonding layer appear as perturbations of that initial state. While different feature can be used to identify and quantify the piezoelectric wafer and bonding layer impact on the dynamic response, the focus of the current work has been turned towards resonance frequency shifts and actuation amplitude variations. These features have been selected as they are essential for structural health monitoring, energy harvesting, and control applications.

Changes in resonance frequencies due to variations in piezoelectric wafer and bonding layer characteristics are found to be negligible at low-frequency ranges. Actuation amplitude, on the other hand, is found to be strongly dependent on bonding layer stiffness. At low frequency, a more rigid bonding layer is found to enhance the actuation authority of the piezoelectric transducer. This effect is also observed at higher frequencies, however, there exists an optimal stiffness beyond which an increase in adhesive stiffness

81

adversely affects the response. This optimal stiffness is a function of bonding layer thickness and the frequency range of interest.

The density of the piezoelectric and adhesive materials is found to have a minimal impact on the dynamic response of the structure considered in this study. These effects will be more significant for thick piezoelectric wafers and bonding layers, or a very thin host structure. The effects of the piezoelectric wafer and bonding layer thicknesses have also been investigated. For low-stiffness adhesives, an increase in thickness generally results in a reduction in all resonance frequencies, as the added mass associated with thickness increase outweighs the gained increase in stiffness. Actuation amplitude is also found to be affected by the bonding layer thickness. While thin bonding layers are advantageous at low-frequency ranges, thicker layers are found to provide more actuation authority at higher frequencies. Therefore, the optimal bonding layer thickness is strongly dependent on the frequency range of interest. This optimal thickness is also affected by the adhesive's rigidity and the characteristics of the piezoelectric wafer.

The results presented in this section highlight the need for including the effects of bonding layer characteristics in damage detection and identification efforts. If not accounted for properly, bonding layer degradation may blur the effects of structural defects, or be misinterpreted as one. This is especially important when high-frequency impedance measurements are utilized for damage characterization. Furthermore, bonding layer characteristics, in terms of thickness and rigidity, can be optimized to enhance actuation authority, which is of interest for control and energy harvesting applications.

CHAPTER FOUR

ELECTROMECHANICAL IMPEDANCE-BASED DAMAGE IDENTIFICATION

4.1   Introduction

Detection and characterization of defects in structural and mechanical components have been the main objective of all SHM practices. In this chapter, a novel optimization-based damage characterization approach that utilizes impedance signature measured by a single piezoelectric wafer is developed. With this approach, length-varying spectral elements are implemented to minimize the number of damage characterization parameters. Only three variables are needed to fully characterize a single open crack, these are the location of the damaged section, its width, and the severity of the damage defined by stiffness reduction. The high-frequency piezoelectric-structure interaction model developed in Chapter 2 is used here to simulate the impedance signature of the pristine and damaged cases.

This chapter starts with damage modeling, where length-varying spectral elements are used to reduce the number of damage identifying parameters. Several objective function definitions are then introduced, and their behavior with respect to width, severity, and damage location parameters is investigated. A novel damage localization method is then developed, and integrated with gradient descent method in a two-stage optimization algorithm for damage characterization. Concluding remarks are finally presented.

4.2   Damage Modeling

Open, non-breathing cracks are modeled as a reduction in axial and bending stiffness in the section where the crack is located (Dilena and Morassi, 2009; Park et al., 2000). Therefore, a single damage can be described by determining three parameters: crack location, crack width, and stiffness reduction, denoted respectively by x_a, x_b, and α. A beam with such a crack is shown in Figure 4.1.a. The piezoelectric augmented beam with a single open crack can be fully described with five spectral elements, as shown in Figure 4.1.b. Element *E4* in the figure is where the crack is located, and its stiffness is reduced by a factor $\alpha \equiv E/E_0 \in (0,1]$, where E is the reduced elasticity modulus of the damaged element, and E_0 is the elasticity modulus of the pristine elements. Three types of elements are used in the spectral element mesh developed for this study, these are:

- A piezoelectric-adhesive-beam element: element *E2*, which is the three-layer element developed in Section 2.4.
- Beam only elements: elements *E1*, *E3*, and *E5*, which are a reduced version of the three-layer element formulated in Section 2.2.2.
- A cracked beam element: element *E4*, which is a beam-only element with a reduced stiffness.

Given the impedance signature of an unknown damage, by minimizing the difference between the simulated response and that of the damaged case the variables x_a, x_b, and α are determined and damage is characterized. With length-varying spectral elements, the proposed spatial discretization significantly reduces the number of variables required for damage characterization. Furthermore, the accuracy to which the damage can be identified, in terms of location and width, is not limited by the resolution of the spectral element mesh, as it is the case with a fixed mesh approaches.

For all numerical experiments presented in this study, a cantilever beam partially covered with a piezoelectric wafer, shown in Figure 4.1.b, is used. The beam is 400 *mm* long, 20 *mm* wide, and 2 *mm* thick, fixed at its left end. A 20 *mm* long, 0.2 *mm* thick piezoelectric wafer is attached to the beam 60 *mm* from its fixed end. The adhesive bonding layer is 0.1 *mm* in thickness. The piezoelectric wafer is excited with a sinusoidal voltage signal applied across its terminals. Material properties for the each of the three layers are summarized in Table 3.1.

(a)

(b)
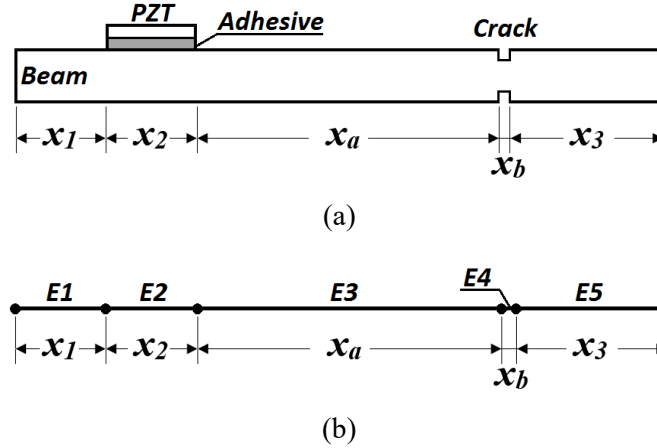
Figure 4.1. (a) Cracked beam with a piezoelectric patch, (b) spectral element mesh with length varying elements. For all cases considered in this study $x_1 = 60$ *mm*, $x_2 = 20$ *mm*, and the overall beam length is 400 *mm*.

4.3   Optimization-based Damage Characterization

In this section, the problem of damage characterization is cast as an optimization problem. Following some of the commonly used damage metrics in the field of impedance-based SHM, three definitions for the objective function are introduced. The effect of each damage parameter, namely width, location and severity, on objective functions behavior is then studied in details. For the ill-posed problem of damage localization, a new method is developed and integrated into a two-stage optimization scheme for damage characterization.

4.3.1   Objective Function Definition

The problem of damage characterization is handled as an optimization problem, where damage identifying parameters, x_a, x_b and α, are determined by minimizing an objective function quantifying the difference between the simulated response and that of the damaged case. The definition of the objective function is known to be deterministic for the behavior of the optimization problem and the number of iterations required for convergence. Following the most common damage metrics used with impedance-based SHM, three objective function definitions are studied in this section. These objective functions are based on the

root mean square deviation (RMSD), the correlation, and the shifts in peak frequencies, denoted by $\mathcal{J}_1, \mathcal{J}_2$, and $\mathcal{J}_3$, respectively. These objective functions are defined as follows

$$\mathcal{J}_1 = RMSD\big(Z(x_a, x_b, \alpha), Z_{Damaged}\big)$$

$$\mathcal{J}_2 = 1 - Correlation\big(Z(x_a, x_b, \alpha), Z_{Damaged}\big)$$

(4.1)

$$\mathcal{J}_3 = \sum_{i=1}^{N} \frac{\big|\omega_p^i(x_a, x_b, \alpha) - \omega_{p,Damaged}^i\big|}{\omega_{p,Damaged}^i}$$

where $Z(x_a, x_b, \alpha)$, is the impedance signature evaluated at specific values of damage parameters, $Z_{Damaged}$ is the impedance signature of the damaged case to be identified, and ω_p^i is the frequency of the ith peak in the impedance signature. For all three objective functions, the global minimum is reached when the value of the objective function approaches zero. This is achievable when the simulated impedance signature matches that of the damaged case. In general, solution uniqueness is not guaranteed, and it depends on the frequency range over which impedance signatures are compared. Several case studies are presented in the following sections to investigate the behavior of each objective function with respect to damage parameters. Solution uniqueness and convergence are also discussed.

4.3.2   Effects of Damage Width and Severity

In general, the presence of damage reduces the effective stiffness of the structure, and hence, shifts all its resonance frequencies to the left compared to the pristine structure. As damage width and severity increase, damage impact on the dynamic response of the structure becomes more significant, which in turn results in a monotonic increase in frequencies shift. Figure 4.2 shows the frequency response functions (FRFs) of the lateral displacement of the cantilever beam tip at different levels of damage width and severity. Figure 4.2.a shows the effects of damage severity on FRFs, where the damaged section is 3 *mm* wide. The effects of damage width on FRFs are shown in Figure 4.2.b, where damage severity is 0.5. For both cases, the damage is located 200 *mm* from the fixed end of the beam. The monotonic decrease in resonance frequencies as damage increases in width and severity are evident in the figures, which agrees with the findings reported in earlier studies (Albakri and Tarazaga, 2014; Lee and Shin, 2002).
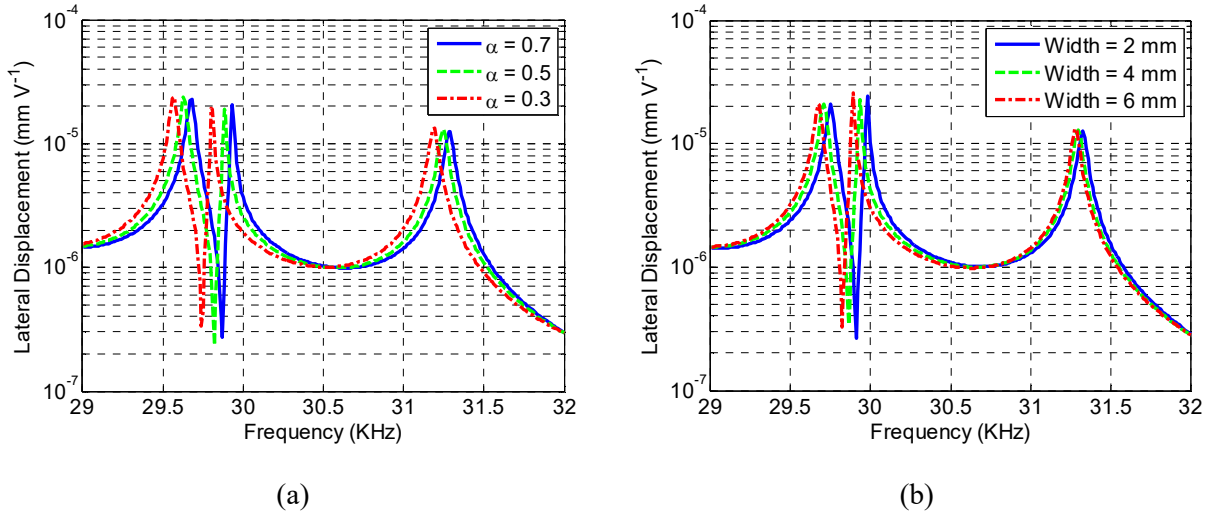
Figure 4.2. Lateral displacement FRFs of the beam's tip with (a) 3 *mm* wide and varying severity, and (b) 0.5 in severity and varying width open cracks located 200 *mm* from the fixed end.
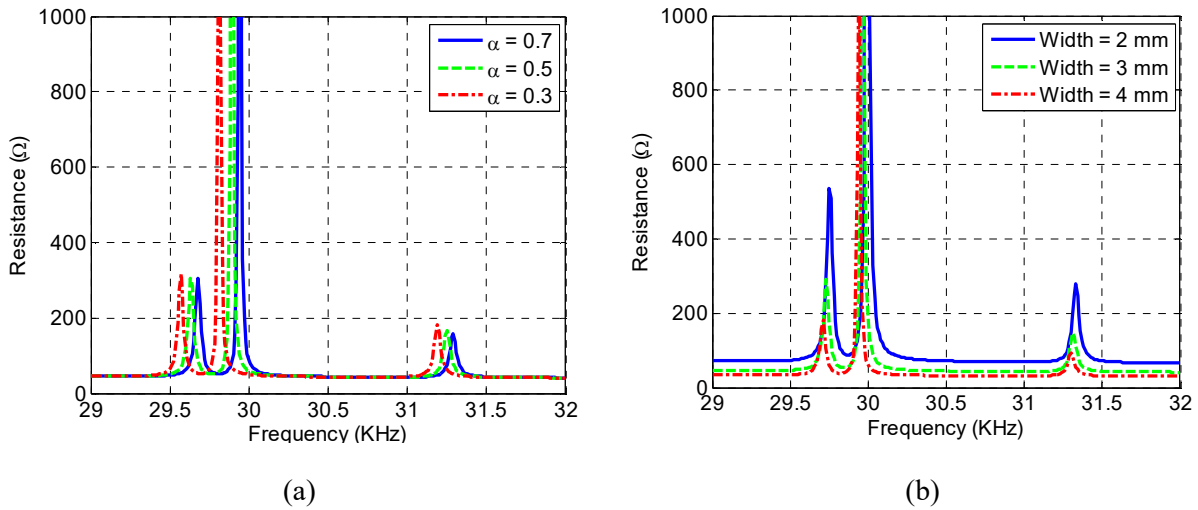
Figure 4.3. Impedance signature of a beam with (a) 3 *mm* wide and varying severity, and (b) 0.5 in severity and varying width open cracks located 200 *mm* from the fixed end.

Similar effects are noticed on impedance signatures, where impedance peaks shift to the left as damage is introduced. These shifts monotonically increase with damage width and severity. Figure 4.3 shows the impedance signature at different levels of damage width and severity for the same damage scenarios of Figure 4.2.

To study the behavior of each of the three objective functions considered in this study with respect to damage severity, two damage scenarios are considered, as summarized in Table 4.1. For the first scenario, denoted by S1, a 1 *mm* wide open crack, with 0.9 severity, is assumed to exist a 100 *mm* from the fixed end of the beam. For the second scenario, S2, the assumed damage is 3 *mm* wide, 0.5 in severity, located 200 *mm* from the beam's fixed end. For both cases, damage severity is varied gradually from 0.2 to 1, while keeping the other two parameters fixed at their original values. Impedance signatures in the range of 29 to 32 kHz are then simulated, and objective functions are evaluated following the definitions given by Eq. 4.1. The results are shown in Figure 4.4.a and 4.4.b for damage S1 and S2, respectively.

Table 4.1. Damage scenarios considered for severity, width, and location case studies.

	Damage Severity		Damage Width		Damage Location		
	S1	S2	W1	W2	L1	L2	L3
Damage Severity ($\alpha \equiv E/E_0$)	0.9	0.5	0.7	0.9	0.5	0.7	0.9
Damage width (x_b, *mm*)	1	3	3	5	1	5	2
Damage location (x_a, *mm*)	20	120	120	220	170	270	70

It is noticed that all three objective functions have a global minimum at the actual damage severity values, 0.9 and 0.5 for S1 and S2 scenarios, respectively. As the severity deviates from the actual value, the objective function value increases. While RMSD- and correlation-based definitions, $\mathcal{J}_1$ and $\mathcal{J}_2$, show a local minima at $\alpha = 0.2$, the peak-shifts based definition, $\mathcal{J}_3$, shows a convex behavior where its value increases monotonically as α moves away from its true value. Moreover, $\mathcal{J}_3$ definition provides better search directions compared to the other two definitions, which results in a faster converging optimization problem. This behavior of $\mathcal{J}_3$ definition is intuitive as impedance signature peaks always shift to lower, or higher, frequencies as the damage severity increases, or decreases, as shown in Figure 4.3.a.

The previous analysis is repeated for the damage width parameter. Two damage scenarios are also considered, as shown in Table 4.1. For damage W1, a 3 *mm* wide, 0.7 in severity crack is assumed to exist 200 *mm* from the fixed end of the beam, while damage W2 assumes a 5 *mm* wide, 0.9 in severity, located 300 *mm* from the beam's fixed end. Damage width is varied gradually from 1 *mm* to 10 *mm* while keeping the overall length of the beam and the other two parameters fixed at their original values. The response is then simulated over the same frequency range, and the objective functions are evaluated. The results are shown in Figure 4.5.a and 4.5.b for damages W1 and W2, respectively.
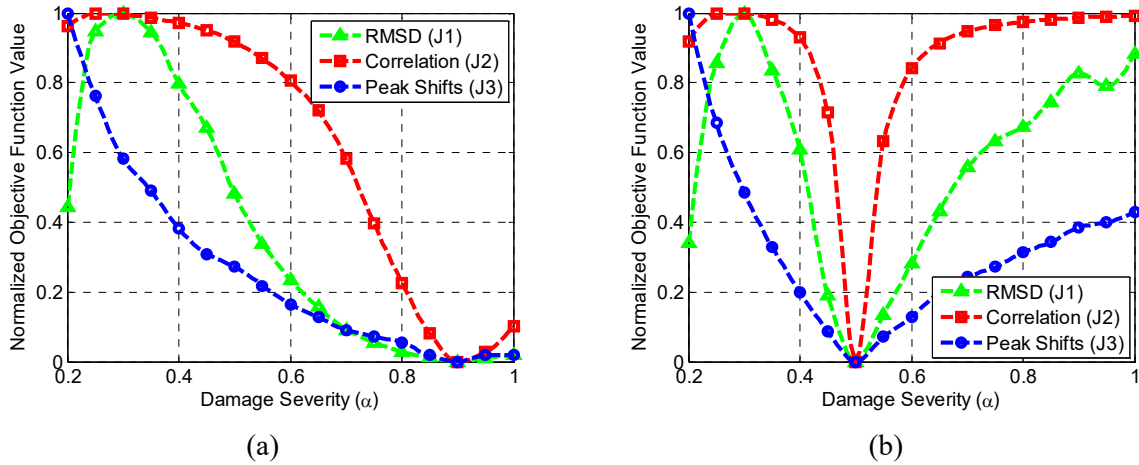
Figure 4.4. Objective functions behavior with respect to damage severity parameter. Actual damage is (a) 1 *mm* wide, 0.9 in severity, located a 100 *mm* from the fixed end, and (b) 3 *mm* wide, 0.5 in severity, located 200 *mm* from the fixed end.
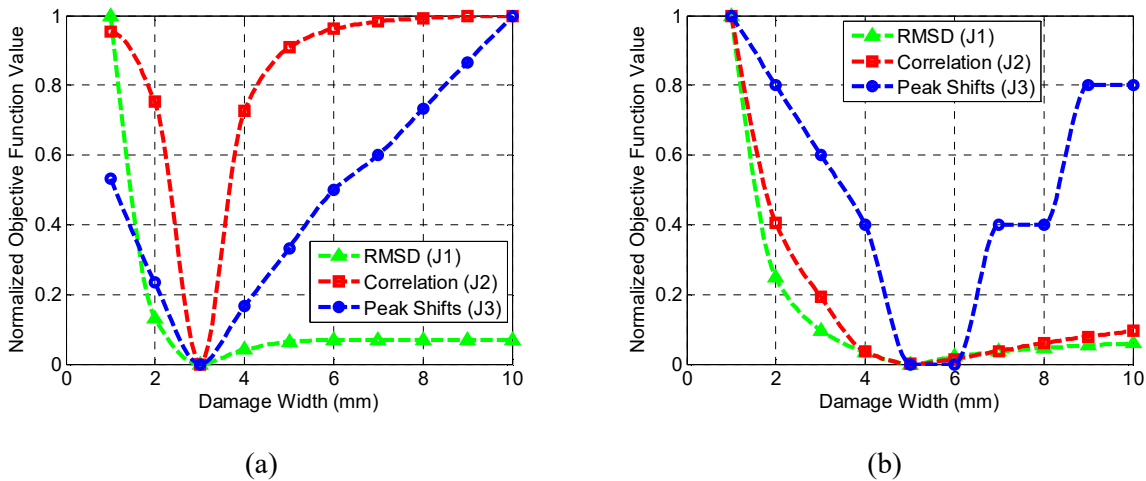
Figure 4.5. Objective functions behavior with respect to damage width parameter. Actual damage is (a) 3 *mm* wide, 0.7 in severity, and located a 200 *mm* from the fixed end, and (b) 5 *mm* wide, 0.9 in severity, and located 300 *mm* from the fixed end.

As is the case with damage severity, all three objective functions have a global minimum at the true damage width value, 3 *mm* and 5 *mm* for damage scenarios W1 and W2, respectively. As damage width deviates from its true value, all objective functions increase monotonically. It is noticed that RMSD and correlation

based definitions have smaller slopes away from the optimal solution, which results in slower convergence compared to peak-shifts based definition. For damage W2, $\mathcal{J}_3$ definition shows a stepwise behavior, where different damage width values yield the same objective function value. Therefore, a unique optimal solution is unattainable, rather, a range of optimal solutions is obtained. This odd behavior is a result of the limited resolution of the frequency sweep used to simulate the impedance signature. Damage W2 represents a slightly damaged case, with only 0.1 reduction in modulus of elasticity. Therefore, the change in the dynamic response, and hence in the impedance signature, induced by such a damage is relatively small and falls below the frequency-sweep resolution.

For a more complete evaluation of the objective functions dependence on damage width and severity parameters, damage width is swept from 1 *mm* to 10 *mm* in 0.5 *mm* steps, damage severity is swept from 0.1 to 1 in 0.05 steps, and the three objective functions are evaluated for the resulting 361 combinations. The results are shown in Figure 4.6.a, 4.6.b, and 4.6.c for $\mathcal{J}_1$, $\mathcal{J}_2$, and $\mathcal{J}_3$, respectively. For all cases, the actual damage (the reference state) is 5 *mm* wide, 0.7 in severity, located 200 *mm* from the fixed end of the beam. All three objective functions have a unique global minimum at x_b = 5 *mm* and α = 0.7. RMSD-based definition, Figure 4.6.a, has two separate local minima. Depending on the optimization algorithm and the initial guess, the solution may converge to either one, and hence, more iterations will be required for accurate damage characterization. On the other hand, Correlation-based definition shows a band with several local minima, as shown in Figure 4.6.b. This band defines the region of equivalent effective damages, i.e. combinations of width and severity that have a similar impact on the objective function as the actual damage. The presence of several local minima in this band, along with few others outside it, makes it harder for the optimization problem to converge to the global minimum, and hence, results in a computationally more demanding problem. The peak-shifts-based objective function, $\mathcal{J}_3$, shows a similar band as in $\mathcal{J}_2$, but with a monotonically decreasing value as damage parameters approach their true values. With a high frequency-sweep resolution, a single minimum exists, which is the global minimum, and descending directions always lead to the optimal solution. Due to its superior behavior as compared to the other two definitions, $\mathcal{J}_3$ will be used for impedance-based damage identification through the rest of this study.
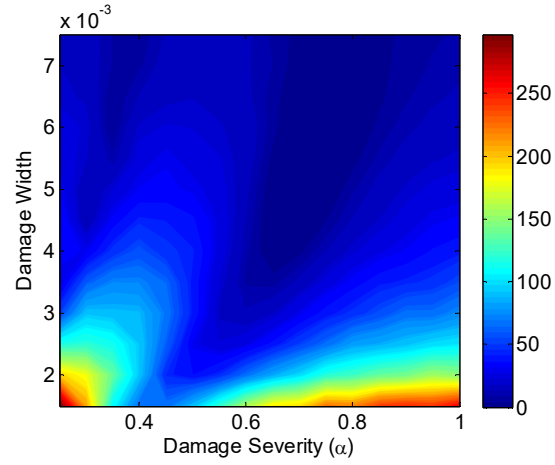
(a)
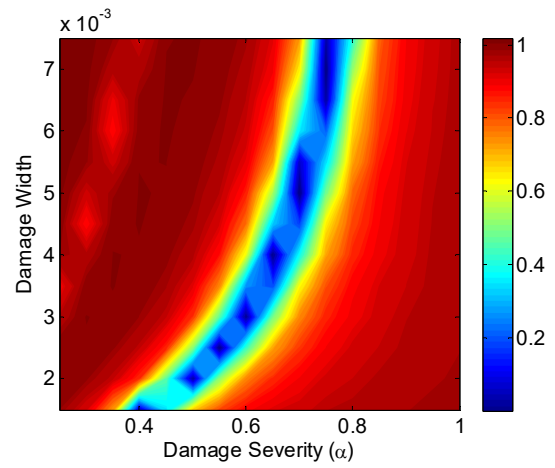
(b)
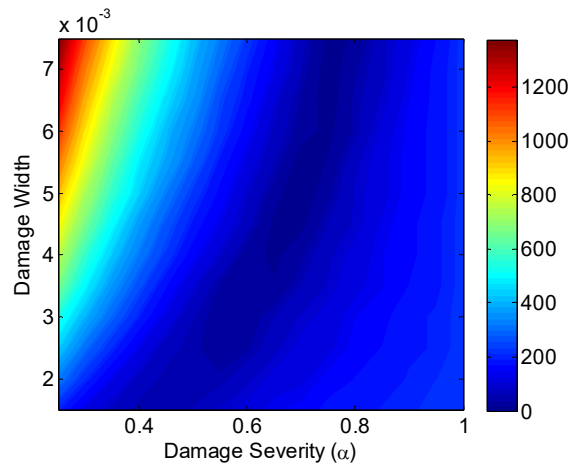
(c)

Figure 4.6. Objective functions behavior contours with varying damage width and severity, (a) RMSD-based objective function, (b) correlation-based objective function, and (c) peak-shifts-based objective function.

4.3.3   Effects of Damage Location

With the proposed spectral element discretization, a single open crack is characterized by three damage parameters, width, severity, and location. The effects of the former two parameters are investigated in the previous section, while the latter is thoroughly investigated in the current section. A phenomenological-driven solution technique for the optimization problem is also introduced. Three damage scenarios are initially considered, as summarized in Table 4.1. For the first scenario, denoted by L1, a 1 *mm* wide open crack with 0.5 severity is assumed to exist 250 *mm* from the fixed end of the beam. For the second scenario, L2, the assumed damage is 5 *mm* wide, 0.7 in severity, located 350 *mm* from the beam's fixed end. The third scenario, L3, is 2 *mm* wide crack, 0.9 in severity, located 150 *mm* from the beam's fixed end. For all three scenarios, damage location is varied gradually from 100 *mm* to 380 *mm* while keeping the other two parameters fixed at their original values. Impedance signatures are simulated over the same frequency range as in the previous cases, and the peak-shifts-based objective function is evaluated. The results are shown in Figure 4.7.

Unlike the effects of damage width and severity where the objective function showed a convex behavior with a single minimum and clear search directions, the effect of damage location on $\mathcal{J}_3$ objective function is far more complicated. Even when the damage location is the only unknown parameter, the objective function shows what appears to be a random behavior, with several local minima and no clear search directions. This makes the optimization problem an ill-posed one, where most conventional iterative methods, such as Newton's and gradient methods, fail. Heuristic optimization algorithms, such as genetic algorithms and particle swarm optimization, are usually resorted to when dealing with such problems, but this comes at the cost of computational efficiency.

(a)	(b)	(c)
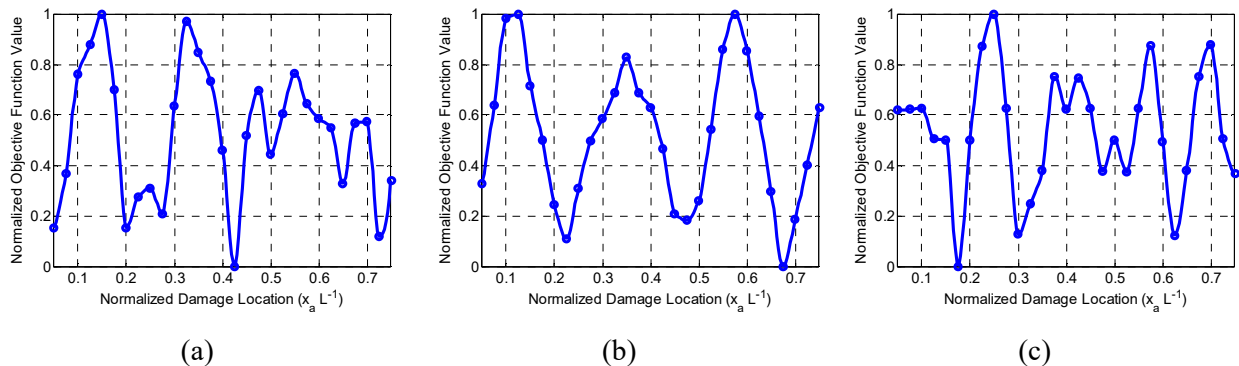
Figure 4.7. Peak-shifts-based objective function behavior with respect to damage location, (a) damage scenario L1, (b) damage scenario L2, and (c) damage scenario L3.

$\mathcal{J}_3$ objective function is defined as the summation of the magnitude of impedance peak frequency shifts normalized by the original frequency, as given by Eq. 4.1.c. For the frequency range of interest, 29 to 32 kHz, impedance signature has three distinct peaks, as shown in Figure 4.3. When individual components of $\mathcal{J}_3$ are considered, i.e. frequency shift of individual peaks, a periodic behavior is observed, as shown in Figure 4.8. This indicates that each peak in the impedance signature shifts in a periodic manner with variations in damage location. Therefore, what appears to be a random behavior, Figure 4.7, has an underlying periodic characteristics. This underlying periodicity can be utilized to solve the problem of damage localiation with a minimal number of objective function evaluations.

The proposed solution technique for the optimization problem at hand starts with evaluating the objective function at certain values of the damage location parameter. These values are selected in a way that spans the solution space of this parameter, $x_a \in (0, x_1) \cup (x_1 + x_2, L - x_b)$. The number of function evaluations is selected so as to avoid spatial aliasing, and the minimum requirements are found to be dependent on the frequency range of interest. For the current problem, 10-15 points are needed to accurately represent the behavior of individual peaks shift. A sinusoidal function is then fitted to each set of peak shift values, these functions are referred to as *frequency-shift functions*. The resulting three functions allow for evaluating the objective function $\mathcal{J}_3$ at a very high resolution of the damage location parameter, which is then utilized for finding the optimal solution with a minimal computational cost. As the proposed solution method relies on the sinusoidal behavior of the frequency shift functions, it will be referred to as *Sine-fit Localization Method* (SLM). With this method, damage location parameter (x_a) is found to be 170.6 mm, 269 mm, and 70.7 mm for cases L1, L2 and L3 damage scenarios, respectively. When normalized by beam length, these values become 0.43, 0.672, and 0.177, which are the locations where all frequency-shift functions intersect with the zero shift axis, as shown in Figure 4.8. These values are within 1% of the actual damage location. Thus, with only 15 evaluations of the objective function, this ill-posed optimization problem is solved with a very high accuracy.

Close examination of individual impedance peak shifts, Figure 4.8, shows that each component crosses the zero shift axis at several values of damage location parameter. Therefore, if the frequency range over which the impedance signature is measured has only one single peak, a unique optimal solution will not be attainable with such objective function. A generalized minimum number of peaks required to guarantee solution uniqueness has not been determined, however, three peaks are found to be sufficient for all the damage scenarios considered in this study.

93
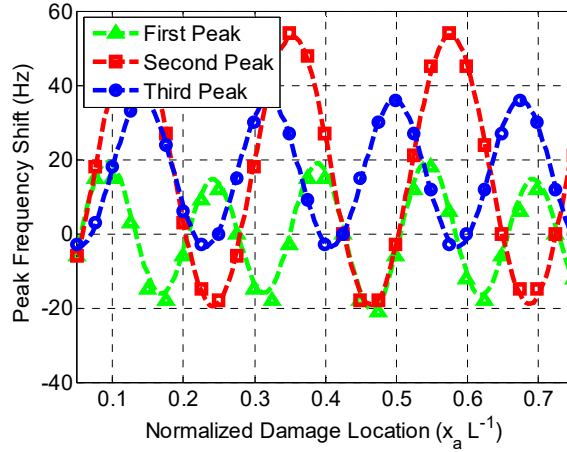
(a)
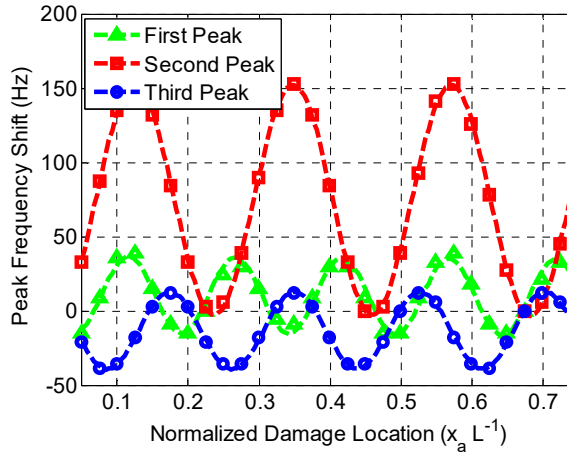
(b)
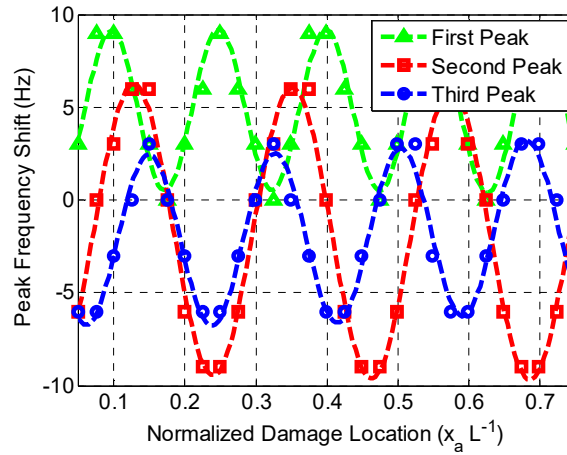
(c)

Figure 4.8. Frequency shifts of individual impedance peaks as a function of damage location, (a) damage scenario L1, (b) damage scenario L2, and (c) damage scenario L3. The periodic behavior of frequency shifts is clear.

4.4   Generalized Damage Characterization

For a general case where all three damage parameters are unknown, a two-stage optimization algorithm, the flowchart of which is shown in Figure 4.9, is developed. The algorithm starts with an initial guess of damage parameters (x_b^0, α^0). With this initial guess, the SLM is used to obtain the frequency-shift functions for all individual peaks. Depending on the offset of each frequency-shift function from the zero shift axis, damage width and severity parameters are updated. If the frequency-shift functions have positive offsets, the damage is underestimated, i.e. the damaged section in the reference to-be-identified case is wider and/or more severely damaged. On the other hand, if all frequency-shift functions have negative offsets, then the initial guess, (x_b^0, α^0), is an overestimate of the actual damage. Based on the analysis presented in Section 4.3.2, the effect of damage severity is in general more significant than that of damage width, therefore damage severity is updated first when the offset is large, while damage width is the parameter to be first updated for relatively small offsets. Once all frequency-shift functions have zero crossing, the damage location estimated by SLM is used with a standard gradient descent optimization technique to fine-tune x_b and α until the objective function value falls below a predetermined tolerance value. If the gradient descent algorithm converges before reaching the desired tolerance, damage location is updated with SLM using the fine-tuned x_b and α, and the whole process is repeated.

The two-stage optimization algorithm is tested with L1 damage scenario, which is a 1 *mm* wide open crack, 0.5 in severity, located 170 *mm* from the piezoelectric wafer edge (250 *mm* from the fixed end). The algorithm is initialized with $(x_b^0, \alpha^0) = (5, 0.7)$. The frequency-shift functions corresponding to this initial guess are first evaluated with SLM, the results are shown in Figure 4.10.a. As the offsets of all three functions are positive, the damage is underestimated, and hence α is updated to 0.6. The frequency-shift functions are re-evaluated for the updated α, the results are shown in Figure 4.10.b. Two of these functions have a negative offset, therefore, x_b is updated to 3mm. The process is repeated one more time, and after the fourth iteration, all three frequency-shift functions have zero crossings as shown in Figure 4.10.c. The estimated damage location after the 4th iteration is 169.2 *mm*. Since the current value of the objective function is above the desired tolerance, which is selected to be 0.0005, the algorithm switches to stage two, and gradient descend optimization algorithm is used to further update x_b and α. After seven iterations with the gradient descent algorithm, the objective function value falls below the specified tolerance, and the optimization algorithm is terminated. Damage parameters are found to be: x_a =169.2 *mm*, x_b = 1.08 *mm*, and α = 0.513, corresponding to 0.47%, 8%, and 2.6% relative error, respectively. Table 4.2 summarizes the results of each iteration of the two-stage damage characterization algorithm. A more accurate estimate

of damage parameters can be obtained by tightening the error tolerance and increasing the frequency sweep resolution, however, this will increase the computational cost of the optimization problem.
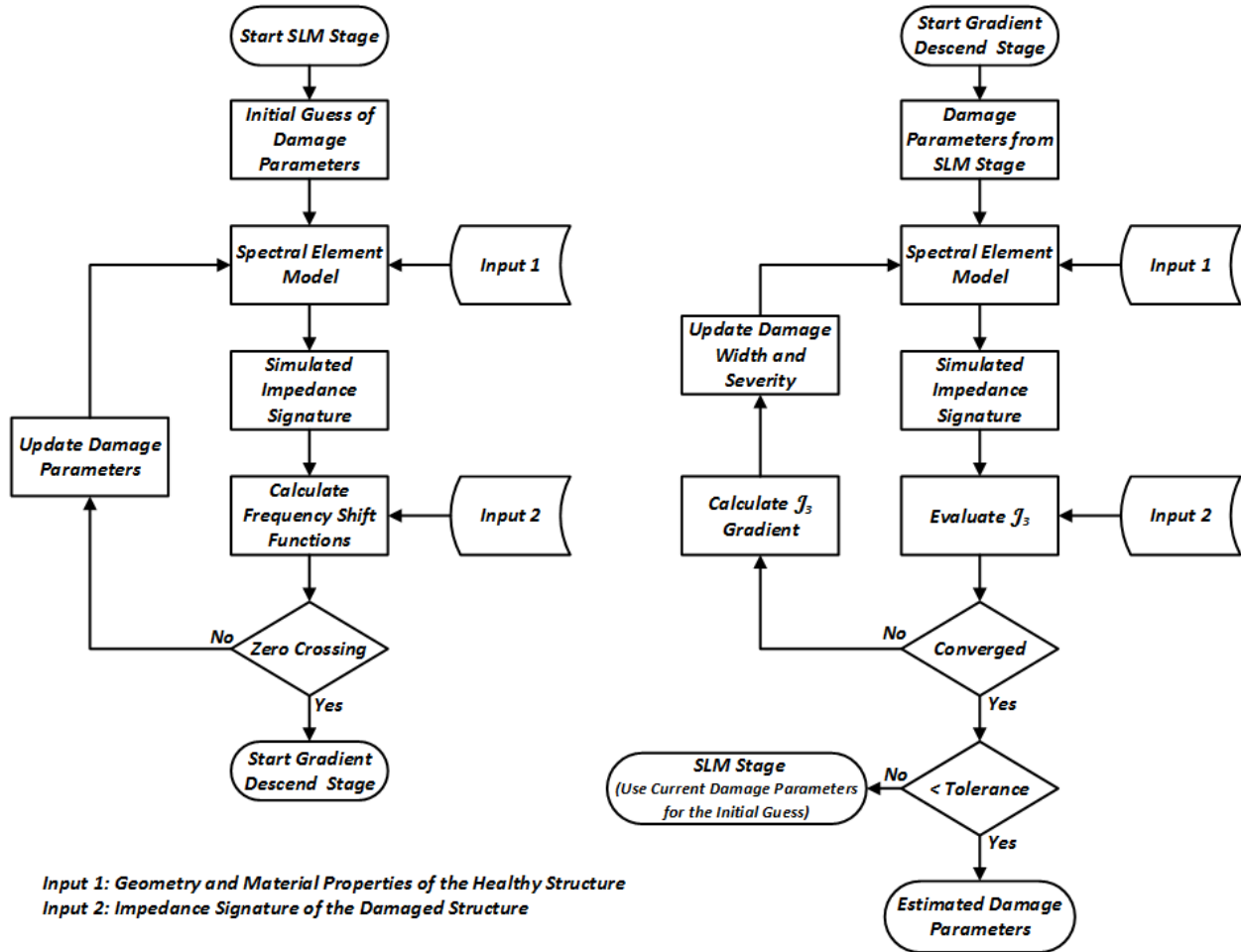
Figure 4.9. The two-stage optimization algorithm for damage characterization.

Table 4.2. Identification of L1 damage scenario, a summary of the two-stage damage characterization algorithm.

Iteration	No. of $\mathcal{J}_3$ evaluations	Damage Parameters			$\mathcal{J}_3$ Value
		Location	Width	Severity	
Initialization	-	-	5 mm	0.7	-
#1 *(SLM)*	10	182 mm	5 mm	0.7	0.0044
#2 *(SLM)*	14	218.4 mm	5 mm	0.6	0.0031
#3 *(SLM)*	12	214.2 mm	3 mm	0.6	0.0015
#4 *(SLM)*	12	169.2 mm	1.5 mm	0.6	0.0007
#5 *(Gradient Descend)*	7	169.2 mm	1.08 mm	0.513	0.0003
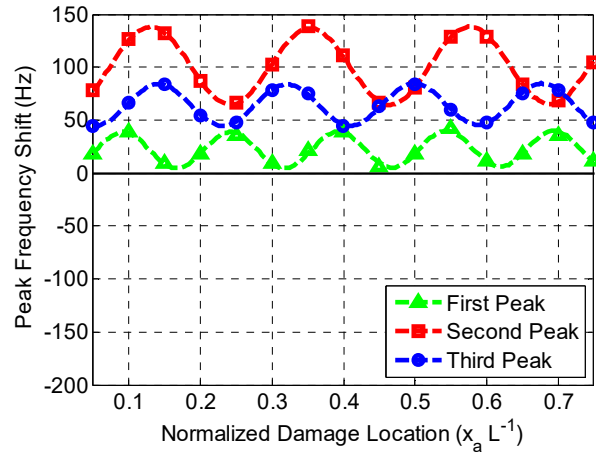
(a)
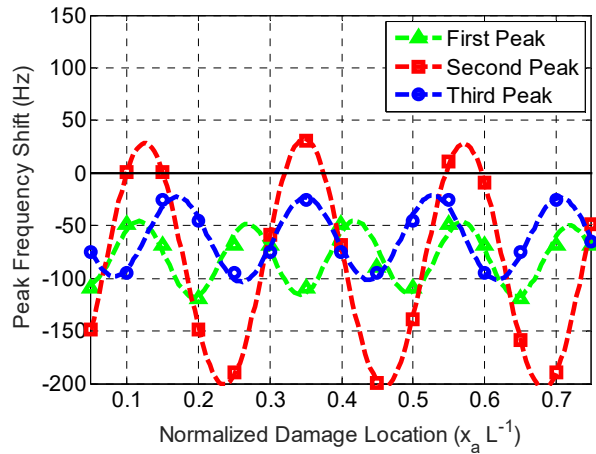
(b)
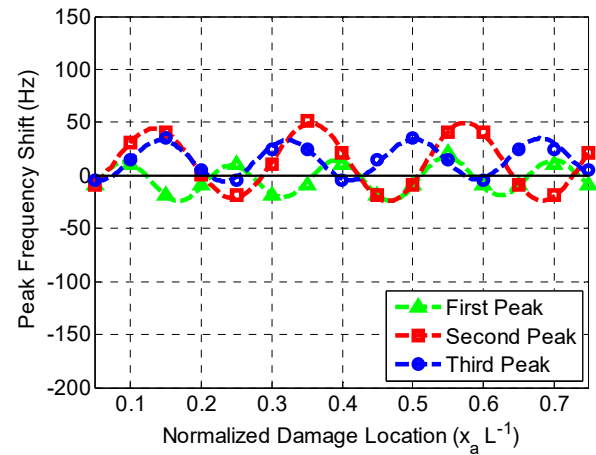
(c)

Figure 4.10. Frequency shifts of individual impedance peaks as a function of damage location, (a) after the first iteration, (b) after the second iteration, and (c) after SLM convergence (the fourth iteration).

97

4.5   **Conclusions**

In this chapter, a novel optimization-based damage characterization approach that utilizes impedance signature measured by a single piezoelectric wafer has been developed. With this approach, a length-varying spectral element mesh is introduced to minimize the number of damage characterization parameters. Only three parameters are required to fully characterize a single open crack, these are the location of damaged section, its width, and the severity of the damage defined by stiffness reduction. Besides the considerable reduction in the number of optimization variables, the proposed spatial discretization allows for more accurate damage characterization. The accuracy to which the damage can be identified, in terms of location and width, is not limited by the resolution of the spectral element mesh, as is the case with fixed mesh approaches.

Motivated by the most common damage metrics used with impedance-based SHM, three objective function definitions have been investigated in this study. These objective functions are based on the root mean square deviation (RMSD), the correlation coefficient, and the shifts in peaks frequency. The objective function definition is found to be deterministic for the behavior of the optimization problem. Considering width and severity parameters, the peak-shifts-based definition is found to have a superior behavior compared to RMSD- and correlation-based definitions. The former definition is found to have a convex behavior with respect to the aforementioned two parameters, with a single global minimum and clear search directions. The later definitions, on the other hand, show several local minima, which makes the optimization problem harder to solve and more computationally demanding.

When damage location is considered, all three definitions resulted in an ill-posed optimization problem with several local minima. However, the peak-shifts-based definition is found to have an underlying periodic nature that is revealed when frequency shifts in individual impedance peaks are analyzed. Each peak in the impedance signature is found to shift in a periodic manner when the location of the damaged section is varied. This underlying periodicity is utilized to develop the sine-fit localization method (SLM), which is a computationally efficient method capable of solving the problem of damage localization with a minimal number of objective function evaluations.

For a general case where all three damage parameters are unknown, SLM provides a clear direction for updating damage width and severity parameters based on the offset of the frequency shift functions relative to the zero shift axis. Based on the developed SLM, a two-stage optimization algorithm for damage characterization has been developed, where SLM is combined with the gradient descent method to solve

for damage location, width, and severity. The algorithm has been tested with several damage scenarios, and with few iterations, damage parameters are determined with high accuracy.

With this approach, solution uniqueness is found to be dependent on the frequency range over which impedance signatures are obtained, along with the resolution of the frequency sweep. A general rule for the number of peaks required to guarantee solution uniqueness has not been determined, however, three peaks are found to be sufficient for all damage scenarios considered in this study. The case of multiple cracks will be investigated in future studies, where issues of convergence, solution uniqueness, and the minimum number of function evaluations required for SLM will be addressed.

CHAPTER FIVE

REFERENCE-FREE ACOUSTOELASTIC-BASED TECHNIQUE FOR STRESS STATE MEASUREMENT IN STRUCTURAL COMPONENTS

5.1   Introduction

The acoustoelastic theory has been widely utilized for nondestructive stress measurement in structural components. Most of the currently available techniques operate at the high-frequency, weakly-dispersive portions of the dispersion curves, and rely on time-of-flight measurements to quantify the effects of stress state on wave speed. High-frequency elastic waves are known to be less sensitive to the state-of-stress acting on the structure, where changes in wave speed are in the order of 10^{-6} per MPa. This, along with the uncertainty in time-of-flight measurements, due to noise contamination, signal attenuation, dispersion, and discretization, adversely affect the accuracy of stress-state measurements.

The effects of excitation frequency on the sensitivity of the acoustoelastic effect have been addressed by a number of researchers. It has been reported that lamb waves are most sensitive to the applied state-of-stress at low-frequency ranges. However, the highly-dispersive nature of the wave modes of interest at low frequencies renders time-of-flight-based measurements impractical, and more advanced analysis techniques are required. The large wavelength of low-frequency lamb waves further complicates the analysis, as the measured waveforms usually consist of incident waves in addition to those reflected from structure's boundaries.

In this work, a model-based stress measurement technique is developed, where the acoustoelastic theory is integrated with a numerical optimization algorithm to calculate the state-of-stress in one-dimensional structures of arbitrary cross sections. The highly-stress-sensitive, low-frequency first anti-symmetric (A_0) lamb wave mode is utilized for this purpose. The semi-analytical finite element (SAFE) method is adopted to study the effects of the initial state-of-stress on lamb waves. A criterion for optimal excitation, in terms of waveform and frequency content, is developed taking into consideration sensitivity to the state-of-stress, robustness against material uncertainties, and physical constraints of the structure being tested. The performance of the proposed stress measurement algorithm is evaluated in the presence of material and geometry related uncertainties. A thorough sensitivity analysis is conducted to quantify the effects of such uncertainties on the measured state-of-stress. The developed stress measurement technique is then validated experimentally, where true reference-free stress measurements are conducted.

5.2   Stress-state Effects on Dispersion Relations

In this section, the effects of axial loading on dispersion relations are studied. Approximate beam theories, namely Timoshenko beam and Elementary rod theories, are first investigated, followed by a more generalized analysis using the semi-analytical finite element (SAFE) method. This aims to shed light on the advantages and challenges associated with utilizing low-frequency elastic waves for stress state measurements and develop the theoretical basis for the stress measurement algorithm discussed in later sections.

5.2.1   Timoshenko Beam and Elementary Rod Approximate Theories

For structures of uniform cross sections, approximate beam theories can be adopted to evaluate the effects of axial loading on dispersion relations. Following the Timoshenko beam and the Elementary rod approximate theories, the displacement field can be described as follows

$$u(x, z, t) = u_0(x, t) - z\phi(x, t)$$
$$w(x, z, t) = w_0(x, t)$$

(5.1)

Where u denotes the longitudinal displacement, w denotes the lateral displacement with u_0 and w_0 being the displacements measured at the beam's neutral axis. ϕ denotes the angle of rotation of the beam's neutral axis normal.

Elastic waves propagating along structures only result in small perturbations of the initial state. Therefore, in the absence of preloading, i.e. with a zero initial state-of-stress, the assumption of infinitesimal strains and deformations can be adopted. Strain-displacement relations can then be described as follows

$$\epsilon_1 = \frac{\partial u}{\partial x} = \frac{\partial u_0}{\partial x} - z\frac{\partial \phi}{\partial x}$$

$$\gamma_{13} = \frac{\partial u}{\partial z} + \frac{\partial w}{\partial x} = \frac{\partial w_0}{\partial x} - \phi \tag{5.2}$$

In the presence of an initial state-of-stress, finite strains and deformations can be induced in the waveguide. If the structure is only uniaxially preloaded such that $\sigma_1^0 \neq 0$, with all other stress components are zero, then the only strain component with a non-zero stress conjugate is E_1. Following Green-Lagrange strain definition, this strain component is defined as

$$E_1 = \frac{\partial u_0}{\partial x} - z\frac{\partial \phi}{\partial x} + \frac{1}{2}\left(\left(\frac{\partial u_0}{\partial x} - z\frac{\partial \phi}{\partial x}\right)^2 + \left(\frac{\partial w}{\partial x}\right)^2\right) \tag{5.3}$$

Following the displacement field described by Eq. 5.1, the kinetic energy functional is defined as follows

$$T = \frac{1}{2}\iiint_V \rho\{\dot{u} \quad \dot{w}\}\begin{Bmatrix}\dot{u}\\\dot{w}\end{Bmatrix}dxdydz = \frac{\rho}{2}\int_0^L\left(A\dot{u}_0^2 + I\dot{\phi}^2 + A\dot{w}_0^2\right)dx \tag{5.4}$$

where ρ is the volumetric mass density of the waveguide, V is the waveguide's volume, A and I are the cross sectional area and second moment of area of the beam, respectively. The potential energy functional, including the strain energy due to the initial state-of-stress, is defined as follows

$$U = \frac{1}{2}\iiint_V\{\epsilon_1 \quad \gamma_{13}\}\begin{bmatrix}E & 0\\0 & G\end{bmatrix}\begin{Bmatrix}\epsilon_1\\\gamma_{13}\end{Bmatrix}dxdydz + \iiint_V E_1\sigma_1^0 dxdydz \tag{5.5}$$

where E and G are the material's elasticity and rigidity moduli, respectively. Finally, the work done by external forces acting on the structure's boundaries can be expressed as

$$W = F_x u_0|_0^L + F_z w_0|_0^L + M\phi|_0^L \tag{5.6}$$

where F_x and F_z are the externally applied forces acting in the x- and z-directions, respectively, and M is the external moment acting on the structure. Upon the application of Hamilton's principle, the dynamic behavior of an axially loaded beam can be described by the following equations

$$\rho \frac{\partial^2 u_0}{\partial t^2} - \hat{E} \frac{\partial^2 u_0}{\partial x^2} = 0$$

$$\rho A \frac{\partial^2 w_0}{\partial t^2} - GA\overline{K} \left(\frac{\partial^2 w_0}{\partial x^2} - \frac{\partial \phi}{\partial x} \right) - \sigma_x^0 \frac{\partial^2 w_0}{\partial x^2} = 0 \tag{5.7}$$

$$\rho I \frac{\partial^2 \phi}{\partial t^2} - \hat{E}I \frac{\partial^2 \phi}{\partial x^2} - GA\overline{K} \left(\frac{\partial w_0}{\partial x} - \phi \right) = 0$$

where $\hat{E} = E + \sigma_x^0$, and $\overline{K}$ is the Timoshenko correction factor. Normally, the applied load is much smaller than the material's modulus of elasticity, thus $\hat{E} \cong E$. With this assumption, the above equations reduce to those of Capron and Williams (1988).

Assuming a spectral solution of the form

$$\boldsymbol{u}(x,t) = \boldsymbol{U}e^{-i(kx-\omega t)} \tag{5.8}$$

where $\boldsymbol{u}(x,t) = \{u_0 \quad w_0 \quad \phi\}^T$, k is the wavenumber, ω is the angular frequency, and $\boldsymbol{U}$ is the amplitude vector for the displacement variables. Substituting the assumed solution in the equation of motion, a non-trivial solution can be obtained upon satisfying the following characteristic equation

$$det\left(\begin{bmatrix} -\rho\omega^2 + \hat{E}k^2 & 0 & 0 \\ 0 & -\rho A\omega^2 + (GA\overline{K} + \sigma_x^0 A)k^2 & -iGA\overline{K}k \\ 0 & iGA\overline{K}k & -\rho I\omega^2 + \hat{E}Ik^2 + GA\overline{K} \end{bmatrix}\right) = 0 \tag{5.9}$$

This results in a 6th order polynomial in k, representing three wave modes. Two of these modes are always propagating, representing the first symmetric and anti-symmetric wave modes. The third mode, which is the second anti-symmetric mode, starts as an evanescent mode and transfers to propagating upon passing through the cut-off frequency $\omega_c = (GA\overline{K}/\rho I)^{1/2}$. As discussed in Section 2.2.2, the correction factor $\overline{K}$ can be determined by either matching the cut-off frequency to that from Rayleigh-Lamb analysis, or by matching the high-frequency wave speed of the unloaded case to that of Rayleigh waves (James F. Doyle, 1997). Following the later criterion, the Timoshenko correction factor is found to be

$$\bar{K} = \frac{C_R^2}{C_S^2} = \left(\frac{0.87 + 1.12\nu}{1 + \nu}\right)^2 \tag{5.10}$$

which yields $\bar{K} = 0.869$ for $\nu = 0.33$. For structures of complex cross sections, approximate theories may fail to describe dispersion relations. In such cases, one can resort to SAFE method, which is discussed in detail in the following section.

5.2.2   Semi-Analytical Finite Element Method

The SAFE method provides a computationally efficient solution to study wave propagation in structures of complex cross sections where exact and approximate theories may fail. In this section, the SAFE formulation is discussed in detail following the procedure outlined in Loveday (2009) and Mazzotti et al. (2012). With SAFE method, the displacement field along the waveguide is assumed to be of the form

$$\boldsymbol{d}(x, y, z, t) = \bar{\boldsymbol{d}}(y, z)e^{-i(kx - \omega t)} \tag{5.11}$$

where $\boldsymbol{d} = \{u \quad v \quad w\}^T$ and $\bar{\boldsymbol{d}} = \{U \quad V \quad W\}^T$ are the displacement vectors, x is the direction along the structure, k and ω follow the same definition as in Eq. 5.8. Thus, the three dimensional problem of wave propagation along the structure is reduced to a two dimensional problem, where only a two dimensional mesh representing the cross section of the structure under test is considered.

As discussed earlier, elastic waves propagating along structures only results in small perturbations of the undeformed state, while the initial state-of-stress may yield finite strains and deformations. The Green-Lagrange strain tensor is adopted to describe strain-displacement relations, which are presented in Voigt notation as follows

$$E = \epsilon_L(u) + \epsilon_{NL}(u) = \begin{Bmatrix} \dfrac{\partial u}{\partial x} \\[2mm] \dfrac{\partial v}{\partial y} \\[2mm] \dfrac{\partial w}{\partial z} \\[2mm] \dfrac{\partial u}{\partial y} + \dfrac{\partial v}{\partial x} \\[2mm] \dfrac{\partial v}{\partial z} + \dfrac{\partial w}{\partial y} \\[2mm] \dfrac{\partial u}{\partial z} + \dfrac{\partial w}{\partial x} \end{Bmatrix} + \begin{Bmatrix} \dfrac{1}{2}\left[\left(\dfrac{\partial u}{\partial x}\right)^2 + \left(\dfrac{\partial v}{\partial x}\right)^2 + \left(\dfrac{\partial w}{\partial x}\right)^2\right] \\[3mm] \dfrac{1}{2}\left[\left(\dfrac{\partial u}{\partial y}\right)^2 + \left(\dfrac{\partial v}{\partial y}\right)^2 + \left(\dfrac{\partial w}{\partial y}\right)^2\right] \\[3mm] \dfrac{1}{2}\left[\left(\dfrac{\partial u}{\partial z}\right)^2 + \left(\dfrac{\partial v}{\partial z}\right)^2 + \left(\dfrac{\partial w}{\partial z}\right)^2\right] \\[3mm] \dfrac{\partial u}{\partial x}\dfrac{\partial u}{\partial y} + \dfrac{\partial v}{\partial x}\dfrac{\partial v}{\partial y} + \dfrac{\partial w}{\partial x}\dfrac{\partial w}{\partial y} \\[3mm] \dfrac{\partial u}{\partial y}\dfrac{\partial u}{\partial z} + \dfrac{\partial v}{\partial y}\dfrac{\partial v}{\partial z} + \dfrac{\partial w}{\partial y}\dfrac{\partial w}{\partial z} \\[3mm] \dfrac{\partial u}{\partial x}\dfrac{\partial u}{\partial z} + \dfrac{\partial v}{\partial x}\dfrac{\partial v}{\partial z} + \dfrac{\partial w}{\partial x}\dfrac{\partial w}{\partial z} \end{Bmatrix} \tag{5.12}$$

Substituting the assumed displacement field defined by Eq. 5.11 in the above relations yields

$$E = (L_0 + kL_1 + k^2 L_2)d \tag{5.13}$$

where

$$L_0 = \begin{bmatrix} 0 & 0 & 0 \\[2mm] \dfrac{1}{2}\dfrac{\partial U}{\partial y}\dfrac{\partial}{\partial y} & \left(\dfrac{1}{2}\dfrac{\partial V}{\partial y}+1\right)\dfrac{\partial}{\partial y} & \dfrac{1}{2}\dfrac{\partial W}{\partial y}\dfrac{\partial}{\partial y} \\[3mm] \dfrac{1}{2}\dfrac{\partial U}{\partial z}\dfrac{\partial}{\partial z} & \dfrac{1}{2}\dfrac{\partial V}{\partial z}\dfrac{\partial}{\partial z} & \left(\dfrac{1}{2}\dfrac{\partial W}{\partial z}+1\right)\dfrac{\partial}{\partial z} \\[3mm] \dfrac{\partial U}{\partial y}\dfrac{\partial}{\partial z} & \left(\dfrac{\partial V}{\partial y}+1\right)\dfrac{\partial}{\partial z} & \left(\dfrac{\partial W}{\partial z}+1\right)\dfrac{\partial}{\partial y} \\[3mm] \dfrac{\partial}{\partial z} & 0 & 0 \\[3mm] \dfrac{\partial}{\partial y} & 0 & 0 \end{bmatrix},$$

$$L_1 = -i \begin{bmatrix} 1 & 0 & 0 \\ 0 & 0 & 0 \\ 0 & 0 & 0 \\ 0 & 0 & 0 \\ \dfrac{\partial U}{\partial z} & \dfrac{\partial V}{\partial z} & 1+\dfrac{\partial W}{\partial z} \\[2mm] \dfrac{\partial U}{\partial y} & 1+\dfrac{\partial V}{\partial y} & \dfrac{\partial W}{\partial y} \end{bmatrix},$$

and

$$L_2 = -\dfrac{1}{2} \begin{bmatrix} U & V & W \\ 0 & 0 & 0 \\ 0 & 0 & 0 \\ 0 & 0 & 0 \\ 0 & 0 & 0 \\ 0 & 0 & 0 \end{bmatrix}.$$

Using eight-noded isoparametric quadrilateral elements to discretize the two-dimensional cross section of the waveguide, the generalized displacement vector, associated with the ith node of an element, $i=1,2,...,8$, is expressed as

$$d_i^e = [U_i \quad V_i \quad W_i]^T e^{-i(kx-\omega t)} \tag{5.14}$$

The displacement field at any point within the element can be defined in terms of the nodal displacement vector, d^e, and shape functions matrix, N, as follows

$$d = Nd^e \tag{5.15}$$

where $d^e = \begin{bmatrix} d_1^{e^T} & d_2^{e^T} & ... & d_8^{e^T} \end{bmatrix}^T$, $N = \begin{bmatrix} N_1 & 0 & 0 & N_2 & 0 & & 0 \\ 0 & N_1 & 0 & 0 & N_2 & \ddots & 0 \\ 0 & 0 & N_1 & 0 & 0 & & N_8 \end{bmatrix}$, with N_i being a second

order Lagrange polynomial associated with the ith node. Substituting Eq. 5.15 into the strain displacement relations, Eq. 5.12, yields

$$E = (B_0 + kB_1 + k^2 B_2)d^e \tag{5.16}$$

where $B_0 = L_0 N$, $B_1 = L_1 N$,and $B_2 = L_2 N$.

On the element level, the kinetic energy functional is defined as follows

$$T = \frac{1}{2} \iint \rho \dot{d}^{e^T} \dot{d}^e dxdy = \frac{1}{2} \dot{d}^{e^T} M^e \dot{d}^e \tag{5.17}$$

where ρ is the volumetric mass density of the waveguide and $M^e = \rho \int_A N^T N dA$ is the element mass matrix. In order to describe the elastic behavior of the wave guide, Piola–Kirchhoff stress tensor, which is the work-conjugate of the Green-Lagrange strain tensor, is adopted. For isotropic and linear-elastic materials, Piola–Kirchhoff stress tensor is defined as follows

$$\sigma = C\epsilon_L \tag{5.18}$$

where $C_{ij} = \frac{\partial \sigma_i}{\partial \epsilon_{Lj}}$ is the fourth order stiffness tensor expressed in Voigt Notation (Mazzotti et al., 2012). The potential energy functional, including the strain energy due to the initial state-of-stress is defined as follows

$$U = \frac{1}{2} \iint_\Omega \epsilon_L^T C \epsilon_L \, dxdy + \iint_\Omega \epsilon_{NL}^T \sigma^0 \, dxdy \qquad (5.19)$$

Equation 5.19 implies the assumption that the induced elastic waves result only in infinitesimal perturbations in the pre-stressed configuration. The equation also indicates that the infinitesimal linear strain energy component associated with the initial state-of-stress vanishes, which highlights the necessity for including the nonlinear strains (ϵ_{NL}) in the development of acoustoelastic models (Chen and Wilcox, 2007b; Gandhi et al., 2012; Mazzotti et al., 2012).

The work done by external forces acting on the boundaries of the structure can be expressed as

$$W = \iint_{\partial\Omega} d^T f \, dxdy \qquad (5.20)$$

where f is the externally applied surface traction vector acting over the waveguide's boundaries.

For uniaxially loaded structures, which are the focus of this study, the only nonzero component of the initial state-of-stress is σ_1^0. For such loading conditions, the potential energy functional, defined in Eq. 5.19, reduces to

$$U = \frac{1}{2} \dot{d}^{e^T} \left(K_0^e + k K_1^e + k^2 (K_2^e + K_{\sigma x}^e) \right) \dot{d}^e \qquad (5.21)$$

where the element stiffness matrices K_0^e, K_1^e, K_2^e, and $K_{\sigma x}^e$, are defined as follows

$$K_0^e = \int_A B_0{}^T C B_0 \, dA$$

$$K_1^e = \int_A \left(B_0{}^T C B_1 - B_1{}^T C B_0 \right) dA$$

$$K_2^e = \int_A \left(B_1{}^T C B_1 \right) dA$$

$$K_{\sigma x}^e = \sigma_1^0 \int_A N^T N dA = \frac{\sigma_{xx}^0}{\rho} M$$

Applying Hamilton's principle, and upon assembling the elemental matrices, the elastodynamic equation of motion for the waveguide is obtained as follows

$$M\ddot{d} + \left(K_0 + kK_1 + k^2(K_2^e + K_{\sigma x}^e)\right)d = F \tag{5.22}$$

where M, K_0, K_1 and K_2 are the global mass and stiffness matrices, d is the global degrees of freedom vector, and F is the global force vector.

Considering the homogeneous part only, and upon substituting the assumed solution form (Eq. 5.11), Eq. 5.22 reduces to

$$(K_0 - M\omega^2 + kK_1 + k^2K_2)d = 0 \tag{5.23}$$

For a nontrivial solution, $d \neq 0$, the matrix $(K_0 - M\omega^2 + kK_1 + k^2K_2)$ must be singular. This leads to a characteristic equation, for each frequency ω, that can be solved for wavenumbers at that given frequency. Thus, dispersion relations for the waveguide are obtained. The process of obtaining a nontrivial solution for Eq. 5.23 at a given frequency is equivalent to solving the quadratic eigenvalue problem for wavenumbers k. Eigenvalues represent the wavenumbers at a given frequency, whereas, eigenvectors represent the corresponding mode shapes.

5.2.3 Numerical Examples

The SAFE method along with the Timoshenko-Elementary approximate theory are used to calculate dispersion curves for a stress-free 10-mm-diameter aluminum circular rod, a rectangular beam with the dimensions and material properties given in Table 5.1, and a 136RE rail. The results are shown in Figure 5.1. It can be noticed that the Timoshenko-Elementary approximate theory accurately predicts A_0 and S_0 modes for simple structures up to the first cut-off frequency, as shown in Figures 5.1.a and 5.1.b. As for waveguides with irregular cross-sections, such as the rail shown in Figure 5.1.c, the SAFE method is required to obtain accurate dispersion relations for all different modes. The applicability of approximate theories is limited to A_0 and S_0 modes at very low frequencies.
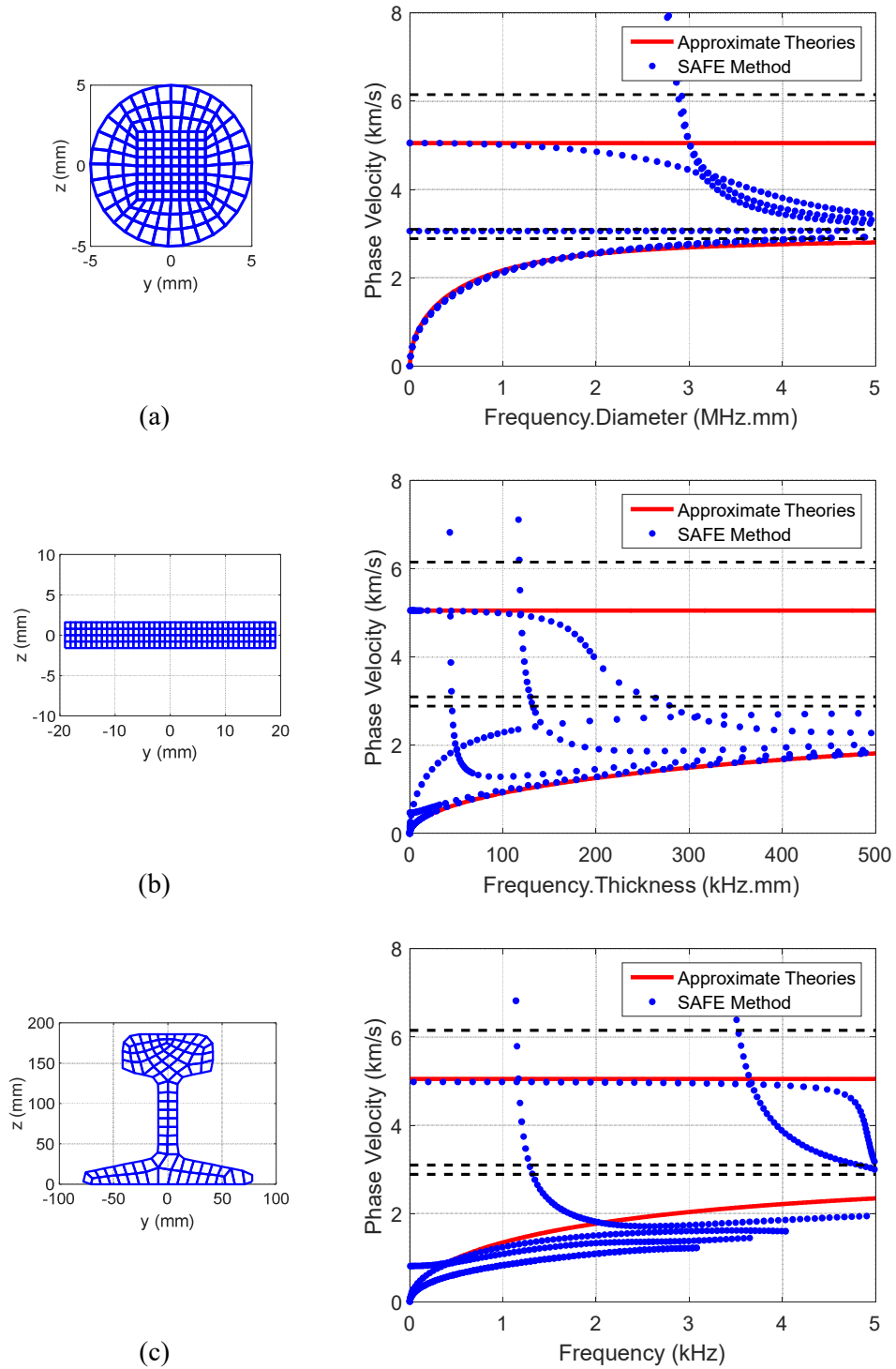
Figure 5.1. Dispersion curves calculated with the SAFE method and the Timoshenko-Elementary approximate theory for a stress-free (a) circular rod (b) rectangular beam, and (c) 136 RE rail. Dashed lines represent C_P, C_S, and C_R values (from up to down, respectively).

Table 5.1. Material properties and dimensions for the rectangular beam (Figure 5.1.b) considered in the study.

	Material (Al 6061)	
$E = 69\ GPa$	$v = 0.33$	$\rho = 2700\ kgm^{-3}$
	Dimensions	
$Thickness = 3.175\ mm$		$Width = 38.1\ mm$

Figure 5.2 shows the dependence of phase velocity on both frequency and loading state, as predicted by Timoshenko-Elementary approximate theories. As it has been reported in the literature, the results suggest that the low-frequency range is the most sensitive to axial loading, however, dispersion effects are most profound there. This renders time-of-flight-based measurements impractical, and a more thorough analysis is required to calculate the state-of-stress based on wave field measurements.
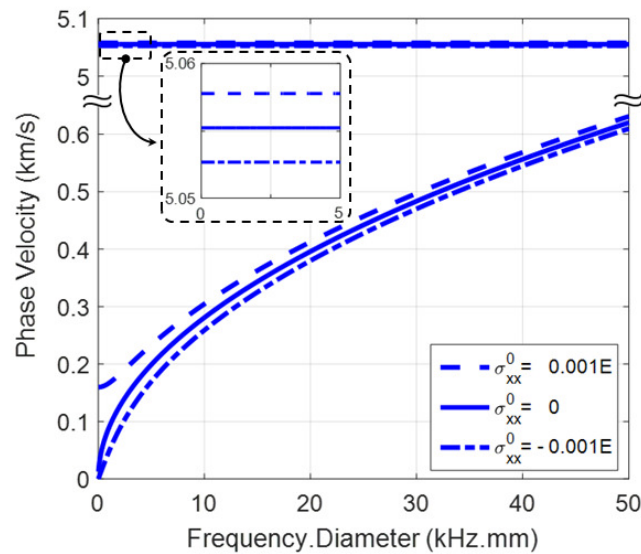
Figure 5.2. Phase velocity curves for A_0 and S_0 modes at different levels of axial loading predicted by Timoshenko-Elementary approximate theories.

5.3   Acoustoelastic-based Optimization Algorithm for Stress Measurement

The previous analysis shows that the acoustoelastic effect better manifests itself at lower frequency ranges, which are normally highly dispersive. Dispersion causes the energy of the signal to spread out in space, which results in signal distortion and renders time-of-flight-based wave speed measurements impractical. In this section, a model-based optimization algorithm is developed to calculate the state-of-stress utilizing dispersive wave modes. The algorithm is first tested numerically at different loading conditions, where the issues of accuracy and robustness are addressed.

Let a propagating wave be measured at p number of points along the structure, and let the distance between these points be known at the current state-of-stress. For a pair of measurement points, i and $i+1$, the waveform measured at x_{i+1} can be expressed in terms of that measured at x_i as follows

$$u(x_{i+1}, t) = \int_{-\infty}^{\infty} \widehat{U}_i(\omega) \sum_m A_m\, e^{i(k_m \Delta x - \omega t)}\, d\omega \tag{5.24}$$

where $\widehat{U}_i$ is the Fourier transform of the signal measured at point i, and Δx is the distance between the two measurement locations. The only unknown in this equation are the wavenumbers k_m, which are function of frequency, the structure being tested, and the state-of-stress, as discussed in the previous section. To solve for this unknown and calculate the state-of-stress acting on the structure, a model-based optimization algorithm is developed, the flow chart of which is shown in Figure 5.3. The algorithm starts with an initial guess of the loading state acting on the structure under consideration. Based on acoustoelastic theory, either approximate theories or SAFE method, dispersion curves are calculated for the assumed loading state. The calculated dispersion relations, along with the waveform measured at location x_i and the distance Δx_i ($\Delta x_i = x_{i+1} - x_i$) are then fed to Eq. 5.24 to calculate the waveform at location x_{i+1}. The state-of-stress is then updated through a steepest gradient optimization algorithm in order to minimize the following objective function

$$\mathcal{J} = \left\| u_{i+1}^{Meas} - u_{i+1}^{Calc}(\sigma) \right\|_2 \tag{5.25}$$

Upon convergence, the algorithm predicts the state-of-stress in the structure. As is the case with all model-based characterization practices, the accuracy of the predicted state-of-stress depends on the accuracy of the underlying model. Either approximate theories or SAFE method can be implemented to describe the
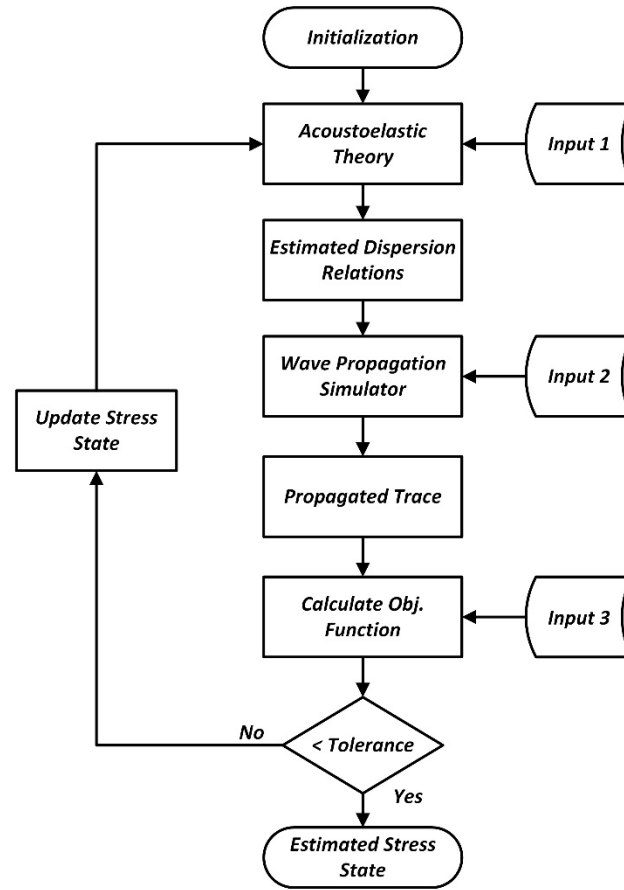
Input 1: Geometry and Material Properties of the Structure
Input 2: Measured waveform U_i and the distance $\Delta x_i = x_{i+1} - x_i$
Input 3: Measured waveform U_{i+1}

Figure 5.3. A flow chart of the acoustoelastic-based optimization algorithm developed for calculating the state-of-stress acting on structures.

effects of loading on dispersion relations. Computational cost, the characteristics of the structure being tested, and the frequency range of interest determine which method to be used. Ideally, two points are sufficient to calculate the state-of-stress, however, having more than two points improves the accuracy of the algorithm's predictions in the presence of noise and random measurement errors.

The behavior of the objective function defined by Eq. 5.25 for the rectangular beam described in Table 5.1 is shown in Figure 5.4. The beam is approximated by the Timoshenko-Elementary theories, which are found to accurately predict dispersion relation in the frequency range considered in this study. A two-cycle, amplitude-modulated, sine wave is used to interrogate the structure, and the response is numerically simulated at two points 100 *mm* apart.
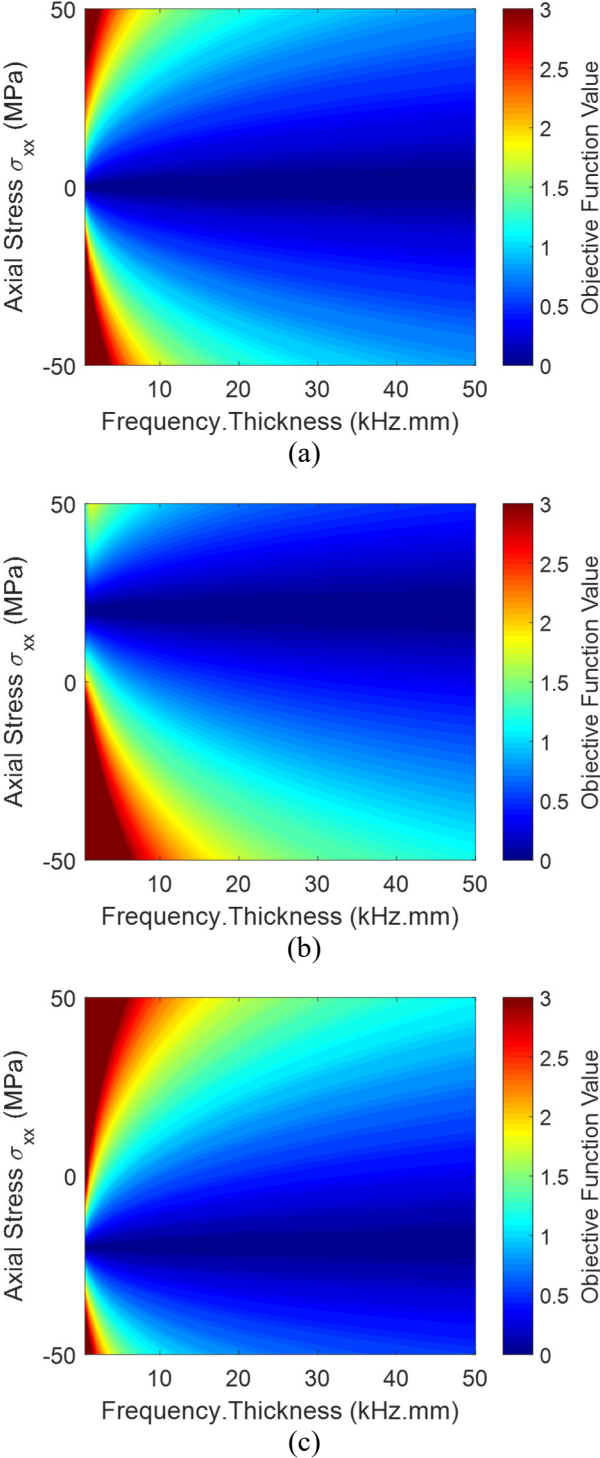
Figure 5.4. Objective function values as a function of the state-of-stress and the frequency of the propagating wave for (a) stress-free, (b) tensile load of 20 MPa, and (c) compressive load of 20 MPa, loading scenarios.

The convex behavior of the objective function is apparent in the figure, where a single global minimum exists at the stress level that matches the actual state-of-stress in the structure. This is found to be true for all excitation frequencies considered in this study. Local minima are also found to exist at very low excitation frequencies, and extreme loading conditions, as noticed in Figure 5.4.b. Even in the presence of such local minima, the optimization problem is well posed, and clear search directions are attainable. The superior sensitivity of low-frequency excitations is also apparent in the figure, where the value of the objective function increases drastically as the assumed state-of-stress deviates from its actual value. As the excitation frequency increases, smaller changes in the objective function are observed as a function of the state-of-stress in the structure.

In general, the developed algorithm is capable of dealing with waveforms including reflections, provided that the structure's boundaries are accurately characterized. Experimentally, this can be a laborsome task depending on how the component of interest is loaded and connected to the surrounding structure. The following section provides a generic criterion for excitation signal selection in order to obtain a reflection-free response at measurement locations.

5.4   Excitation Signal Selection

For structures where boundary conditions cannot be accurately characterized, a near reflection-free response at the measurement location is necessary for the successful implementation of the proposed acoustoelastic-based stress measurement algorithm. This section investigates the effects of excitation signal type and frequency content on reflections interference with the measured response, where a criterion for excitation signal selection is developed.

Let a transmitter-receiver pair be located L_1 meters from each other, and the boundaries of the structure under consideration be L_2 meters from the receiver, as shown in Figure 5.5. In order to obtain a reflection-free response at the receiver, the following inequality needs to be satisfied (Albakri and Tarazaga, 2016)

$$\frac{L_1 + 2L_2}{c_{max}} \geq \frac{L_1}{c_{min}} + nT_{max},$$

(5.26)
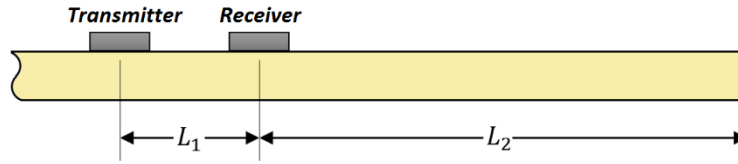
Figure 5.5. Schematic of a beam with a transmitter-receiver pair showing the separation distance between the transducers and structure's boundaries.

where c_{max} and c_{min} are respectively the maximum and minimum phase velocities of the incident wave, T_{max} is the period of the lowest frequency component of the incident wave, which is normally associated with c_{min}, and n is the number of cycles of the excitation signal.

Excitation signal type and frequency content play a key role in acoustoelastic-based measurements. Besides determining the frequency range over which the structure is interrogated and the information is retrieved, the excitation signal, along with the structure's material and geometric characteristics, also determines how reflections interfere with the measured response. Several excitation signal types are investigated in this section, including impact excitations, n-cycle tone bursts, and n-cycle modulated tone bursts. When comparing the performance of different excitation signals, the following factors are taken into consideration:

1- Minimum distance required for obtaining a reflection-free response at the measurement location
2- Measurement sensitivity to the applied state-of-stress
3- Measurement robustness against material and geometric uncertainties
4- Measurement robustness against noise contamination

While the first factor can be quantified by the aforementioned inequality, Eq. 5.26, the remaining factors are discussed qualitatively in here and are addressed in more detail in later sections. As discussed earlier, the sensitivity of acoustoelastic-based stress measurements is mainly determined by the frequency range over which the structure is interrogated, with lower frequencies being more sensitive to the applied state-of-stress. Robustness, on the other hand, depends on the form of the incident wave along with its frequency. In general, the wider the band of the excitation wave, the more robust the measurement will be against uncertainties in material and geometric characteristics. This can be ascribed to the fact that a wideband excitation carries more information about dispersion curves as compared to a narrowband one. Therefore, variations in dispersion relations due to material and geometric characteristics uncertainties can more clearly be distinguished from those induced by the applied state-of-stress. This also depends on the

115

frequency range of excitation, with lower frequencies being more robust. While the effects of measurement noise on stress measurements can be minimized by averaging and filtering, accurate selection of excitation signal type can provide added robustness. In general, when transferring between time and frequency domains, a signal with a single-band frequency content will be less affected by noise than a one with multiple frequency bands. Although they are qualitative, the aforementioned factors are used in following pages to guide the process of excitation signal selection.

Figure 5.6 shows impact excitations of different durations, along with their normalized energy spectral density and group velocity curves. Impacts, such as hammer excitations, can be characterized as low-frequency wideband excitations, with a bandwidth inversely proportional to the impact duration. Regardless of their duration, impact excitations carry information about the low-frequency portions of dispersions curves, which are the most sensitive to the applied state-of-stress. Furthermore, the wideband nature of such excitations is expected to result in more robust stress measurements in the presence of material and geometric uncertainties. However, the very low-frequency content of such excitations makes it impossible to get a reflection-free response for most practical structures. This can be ascribed to the large wavelength of such low-frequency components, along with the large variation in wave speed between the fastest and the slowest components, i.e. $c_{max} \gg c_{min}$ as suggested by shaded areas in Figure 5.6. Thus, multiple reflections may occur before the low-frequency content passes through the measurement location. Therefore, pulses and impacts are unsuitable for the problem at hand, as the measured response will always be contaminated with reflections or missing some low-frequency components, which adversely affect the accuracy of stress measurements.

For structures where boundary conditions can be accurately characterized, the algorithm's capabilities can be extended to include the effects of reflections. In such cases, impacts can be the excitation type of choice for stress measurement purposes. However, most boundary conditions encountered in practical applications are complex in nature and can be affected by the applied state-of-stress. This makes the characterization of such boundary conditions a tedious process, and thus, hinders the utilization of impact excitations.
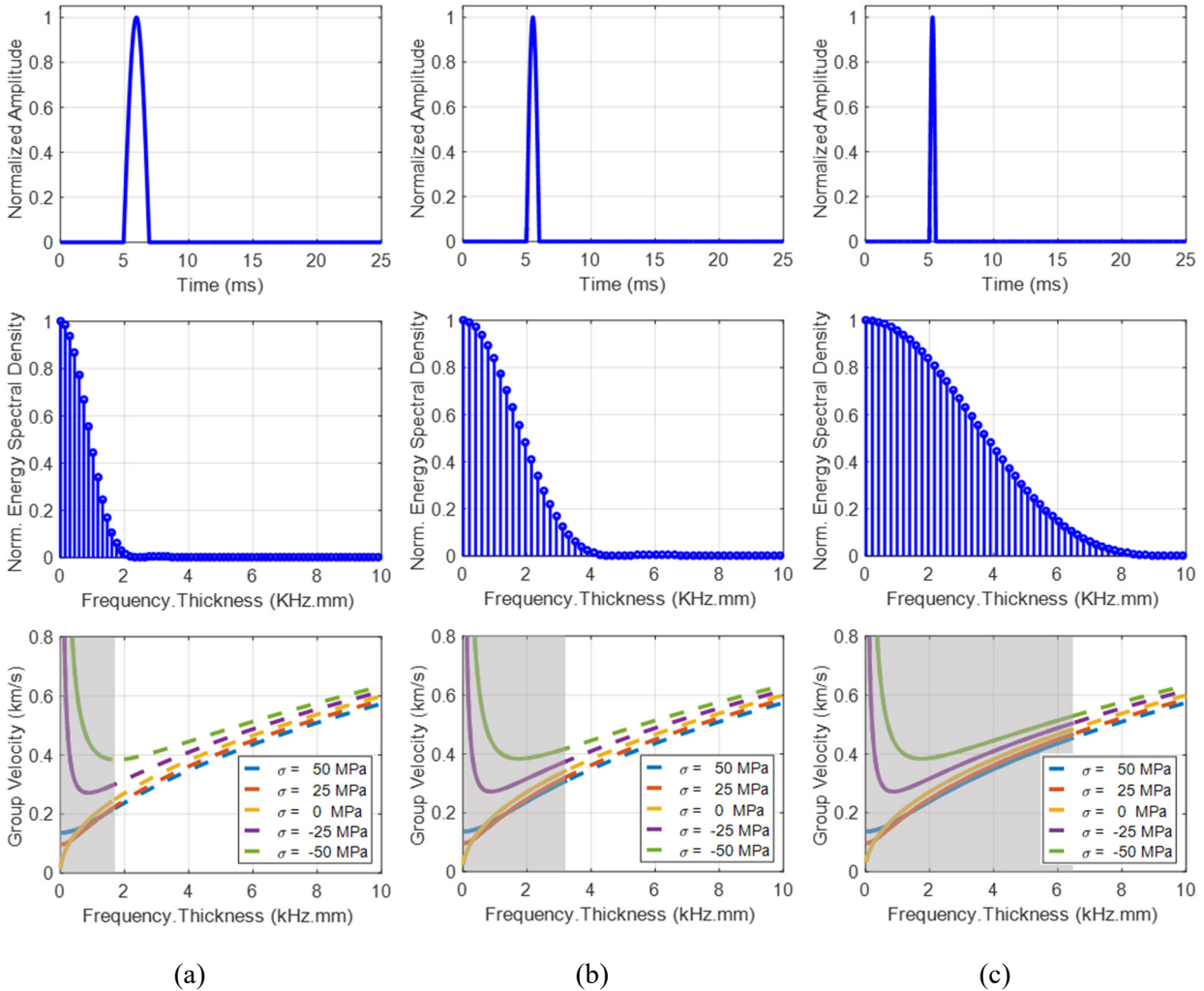
Figure 5.6. Impact excitations with different durations showing the waveform, normalized energy spectral density, and group velocity curves for (a) 2 ms impact, (b) 1 ms impact, and (c) 0.5 ms impact. The shaded area highlights the band over which information is carried by the corresponding waveform.

For *n*-cycle sinewave tone burst excitation signals, shown in Figure 5.7, energy is mostly contained in a relatively narrowband centered at the main excitation frequency. This allows the selection of the excitation frequency according to the dimensional constraints imposed by the structure being tested. However, a small fraction of the energy is carried by significantly lower frequencies, clearly shown in Figures 5.7.b and c. This adversely affects measurement robustness against noise, as previously discussed. Furthermore, such low-frequency energy bands increase the minimum length required to obtain a reflection-free response at a given frequency, as c_{min} is normally associated with these low-frequency bands. As the number of cycles in the tone burst signal increases, the bandwidth of the signal decreases, which adversely affects robustness against material and geometry related uncertainties.
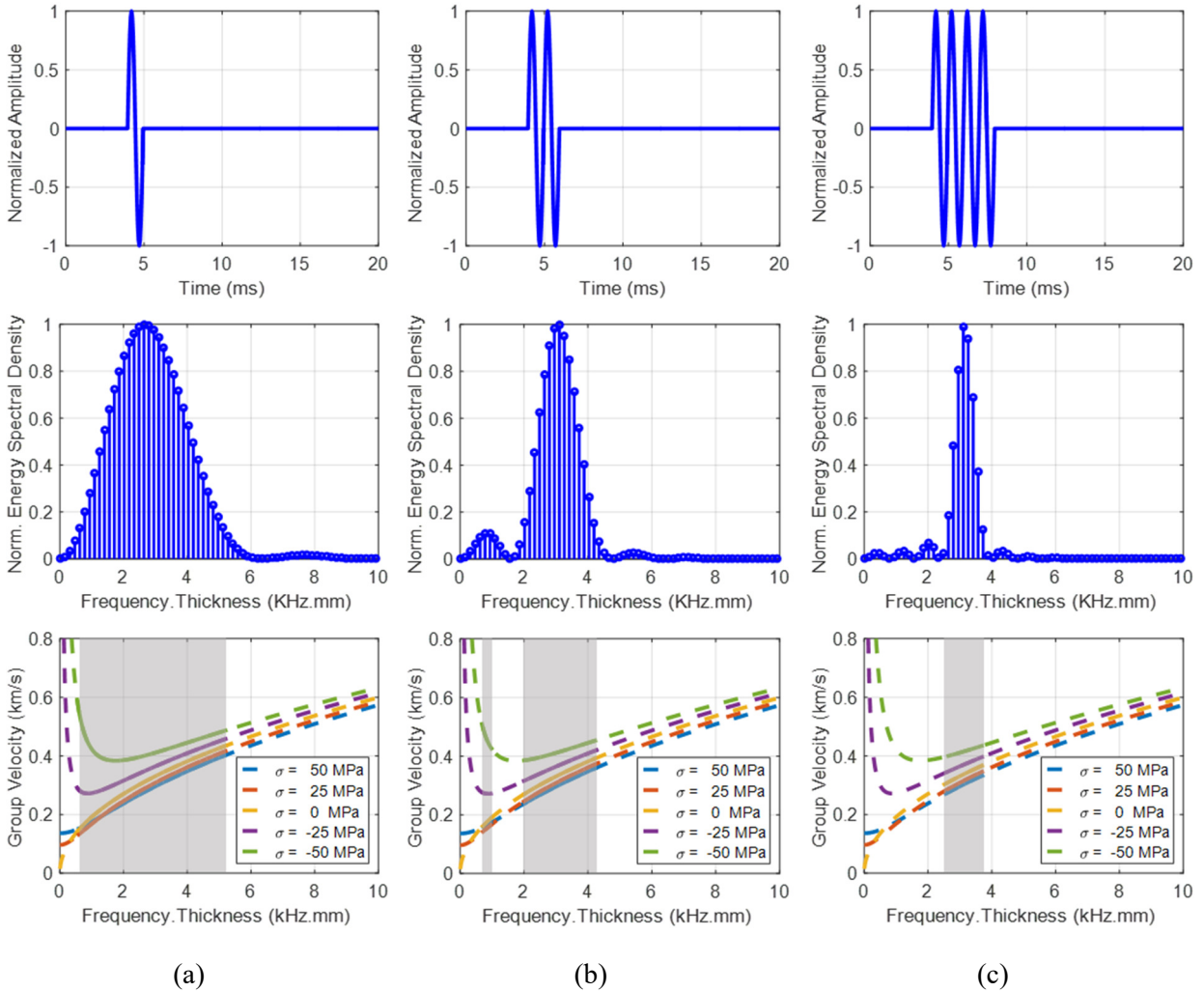
Figure 5.7. A 1 kHz sinewave tone burst of (a) one cycle, (b) two cycles, and (c) four cycles. In the figure, the waveform, normalized energy spectral density, and group velocity curves are shown, with the shaded area highlighting the band over which information is carried by each waveform.

A more confined energy spectrum can be achieved by modulating the amplitude of the previously discussed sinewave tone bursts with a Hanning window, as shown in Figure 5.8. This eliminates the small, low-frequency energy bands noticed in the unmodulated signals, and hence, all information carried by this type of excitation signals is confined in a single band centered at the main excitation frequency, as shown by the energy spectral density plots in Figures 5.8.a-c. This enhances measurements robustness against noise while minimizing the distance required for obtaining reflection-free responses for a given center frequency and number of cycles.
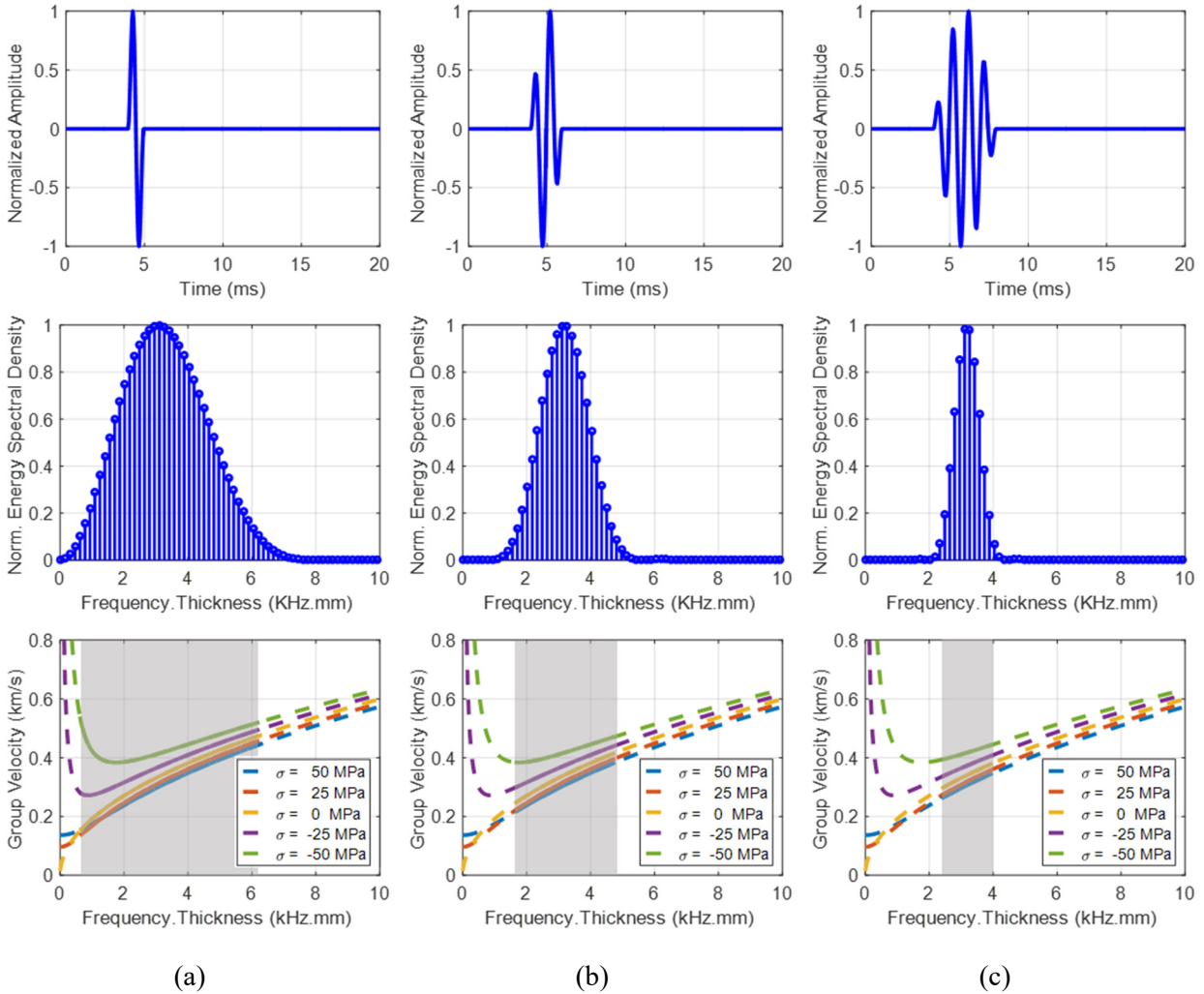
Figure 5.8. An amplitude modulated, 1 kHz, sinewave tone burst of (a) one cycle, (b) two cycles, and (c) four cycles. In the figure, the waveform, normalized energy spectral density, and group velocity curves are shown, with the shaded area highlighting the band over which information is carried by each waveform.

As is the case with unmodulated tone bursts, increasing the number of cycles in the excitation signal adversely affects robustness against material and geometry uncertainties due to the accompanying reduction in the signal's bandwidth. Therefore, $n = 1$, where n is the number of cycles in the tone burst, is the optimal choice for robustness requirements. On the other hand, the effects of the number of cycles on the minimum length required for a reflection-free response, L_2, are driven by two contradicting factors; excitation signal duration and its bandwidth. Increasing the number of cycles in the excitation signal has the direct effect of increasing L_2, as suggested by Eq. 5.26. However, the bandwidth reduction associated with larger number

of cycles reduces the c_{max}/c_{min} ratio, as suggested by the shaded areas in Figure 5.8, which in turn reduces the required L_2.

In order to quantify these effects, the minimum length required to obtain a reflection-free response is calculated as a function of excitation frequency and stress level for the structure described in Table 5.1. One-, two-, and four-cycle, amplitude modulated sine waves are selected as excitation signals, and the results are shown in Figure 5.9. This is calculated following Eq. 5.26 with $L_1 = 100\ mm$. Although it minimizes the number of cycles, a single cycle sine wave tone burst is associated with the largest separation requirements between the point of measurement and structure's boundaries, as shown in Figure 5.9.a. This can be ascribed to the wideband frequency content of this waveform, which in turn results in a large maximum to minimum speed ratio, $c_{max}/c_{min} \gg 1$, as suggested by Figure 5.8.a. This effect is found to be more significant at low-frequency ranges and large tensile stresses, as changes in wave speed are more drastic at such frequency-stress combinations.

The required L_2 is found to decrease as the number of cycles in the excitation signal increases from one to two, as shown in Figure 5.9.b. This is ascribed to the bandwidth reduction of frequency content, shown in Figure 5.8.b, which results in smaller maximum-to-minimum speed ratios. For such small number of cycles in the excitation signal, the maximum-to-minimum speed ratio is found to be more significant in determining L_2 value than the number of cycles itself. Such a reduction in L_2 requirements makes this excitation signal more suitable for practical applications. No further improvement on L_2 is achieved by using a four-cycle sine wave tone burst as an excitation signal. For this waveform, the potential reduction in L_2 due to the smaller maximum-to-minimum speed ratio is counteracted by the larger number of cycles in the excitation signal. Further increase in number of cycles results in larger L_2 requirements, as the effect of number of cycles becomes more dominant than the gained reduction in the maximum-to-minimum speed ratio.

Based on these results, it can be concluded that a two-cycle, amplitude modulated sine wave tone burst is the optimal choice for acoustoelastic-based stress measurements as compared to impacts and other forms of sine wave tone bursts. The advantages of using such excitation signal can be summarized as follows:

- Minimum L_2 requirements for obtaining reflection-free responses at measurement locations.
- Largest bandwidth compared to other waveforms with similar L_2 requirements. This enhances measurements robustness against material and geometry related uncertainties.
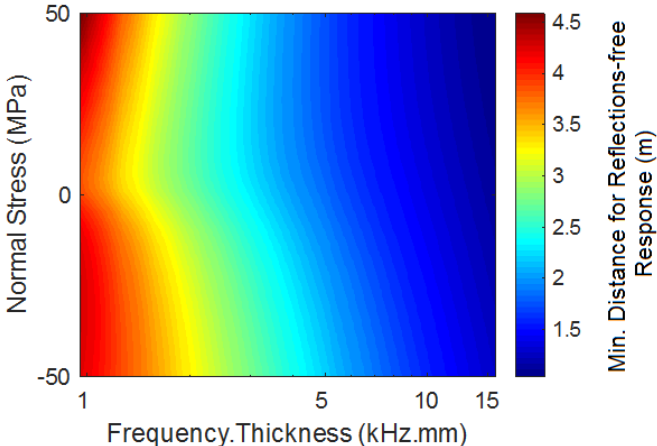
(a)
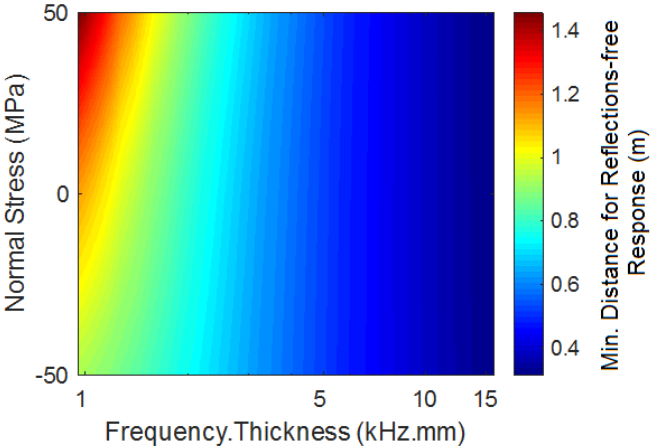
(b)
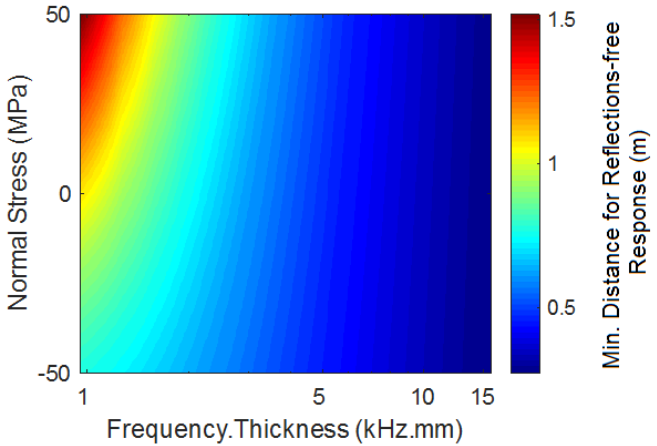
(c)

Figure 5.9. Minimum distance, in meters, required for obtaining reflection-free response using modulated sine wave tone burst excitation signal with (a) one cycle, (b) two cycles, and (c) four cycles.

For optimal sensitivity to measured state-of-stress, the center frequency of the excitation signal shall be selected as the lowest frequency for which L_2 requirements can be accommodated by the physical dimensions of the structure being tested.

In this work, a two-cycle sine wave tone burst modulated by a Hanning window is used as the excitation signal for all numerical and experimental studies. The fraction of the reflected wave that can be accommodated by the measured response is determined by the frequencies at which c_{max} and c_{min}, in Eq. 5.26, are calculated. For all the results shown in Figure 5.9, maximum and minimum phase velocities of the incident wave are determined within the frequency band where the normalized energy spectral density is greater than 0.1. This is depicted in Figure 5.10.a for a 3 kHz excitation signal. A smaller than 0.1 threshold results in a less reflections-contaminated measurement at the cost of larger separation distance between the point of measurement and structure's boundaries. If merely the center frequency is taken into consideration, i.e. with an energy threshold of 1, the calculated separation distance is significantly underestimated, resulting in reflections-contaminated measurements.

Figure 5.10.b shows the time history at the excitation location, $x = 0$, and that at a measurement location of $x = 100$ *mm* with a 1 kHz excitation signal. A fixed boundary condition is assumed to be located 649 *mm* from the point of measurement, which is calculated following Eq. 5.26 with a 0.1 energy threshold. With such separation between the point of measurement and structure's boundaries, the incident wave can be clearly distinguished from the reflected wave. This suggests that a 0.1 energy threshold is sufficient to obtain a response with negligible reflections contamination. No further reduction in threshold values is necessary.

(a)

(b)
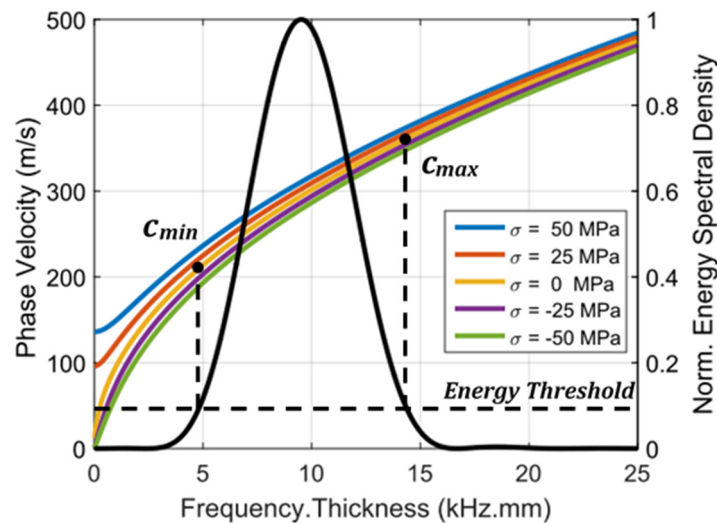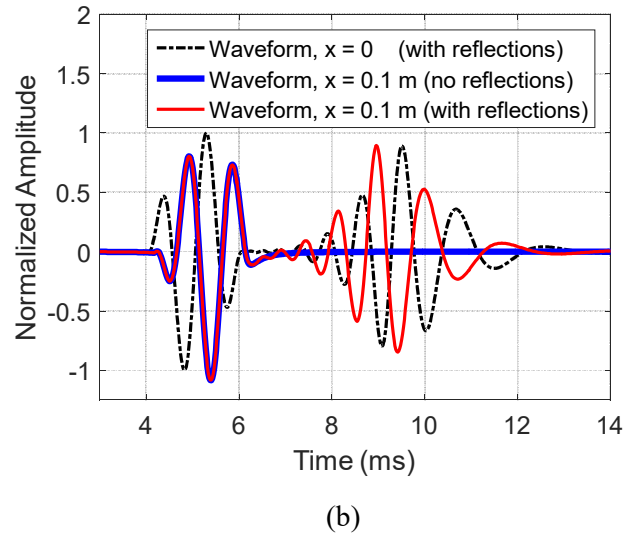
Figure 5.10. An amplitude modulated sine wave tone burst of two cycles showing (a) energy spectral density of the incident wave along with dispersion curves for a 1.5 inches x 0.125 inch aluminum beam, and (b) incident and reflected waveforms at $x = 0$ and $x = 100$ *mm*.

5.5   Sensitivity Analysis

In this section, the effects of uncertainties on the performance of the proposed acoustoelastic-optimization-based stress measurement algorithm are evaluated through a series of numerical experiments. Uncertainties in the material properties and geometric characteristics of the structure being tested are considered. The focus of the current work is homogeneous, isotropic, and linear-elastic structures, therefore, systematic errors in modulus of elasticity and mass density are selected to address material-related uncertainties. Geometry-related uncertainties, on the other hand, include random errors in structure's dimensions, along with random errors in measurement locations.

5.5.1   Effects of Material Properties Uncertainties on Stress Measurements

While the properties for most engineering materials are well documented, several factors, such as manufacturing discrepancies, contribute to the uncertainty with which such properties can be determined. Furthermore, specifying the exact alloy composition is not always possible for many in-service structures, as is the case for railroad tracks. The later source of uncertainty is considered as a systematic error, which normally has a more significant contribution to the uncertainty bounds

compared to random manufacturing discrepancies. In this work, an Aluminum beam has been selected as the structure under test. Although the alloy out of which the beam is made is known to be Aluminum 6061-T651 (the properties of which are shown in Table 5.1) other Aluminum alloys are considered to determine the uncertainty bounds of its material properties. Based on 2xxx, 5xxx, 6xxx, and 7xxx alloys, the elastic modulus and mass density of the structure under test are assumed to be 71±2.1 GPa and 2730±65 kgm^{-3}, respectively. In this section, the sensitivity of stress estimates to material properties uncertainties is evaluated as a function of frequency.

The objective function behavior with different levels of uncertainty in the material's modulus of elasticity is shown in Figure 5.11.a. These curves are calculated for a 0 MPa, 40MPa and -20MPa reference states of stress, and a 1 kHz excitation signal. It can be noticed that ±2.1 GPa uncertainty in elasticity modulus results in ∓2.2 MPa uncertainty in the estimated state-of-stress for the stress-free case. This error is found to be weakly dependent on the reference state-of-stress, where the aforementioned level of uncertainty in elasticity modulus results in ∓1.8 MPa and ∓2.5 MPa uncertainty in the estimated state-of-stress for the 40 MPa and -20 MPa reference stresses, respectively. The robustness of the proposed algorithm against uncertainties in the elasticity modulus is strongly dependent on the excitation frequency. Figure 5.11.b shows the error in the estimated state-of-stress as a function of elasticity modulus uncertainty and the excitation frequency for the stress-free reference state. The robustness of the stress measurement algorithm is found to improve with lower excitation frequencies. This can be ascribed to the superior sensitivity of dispersion curves to axial stresses at low-frequency ranges, as discussed in Section 5.2. Such low-frequency robustness comes at the cost of a larger separation distance between the point of measurement and structure's boundaries to obtain a reflection-free response.

For a given excitation frequency, the error in the estimated state-of-stress varies linearly with the elasticity modulus uncertainty. Figure 5.12.a shows such variations with 500 Hz, 1 kHz, and 2 kHz excitation signals. The linear behavior along with low-frequency superior robustness are evident in the figure. The sensitivity of the estimated state-of-stress for the modulus of elasticity, denoted by $\partial\sigma/\partial E$, is obtained by differentiating the error in the estimated state-of-stress with respect to the change in elasticity modulus at constant frequency. The results are shown in Figure 5.12.b. This sensitivity is found to change linearly with frequency. The rate of change of $\partial\sigma/\partial E$ with respect to the excitation frequency is found to be constant, with a value of -0.328 MPa/GPa.kHz.*mm*.

(a)

(b)
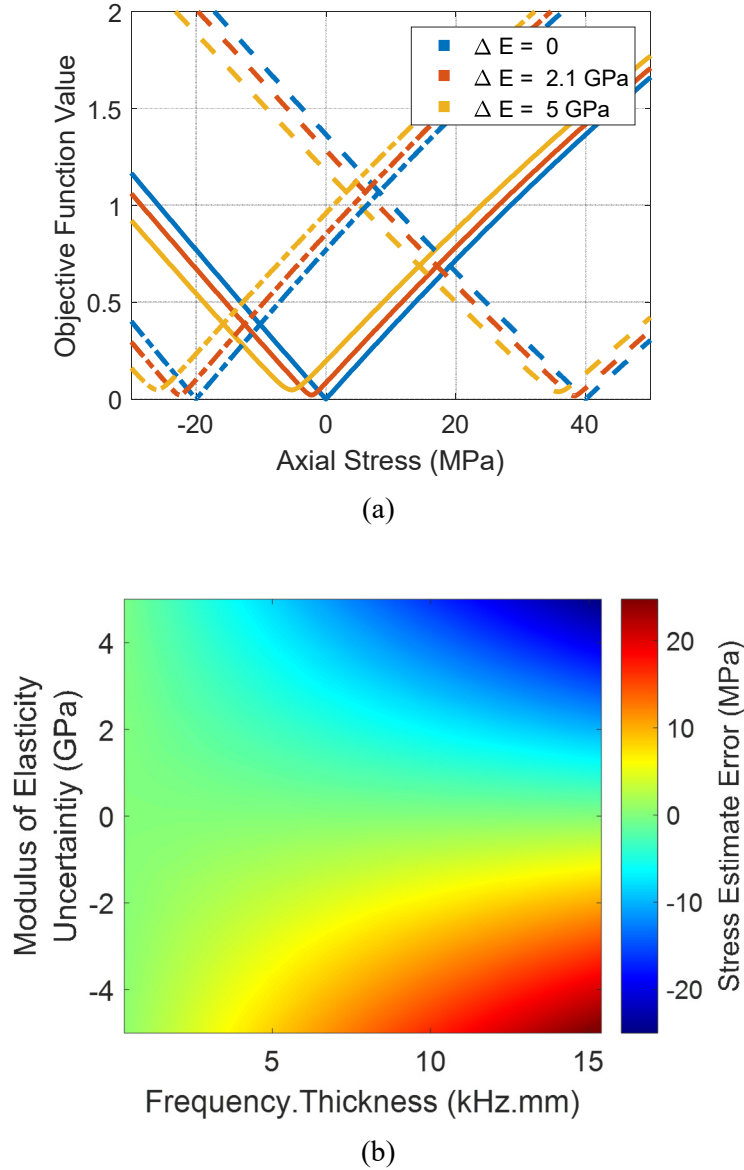
Figure 5.11. Effects of elasticity modulus uncertainty on stress measurements, (a) objective function
curves for a 1 kHz excitation and zero (——), 40 MPa (– – –) and -20 MPa (– · –) axial stress levels, and
(b) stress estimate error as a function of elasticity modulus uncertainty and excitation frequency.
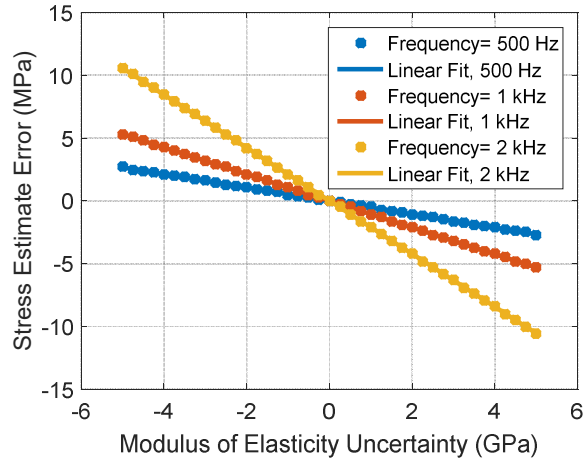
(a)
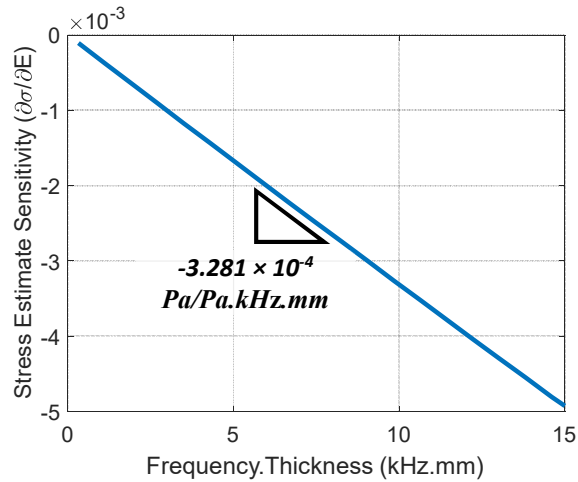
(b)

Figure 5.12. (a) Error in the estimated state-of-stress as a result of elasticity modulus uncertainty, and (b) estimated stress-state sensitivity to elasticity modulus as a function of excitation frequency.

Uncertainties in the material's volumetric mass density are found to have a similar impact on the performance of the proposed stress measurement algorithm as the elasticity modulus. Figure 5.13.a shows the error in the estimated state-of-stress as a function of density uncertainty and the excitation frequency for the stress-free reference state. An overestimation of the materials mass density always results in an overestimation of the state-of-stress. These effects are found to be strongly dependent on frequency, where the robustness of the stress measurement algorithm is inversely proportional to the excitation frequency. The rate of change of $\partial\sigma/\partial\rho$ with respect to the excitation frequency is also found to be constant, with a value of -8.65×10^{-3} MPa.m^3/kg.kHz.mm.
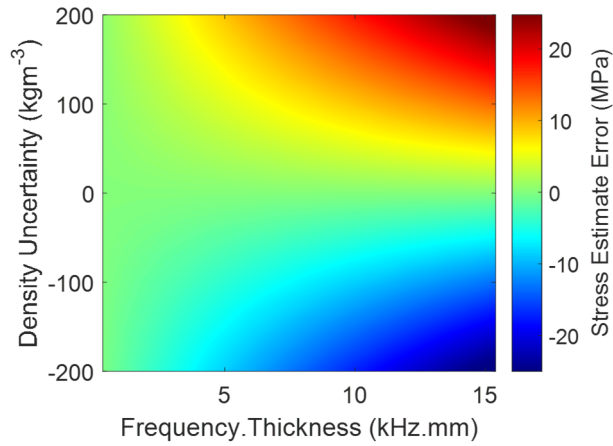
(a)
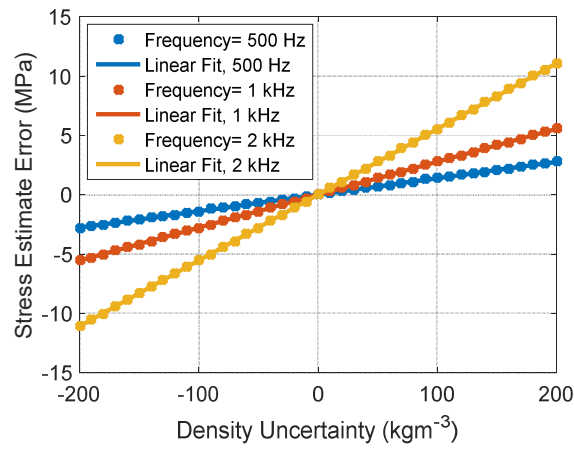
(b)
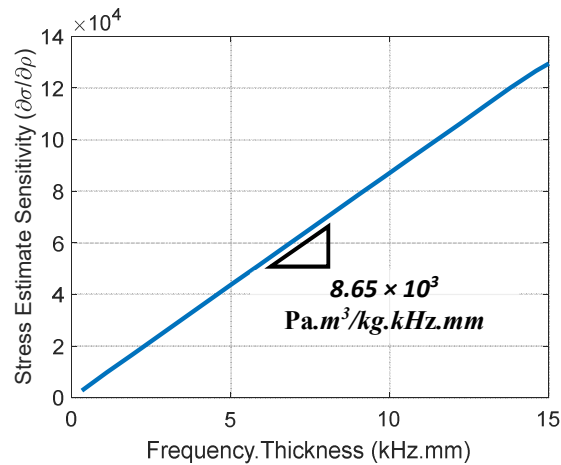
(c)

Figure 5.13. Effects of density uncertainty on stress measurements, (a) stress estimate error as a function of density uncertainty and excitation frequency, (b) error in the estimated state-of-stress at a constant frequency, and (c) estimated stress-state sensitivity.

5.5.2   Effects of Geometric Uncertainties on Stress Measurements

In this section, the effects of uncertainties in the geometry of the structure being tested on the measured state-of-stress are investigated. Such uncertainties arise from the random variations of structure's dimensions, which are normally determined by the manufacturer. For a beam with a rectangular cross section, width and thickness are the only two geometry-related parameters to be considered. The beam is assumed to be long enough such that reflection-free responses are attainable at all measurement locations. The beam investigated in this study is 38.1±0.36 *mm* (95%) wide and 3.175±0.09 *mm* (95%) thick.

Wave speed, in general, is determined by the ratio of elastic restoring forces to inertial forces, through terms such as *EI* and *ρA*. Such terms are equally affected by the beam's width, and hence, the width parameter has no effect on wave propagation in one-dimensional structures. However, it plays a role in determining the frequency range within which the one-dimensional approximation is valid. Therefore, for the current analysis, uncertainty in beam's width does not affect the measured state-of-stress. Beam's Thickness, on the other hand, has a significant impact on the second moment of area, and hence, thickness related uncertainties cannot be ignored.

The effects of beam's thickness uncertainty on the measured state-of-stress are summarized in Figure 5.14. The limits of uncertainty in thickness are determined based on the previously stated manufacturer tolerances. Figure 5.14.a shows the error in the estimated state-of-stress as a function of thickness uncertainty and the excitation frequency. The reference state-of-stress is selected in this analysis to be the stress-free state. For a given level of thickness uncertainty, the error in the estimated state-of-stress is found to decrease with lower excitation frequencies. This agrees with the general trend found for material-related uncertainties and is a direct result of the stronger acoustoelastic effects at low-frequency ranges.

For a given excitation signal frequency, the error in the estimated state-of-stress is found to vary linearly with thickness uncertainty, as shown in Figure 5.14.b. The slope of these lines represents the sensitivity of the estimated state-of-stress for the beam's thickness, $\partial\sigma/\partial h$, at the corresponding excitation frequency. In the figure, $\partial\sigma/\partial h$ is found to be -23.74 MPa/*mm*, -47.34 MPa/mm and -95.1 MPa/*mm* for 500 Hz, 1 kHz, and 2 kHz excitations, respectively. These values are calculated for the 3.175-*mm*-thick beam considered in this study, and they will vary for beams of different thicknesses. As is the case for the material-related uncertainties, the sensitivity of the estimated state-of-stress to beam thickness changes linearly with excitation frequency, as shown in Figure 5.14.c. The rate of change of $\partial\sigma/\partial h$ with respect to the excitation frequency is constant, with a value of -15.55 MPa/kHz.mm^2.
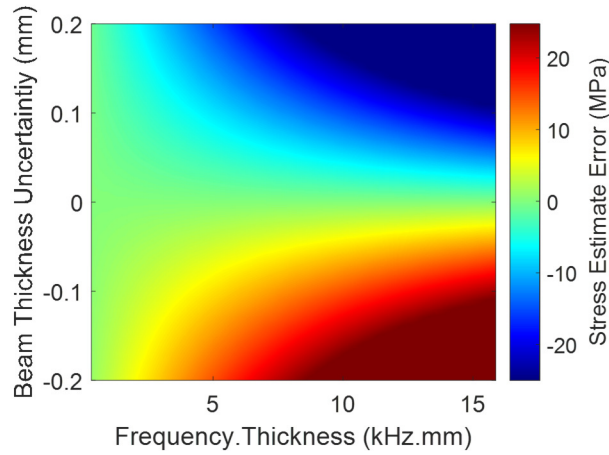
(a)
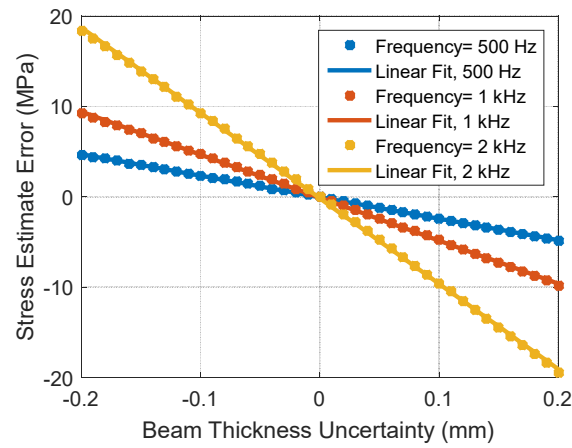
(b)
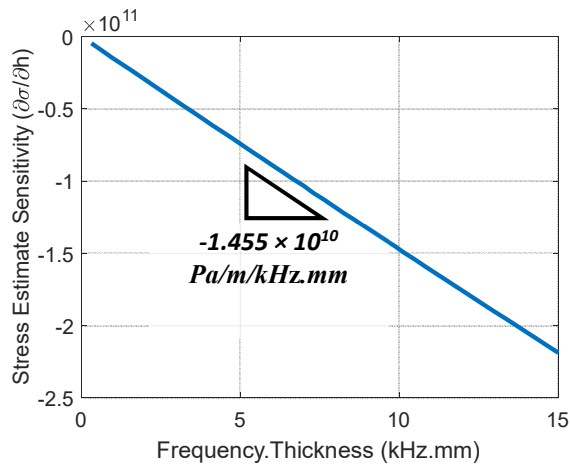
(c)

Figure 5.14. Effects of beam thickness uncertainty on stress measurements, (a) stress estimate error as a function of thickness uncertainty and the excitation frequency, (b) error in the estimated state-of-stress at a constant frequency, and (c) estimated stress-state sensitivity.

5.5.3   Effects of Measurement Location Uncertainty on Stress Measurements

The proposed stress measurement algorithm utilizes the distance Δx, to propagate waveforms between different measurement locations. Depending on the experimental technique implemented to measure propagating waveforms, location information can be prone to uncertainties. Such uncertainties may arise from random errors in initial coordinates measurement, as well as the finite deformations induced by the applied loads. In the most general case, the state-of-stress at the time of measurement system installation is unknown, and thus, calibration experiments to compensate for erroneous location information may not be possible. In this section, the effect of measurement location uncertainties on the performance of the proposed stress measurement algorithm is investigated.

As a consequence of the acoustoelastic effect, uncertainties in measurement locations can be misinterpreted as changes in the state-of-stress acting on the structure. Figure 5.15 shows the error in the estimated state-of-stress due to location uncertainty of different measurement locations. Let the measurement location be given by

$$x = \bar{x} \pm u_x \qquad\qquad (5.27)$$

where $\bar{x}$ is the averaged measurement location, which is assumed to match the true measurement location, and u_x is the uncertainty in measurement location. In general, an over estimation of measurement location, $x > \bar{x}$, results in an over estimation of the state-of-stress, and vice versa. For a given u_x, the resulting error in stress estimate is inversely proportional to the value of $\bar{x}$, as suggested by Figure 5.15. This is in fact intuitive as a fixed absolute uncertainty has less impact on larger means compared to smaller ones. For example, with $u_x = 1\ mm$ and with 1 kHz excitation frequency, the error in stress estimate is found to be 3 MPa, 1.51 MPa, and 0.6 MPa for a 100 mm, 200 mm, and 500 mm measurement locations, respectively. If the uncertainty is normalized by the mean value, $\bar{u}_x = u_x/\bar{x}$, then identical stress error levels are obtained for a given $\bar{u}_x$ regardless of the actual measurement location. For example, with $\bar{u}_x = 0.01$ and with 1 kHz excitation frequency, the error in stress estimate is found to be 3 MPa for all three measurement locations.

The error in the estimated state-of-stress due to normalized measurement location uncertainty of $\pm\ 0.02$ is shown in Figure 5.16.a. The strong dependence on excitation frequency is evident in the figure, with measurements utilizing low-frequency excitations being more robust against location uncertainties. For
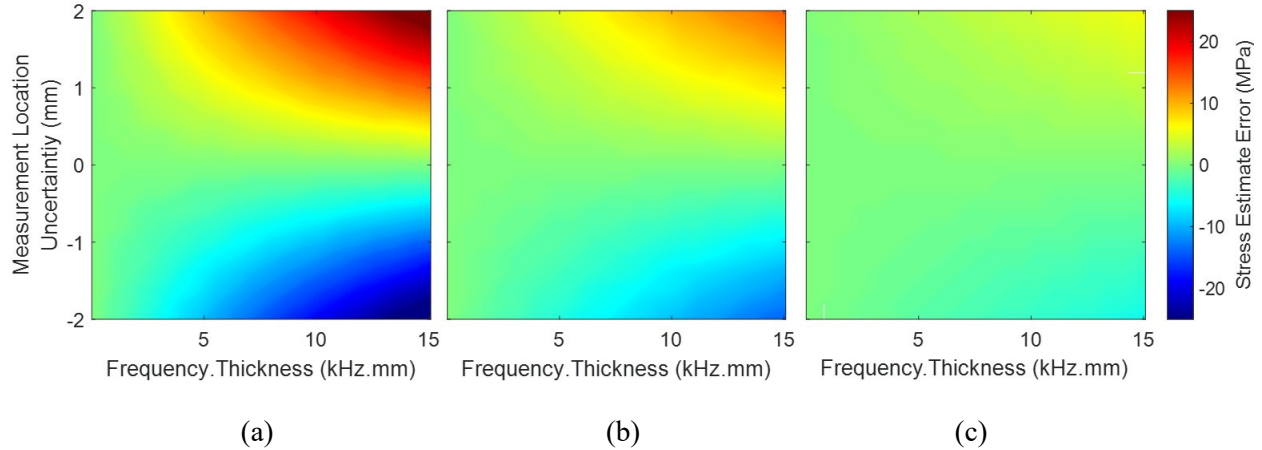
Figure 5.15. Effects of measurement location uncertainty on the estimated state-of-stress for (a) 100 *mm*, (b) 200 *mm*, and (c) 500 *mm* measurement locations.

instance, with $\bar{u}_x = 0.01$, error margins of the estimated state-of-stress grows form ± 1.51 MPa to ± 15.83 MPa as the excitation frequency changes from 500 Hz to 5 kHz. Depending on the structure being tested, it can be necessary to account for reflections in order to utilize lower excitation frequencies, otherwise, calibration might be needed to correct for such uncertainties.

For a given excitation frequency, the error in the estimated state-of-stress is found to vary linearly with the normalized location uncertainty, as shown in Figure 5.16.b. The slope of these lines represent the sensitivity of the estimated state-of-stress to the normalized uncertainty in measurement location, $\partial\sigma/\partial\bar{u}_x$, for the corresponding excitation frequency. In the figure, $\partial\sigma/\partial\bar{u}_x$ is found to be 1.52 MPa, 3.01 MPa and 6 MPa per percent for 500 Hz, 1 kHz, and 2 kHz excitations, respectively. The effect of excitation frequency on $\partial\sigma/\partial\bar{u}_x$ is depicted in Figure 5.16.c. The sensitivity $\partial\sigma/\partial\bar{u}_x$ is found to change linearly as a function of excitation frequency with a rate of change of 0.954 MPa/kHz.*mm* per percent. For all practical considerations, $\partial\sigma/\partial\bar{u}_x = 0$ at zero frequency.
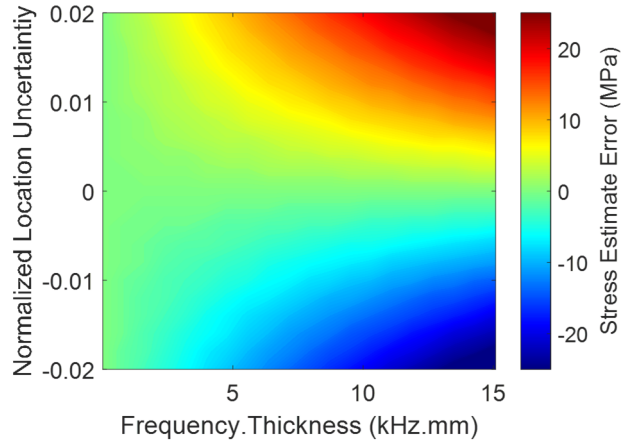
(a)
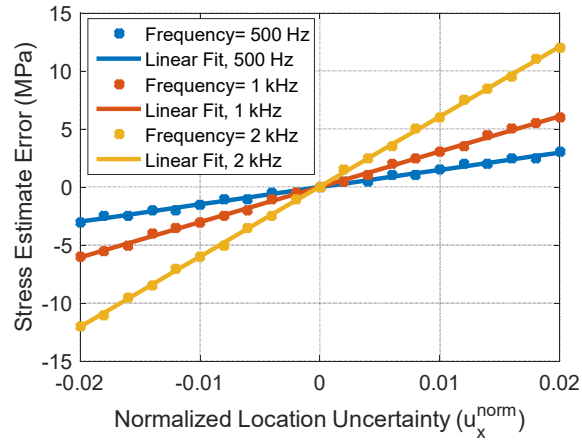
(b)
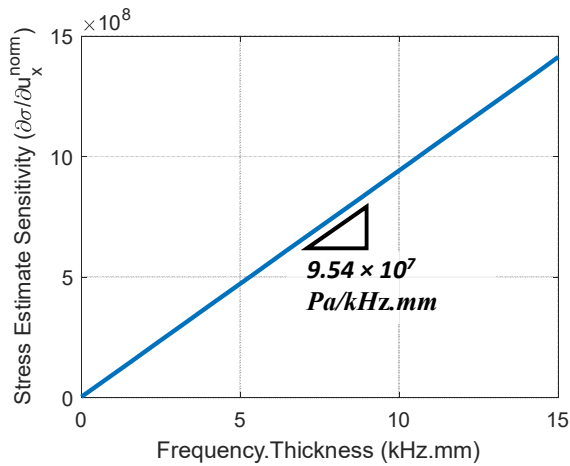
(c)

Figure 5.16. Effects of measurement location uncertainty on stress measurements, (a) stress estimate error as a function of u_x^{norm} and the excitation frequency, (b) error in the estimated state-of-stress at a constant frequency, and (c) estimated stress-state sensitivity.

5.5.4   Error Propagation Analysis

The sensitivity of stress measurements to individual material and geometric uncertainties have been quantified in Sections 5.5.1-5.5.3. In practice, all types of uncertainties coexist and affect the measurement at the same time. To gauge the effects of such uncertainties, standard error propagation techniques are adopted in this section, taking into consideration error types, margins for each error source, and the sensitivity of stress measurements to these errors. Table 5.2 summarizes the error sources considered in this study.

Material-related errors are mainly systematic errors described by the bias values given in the table. Geometry-related errors, on the other hand, are random in nature, described by standard random uncertainties with 95% confidence. The uncertainty in the measured state-of-stress due to material and geometry related errors can be determined as follows (Figliola and Beasley, 2010)

$$u_\sigma = \left[\sum_{i=1}^{5} \left(\frac{\partial \sigma}{\partial u_i} u_i \right)^2 \right]^{1/2} \tag{5.28}$$

Since the sensitivity to each error source is frequency dependent, the uncertainty in stress measurements will be in turn frequency dependent. Figure 5.17 shows the expected uncertainty in stress measurements as a function of excitation frequency. For the error bounds shown in Table 5.2, the effect of measurement location uncertainty is negligible, except for very close measurement locations, $\bar{x} < 0.05\,m$, where $\bar{u}_x$ becomes significantly large. For $\bar{x} > 0.1\,m$, u_σ contours are parallel to the measurement location axis, indicating that other sources of error are dominant. For the current analysis, beam's thickness uncertainty is the most dominant source of errors. A more accurate measurement of beam's thickness will significantly improve the accuracy of stress measurements.

Table 5.2. Error sources encountered in stress measurement experiments.

Error Source	*Uncertainty*	*Sensitivity ($\partial\sigma/\partial u$)*	*Comments*
Mod. of Elasticity (u_E)	±2.1 GPa	$-0.328\,fh_b$ MPa/GPa	Statistical distribution of 2xxx, 5xxx,
Density (u_ρ)	±65 kgm^{-3}	$8.65\times10^{-3}\,fh_b$ MPa/kgm^{-3}	6xxx, and 7xxx alloys.
Thickness (u_h)	±0.09 mm	$-15.55\,fh_b$ MPa/mm	Specified by the Manufacturer.
Width (u_w)	±0.36 mm	0	
Meas. location (u_x)	±0.5 mm	$0.954\,fh_b$ MPa/ perc.	Zero-order uncertainty for the geometric laser unit.
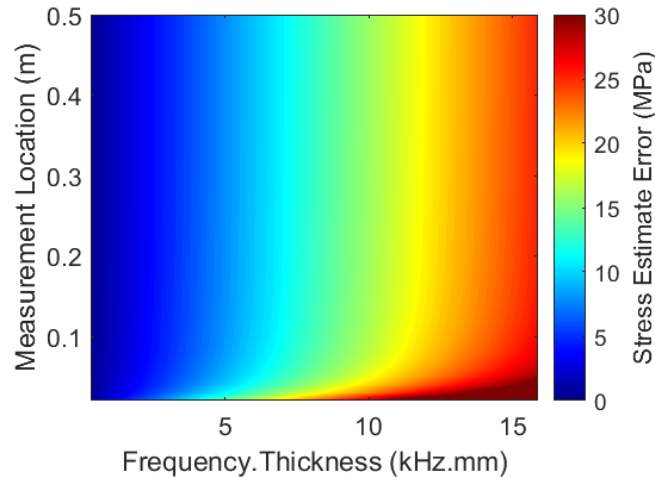
Figure 5.17. Uncertainty in the measured state-of-stress as a function of excitation frequency and measurement locations.

5.6   Experimental Implementation

In this section, the acoustoelastic-based stress measurement algorithm is validated experimentally. The experimental setup is first discussed in detail. The effects of axial stress on the steady-state response, frequency response functions and impedance signatures, are discussed. The performance of the stress measurement algorithm developed in the previous sections is then evaluated, and its capabilities to perform true reference-free stress measurements are demonstrated.

5.6.1   Experimental Setup

A schematic of the experimental setup used for the experimental validation of the developed acoustoelastic-based stress measurement technique is shown in Figure 5.18. For these experiments, an aluminum beam, with the dimensions and material characteristics given in Table 5.1, is tested at several levels of axial stress. A Macro Fiber Composite (MFC) piezoelectric transducer is used to excite the beam under test at the desired frequency, while a three-dimensional, Polytech laser Doppler vibrometer and scanner (PSV- 400) is used to measure the wave field along the beam.
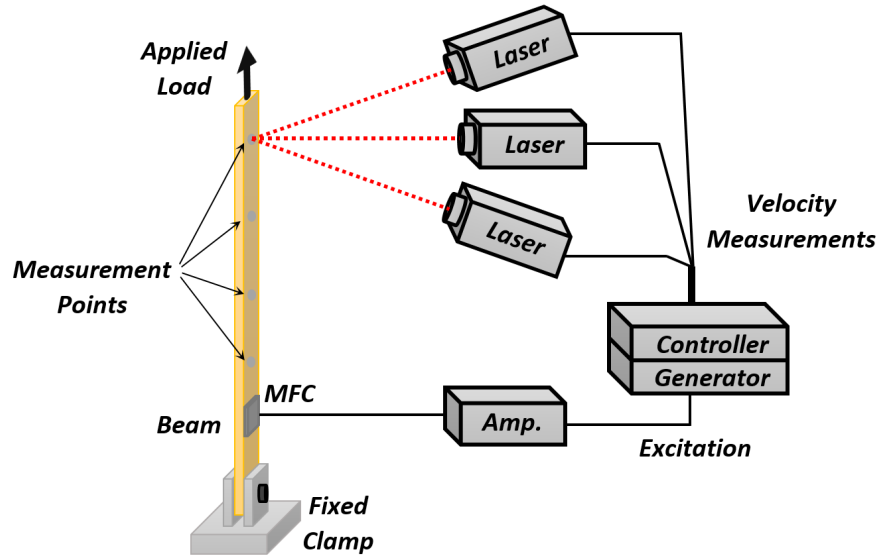
Figure 5.18. A schematic of the experimental setup used for stress-state measurements.

Since a single MFC attached to the beam's surface is used in this experiment, both symmetric and anti-symmetric wave modes are excited. The use of the three-dimensional, laser vibrometer system allows for these modes to be separated. Only out-of-plane displacements, corresponding to the first anti-symmetric mode, are considered in this work to calculate the state-of-stress.

In order to control the axial load acting on the structure under test, a loading stage, shown in Figure 5.19, has been designed and manufactured. The stage consists of a 72 inches long, 4 inches wide and ½ inch thick steel base, with 2-inch-high end plates. Two L-shaped fixtures are used to attach the beam to the loading stage. Each fixture has a threaded end that goes through the end plates, as shown in the figure. The tension in the beam under test is controlled by tightening or loosening a nut at the fixture's threaded end. A strain gauge attached to the beam under test is used to provide a reference measurement of the state-of-stress for comparison purposes. The beam is excited with an MFC located 4 inches off the beam's center. All measurement locations, for both strain gauge and laser measurements, are at least eight beam-widths away from the tensioning fixtures. This guarantees that a uniform state-of-stress exists throughout the section where the response is measured. Although the loading stage is designed to apply both tensile and compressive loads to the beam under test, only tensile loads are considered in this study. This is due to the fact that the test beam loses stability and buckles at very small compressive loads.
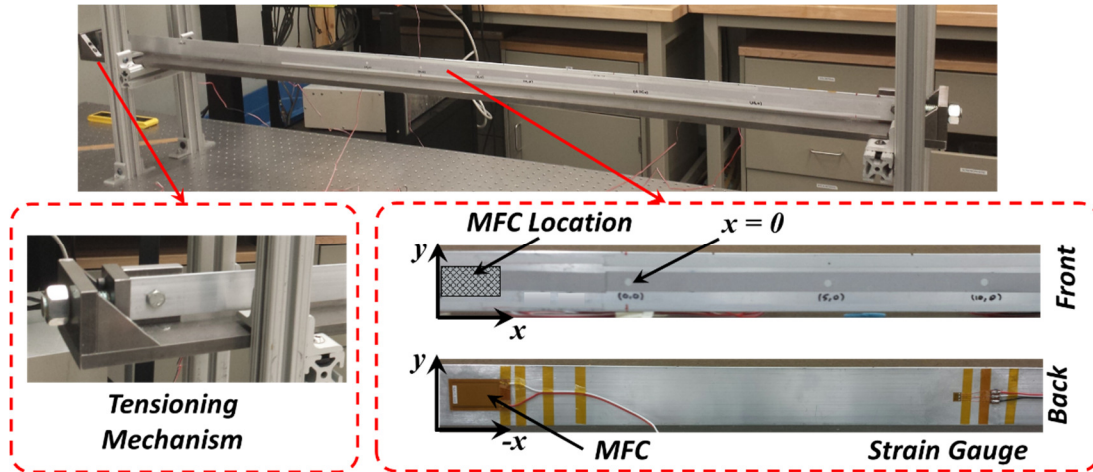
Figure 5.19. Stress state measurement experimental setup showing the loading stage, the tensioning fixture, along with excitation and measurement locations.

With the aid of this loading stage, several tensile loads have been applied to the beam under test including the stress-free case, 10, 20 and 40 MPa. For each stress level, steady-state and transient responses are measured. Both frequency response functions and impedance signatures are measured to study loading effects on the steady-state dynamic response of the beam. Transient responses, on the other hand, include the measurement of 0.5, 1, 2, and 5 kHz waveforms as they propagate along the structure. For all cases, the response is measured at eleven equally spaced points along the beam covering a span of 400 *mm*.

5.6.2   Steady-state Dynamic Response

The effects of the state-of-stress on the steady-state dynamic response of an axially loaded beam are discussed in this section. Following from the acoustoelastic theory, the state-of-stress acting on the structure affects the wavelength and speed of elastic waves propagating along the structure. This, in turn, affects the constructive and destructive interactions of the incident and reflected waves, which is manifested at steady-state as a shift in resonance frequencies. Figure 5.20 shows the transfer FRFs for the out-of-plane velocity measured at the beam's center ($x = 0$) as the beam is excited with the MFC transducer. Excitation and measurement locations are shown Figure 5.19. The response is plotted for the 3-5 kHz frequency range with 10, 20 and 40 MPa longitudinal stresses. Resonance frequencies are found to shift to the right as tensile loads are increased. For instance, the resonance peak marked in the figure shifts from 3659 Hz at 10 MPa longitudinal stress to 3822 Hz at 40 MPa, which is approximately 5.5% change. This shift is found to get less significant as higher frequency resonant peaks are examined.

Impedance signatures of the beam under the aforementioned stress levels are shown in Figure 5.21 for the
1.25-3 kHz frequency range. As noticed with FRFs, impedance peaks are found to shift to higher
frequencies as the tensile stress is increased. For the impedance peaks marked in the figure, peak frequency
is found to shift from 1505 Hz at 10 MPa longitudinal stress to 1622 Hz at 40 MPa, which is approximately
7.8% change. Compared to the shift noticed at higher frequency ranges, the impact of the state-of-stress on
the structure's steady-state dynamic response is more profound at low frequencies. This agrees with the
analytical findings, presented in earlier sections, regarding the superior sensitivity of low-frequency elastic
waves to the applied state-of-stress.
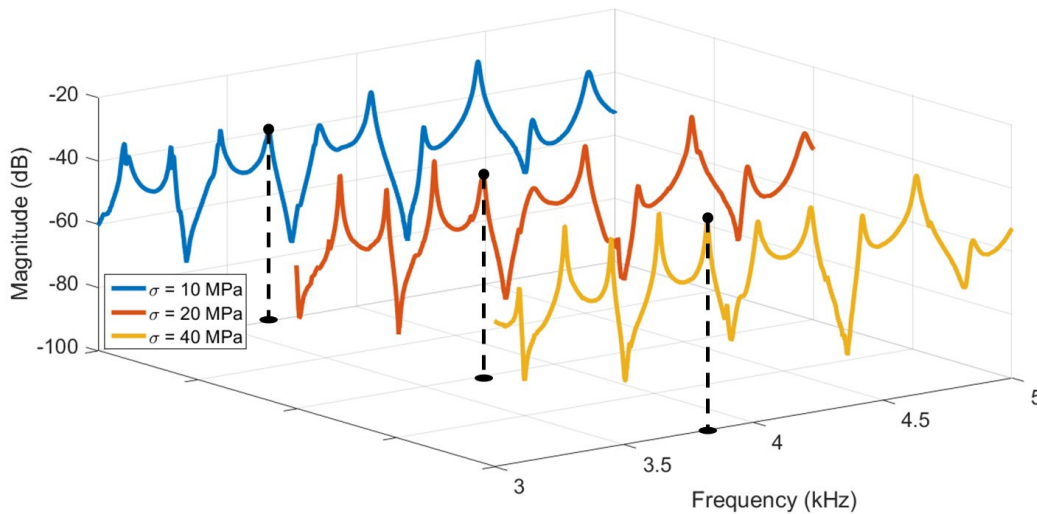
Figure 5.20. Effects of longitudinal state-of-stress on mobility frequency response functions measured at
the center of the beam.
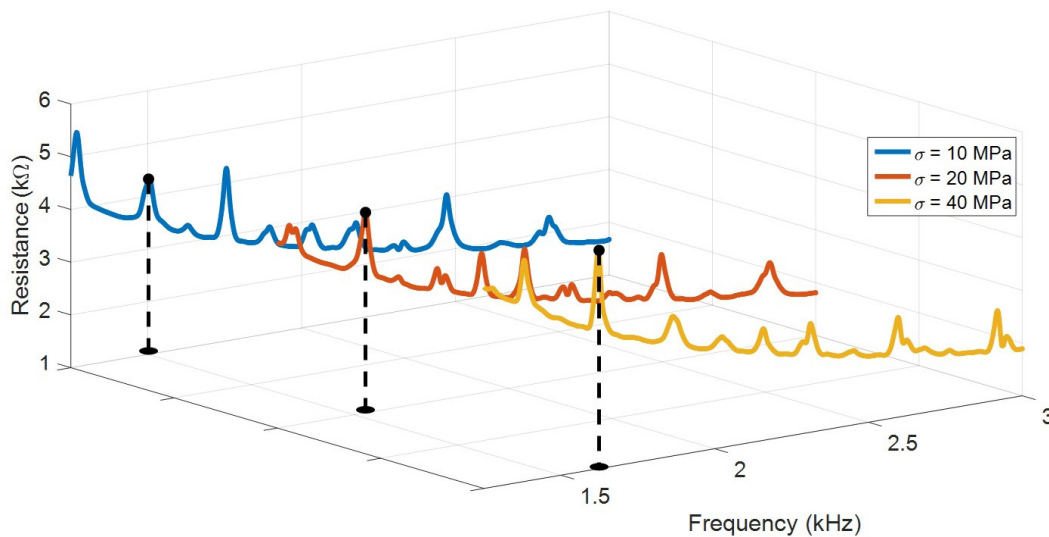
Figure 5.21. Effects of longitudinal state-of-stress on electromechanical impedance signatures.

The results presented in this section suggest that the effects of the state-of-stress acting on the structure can be clearly detected by examining the steady-state dynamic response of the structure being tested. Model updating techniques can then be employed to calculate the state-of-stress. In spite of the simplicity of this approach, along with the ease and convenience with which steady-state responses can be measured, successful implementation of such techniques require an accurate characterization of structure's boundaries. In practice, most boundary conditions are complex in nature and can be affected by the applied state-of-stress, which makes their characterization a tedious process. In order to avoid these limitations, the transient response is analyzed in the following section to calculate the state-of-stress in the structure with the aid of the developed acoustoelastic-optimization-based algorithm.

5.6.3   Acoustoelastic-optimization-based Measurements

Propagating elastic waves are utilized in this section to calculate the state-of-stress acting on the beam under test. Based on the findings of Section 5.4, amplitude modulated, two-cycle sine wave tone bursts with 500 Hz, 1, 2 and 5 kHz center frequency are generated using the MFC transducer bonded to the beam's surface. With the aid of the loading stage, stress-free, 10, 20 and 40 MPa loading scenarios are investigated. For each loading scenario, the propagating waveform is measured at 11 equally spaced points along the beam covering a span of 400 *mm*.

Figure 5.22 shows the waveforms measured at $x = 0$, $x = 80$ *mm*, and $x = 160$ *mm* for the 500 Hz excitation signal and the stress free condition. At this frequency, dispersion effects can be clearly noticed in the form of signal distortion. For each measurement location, the measured waveform consists of both incident and reflected waves, with no clear separation between them. This is due to the fact that the distance between measurement locations and beam's edge is less than the minimum distance required for a reflection-free response at this excitation frequency.

In order to calculate the state-of-stress in the structure, the waveform measured at $x = 0$ is considered as the reference signal that will be propagated by the developed algorithm and then compared to the waveforms measured at other locations. This approach allows bypassing the uncertainties associated with signal amplification and MFC excitation stages (shown in Figure 5.18). However, it introduces the need for isolating incident and reflected components of this reference waveform. This can be successfully achieved when the distance between the reference measurement location ($x = 0$) and structure's boundaries satisfies Eq. 5.26. Otherwise, reflections contamination will affect the performance of the algorithm and the accuracy of the estimated state-of-stress.
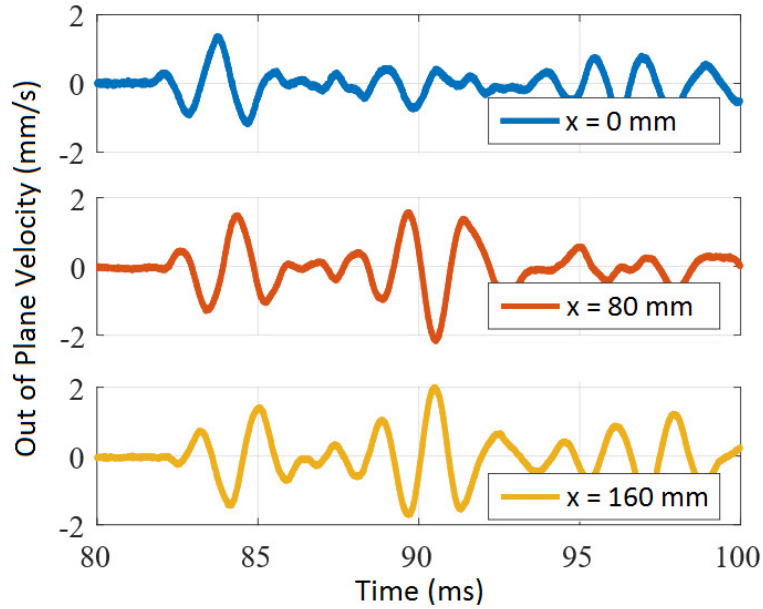
Figure 5.22. Measured waveforms at x = 0, 80 *mm* and 160 *mm* for a 500 Hz excitation signal and stress-free condition.

Following the aforementioned approach, the first step towards estimating the state-of-stress in the structure is to isolate the incident waveform the response measured at x = 0. This is performed manually and is subject to the judgment of the data analyst. A low-pass, zero-lag filter is also employed to denoise the isolated signal as well as all other waveforms measured along the beam. The reference waveform for a 500 Hz excitation signal and the stress-free condition is shown in Figure 5.23, along with the isolated and filtered incident wave, labeled as *Processed* in the figure.
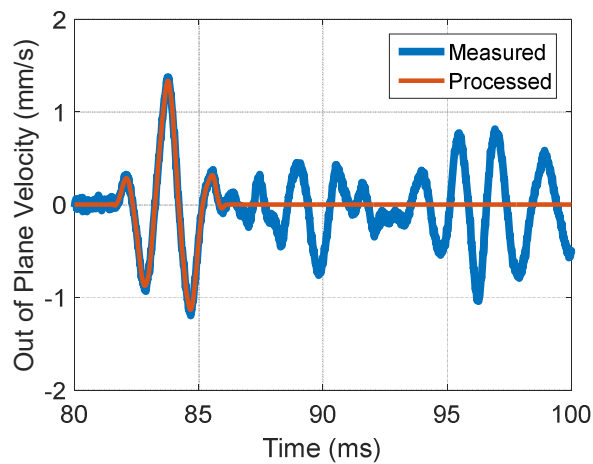
Figure 5.23. Reference waveform measured at x = 0, along with the isolated and filtered incident wave, for a 500 Hz excitation signal and the stress-free condition.

139

Once the incident wave is isolated and filtered, it is fed to the stress measurement algorithm as *Input 2* (refer to Figure 5.3). Material properties of the beam under test and its dimensions are also fed to the algorithm. As discussed in Section 5.3, the algorithm propagates the incident wave to the next measurement location, (x_{i+1}), and updates the state-of-stress to minimize the error function defined as the L_2 norm of the difference between the waveform measured at x_{i+1} and the incident wave that has been propagated to that location. Upon convergence, an estimate of the state-of-stress acting on the structure is obtained. Figure 5.24 shows the waveforms measured at $x = 80$ *mm* and $x = 160$ *mm*, along with the processed incident wave and the ones propagated to the aforementioned locations with zero stress. Both measured and propagated waveforms are in very good agreement. The algorithm does not take the beam's boundaries into consideration, therefore, propagated waveforms do not show any reflected components. Based on these two measurement locations, $x = 80$ *mm* and $x = 160$ *mm*, the optimal state-of-stress is found to be 0.8 MPa and -1.3 MPa, respectively.

The discrepancies in the estimated state-of-stress can be ascribed to the uncertainties in measurement locations, random beam-thickness variations, and imperfect (reflections contaminated) incident wave. However, both stress estimates are within the theoretical uncertainty levels determined in the previous section.

(a)   (b)
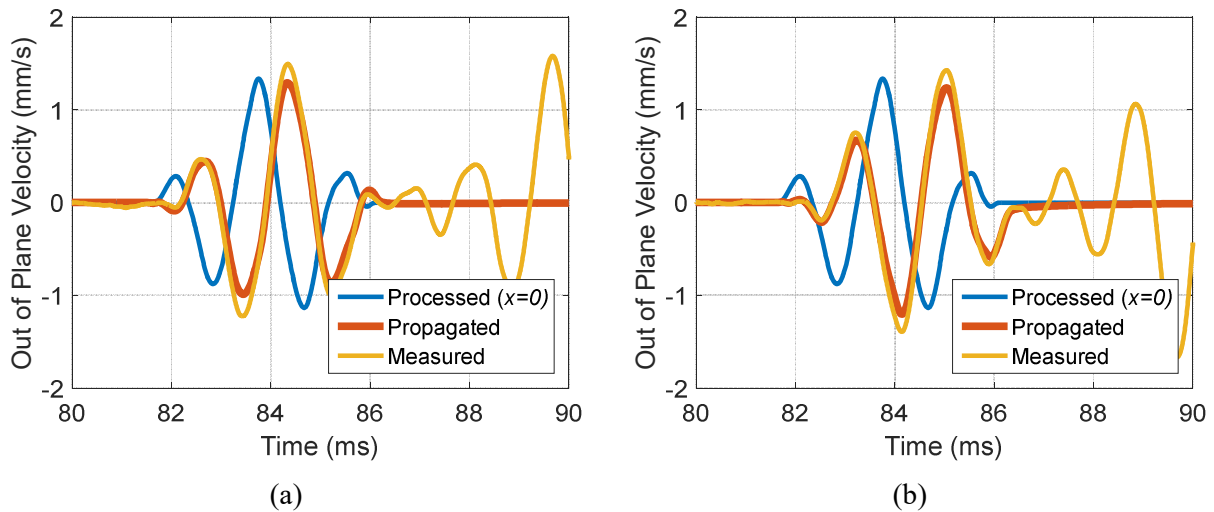
Figure 5.24. Measured waveforms at (a) $x = 80$ *mm*, and (b) $x = 160$ *mm*, along with the processed incident wave and the ones propagated to the corresponding location. Results are obtained for 500 Hz excitation signal and stress-free condition.

In the presence of uncertainties, the objective function value at its global minimum will be greater than zero, as suggested by Figures 5.11.a. This minimum value of the objective function serves as a measure of the stress estimate quality. If the propagating wave is measured at several locations along the structure being tested, weighted averaging can be implemented to obtain an average estimate of the state-of-stress. The objective function global minimum at each measurement location can be used as the weighting coefficient for the corresponding stress measurement, and the average state-of-stress is calculated as follows

$$\bar{\sigma} = \frac{\sum_{i=2}^{N} \sigma_i / \mathcal{J}(x_i, \sigma_i)}{\sum_{i=2}^{N} 1 / \mathcal{J}(x_i, \sigma_i)} \tag{5.29}$$

where $\bar{\sigma}$ is the average state-of-stress based on N-point measurements, σ_i is the stress estimate obtained based on the waveform measured at location x_i, and $\mathcal{J}(x_i, \sigma_i)$ is the minimum value of the objective function at this location. It is implicit in this definition that the waveform measured at x_1 is considered to be the reference waveform, as discussed earlier in this section. This weighted averaging scheme is especially beneficial with measurement location and thickness errors, since these errors are random in nature.

For the 500 Hz excitation signal and stress-free condition, and based on the first four measurement points, i.e. $x = 40\ mm$, $80\ mm$, $120\ mm$, and $160\ mm$, the estimated state-of-stress along with the minimum objective function values are summarized in Table 5.3. Based on these four locations, the average state-of-stress is found to be -0.52 MPa. The remaining measurement locations, $x \geq 200\ mm$, yield larger uncertainty levels as the waveforms measured there are strongly contaminated with reflections. This can be ascribed to the physical proximity of such locations to the beam's edge and the large wavelength of the incident wave at this excitation frequency.

The same analysis has been repeated for the 10, 20 and 40 MPa stress levels with the 500 Hz excitation signals. Figure 5.25 depicts the incident wave for each case, along with the measured and propagated waveforms at $x = 80\ mm$, and $x = 160\ mm$. It can be noticed that the algorithm is able to propagate the incident wave to closely match the measured wave at these locations, in spite of the uncertainties associated with incident wave isolation. All measured waveforms are clearly contaminated with reflections, as the dimensions of the structure under test do not satisfy the minimum length for reflections free responses.

Table 5.3. Estimated state-of-stress and the minimum objective function values obtained at several measurement locations for 500 Hz excitation signal.

			Measurement Location (*mm*)				Average Stress
			40	80	120	160	
Reference State-of-stress	0 MPa	Optimal Stress Estimate (MPa)	0.1	0.8	-0.4	-1.3	-0.52 MPa
		Minimum Objective Function	1.5×10^{-2}	2.2×10^{-2}	1.2×10^{-2}	2.3×10^{-2}	
	10 MPa	Optimal Stress Estimate (MPa)	13	10.8	9.1	8.9	10.31 MPa
		Minimum Objective Function	10.3×10^{-3}	9.7×10^{-3}	8.1×10^{-3}	8.3×10^{-3}	
	20 MPa	Optimal Stress Estimate (MPa)	17.8	18.6	18.7	18.25	18.32 MPa
		Minimum Objective Function	5.5×10^{-3}	7.9×10^{-3}	5.6×10^{-3}	8.1×10^{-3}	
	40 MPa	Optimal Stress Estimate (MPa)	36.8	28.5	32.3	35.7	33.2 MPa
		Minimum Objective Function	2×10^{-2}	3.6×10^{-2}	6.5×10^{-2}	5.9×10^{-2}	

For each of the aforementioned loading scenarios, the estimated states-of-stress based on the first four measurement locations are summarized in Table 5.3. Based on these measurement locations, the average state-of-stress is found to be 10.31 MPa, 18.32 MPa, and 33.2 MPa for the 10 MPa, 20 MPa, and 40 MPa reference stresses, respectively. It can be noted that the error in the estimated state-of-stress increases for large reference stresses, the 40 MPa case in particular. This can be ascribed to the fact that the loading stage, shown in Figure 5.19, slightly buckles when large states-of-stress are applied, which in turn affects the loading state of the beam and, more importantly, the coordinates of measurement locations.

The analyses conducted for the 500 Hz excitation signal has been repeated for 1 kHz, 2 kHz, and 5 kHz excitations. Incident waves, along with the measured and propagated waveforms are shown in Appendix E. With high-frequency excitation signals, shorter distance is required to obtain a reflection-free response. Thus, the incident wave can clearly be separated from reflections, as shown in Figures E.1-E.5. However, this comes at the cost of lower sensitivity to the applied state-of-stress. As discussed in Section 5.5, this reduction in sensitivity adversely affects the robustness of stress measurement algorithm, and thus, material and geometry related uncertainties result in larger error bounds in the estimated state-of-stress.
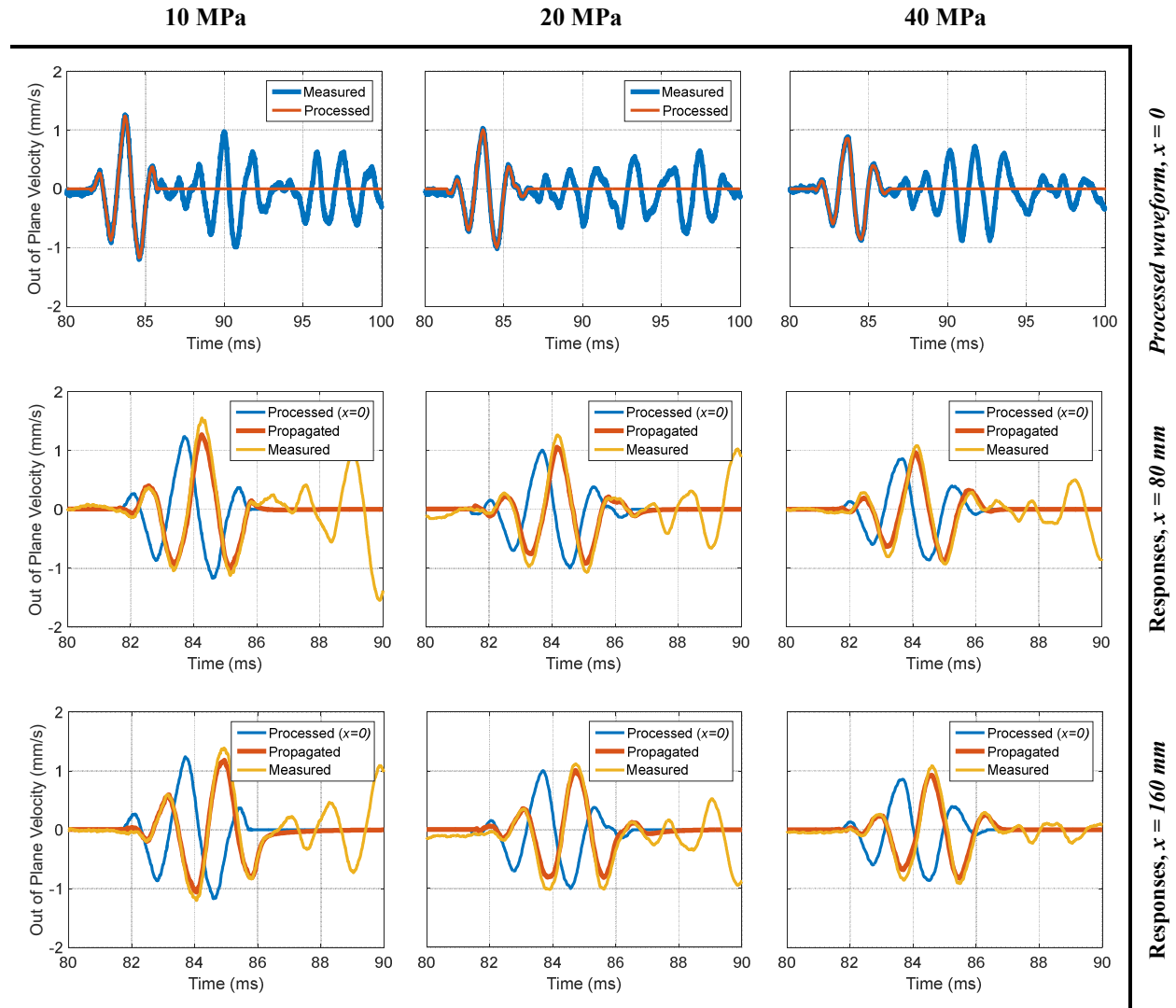
Figure 5.25. Incident, measured and propagated waveforms obtained with 500 Hz excitation signals and 10, 20 and 40 MPa reference states-of-stress.

The average states of stress obtained with different excitation frequencies are summarized in Table 5.4. As is the case for the 500 Hz excitation signal, these averages are obtained by applying Eq. 5.29 to the first four measurement locations. All stress estimates are calculated based on the nominal material and geometric characteristics reported in Table 5.1. No calibration experiments have been conducted, and a reference state-of-stress has not been utilized in the analysis except for comparison purposes. These are true reference-free, uncalibrated acoustoelastic-based stress measurements, which explains the large errors at high-frequency ranges.

Table 5.4. Estimated states-of-stress at several excitation frequencies.

Stress Level	500 Hz	1 kHz	2 kHz	5 kHz
Unloaded	-0.5 MPa	-2.3 MPa	-7.4 MPa	-19.3 MPa
10 MPa	10.3 MPa	9.4 MPa	-2.6 MPa	-12.7 MPa
20 MPa	18.3 MPa	22.9 MPa	13.4 MPa	3.8 MPa
40 MPa	33.2 MPa	32.8 MPa	29.2 MPa	22.7 MPa

In spite of being contaminated with reflections, waveforms obtained with 500 Hz excitation frequency yield the most accurate stress estimates. This agrees with the theoretical findings and is a direct result of the low-frequency superior sensitivity to applied state-of-stress. Stress estimates obtained with 1 kHz excitations are also in good agreement with strain gauge measurements, except for the 40 MPa loading scenario. As discussed earlier, this is ascribed to loading stage buckling at such a large load, which resulted in erroneous measurement locations coordinates. The accuracy of the estimated state-of-stress rapidly deteriorates as the frequency of the propagating waves increases, as seen for the 2 kHz and 5 kHz cases. However, these large errors in the estimated state-of-stress fall within the theoretical uncertainty limits defined in Figure 5.17. This highlights the need for calibration when high-frequency elastic waves are utilized for stress measurements, which is the case for current ultrasonic practices.

A close examination of the results presented in Table 5.4 shows that current measurements tend to underestimate the state-of-stress. Such systematic errors in stress estimates suggest that one or more of the material and geometric characteristics fed to the stress measurement algorithm, given by Table 5.1, is not accurately representative of the beam under test. For instance, the material's modulus of elasticity or the beam's thickness can be overestimated. In spite of these systematic errors, the proposed technique performs very well when low-frequency waves are utilized.

5.7   Conclusions

The acoustoelastic theory has been revisited in this chapter. The effects of pre-loading on dispersion relations have been investigated through approximate beam theories and the SAFE method. For structures that can be approximated as simple beams or rods, the Timoshenko beam and Elementary rod theories are found to be adequate to describe the dependence of dispersion relations on longitudinal state-of-stress. Structures with arbitrary cross sections, on the other hand, are studied with the aid of the SAFE method. The formulation for the SAFE method is presented in detail, and the results obtained by both techniques, i.e. approximate theories and the SAFE method, are compared for a circular rod, a rectangular beam, and a rail section. The superior sensitivity of the first anti-symmetric wave mode to the state-of-stress acting on the structure is evident at low-frequency ranges. This suggests that a successful reference-free stress measurement can be achieved by utilizing such low-frequency ranges. However, this requires tackling dispersion and reflections related challenges.

A novel acoustoelastic-optimization-based stress measurement technique has been developed to analyze dispersive waves and calculate the state-of-stress in the structure. The technique is model-based in nature, that utilizes the acoustoelastic theory to propagate the waveform measured at location x_i and compares it to the response measured at x_{i+1}. The state-of-stress is updated accordingly until convergence. The algorithm successfully mitigates the limitations of conventional time-of-flight based measurements and allows the utilization of low-frequency, strongly-dispersive, elastic waves for stress measurements.

Several excitation signals have been investigated in this chapter and a criterion for optimal selection of excitation waveforms has been developed. This criterion takes into consideration the sensitivity to the state-of-stress, the robustness against material and geometric uncertainties, and the ability to obtain a reflection-free response at desired measurement locations. It is found that a two-cycle, amplitude modulated, sine wave tone burst is the optimal excitation waveform for the problem at hand. The center frequency of the waveform is determined based on the physical dimensions of the structure under test.

A thorough sensitivity analysis has been conducted to evaluate the effects of material and geometry related uncertainties on the estimated state-of-stress. Five parameters have been investigated in this study including material's modulus of elasticity, material's density, structure's width and thickness, and measurement locations. Statistical distributions for each of the aforementioned parameters have been determined based on variations in material characteristics for different aluminum alloys, variations in beams

dimensions as specified by manufacturers, and the resolution of the location measurement device used in this work.

Sensitivity functions relating the error in stress estimates to the uncertainty in each of the aforementioned parameters have been determined as a function of frequency. The effects of multiple sources of uncertainties have also been quantified using standard error propagation techniques. Among the different parameters investigated in this work, uncertainty in beam's thickness is found to have the most profound impact on the measured state-of-stress. These effects are strongly dependent on the frequency content of the propagating waves, where robustness enhances at lower frequency ranges. This gained robustness comes at the cost of increased separation requirements between measurement locations and structure's boundaries in order to obtain reflection-free responses.

Experimental validation of the developed stress measurement technique is also presented in this chapter. For this purpose, an aluminum beam has been tested where the state-of-stress is controlled with the aid of a specially designed loading stage. Elastic waves are induced in the structure via a macro-fiber composite piezoelectric transducer, while the response is measured using a three-dimensional Polytech laser vibrometer. Several excitation frequencies and stress levels combinations have been investigated. Experimental results shows that the stress measurement technique developed in this chapter is capable of analyzing dispersive waves to calculate the state-of-stress in the beam under test. Stress states have been calculated based on the nominal material and geometric characteristics of the beam under test. No calibration experiments have been conducted, and a reference state-of-stress has not been utilized in the analyses except for comparison purposes. Accurate stress estimates have been obtained with low-frequency anti-symmetric waves, such as 500 Hz and 1 kHz center frequencies. The accuracy of the estimated state-of-stress is found to rapidly deteriorate as the frequency of the propagating wave increases.

In summary, true reference-free, uncalibrated, acoustoelastic-based stress measurements have been successfully conducted in this work. The developed technique is ideal for in-service structures where calibration experiments cannot be conducted. Furthermore, by utilizing the low-frequency, anti-symmetric waves the sensitivity of this technique is unprecedented in the field of ultrasonic testing.

CHAPTER SIX

STRUCTURAL HEALTH AND LOADING MONITORING OF RAILROAD TRACK COMPONENTS

6.1   Introduction

Accurate and reliable loading condition and structural integrity monitoring solutions are sought for by a wide spectrum of industries. One particular industry that can greatly benefit from such solutions is the railroad industry. Track defects, in the form of mechanical failure of track components or thermally induced buckling of rail sections, are considered as a major safety concern for the railroad industry. According to the office of safety analysis at the federal railroad administration, 1124 derailment incidents have been reported in 2014 with a total damage cost exceeding $184 million. Out of these incidents, 432 occurred as a result of track defects.

Current track inspection techniques rely mainly on ultrasonic measurements, where testing cars equipped with an array of ultrasonic transmitters and receivers are used to scan the track. While such approaches have proven successful in detecting anomalies in rails, they are not suited for testing rail joints and switches. These track components are still manually and visually inspected, which is costly, time-consuming, traffic disturbing, and prone to human error. Furthermore, practical, nondestructive solutions for rail-thermal stresses and neutral temperature measurements are yet to be developed. Impedance-based SHM and acoustoelastic-based stress measurement techniques promise a non-destructive, non-intrusive, cost effective and standalone solutions for the aforementioned challenges. These techniques are capable of

continuously monitoring mechanical defects and thermal loads in railroad track components for prompt detection of track defects, which as a result enhances railroad safety and facilitates rails thermal management.

In this chapter, impedance-based SHM and acoustoelastic-based stress measurement techniques are introduced to the railroad industry. Both in-lab and in-field experiments have been conducted to evaluate the performance of these techniques and demonstrate their capabilities. Several aspects pertaining the practical implementation of these techniques are discussed including damping effects, excitation level, and environmental conditions.

6.2   Impedance-based SHM of Insulated Rail Joints

Insulated rail joints are widely used for signaling purposes. These joints electrically insulate adjacent rail sections while keeping them mechanically connected. With a low voltage electrical signal running through each rail section, the presence of a locomotive on a certain section of the track short-circuits the two opposing rails, and thus, the exact location of the locomotive can be determined. A bolted insulated joint, an example of which is shown in Figure 6.1, consists of two joint bars connecting adjacent rail sections, along with a number of bolts (4 or 6 bolts depending on rail size). All components are electrically insulated and glued together with a high-stiffness adhesive. As a result of the mechanical discontinuity of the rail, insulated joints are normally considered as a weak link in the track where several types of defects can take place. Railroad industry classifies insulated joint related defects into four main categories:

I.   Rail damage: occurs when one or both rail sections attached by the joint are damaged. Most common damage types include horizontal cracking, vertical cracking, and plastic flow of the railhead. This type of damage is mainly induced by cyclic loading due to wheel/rail interaction and wheel impacts with railhead.

II.   Bolts loosening: occurs when one or several bolts reinforcing the joint go loose. This type of damage is mainly induced by the severe vibrations resulting from the successive loading and unloading cycles as locomotives pass by the joint

III.   Joint bar damage: occurs when one or both joint bars connecting the rail sections are damaged. Although this type of damage is relatively uncommon compared to other failure modes, it has a deterministic impact on joint's integrity.

IV.   Insulation failure: occurs when the insulation material degrades resulting in direct contact between joint components. Although this type of damage has a smaller impact on the joint's mechanical integrity, it renders the joint defective for signaling purposes.

The capabilities and limitations of impedance-based SHM have first been investigated in the laboratory with the aid of a representative lab-scale insulated joint. A full-scale insulated joint has then been tested, and the capabilities of the technique are evaluated under real-life operating conditions. The following sections present and discuss the major findings of this study.

6.2.1   Impedance-based SHM of a Lab-scale Insulated Joint

A lab-scale insulated joint is designed and tested to conduct an initial assessment of the performance of impedance-based SHM. The joint is made of two Al 6061 American Standard I-beams, representing rail sections, connected together with two Al 6061 bars and four bolts, as shown in Figure 6.2. Each I-beam is 20 inches long, 3 inches deep, with 2.5-inch flange and 0.35-inch web. Joint bars, on the other hand, are 8 inches long, 1.5 inches wide and 0.375 inch in thickness. A thin layer of rubber, a sixteenth of an inch thick, is inserted between rail sections and joint bars to simulate the effect of the insulation in actual joints.
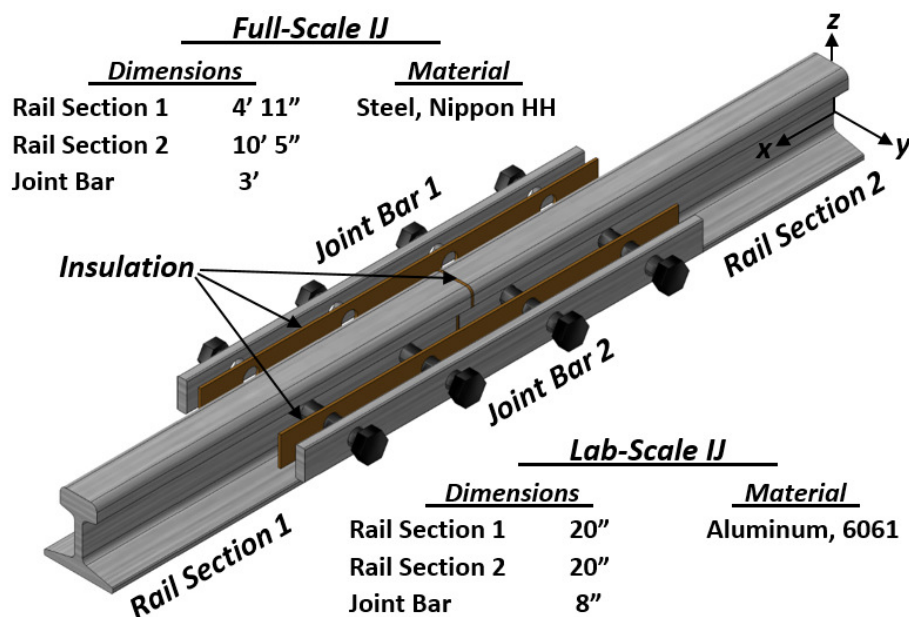
Figure 6.1. Schematic of an insulated rail joint showing main components. Material and geometric specifications for the lab-scale and full-scale insulated joints tested in this work are listed in the figure.
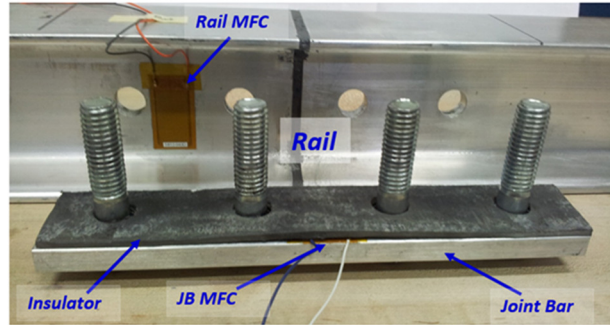
Figure 6.2. Lab-scale insulated joint instrumented with two MFCs attached to the rail and the joint bar.

Several experiments have been conducted with the aid of this lab-scale insulated joint. The main objectives of these experiments can be summarized as follows

1- Evaluate the capabilities of impedance-based SHM in detecting different joint-related damage types.
2- Determine optimal transducers configuration for sensitivity to structural defects.
3- Determine the number of sensors required to detect different damage types.

Except for insulation failure, all types of joint-related defects were introduced to the insulated joint in a reversible manner. This was achieved by altering the torque level of the bolts or by adding mass to the rail and the joint bar. In order to facilitate sensors configuration changes, joint bars and rail sections were not glued to each other in the fully assembled lab-scale insulated joint.

Frequency Range Selection

It has been reported that the frequency range over which the structure is tested has a significant impact on the sensitivity of impedance measurements to structural defects. The optimal frequency range for impedance-based SHM is a function of material and geometric characteristics of the structure being tested, type and severity of the damage to be detected, and the characteristics of the piezoelectric transducers. In general, a frequency range with high mode density (indicated by peaks in the real part of the measured impedance signature) is favorable for SHM purposes (Sun. et al., 1995; Piers et al., 2007). Furthermore, detecting incipient-type damage requires the utilization of high-frequency excitations, as the wavelength of excitation signal need to be smaller than the characteristic length of the damage to be detected (Stokes and Clouds 1993). However, the utilization of high-frequency excitations is adversely affected by the presence of damping, rendering them impractical for highly-damped structures.

In this section, the optimal frequency range for impedance-based SHM of the lab-scale insulated joint is determined based on measurements sensitivity to the damage types of interest. The impedance signature of the pristine structure along with those associated with several damage types are measured over the frequency range of 10-250 kHz, with 10 Hz resolution. Three joint-related damage types are considered in this study; rail damage, joint bar damage, and bolt loosening. The former two damage types are simulated by adding a small mass to the rail and the joint bar, respectively. Bolt loosening damage, on the other hand, is introduced by completely loosening the right most bolt in the joint, referred to as Bolt 1, compared to a 30 Nm torque in the pristine case. Insulation failure has not been investigated in this part, as it is not possible to introduce this damage type in a reversible manner. Figure 6.3 shows the impedance signatures of the three aforementioned defect types compared to the baseline signature. All these signatures are measured using an MFC bonded to the free surface of the joint bar.

In order to determine the most sensitive frequency range for each damage type, the 10-250 kHz frequency range is divided into 10 kHz intervals, and root-mean-square-deviation (RMSD) and correlation coefficient damage metrics, defined in Chapter 4, are calculated for each interval. The results are depicted in Figure 6.4. For the joint bar and bolt loosening damage types, the frequency band from 60 kHz to 70 kHz is found to yield the largest damage metric values, indicating higher sensitivity. Impedance signatures over this frequency band are closely depicted in Figure 6.3. Other frequency bands, such as 90-100 kHz and 120-130 kHz, are also found to be of good sensitivity. While impedance signatures measured at the joint bar are sensitive to joint bar and bolt loosening damage types over certain frequency bands, they are found to perform poorly when rail damage is of concern. Rail damage results in minimal changes in the impedance signature and close-to-zero damage metrics over the entire frequency range, as shown in Figure 6.3.c and 6.4. This indicates that impedance signatures measured at the joint bar are incapable of detecting rail damages. Such insensitivity is attributed to the fact that the rail acts as a boundary structure to the joint bar, therefore small changes in the rail have no impact on the joint bar dynamic response.

To investigate the capabilities of impedance-based SHM to detect rail damages, the previous analysis has been repeated using impedance signatures measured with an MFC bonded to the free surface of the rail web. Impedance signatures of the pristine and damaged scenarios, along with damage metric values are shown in Figure 6.6. The effects of mass added to the rail can be clearly detected with impedance signatures measured at the rail itself. The 20-30 kHz frequency band is found to be the most sensitive to this damage, followed by the 60-70 kHz frequency band.

(a)

(b)

(c)
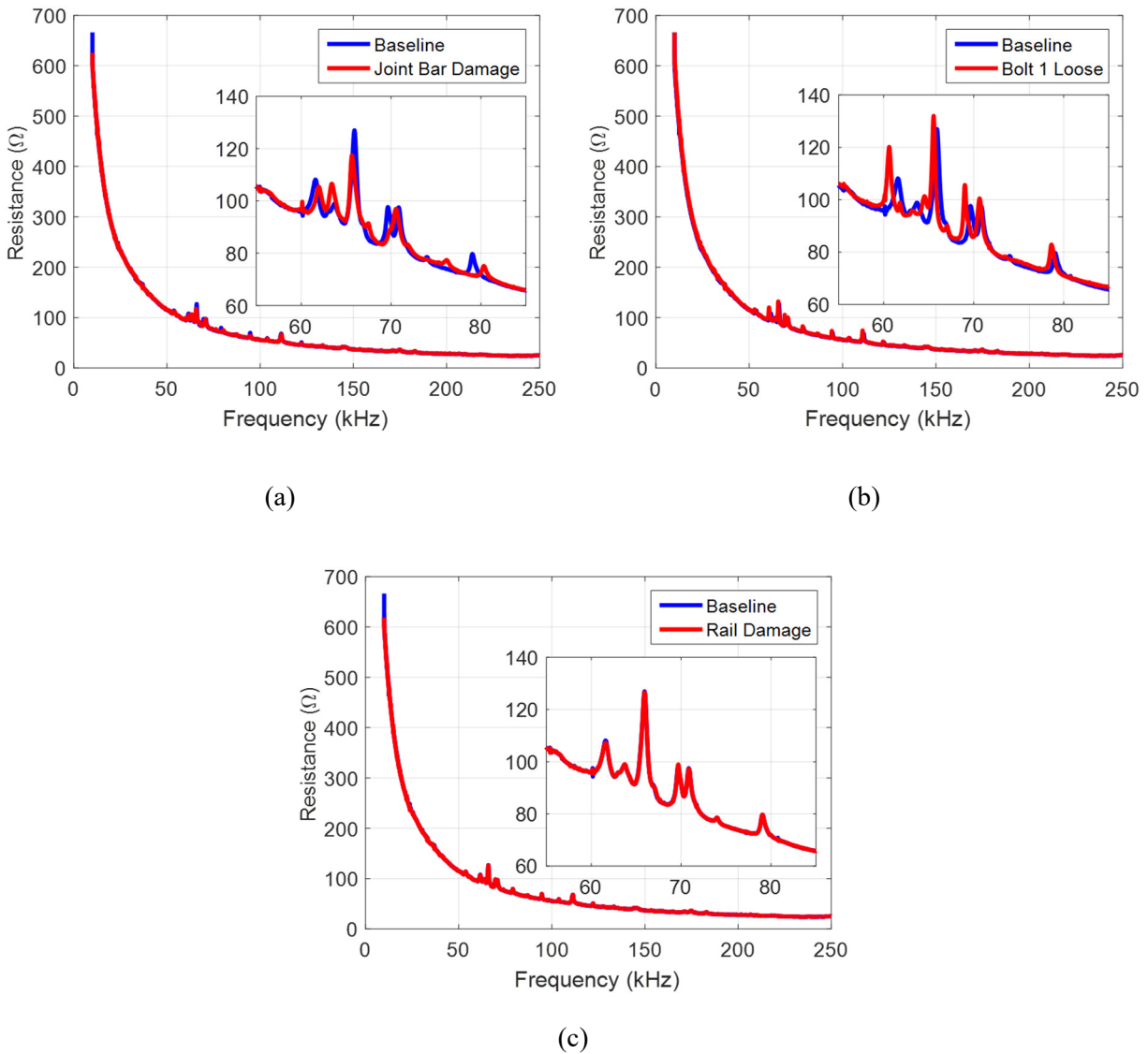
Figure 6.3. Impedance signatures for the damaged insulated joint in comparison to the baseline signature for (a) joint bar damage, (b) bolt loosening damage, and (c) rail damage.

These results suggest that the optimal frequency range for all three types of joint-related damages is 60-70 kHz. This frequency range is utilized for the rest of this study to further evaluate the capabilities of impedance-based SHM and determine optimal transducers configuration for the lab-scale insulated joint.

(a)   (b)
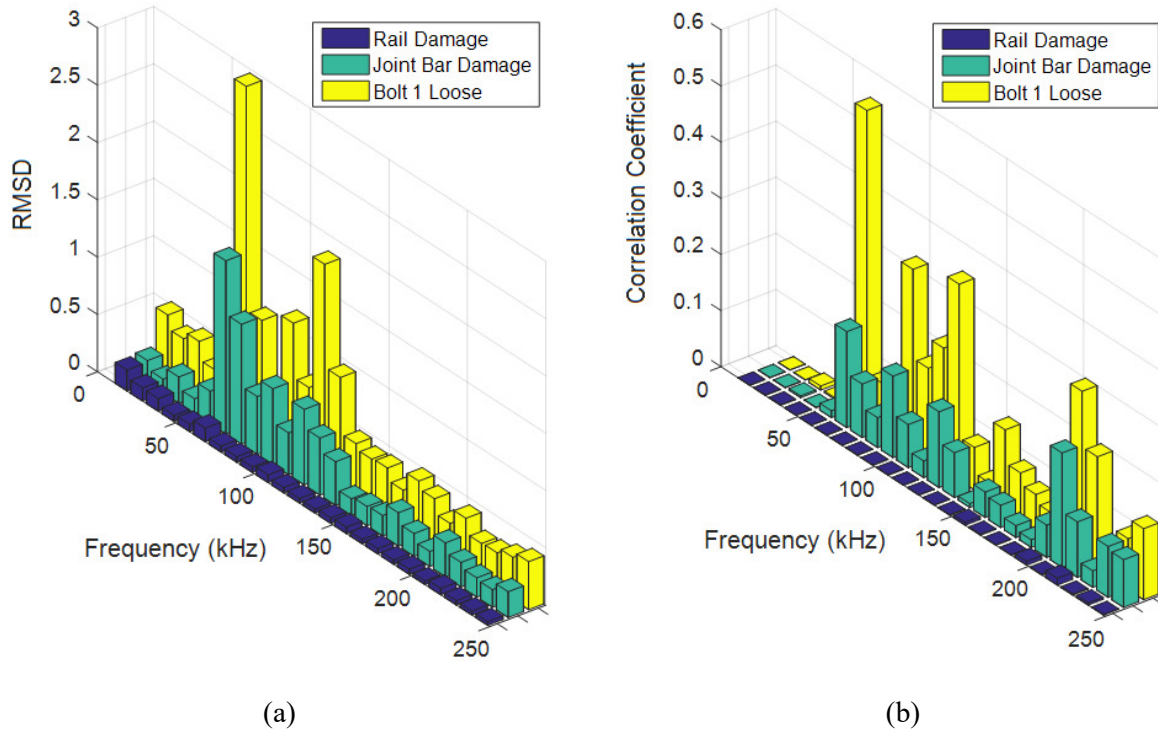
Figure 6.4. Damage metrics calculated for different joint-related damage types using impedance signatures measured at the joint bar, (a) RMSD and (b) correlation coefficient.

(a)   (b)
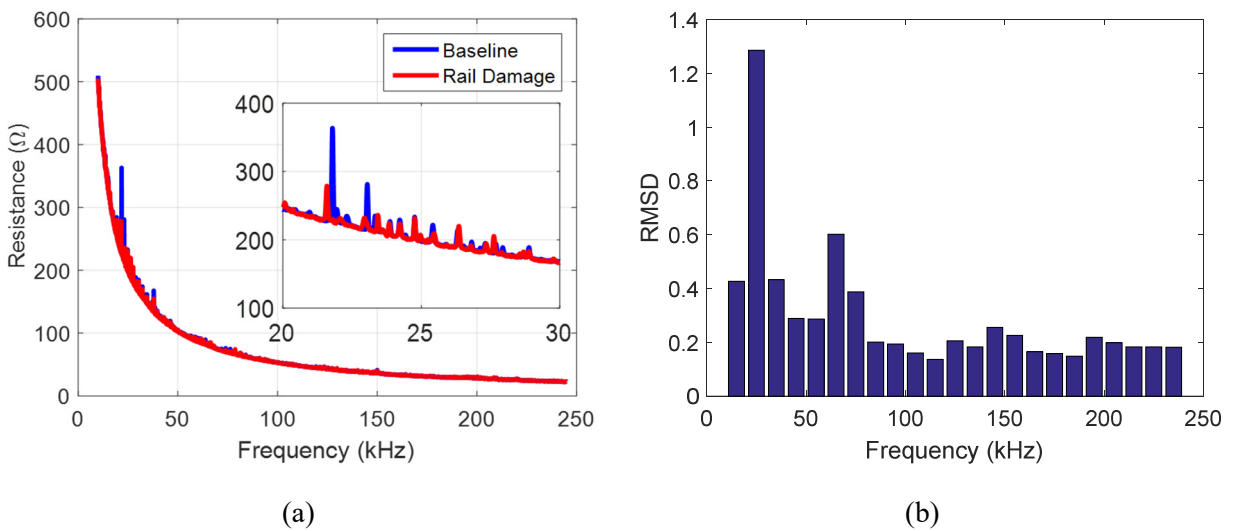
Figure 6.5. (a) Impedance signatures measured at the rail, and (b) damage metrics calculated over 10 kHz frequency bands.

Transducer Configurations for Enhanced Sensitivity

Impedance-based SHM relies on the energy transfer between the piezoelectric transducers, MFCs in the current work, and the structure being tested. These transducers are either bonded to the free surface of the host structure or imbedded within the structure itself. While the former approach is minimally intrusive and facilitates transducers mounting on existing structures, it provides no protection to the piezoelectric transducers. This becomes crucial when the host structure undergoes extreme operational and environmental conditions, as is the case of insulated rail joints.

In this work, four configurations are considered for mounting MFCs on the lab-scale insulated joint, as shown in Figure 6.6. The sensitivity of impedance measurements to different joint-related damage types is evaluated. The conventional mounting approach, shown in Figure 6.6.a, where the MFC is mounted on the free surface of the joint bar, is considered to be the reference case to which all other mounting configurations are compared. The results for this MFC mounting configuration are shown in Figure 6.3. Comparable results have been obtained by bonding the MFC to the inner surface of the joint bar, the mounting configuration shown in Figure 6.6.b. Besides having a comparable sensitivity to the joint bar and bolt loosening damage types, this configuration provides protection for the MFC transducer.
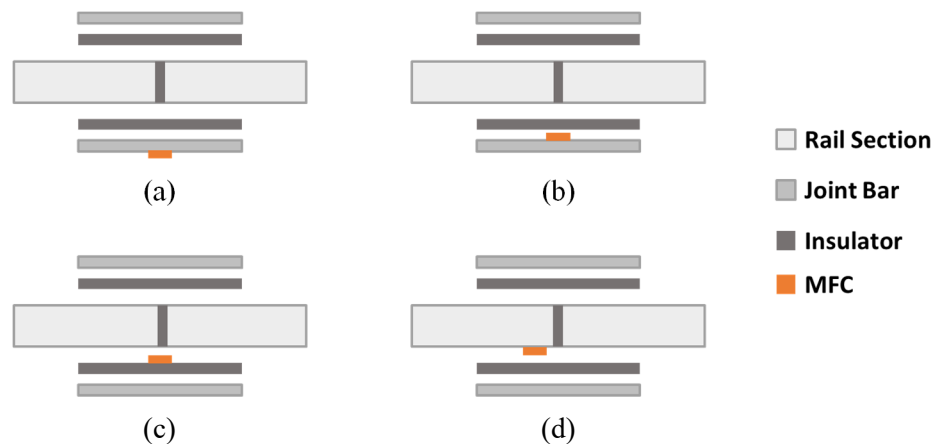
Figure 6.6. MFC mounting configurations for impedance-based SHM of insulated rail joints, (a) on the outer surface of the joint bar, (b) on the inner surface of the joint bar, (c) on the joint bar insulation, and (d) on the rail web.

For an MFC bonded to the insulation layer, the configuration shown in Figure 6.6.c, the dynamic response of the host structure is not reflected on the measured electromechanical impedance, and the impedance signature is mostly dominated by the electrical characteristics of the MFC transducer. This can be ascribed to the low stiffness and high damping of the insulation layer, which impede energy transfer between the MFC transducer and the host structure. This is similar to the behavior observed in Chapter 3 with an extremely thick and soft bonding layer. Therefore, this configuration is not suitable for SHM applications and will not be used in this work.

The fourth configuration considered in this analysis is shown in Figure 6.6.d, where the MFC is attached to the rail. As discussed in the previous section, this configuration is found to be sensitive to rail defects, as shown in Figure 6.5. Furthermore, it provides protection for the transducer against extreme operational and environmental conditions. Therefore, this configuration complements that of Figure 6.6.b, and both are utilized in this work for in-lab and in-field SHM experiments.

Joint Bar Damage

The previous analysis showed that for the detection of joint bar damages, the optimal frequency range is 60-70 kHz, and an MFC attached to the inner surface of the joint bar provides the desired balance between sensitivity and transducer's survivability. This frequency range and transducer configuration are adopted in this section to further investigate the sensitivity of impedance-based SHM to this type of damage.

Joint bar damage is simulated by a small mass attached to the bar at different locations, as shown in Figure 6.7. The added mass is approximately 4% of the total mass of the lab-scale joint bar. Five pristine-state impedance signatures are measured during the experiment, every time the mass is removed, and the baseline is calculated as the average of these five measurements. The impedance signatures, along with the RMSD and correlation coefficient damage metrics for the pristine and damaged cases are shown in Figure 6.8. Small variations among impedance signatures measured for the pristine states have been observed. These variations can be ascribed to noise contamination and minor disturbances to the structure as the mass being added and removed. Damage metrics for the pristine cases are used to define the acceptable threshold beyond which the structure is classified as damaged.
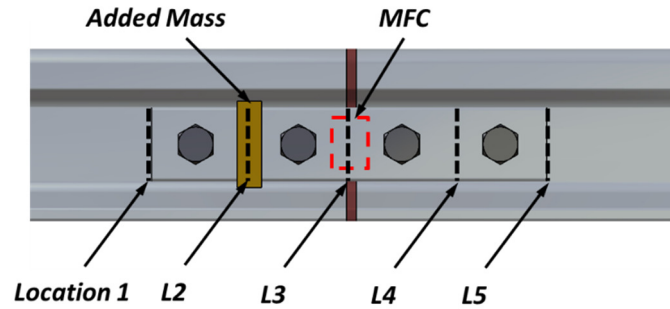
Figure 6.7. Schematic for the joint bar damage experiment. Damage locations are 2 in. apart.

The symmetry in the impedance signatures, and their corresponding damage metrics, is evident when comparing the cases where the mass is added at locations 1 and 5, and locations 2 and 4. This is a direct result of the symmetry in the structure and damage locations with respect to the MFC location, as suggested by Figure 6.7. It is also noticed that adding the mass right at the edge of the structure results in a minimal change in its response, as is the case for damage locations 1 and 5.

Bolt Loosening

In order to evaluate the capabilities of impedance-based SHM to detect bolt-loosening damage type, the sensitivity of impedance measurements to torque level change in the bolted joint is investigated in this section. As is the case for joint bar damage, all impedance signatures presented in this section are measured by the MFC attached to the inner surface of the joint bar over the frequency range of 60-70 kHz. The pristine state of the structure is considered to be when all 4 bolts are torqued to the 30 Nm. Figure 6.9 shows the lab-scale insulated joint with the 4 bolts, and the location of the MFC used for impedance measurements.

(a)

(b)
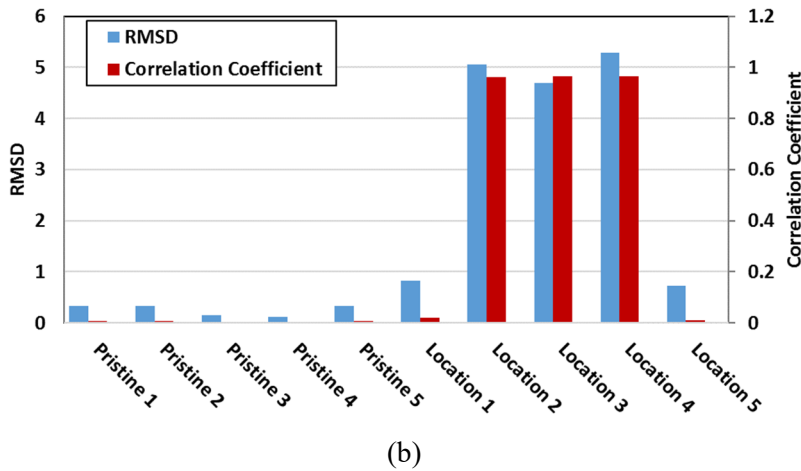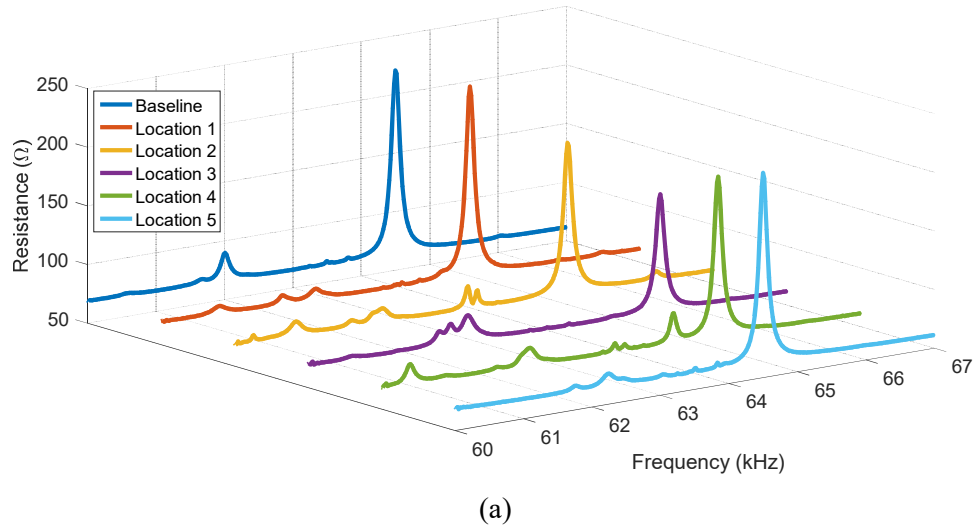
Figure 6.8. Joint bar damage at several locations, (a) impedance signatures, and (b) damage metrics.

Torque level is changed in one bolt at a time. The real parts of the impedance signatures measured for the pristine state and when one of the four bolts is completely loose are shown in Figure 6.10. The baseline signature is calculated as the average of the four pristine state signatures measured after resetting the torque to its original value. The figure shows that a complete loss of the torque in any one of the four bolts results in significant changes in the measured impedance signature. Such changes are in the form of peaks shifts and emergence of new impedance peaks. Due to the symmetry in the structure and bolts location with respect to the impedance measurement location, the effects of torque loss in Bolts 1 and 2, are similar to those in bolts 3 and 4, as shown in Figure 6.10.
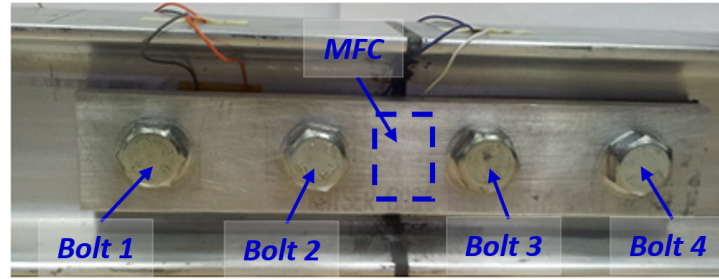
Figure 6.9. Front view of the lab-scale insulated joint showing the four bolts and the location of the MFC transducer attached to the inner surface of the joint bar.

To assess the sensitivity of impedance-based SHM to the loss of torque in the bolted joint, the torque level in Bolt 1 is gradually decreased from the pristine state to the completely loose state in 10% steps. The real part of impedance signatures for theses cases are shown in Figure 6.11.a, whereas the corresponding damage metrics are shown in Figure 6.11.b. The gradual change in the impedance signature as the torque level in Bolt 1 decreases is evident in the figure. This gradual change is reflected on damage metric values which are found to increase with torque level reduction. It is also noticed that impedance peaks shift to the left as the torque level decreases. This indicates softening in the structure, which is a typical result of torque loss in bolted joints.
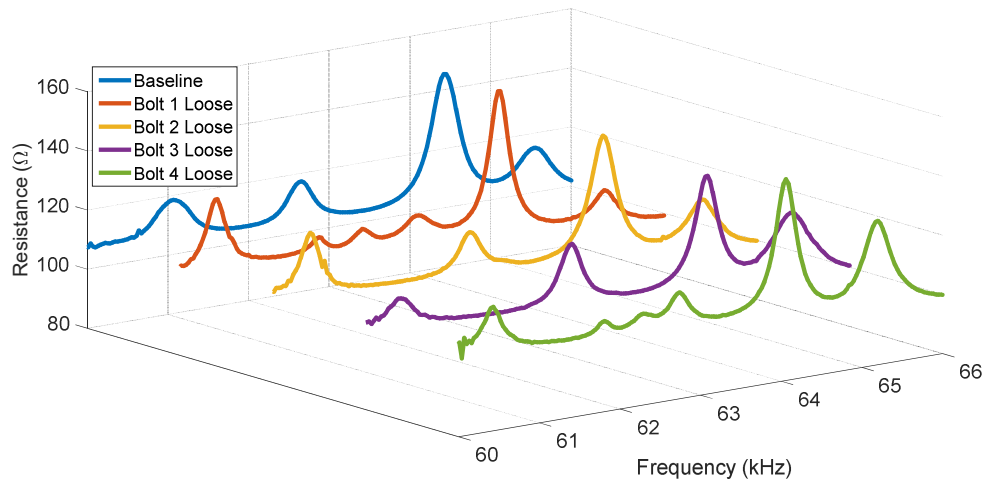
Figure 6.10. Impedance signatures for the pristine state, along with the states where a single bolt is completely loose.
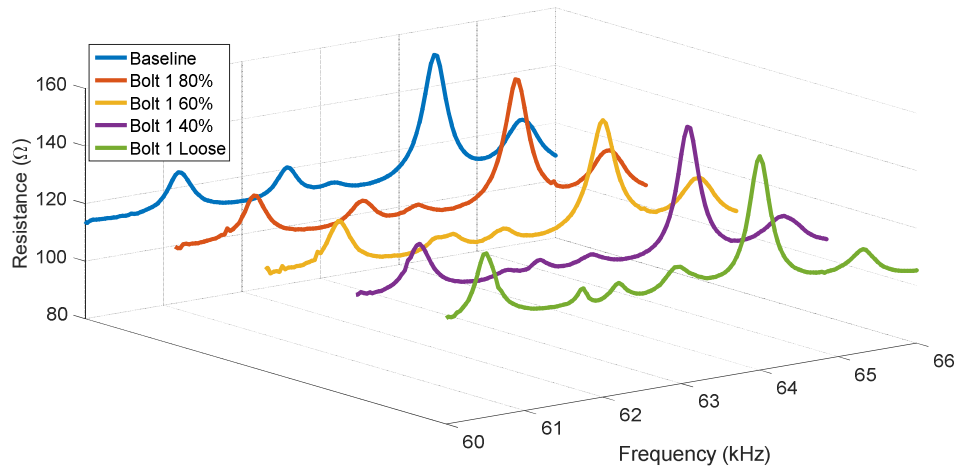
(a)
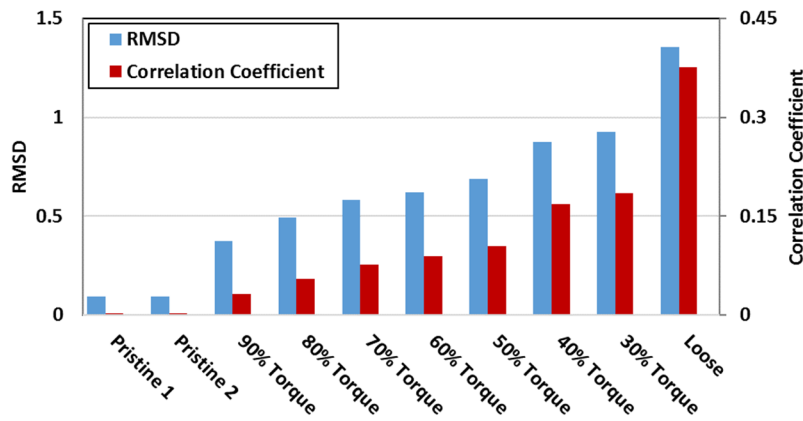
(b)

Figure 6.11. Varying torque levels in Bolt 1, (a) impedance signatures, and (b) damage metrics.

In spite of the clear progressive trend in damage metrics as the torque level in Bolt 1 decreases, the utilization of such metrics for more than damage detection is not feasible. This can be ascribed to the fact that different damage types can result in the same damage metrics values. Damage characterization requires analyzing the measured impedance signatures with the aid of numerical models or machine learning techniques. While model-based damage characterization techniques are applicable to simple structures, as discussed in Chapter 4 of this work, computationally efficient numerical simulations of the high-frequency dynamic response of complex structures remain a challenge. Machine learning techniques, on the other hand, require building an extensive database for different combinations of damage types, locations, and severity, which can be tedious in many cases. Further investigation of damage characterization techniques for insulated joints will be the focus of future studies.

Rail Damage

As discussed in the previous sections, impedance signatures measured at the joint bar are insensitive to rail damages. Therefore, an MFC attached to the rail's web, as shown in Figure 6.2, is used to detect defects in rail sections. Rail damage is simulated by a small mass attached to the railhead. The added mass is approximately 35 grams, equivalent to a $< 1\%$ change in the overall mass of the rail. The mass is added to the rail at five different locations, 4 in. apart from each other, as shown in Figure 6.12. Impedance signature is measured over the 60-70 kHz frequency range, which is found in the *Frequency Range Selection* section to be the second most sensitive range for rail damage. Figure 6.13 shows the real part of the impedance signatures, for the 63-66 kHz frequency range along with the corresponding damage metrics for the pristine state and the damaged ones.
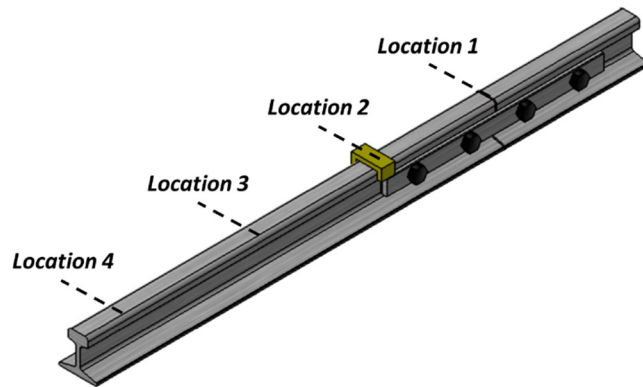
Figure 6.12. Schematic of the insulated joint with an added mass to simulate rail damage. Four out of the five damage locations considered in this study are shown in the figure.

(a)

(b)
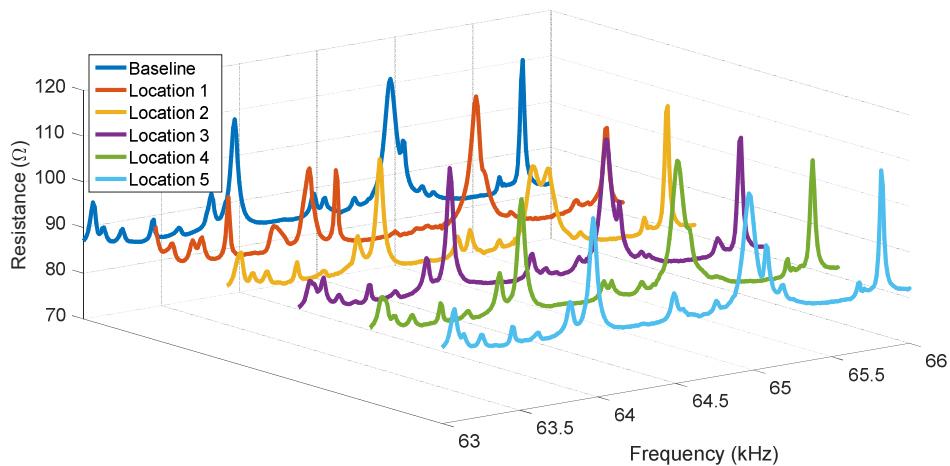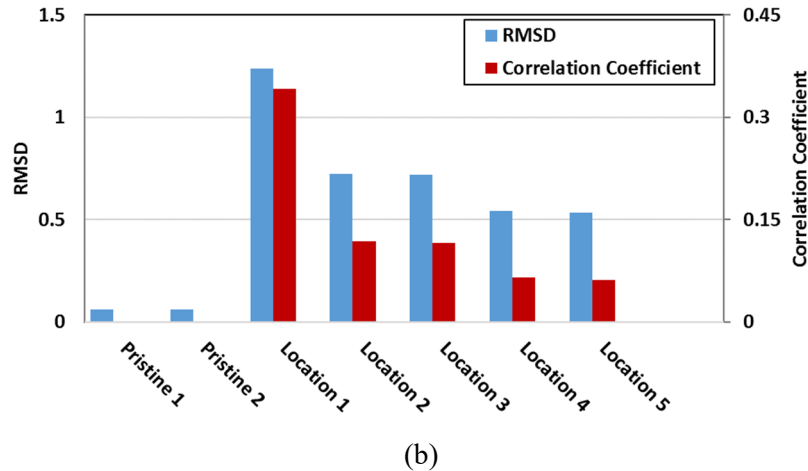
Figure 6.13. Rail damage at several locations, (a) impedance signatures, and (b) damage metrics.

It could be noticed that impedance measurements at the rail's web are capable of detecting the effects of a small mass added to the railhead. Rail damage at all five locations considered in this study has been successfully detected with a single MFC located at the rail's edge. Damage metrics indicate the presence of the added mass, however, there is no clear relation between damage locations and damage metric values.

Insulation Failure

The fourth joint-related damage type investigated in this work is insulation failure. Although this damage type is more of a concern for the signaling functionality of the insulated joint, it does affect the mechanical integrity of the joint as well. To investigate the impact of this damage type on impedance measurements, a simple bolted-glued joint is designed, as shown in Figure 6.14.a. The joint consists of two Aluminum beams of the same dimensions as the joint bars described earlier in this section. The two bars are attached together by means of high strength epoxy along with 4 bolts torqued to 30 Nm. An MFC is attached to the inner surface of one beam, and the signature is measured over the same frequency range utilized for other damage types.
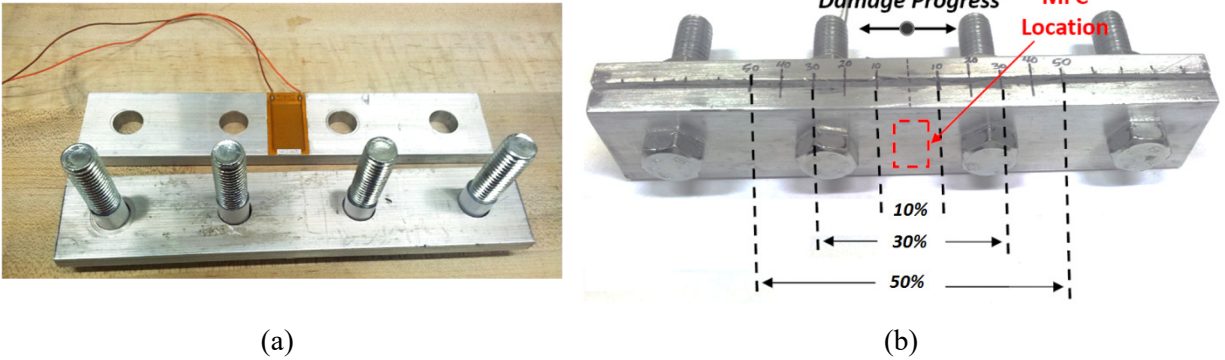
Figure 6.14. A bolted-glued joint used for insulation failure experiments, (a) joint components showing the MFC attached to the inner surface of one beam, and (b) the assembled joint with several levels of insulation damage.

Insulation damage is introduced to the joint by cutting through the epoxy with a thin wire embedded in the joint. Damage is gradually introduced to the pristine state with 10% increments, as shown in Figure 6.14.b. Impedance signatures are measured at each damage level, the results are summarized in Figure 6.15. In this experiment, the damage introduced to the structure is irreversible, thus, a single baseline is measured at the beginning for the pristine state. For all damage levels, the calculated damage metrics were large enough to indicate that the structure is defective. Damage metrics associated with the 40% failure level are found to be smaller than the other less severe scenarios. This highlights the fact that abstract damage metrics, such as root mean square deviation and correlation coefficient can only serve damage detection purposes, and shall not be relied on for characterization purposes.

It should be pointed out that the approach adopted here to introduce insulation failure is more intrusive than the actual mechanisms causing this type of damage. In the field, several factors cause such failure including epoxy aging, loading cycles along with environmental factors. Testing such factors in the lab is beyond the scope of this work, and insulation failure is simply introduced by cutting through the epoxy. Therefore, the observed changes in impedance measurements are expected to be exaggerated, which needs to be taken into consideration when this technique is implemented in the field.
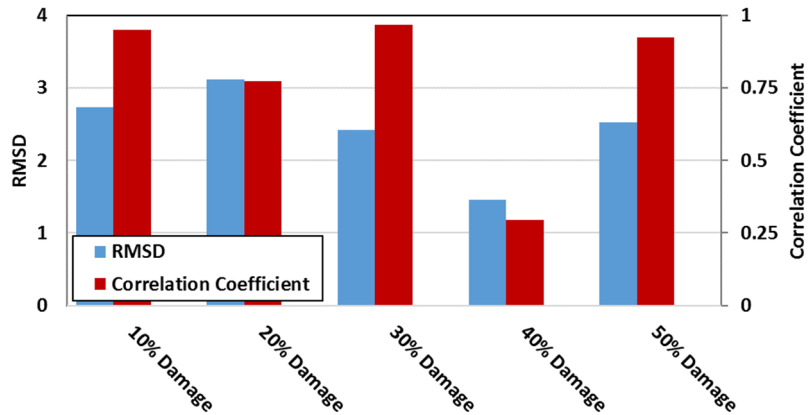
Figure 6.15. Damage metrics for gradually increasing insulation failure.

6.2.2   Impedance-based SHM of a Full-scale Insulated Joint

Motivated by the success of impedance-based SHM in detecting several joint-related damage types with the lab-scale insulated joint, and guided by the findings presented in the previous section, the study is further extended to assess the performance of this SHM technique with a full-scale insulated joint. For this purpose, a 4.5-feet-long 136 A.R.E.A. rail section, shown in Figure 6.16.a, along with compatible Koppers insulated joint kits, Figure 6.16.b, have been thoroughly tested. The insulated joint kit consists of two joint bars, 3 feet long, with an insulating mesh pre-attached to their inner surfaces. The insulated joint bars are attached to the rail with six bolts and ES39-6 industrial grade epoxy. The kit also includes plastic inserts for the insulation of rail sections and bolts.

Frequency Range Selection

As discussed in the previous section, the frequency range over which the structure is interrogated significantly affects the sensitivity of impedance measurements to structural defects. The optimal frequency range for impedance-based SHM is a function of, among other factors, material and geometric characteristics of the structure being tested. Therefore, the previous findings for the lab-scale insulated joint are not transferable to the full-scale one, and the analysis presented in the previous section needs to be repeated.
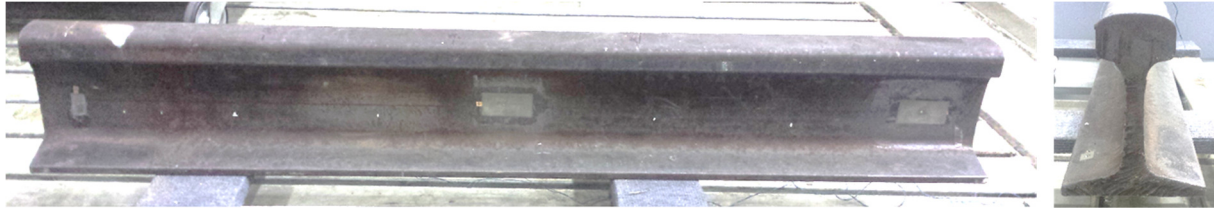
(a)

(b)

Figure 6.16. Full-scale track components, (a) 136 A.R.E.A. rail section, and (b) Koppers insulated joint kit.

For this purpose, the impedance signature of the pristine components along with those associated with several damage types are measured over the frequency range of 10-100 kHz, with 10 Hz resolution. For frequencies higher than 100 kHz, very low modal density has been observed in the signatures of the full-scale components as indicated by the absence of impedance peaks. This can be ascribed to the higher characteristic damping of the full-scale components compared to the lab-scale ones. Therefore, the analysis presented in this section is limited to 100 kHz, and no attempt is made to evaluate the performance of the SHM technique at higher frequencies.

Two types of piezoelectric transducers are utilized to instrument the full-scale joint, these are MFCs and monolithic piezoelectric discs. Rail sections are instrumented with M2814-P1 and M8557-P1 MFCs, which operate in the 33-mode with an active area of 28×14 mm^2 and 85×57 mm^2, respectively. Joint bars, on the other hand, are instrumented with M2814-P1 and M4010-P1 MFCs. Monolithic PZT5 piezoelectric discs, 10 mm in diameter and 1 mm in thickness, are used to instrument a subset of the joint's bolts. Piezoelectric discs are attached directly to the bolt's head. Figure 6.17 shows the impedance signatures for the

aforementioned types and sizes of piezoelectric transducers in their free configuration. As shown in the figure, a number of impedance peaks are observed in the free impedance signature of the piezoelectric transducer. The frequency range where these peaks appear depends on transducer's size and material. In general, longer MFCs have their fundamental impedance peaks at lower frequency ranges compared to shorter transducers of the same material, which agrees with findings of monolithic piezoelectric transducer numerical models discussed in Chapter 3.
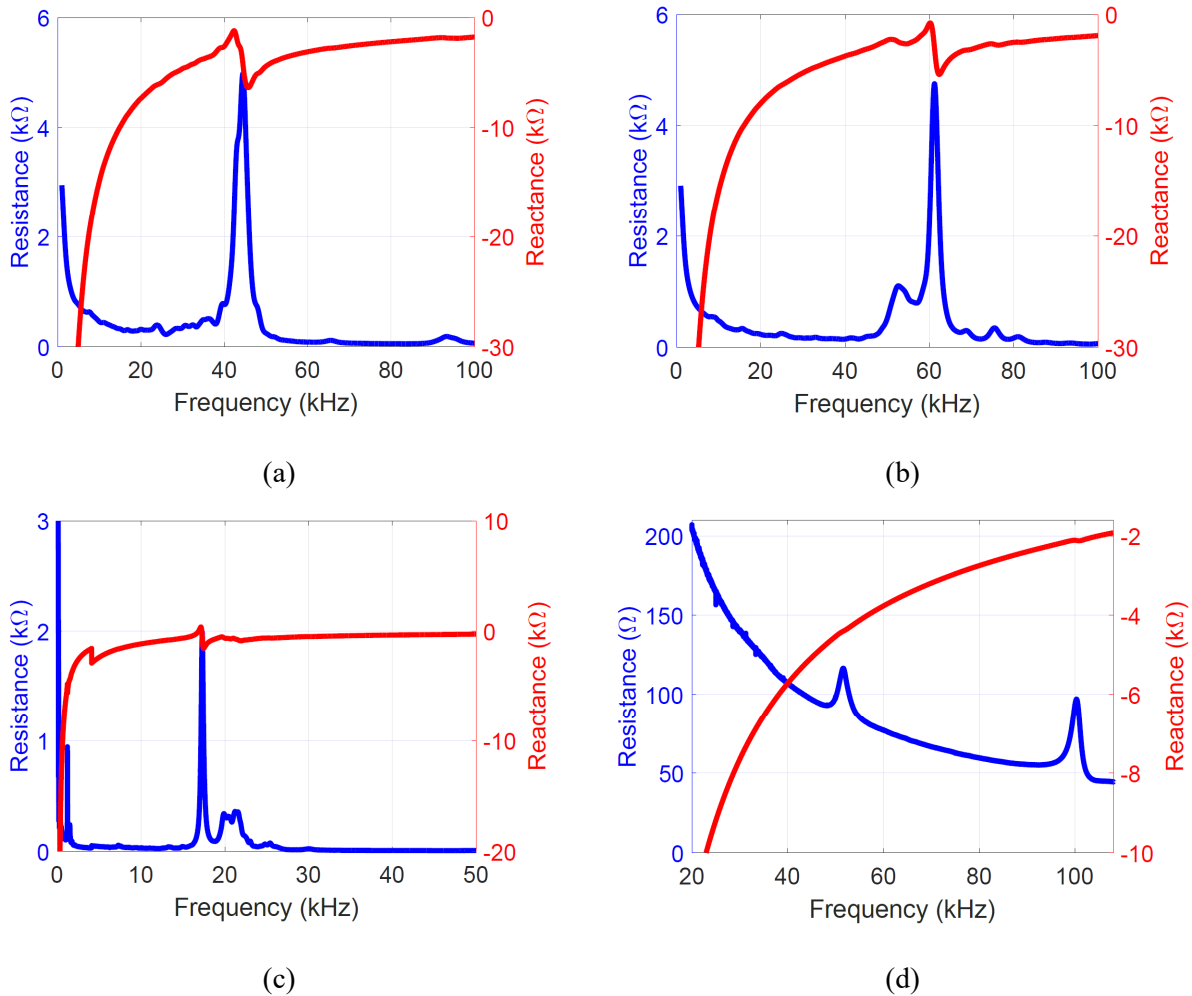
Figure 6.17. Impedance signatures for the free piezoelectric transducers used to instrument the full-scale insulated joint, (a) M4010-P1 MFC, (b) M2814-P1 MFC, (c) M8557-P1 MFC, and (d) 10-*mm*-diameter, 1-*mm*-thick PZT5 disk.

Three joint-related damage types have been investigated for the full-scale insulated joint; rail damage, joint bar damage, and bolt loosening. Unassembled components are first instrumented and individually tested in the lab, where damage is introduced to each component in a reversible manner. Joint bar and rail damage types are simulated by mass addition, whereas bolt loosening damage is introduced by altering the torque level applied to the instrumented bolts. In order to evaluate the sensitivity of impedance measurements to each damage type, the impedance signatures of the pristine components and damaged ones are measured over the frequency range of 10-100 kHz. This frequency range is then divided into 5 kHz intervals, and damage metrics are calculated for each interval.

(a)

(b)

(c)
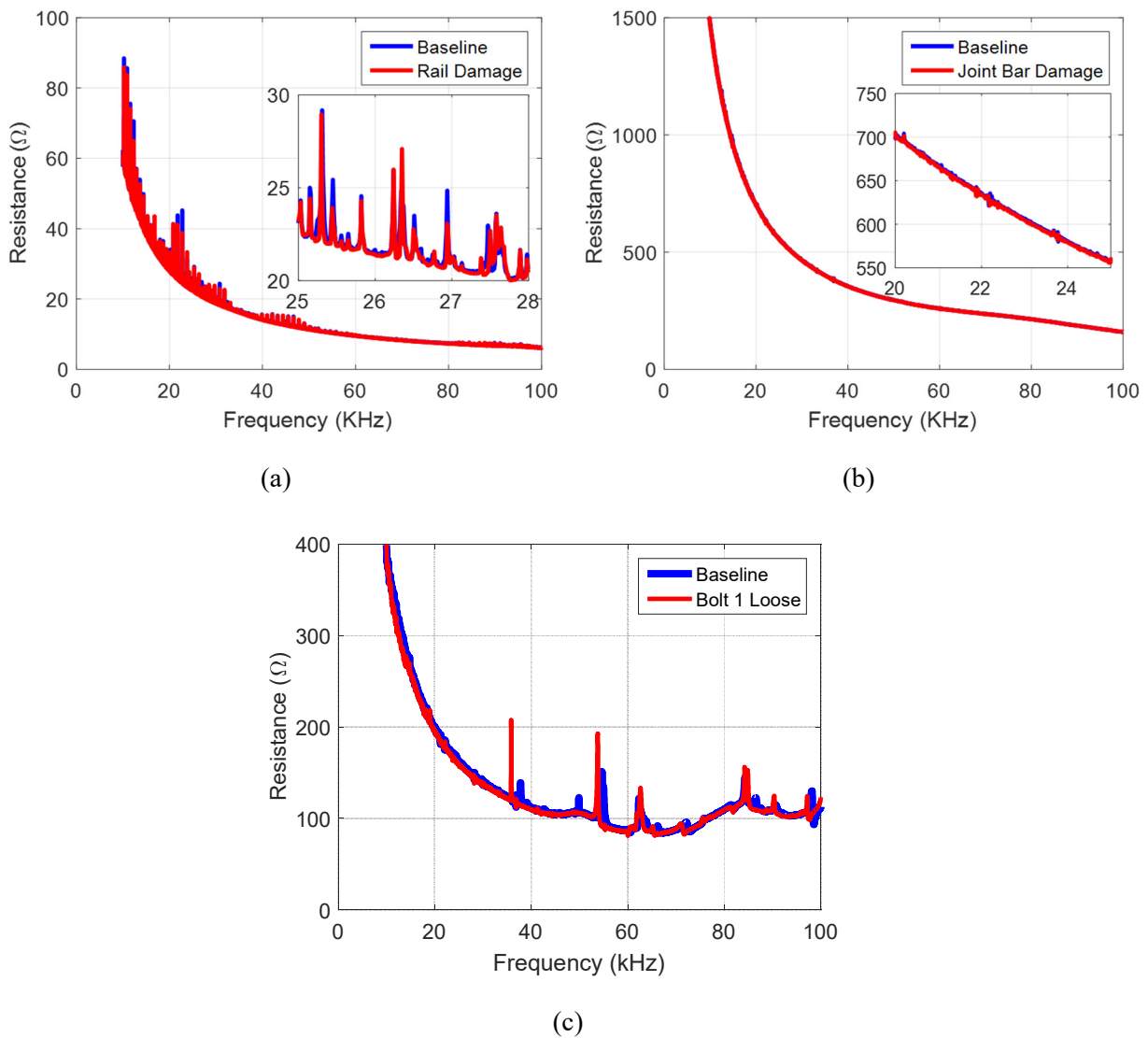
Figure 6.18. Impedance signatures for the damaged components as compared to baseline signatures for (a) rail damage, (b) joint bar damage, and (c) torque loss.

Figures 6.18 shows the real part of the impedance signatures for the rail, the joint bar and a bolt in their pristine and damaged states. The corresponding damage metrics are shown in Figure 6.19. The results suggest that rail impedance signatures are highly sensitive to railhead damage over the frequency range of 20-30 kHz. On the other hand, several frequency ranges are found to be sensitive to torque loss damage type. The frequency range of 50-55 kHz yields the largest RMSD value, whereas the frequency range of 65-75 kHz yields the largest correlation coefficient value. Finally, joint bar damage has not been successfully detected with standard impedance measurements, and high-voltage impedance measurements need to be implemented to detect this damage type.

(a)

(b)

(c)
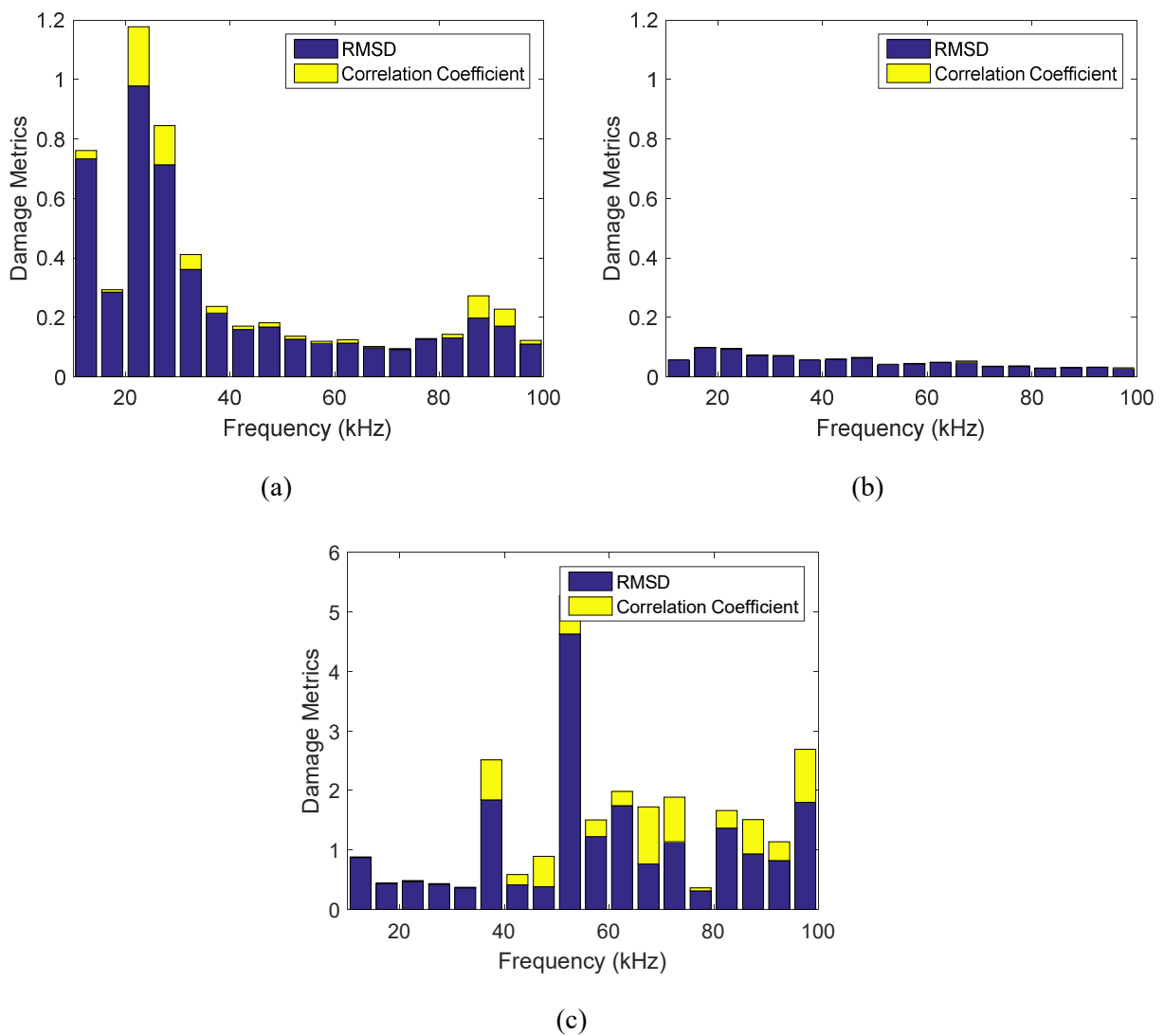
Figure 6.19. Damage metrics calculated for different joint-related damage types using impedance signatures measured at individual components. a) Rail damage, (b) joint bar damage, and (c) torque loss.

High voltage impedance measurements

Standard impedance measurements conducted with commercial impedance analyzers excite the piezoelectric transducers with a maximum of 1-volt peak-to-peak sinusoidal voltage signal. While this level of excitation is sufficient for lightly-damped structures, larger levels of excitation are required to reach the steady-state response for highly-damped structures. Therefore, and in order to facilitate damage detection for joint bars, a high-voltage impedance analyzer has been designed and implemented. For this analyzer, the voltage signal is generated by a National instruments, PXI-6115 card and then amplified by an HP bipolar 6825A amplifier. The amplified signal is applied to an electrical circuit consisting of an MFC, which is bonded to the host structure, and a variable resistor connected in series. The experimental setup is depicted in Figure 6.20. As a voltage signal of known amplitude is applied to the electric circuit, the current in the circuit is the only unknown in the system. The current is dependent on the electrical impedance of the circuit, which is a function of the combined electrical and mechanical impedances of the MFC and the host structure. By measuring the potential drop across the in-series resistor, the current value is calculated. The impedance response is then obtained by computing the transfer function between the input signal, V_{in}, and the voltage drop across the resistor, V_R, as follows

$$Z_{EM} = \frac{V_{Excitation}}{I} = \frac{G.V_{in} - V_R}{V_R/R} = R.G.\left(\frac{V_{in}}{V_R}\right) - R \tag{6.1}$$

where Z_{EM} is the electromechanical impedance of the combined MFC and the host structure, $V_{Excitation}$, V_R and V_{in} are the voltages across the MFC, the in-series resistor and the signal produced by the signal generator, respectively. The terms R and G are respectively the in-series resistance and the gain of the amplifier.
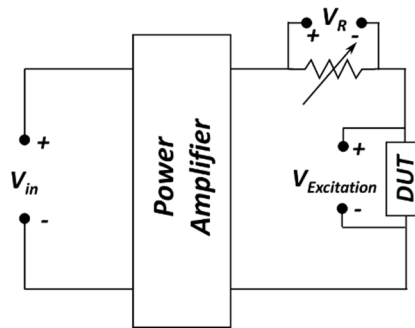
Figure 6.20. High voltage impedance measurement system.

The transfer function measured in this experiment, (V_{in}/V_R), is related to the electro-mechanical impedance of the system through the constants R and G, as shown in Eq. 6.1. Thus, this transfer function is just a scaled version of Z_{EM}, and contains the same information about the structure being tested.

Rail Damage

The sensitivity of impedance-based SHM to rail damage location is investigated in this section. For this purpose, impedance measurements over the frequency range of 20-30 kHz, which was found in the previous section to be the most sensitive range for rail damage, are conducted. Rail damage is introduced by adding a small clamp to the railhead. The added mass is ~0.8% of the total mass of the rail section. The mass is added to the rail at 5 different locations, 10 in. apart from each other, as shown in Figure 6.21. Impedance signature is measured for each case and compared to the pristine state. Figure 6.22 shows the real part of the impedance signatures, for the 20-25 kHz frequency band, along with the corresponding damage metrics.

As is the case with the lab-scale insulated joint, impedance measurements at the rail's web are capable of detecting the effects of a small mass added to the railhead. Rail damage at all five locations considered in this study has been successfully detected with a single MFC located at the rail's edge. Damage metrics indicate the presence of the added mass, with no clear trend between damage location and damage metric values.
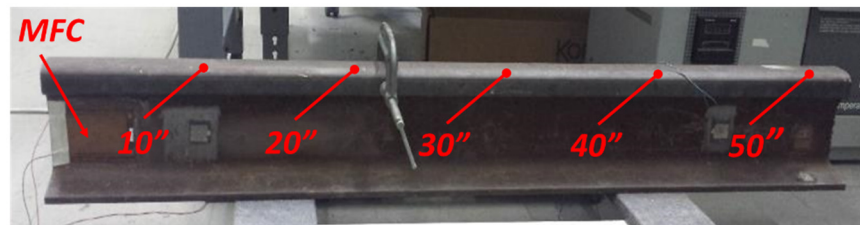
Figure 6.21. 136 AREA rail section with a clamp attached to simulate railhead damage. The figure shows the five damage locations considered in this study.

(a)

(b)
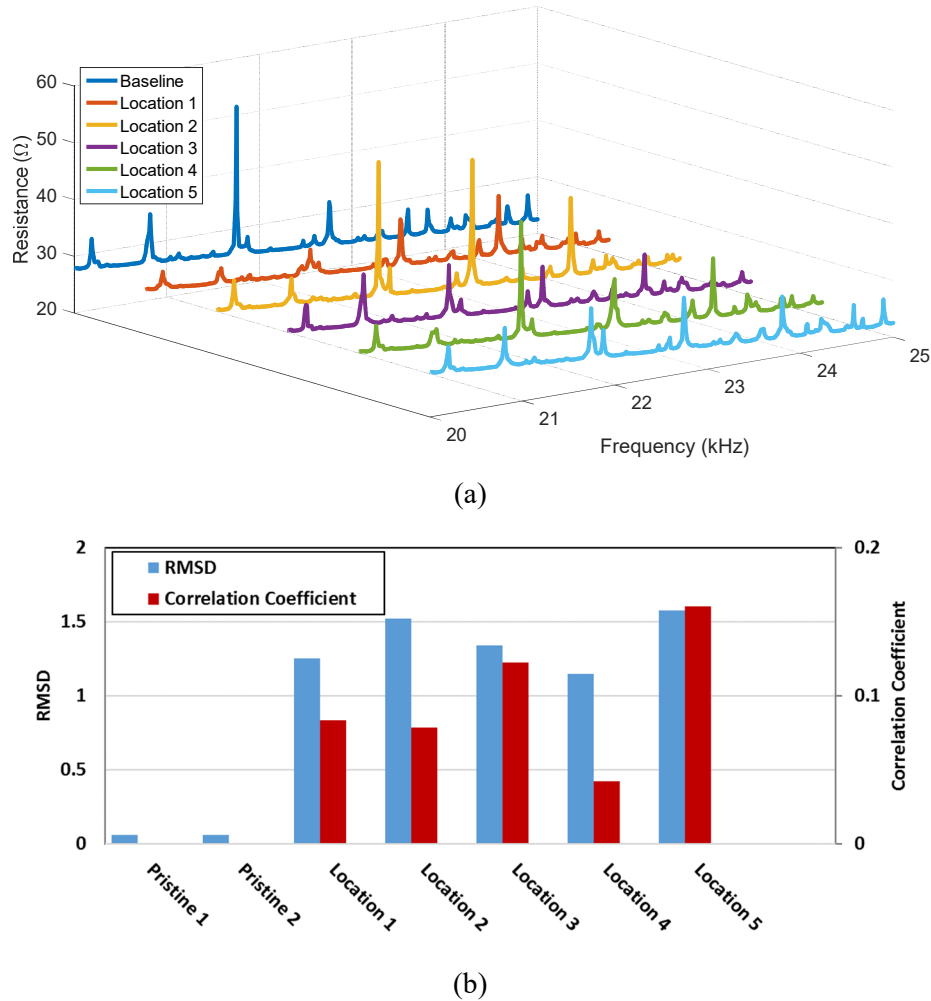
Figure 6.22. Railhead damage at different locations. (a) Impedance signatures, and (b) damage metrics.

Bolt Loosening and Sensors Protection

The sensitivity of impedance-based SHM to torque loss in the full-scale joint is investigated in this section. The most torque-sensitive configuration has been considered in this study where individual bolts are instrumented with piezoelectric discs, as shown in Figure 6.23.a. Therefore, torque loss effects on the dynamic response of the bolts themselves are measured rather than relying on the dynamic response of the joint bar as was the case with the lab-scale joint. This promises more sensitivity to torque changes and simplifies the effort of damage characterization, however, it comes at the cost of increasing the number of transducers required to monitor the system. In order for the transducers to survive the harsh railroad environment, protective coating is necessary. In this work, ES39-6 industrial grade epoxy is used as a

protective layer, as shown in Figure 6.23.b. This has been selected as it is the same epoxy type used for insulated joints, thus it is expected to survive the railroad operating and environmental conditions. In order to evaluate the effect of protective coating on the sensitivity of impedance measurements to torque variations, the response of a coated bolt is compared to that of an uncoated one, the results are summarized in Figure 6.24.

Based on the findings of *Frequency Range Selection* study, the impedance signature of the instrumented bolts is measured over the frequency range of 50-100 kHz, a subrange of which is shown in Figure 6.24. The torque level on the bolts is reduced gradually from the pristine state, 75 ft.lb, to the completely loose state. The effect of torque loss is clearly reflected on the measured impedance signatures, where impedance peaks are found to shift to lower frequency ranges as torque level is decreased. This trend is observed with both the protected and unprotected cases. The presence of the protective layer is found to add more damping to the system, which appears as amplitude reduction of impedance peaks. However, the sensitivity to torque loss has not been affected by the protective layer, as suggseted by impedance signatures and their corresponding damage metrics. Therefore, this coating is used for in-filed testing to protect all piezoelectric transducers attached to the free surfaces of the rail, the joint bars, and the bolts.

(a)   (b)
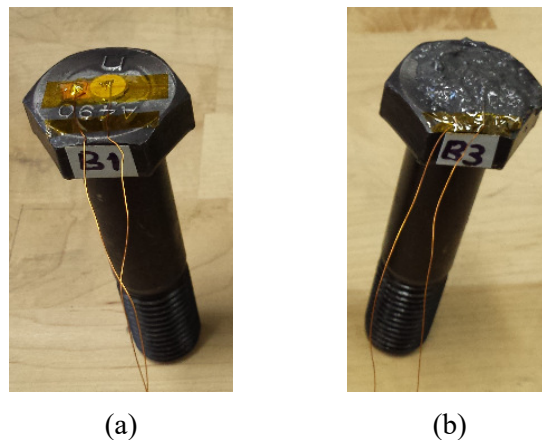
Figure 6.23. Piezoelectric instrumented bolts with (a) no protective coating, and (b) ES39-6 epoxy protective coating.
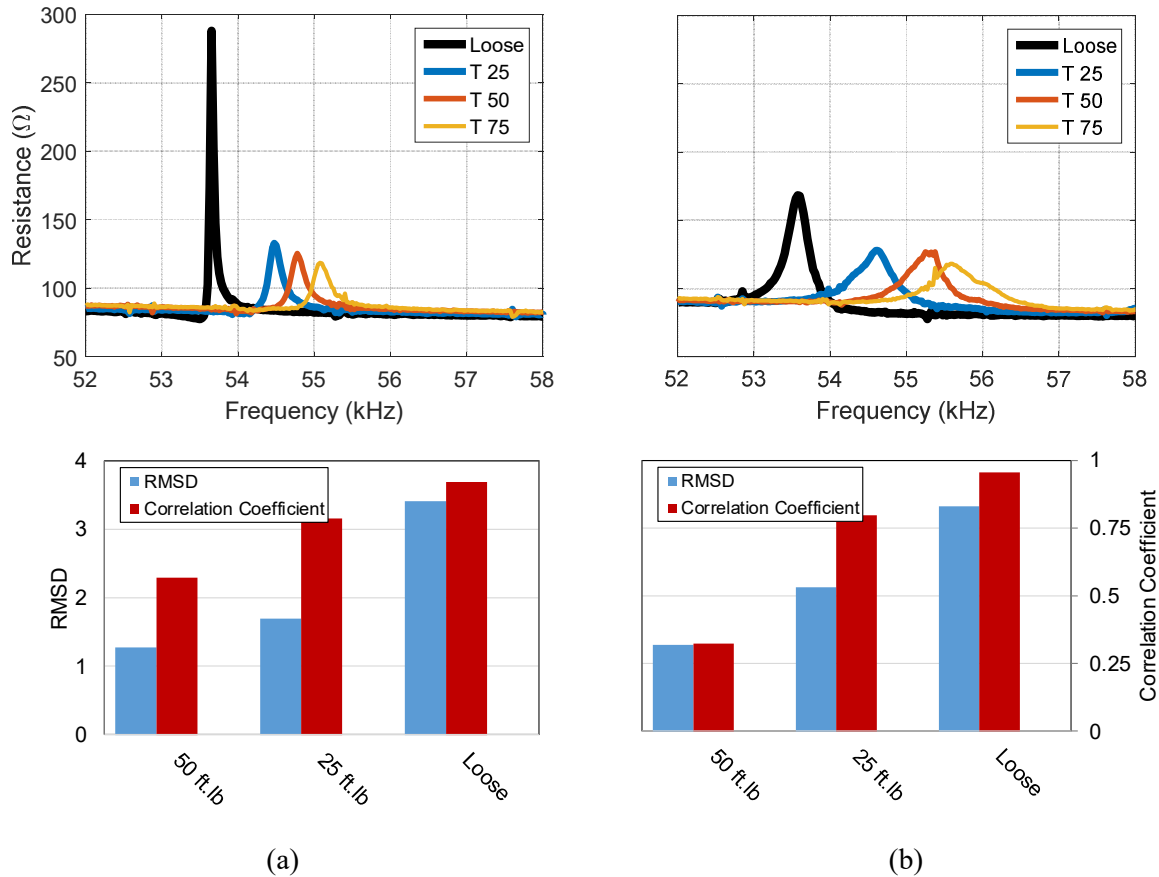
Figure 6.24. Torque loss effects on impedance signatures along with the corresponding damage metrics (a) without protective coating, and (b) with ES39-6 protective coating.

6.2.3   In-field Testing

In-lab experiments on full-scale insulated joint components concluded that conventional impedance-based SHM is capable of detecting rail damage and torque loss in bolts, while high-voltage impedance measurements are necessary for the highly-damped joint bars. To further investigate the performance of the SHM technique under real-life operation and environmental conditions, instrumented rail joints have been installed on operational tracks and tested in the field. This work has been carried out in collaboration with Norfolk Southern, Roanoke, VA, and Transportation Technology Center Inc., Pueblo, Co. The following sections describe the instrumentation and assembly processes of the insulated joints, along with the main results of the in-field experiments.

Insulated Rail Joints Instrumentation and Assembly

Two full-scale insulated joints along with their corresponding rail sections have been instrumented for in-field testing. Each insulated joint consists of 4 feet 11 inches and 10 feet 5 inches long 136 A.R.E.A. rail sections connected together with a 3 feet long Koppers joint bars. Components instrumentation and assembly were carried out at Norfolk Southern testing facilities, Roanoke, VA.

Guided by the findings of in-lab experiments, individual joint components are first instrumented with MFC and monolithic piezoelectric transducers. One of the rail sections is instrumented with M2814-P1 MFC, while the other is instrumented with an M8557-P1 MFC, as shown in Figure 6.25. Both rail transducers are placed at the area that is later covered by the joint bar upon joint assembly, as shown in the figure. Although this places significant pressure on the MFC transducers, it provides them with permanent protection and supports the adhesive bonding layer between the MFCs and the rail.

Joint bars, on the other hand, are instrumented with M4010-P1 and M2814-P1 MFCs. The former is placed at the middle of the joint bar, where a symmetric response to joint bar damage and torque loss in the bolts is expected, as discussed in Section 6.2.1. The later MFC is placed towards the bar's edge so as to avoid the aforementioned symmetries. Although one transducer is sufficient to detect the existence of joint bar related damages, the measurements obtained by these two transducers can be utilized, in later studies, for damage identification purposes. Lastly, monolithic piezoelectric transducers are used for bolts instrumentation. Three bolts are instrumented per joint, where piezoelectric discs are attached to the bolts' heads as discussed in the previous section. All piezoelectric transducers that are attached to free surfaces, which is the case for the joint bar and the instrumented bolts, have been coated with ES39-6 industrial grade epoxy.
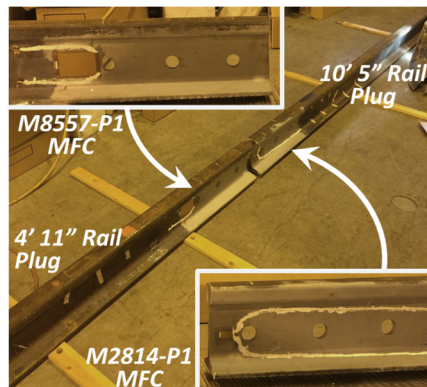
Figure 6.25. Instrumented rail sections for in-field testing.

Instrumented components are tested individually to check the performance of all piezoelectric transducers. Once all transducers are verified, the insulated joints are assembled. The assembly process includes applying the ES39-6 epoxy to all internal surfaces and torquing the bolts to 1100 ft.lb. The joints are then cured for two hours at 160°F. To achieve this temperature, each joint and the surrounding rail sections are placed in a heat box and then heated up with a 60 kBtu forced air propane heater. Joint temperature is monitored during the process using a K-type thermocouple attached to the railhead, and the heater is manually controlled to maintain the desired temperature. The assembled joints are then allowed to cool down for twelve hours before measurements are taken.

Initial Testing of Assembled Joints

Assembled instrumented rail joints have been tested at Norfolk Southern's facility before being installed in the field. Baseline impedance signatures have been first measured for all piezoelectric transducers mounted on the joints. Reversible damages, in the form of bolt loosening and added mass to the railhead, have been also studied. In this section, only the results of bolts loosening experiments are discussed. Pristine and added mass simulated damage cases, on the other hand, have been further investigated in the field, and are discussed in detail in the next section.

Figure 6.26 shows a schematic of an instrumented insulated rail joint with all bolts being numbered. For the torque loss experiment, bolts have been tightened to the fully-torqued condition, 1100 ft.lb, starting from the loose state where the joint is only kept together by the cured epoxy. Bolt 1 has first been tightened gradually in 300 ft.lb increments. The electromechanical impedance is measured at each step using the piezoelectric disk attached to the bolt's head. Two frequency ranges have been investigated in this work, 50-100 kHz and 212-264 kHz, the results are shown in Figure 6.27. The effect of torque loss on both frequency ranges is clearly detectable. Tracking a single peak in the impedance signature, the one at 70 kHz for example, reveals that as the torque is increased impedance peaks monotonically shift to higher frequencies. This indicates an increase in the bolt's stiffness with tensile loading, which agrees with the findings reported in Section 5.6.2. Similar results are found for Bolt 3 and Bolt 5.

Once Bolt 1 is fully torqued, other bolts are tightened in the following order: Bolt 6, Bolt 4, Bolt 3, Bolt 2 and finally Bolt 5. This sequence is followed in order to keep the joint uniformly loaded. As each bolt is torqued, impedance signature is measured at Bolt 1 and at the rail's M8557-P1 MFC, which is attached to Rail Section 1 shown in Figure 6.26. Impedance signatures measured at these two locations are shown in Figure 6.28.
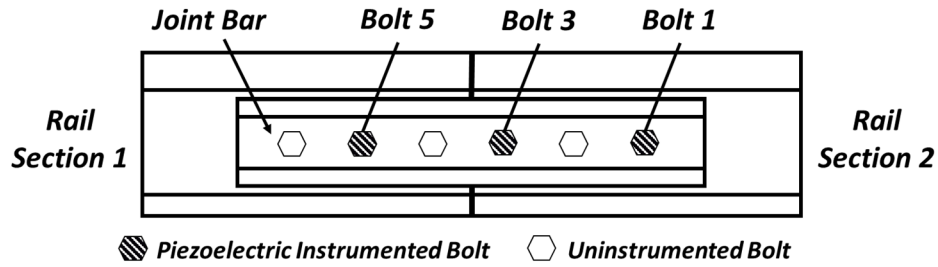
Figure 6.26. Schematic of the instrumented rail joint showing bolts numbers.
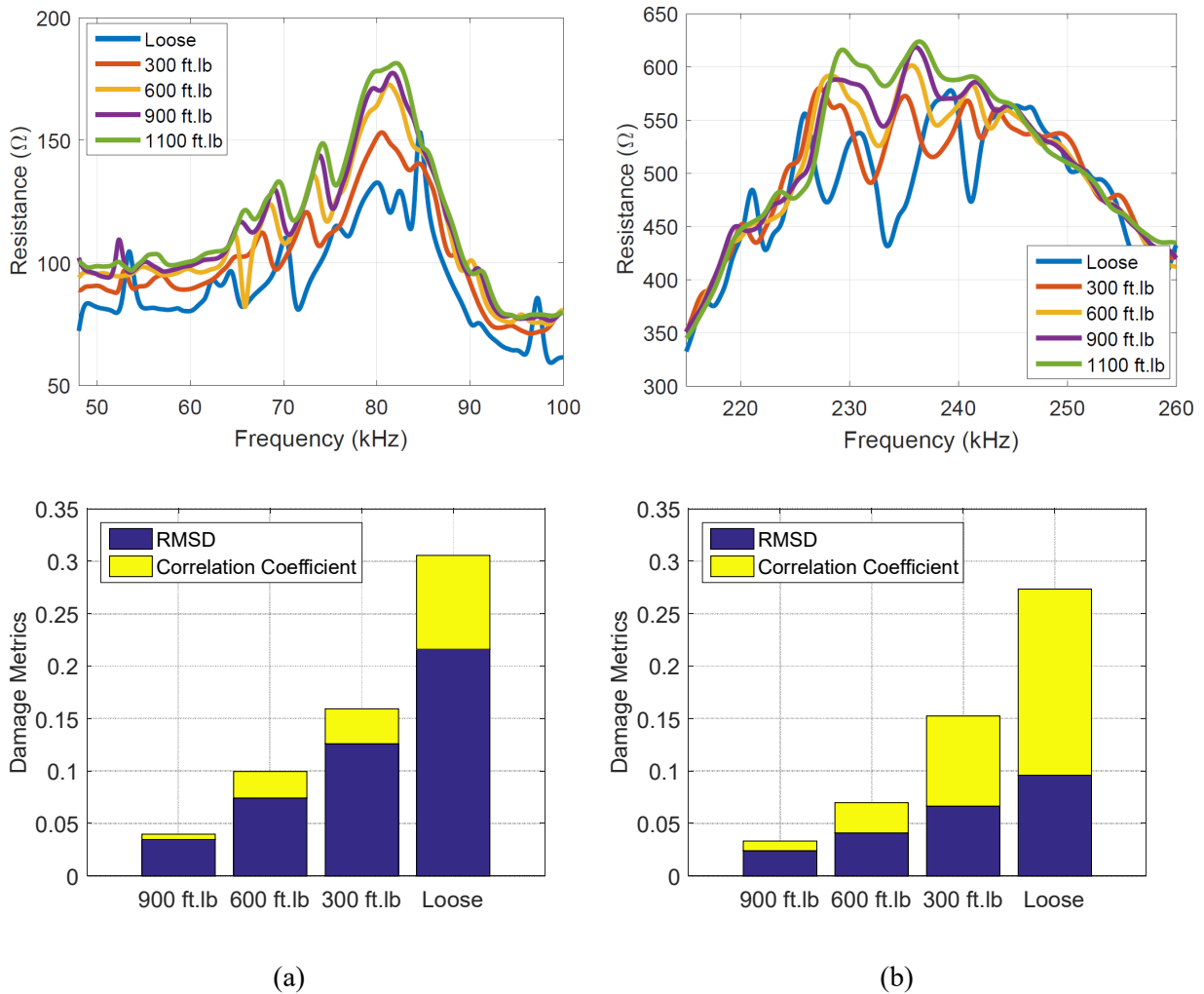
Figure 6.27. Electromechanical impedance of Bolt 1 measured at several torque levels, along with the corresponding damage metrics, for (a) 48-100 kHz, and (b) 212-260 kHz frequency ranges.

The effect of torque level changes in other bolts on the impedance signature measured on Bolt 1 is shown in Figure 6.28.a. This appears as a slight reduction in impedance magnitude, accompanied by a slight shift in impedance peaks to the left. These features are consistent with those observed when torque level in Bolt 1 decreases. This indicates that torquing a given bolt results in a reduction in the torque level of the previously torqued ones, which has been verified experimentally. In general, these changes are more severe than what is reported in Figure 6.28.a, however, when this experiment has been conducted, torque levels in all bolts have been rechecked every time a new bolt is torqued. These results indicate that impedance signatures measured at a given bolt are only sensitive to the dynamic response of the bolt itself. Any changes occurring in the surrounding structure will not be reflected on the impedance measurement unless they have a direct impact on that specific bolt, in the form of loading condition changes for instance.

Similar trends have been observed with impedance signatures measured at the rail, as shown in Figure 6.28.b. Changes in the torque level in the bolted joint is found to result mainly in variations in impedance magnitude. In general, as more pressure is applied to the MFC, impedance magnitude slightly increases. This is clear when the response of the "All Loose" case is compared to that when Bolt 6 is torqued. Since Bolt 6 is the closest to the MFC, the increase in its torque level results in a clear increase in impedance magnitude.
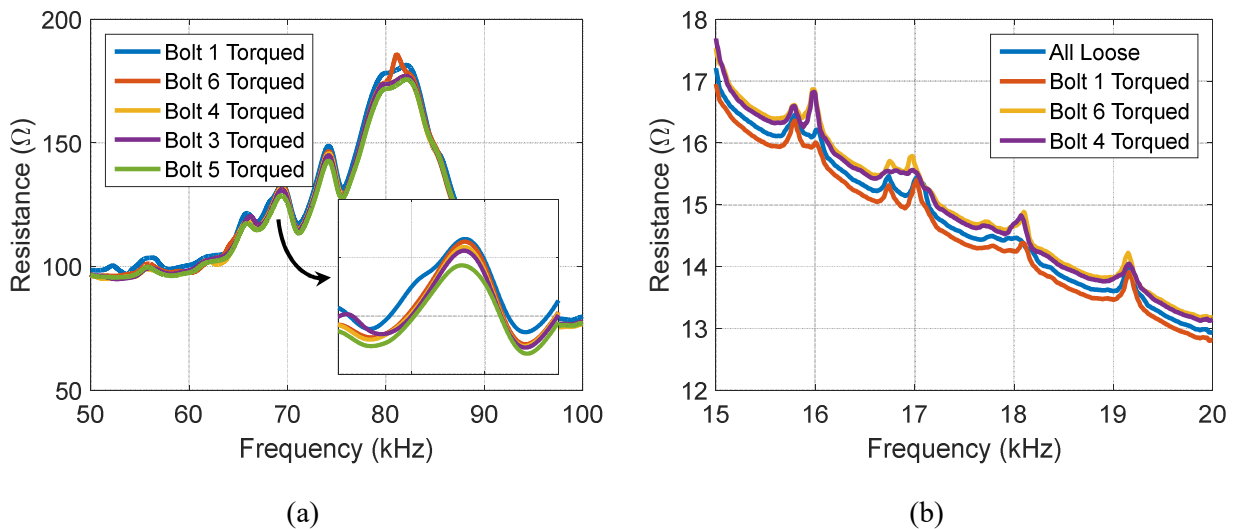
Figure 6.28. Electromechanical impedance of (a) Bolt 1 and (b) rail's MFC as different bolts in the insulated joint are fully torqued.

In-filed SHM of Insulated Rail Joints

The instrumented joints have been installed on operating tracks in order to investigate the performance of the SHM technique in real operating conditions. One joint has been installed at a Norfolk Southern track located in Radford area, VA. This joint is intended serve a long-term monitoring study to investigate how the performance of the system changes with time. It will also be used for long-term tracking of damage sensitive features, which will later be associated with traffic data and utilized for prognosis analysis. This long-term study is not intended to be part of this research effort, rather, it is one of the research directions to be pursued in the future. The second instrumented joint has been installed at the Facility for Accelerated Service Testing (FAST) track located at the Transportation Technology Center Inc., Pueblo, Co. This joint is intended to serve a short-term extensive study in order to evaluate the effects of operating and environmental conditions on the pristine state impedance signatures.

Using the later joint, a total of twelve sets of baseline measurements have been carried out in a span of nine hours. Eight of these baseline sets are measured at the zero-ton mark, where the joint plug has been merely welded to the track without any locomotives passing over it. An 111,000 lbs. welder has then been used to load the joint, and four other sets of baselines have been measured. Table 6.1 shows the time at which each baseline set has been measured, along with the rail temperature and longitudinal stress at the time of measurement, as provided by TTCi. Due to the fact that the insulated joint is fully constrained by the surrounding track, changes in temperature are accompanied by changes in rail longitudinal stress, as shown in the table. Therefore, baselines measured at different times of the day are not only affected by temperature variations, but also by the variations in the state-of-stress.

Figure 6.29 shows a subset of the baselines measured for Bolt 1 and Bolt 5, numbers follow the convention defined in Figure 6.26. These impedance signatures are measured using a KEYSIGHT E4990A impedance analyzer with one-volt peak-to-peak excitation voltage. As the rail temperature increases, the longitudinal state-of-stress in the rail decreases due to the added compressive thermal stresses. This combined effect appears as changes in the magnitude and slope of the measured impedance signature. In spite of the significant change in baseline signatures, only minimal changes in individual impedance peaks frequency have been observed. These are the features, i.e. impedance peaks frequency, that are found to change drastically with torque level, as discussed in the previous section. Thus, selecting and tracking damage sensitive features, rather than relying on conventional damage metrics, facilitates damage detection and characterization efforts by allowing the distinction between temperature related impedance changes and those induced by structural defects. This will be addressed in detail in future studies.

Table 6.1. Rail temperature and longitudinal stress at the time of baseline measurement.

Baseline No.	Measurement Time	Temperature (°C)	Longitudinal Stress (MPa)
Baseline 1	7:45	18 ± 0.5	760
Baseline 2	8:45	21.5 ± 0.5	685
Baseline 3	9:40	28.5 ± 1	535
Baseline 4	10:35	36.5 ± 0.5	385
Baseline 5	11:30	39.5 ± 0.5	300
Baseline 6	12:25	44 ± 0.5	205
Baseline 7	13:10	48.5 ± 0.5	115
Baseline 8	13:45	51	35
Loaded 1	14:35	44.5	70
Unloaded 1	15:05	43 ± 1	130
Loaded 2	15:25	41	165
Unloaded 2	15:50	42 ± 1	185

Baseline impedance signatures for the joint bar and the rail are measured using the high voltage impedance measurement setup described in Section 6.2.2. Two excitation voltages have been investigated in this study, 40 volts and 100 volts. For both cases, measurements are carried out over the frequency range of 10-35 kHz, with a fixed 450 Ω in-series resistor and a fixed amplifier gain of 100. A subset of joint bar and rail

(a)   (b)
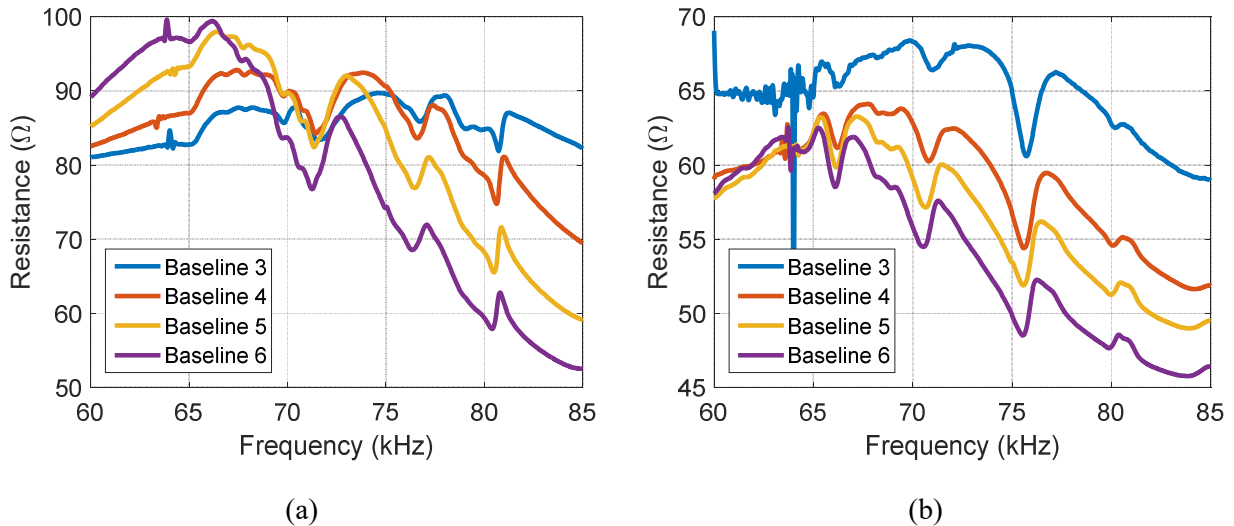
Figure 6.29. Baseline impedance signatures for (a) Bolt 1, and (b) Bolt 5, measured at different rail temperatures and longitudinal stress values.

baselines signatures are shown in Figure 6.30. As discussed in the previous section, the insulation attached to the inner surface of the joint bar introduced significant damping to the system. Once the joint bar is assembled with the rest of the insulated joint, damping effects are found to increase even more. This is reflected clearly on the measured impedance signature, where the response is strongly dominated by the dielectric characteristics of the MFC transducer, as shown in Figure 6.30.a. Temperature effects appear as a vertical shift in the impedance measurement. Isolated impedance peaks are found to exist at certain frequency ranges, as shown in the close-up view in the figure. These peaks shift with temperature and rail stress variations. However, no clear trends are observed. Further investigation is necessary to overcome damping effects and obtain more sensitive impedance signatures. Similar trends are found with rail impedance signature, shown in Figure 6.30.b. This drastic change compared to lab measurements, shown in Figure 6.19, can be ascribed to two main reasons:

I.   The added damping due to the rail being connected to the ties underneath through anchors and tie plates.

II.   The rail section being welded to the track, which makes it resemble an infinite structure with no distinct resonance peaks in its frequency response.

Therefore, impedance signatures measured at the rail section cannot be used for SHM practices as they do not carry clear information about the dynamic response of the structure. This limitation is expected to be common among all steady-state vibration-based damage identification techniques.

(a)   (b)
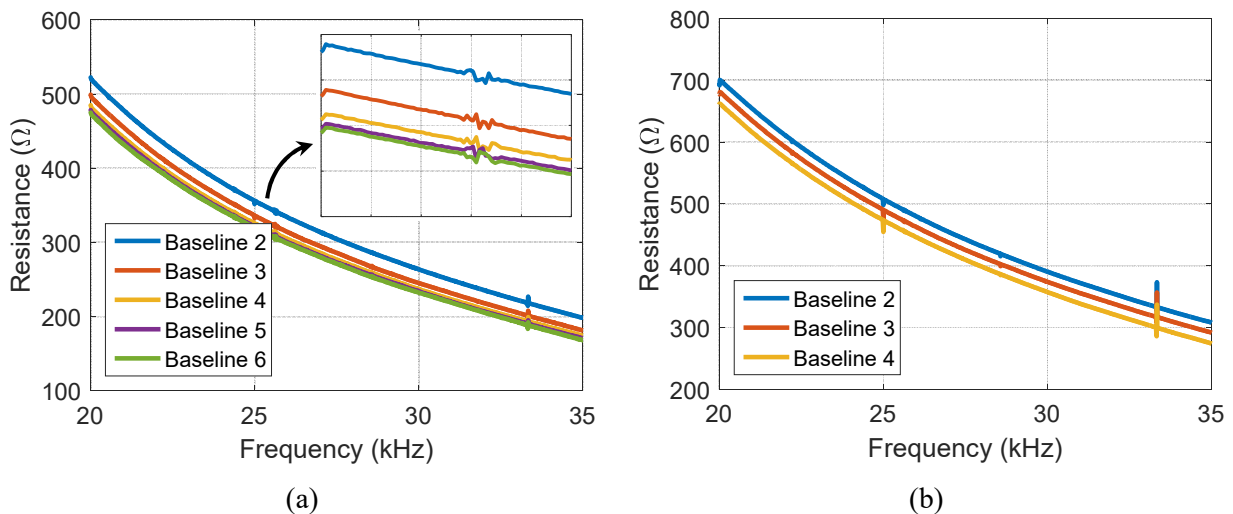
Figure 6.30. High-voltage baseline impedance signatures measured at different temperatures for (a) joint bar with 40 V excitation, and (b) rail section with 100 V excitation.

Loading effects on baseline impedance signatures have also been investigated in this wok. For this purpose, An 111000 lbs welder with a nominal wheel load of 13875 lbs, has been utilized to load the instrumented joint along with the adjacent rail sections, as shown in Figure 6.31. Four other sets of baselines have been measured during two loading cycles, the results are shown in Figure 6.32.

(a)   (b)

Figure 6.31. In-field loading experiment showing (a) the welder used to load the insulated joint, and (b) the wheels loading the insulated joint and the instrumented rail section used for stress measurements.

(a)   (b)
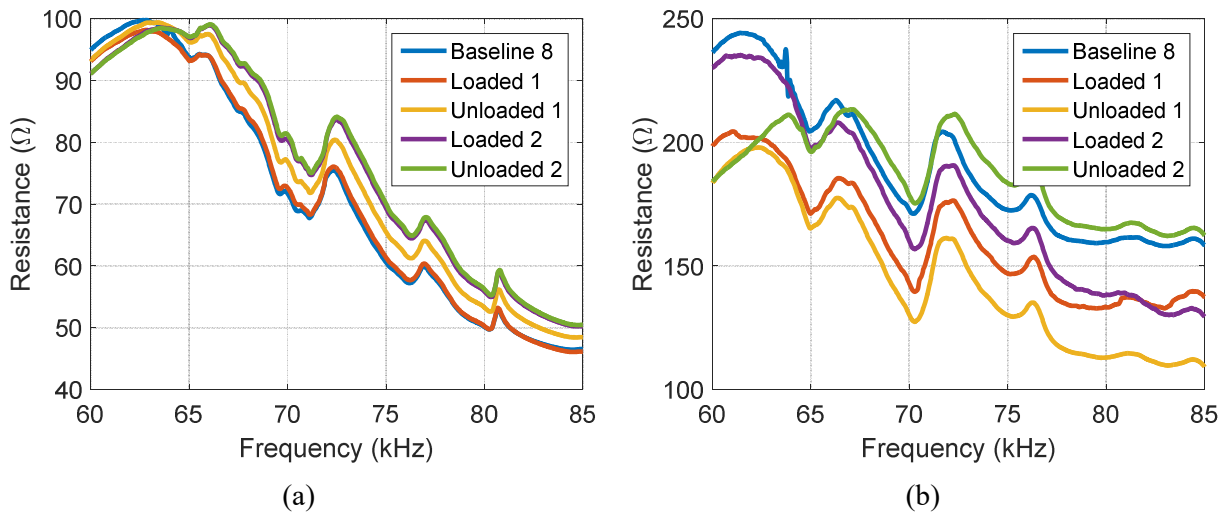
Figure 6.32. Baseline impedance signatures for (a) Bolt 1, and (b) Bolt 3, measured at different temperatures and loading conditions.

6.3   Rail Longitudinal Stress and Neutral Temperature Measurement

The temperature at which the rail experiences zero stress is referred to as the rail neutral temperature (RNT). Normally rails are pre-stressed when installed in order to raise their neutral temperature and expand their buckling-free margins. However, the predetermined RNT degrades due to rail kinematics, including creep, breathing and ballast settlement, rail maintenance operations such as realignment, distressing, and repairs, and support conditions (Kish and Samavedam, 2005). This uncertainty in RNT increases the risk of unpredicted rail buckling and breakage, which in turn compromise railroad safety. The proposed stress monitoring technique provides a reference-free, non-destructive solution for in-situ RNT measurement. This allows predicting and detecting buckling prone conditions, which enhances railroad safety and facilitates rails thermal management.

The envisioned RNT measurement system utilizes an array of piezoelectric disks attached to the web of a rail where the neutral temperature is to be measured, as shown in Figure 6.33. The central piezoelectric disk operates as an actuator to generate plane elastic waves with the desired frequency content. The two other piezoelectric disks centered around the source disk are used to measure the propagating wave. The first receiver disk, denoted by *R1*, measures the waveform along the loading direction, while *R2* measures it along the normal, stress-free direction, as shown in the figure. Dispersion curves along these two principal directions are then calculated through the stress measurement algorithm discussed in Chapter 5. An error function is then defined to quantify the difference between the two dispersion curves. Evaluating this error function at different temperatures during the day allows predicting the RNT. As more measurements are taken, the accuracy of the RNT prediction improves. The utilization of the loading-normal direction allows for the system to be self-calibrated. Therefore, uncertainties in material properties are implicitly compensated for.

Practical implementation of the previously discussed configuration requires addressing several challenges including reflections from railhead and base, compensation for thickness variations along the web, and accounting for the effects of residual stresses in the assumed stress-free direction. These challenges are still active areas of research and will not be addressed in here. The work discussed in this section represents the one-dimensional version of the envisioned RNT measurement approach. Elastic waves propagating along the loading direction are analyzed, utilizing the technique developed in Chapter 5, to evaluate the longitudinal state-of-stress of the rail. RNT is then calculated based on the rail's longitudinal stress variations as a function of its temperature.
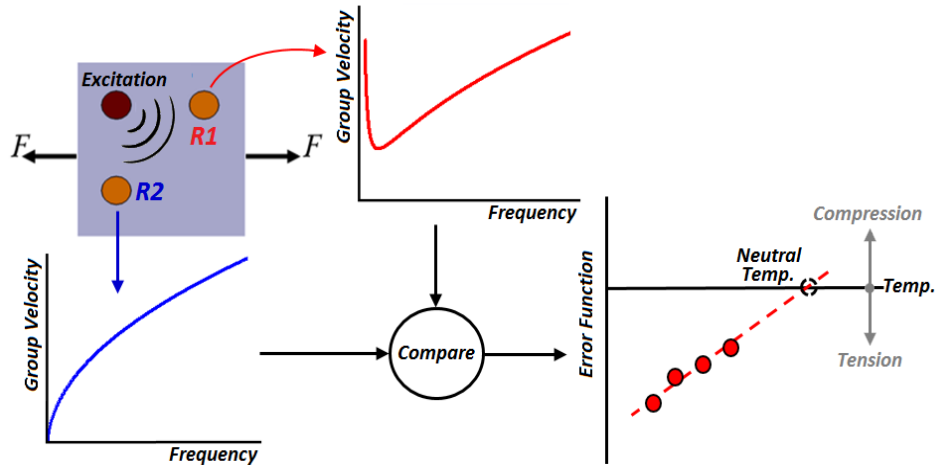
Figure 6.33. Schematic of reference-free rail neutral temperature measurement approach.

Experimental implementation of the RNT measurement technique has been conducted in collaboration with the Transportation Technology Center Inc. (TTCi), Pueblo, Co. As discussed in the Section 6.2.3, a rail section on TTCi's FAST track has been instrumented and tested. A piezoelectric actuator, M2814-P1 type MFC, is bonded to the rail's web in order to generate the desired waveform, while six accelerometers are used to measure the propagating wave, as shown in Figure 6.34. With this excitation approach, two main wave modes are generated in rail's web, these are the first symmetric and the first anti-symmetric modes, denoted respectively by S_0 and A_0. Distinguishing between these two modes using single-axis accelerometers is not possible. However, the contribution of the S_0-mode to the out of plane acceleration is negligible, and thus, waveforms measured by the accelerometers can be assumed to be pure A_0-waves.
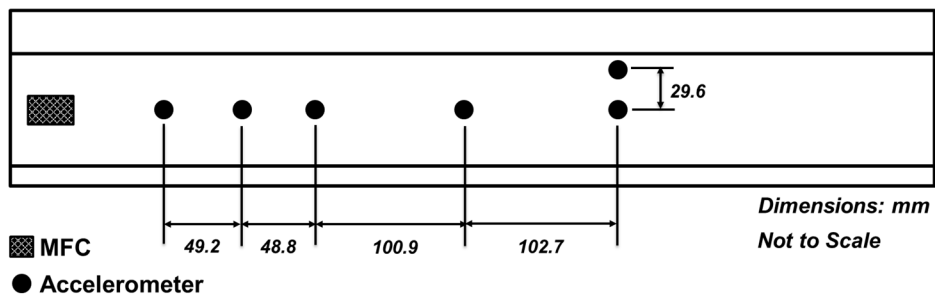
Figure 6.34. Schematic of the instrumented rail section showing the location of the MFC and the six accelerometers used in the RNT experiment.
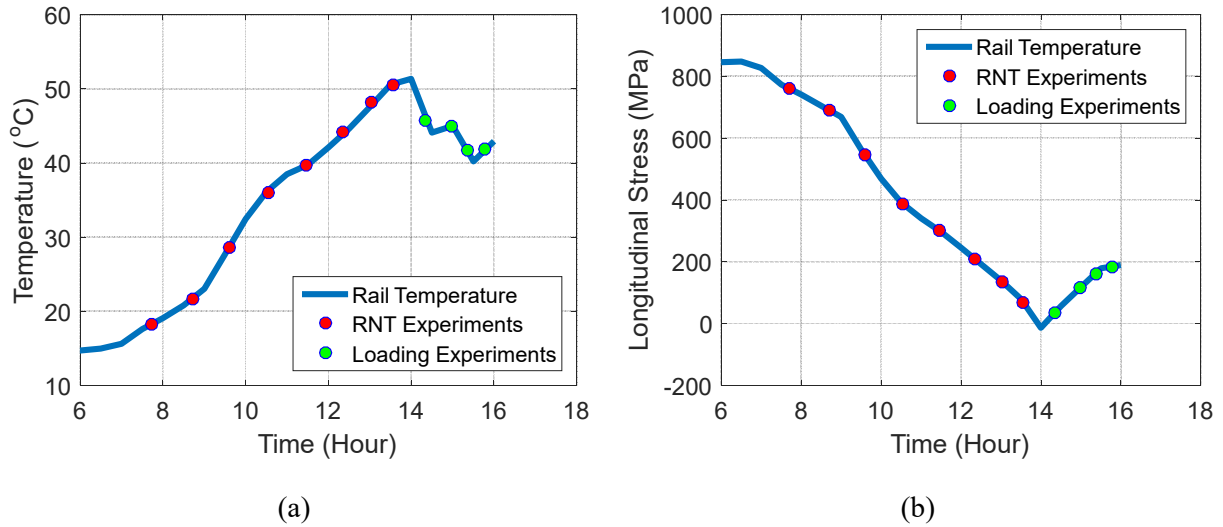
Figure 6.35. (a)Rail temperature and (b) longitudinal stress state measured at the time of the experiment.

Based on the findings of Section 5.4, two-cycle, amplitude modulated, sine wave tone bursts have been used to excite the rail, with 500 Hz, 1 kHz, and 2 kHz central frequencies. Although lower frequencies are more sensitive to longitudinal stresses, the utilization of MFCs for actuation imposes a lower limit on the excitation frequency. The experiments have been carried out at different times during the day, temperatures and longitudinal rail stress values at the time of the experiments are shown in Figure 6.35.a and 6.35.b, respectively. In the figure, longitudinal stresses are measured using a calibrated strain gauge attached to the rail section.

The change in longitudinal rail stress varies linearly with rail temperature, as shown in Figure 6.36. It could be noticed that RNT can be accurately predicted with as little as two stress measurements at two different temperatures. The effects of loading and unloading cycles are also shown in the figure. The presence of the welder, described in Section 6.2.3, on the rail section appears as a temperature independent drop in rail stress, and vice versa. This is indicated by the green dots in the figure and explains the reason behind stress level variations along heating and cooling paths shown in the figure.

For reference-free stress measurements, the acoustoelastic-based technique developed in Chapter 5 has been utilized in this section. The analysis in here follows the same steps as of Section 5.6.3. At a given temperature, the acceleration signal measured by the first accelerometer is considered as the reference signal that is later propagated by the developed algorithm and compared to the waveforms measured by the other accelerometers. This allows bypassing the uncertainties associated with signal amplification and MFC
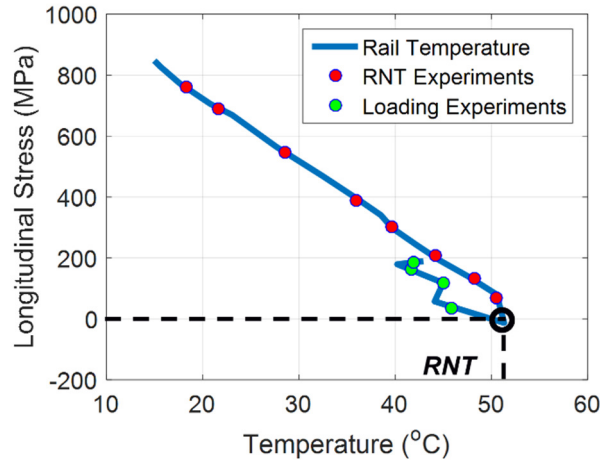
Figure 6.36. Longitudinal stress state in the rail as a function of its temperature. RNT is shown in the figure.

excitation stages. All measured signals are first processed to isolated the incident wave, then filtered, and padded with zeros, as shown in Figure 6.37 for the 1 kHz excitation frequency measured at 7:43 am, with a rail longitudinal stress of 760 MPa. Processed signals are then fed to the stress measurement algorithm as *Input 2* and *Input 3* (refer to Figure 5.3). Material properties of the rail being tested along with its cross-section dimensions, 136 A.R.E.A. rail with E = 275 GPa, ρ = 7800 kgm^{-3} and v = 0.3, are also fed to the algorithm. As discussed in Section 5.3, the algorithm propagates the incident wave to the next measurement location, (x_{i+1}), and updates the state-of-stress to minimize the error function defined as the L_2 norm of the difference between the waveform measured at x_{i+1} and the propagated waveform at that location. Upon convergence, an estimate of the state-of-stress acting on the structure is obtained.

Figure 6.38 shows the waveforms measured at each of the four accelerometers placed at the rail's web centerline, accelerometers 2-5 in the previous figure, along with the reference incident wave and those propagated to the aforementioned locations. For all cases shown in the figure, the strain-gauge-measured state-of-stress, which is 760 MPa, is used to propagate the reference incident wave. Measured and propagated waveforms are in good agreement, however, discrepancies are observed in the signals due to noise and reflections contaminations. Based on these measurement locations, the states of stress estimated by the stress measurement algorithm is found to be 1330 MPa, almost twice as much as the actual value.
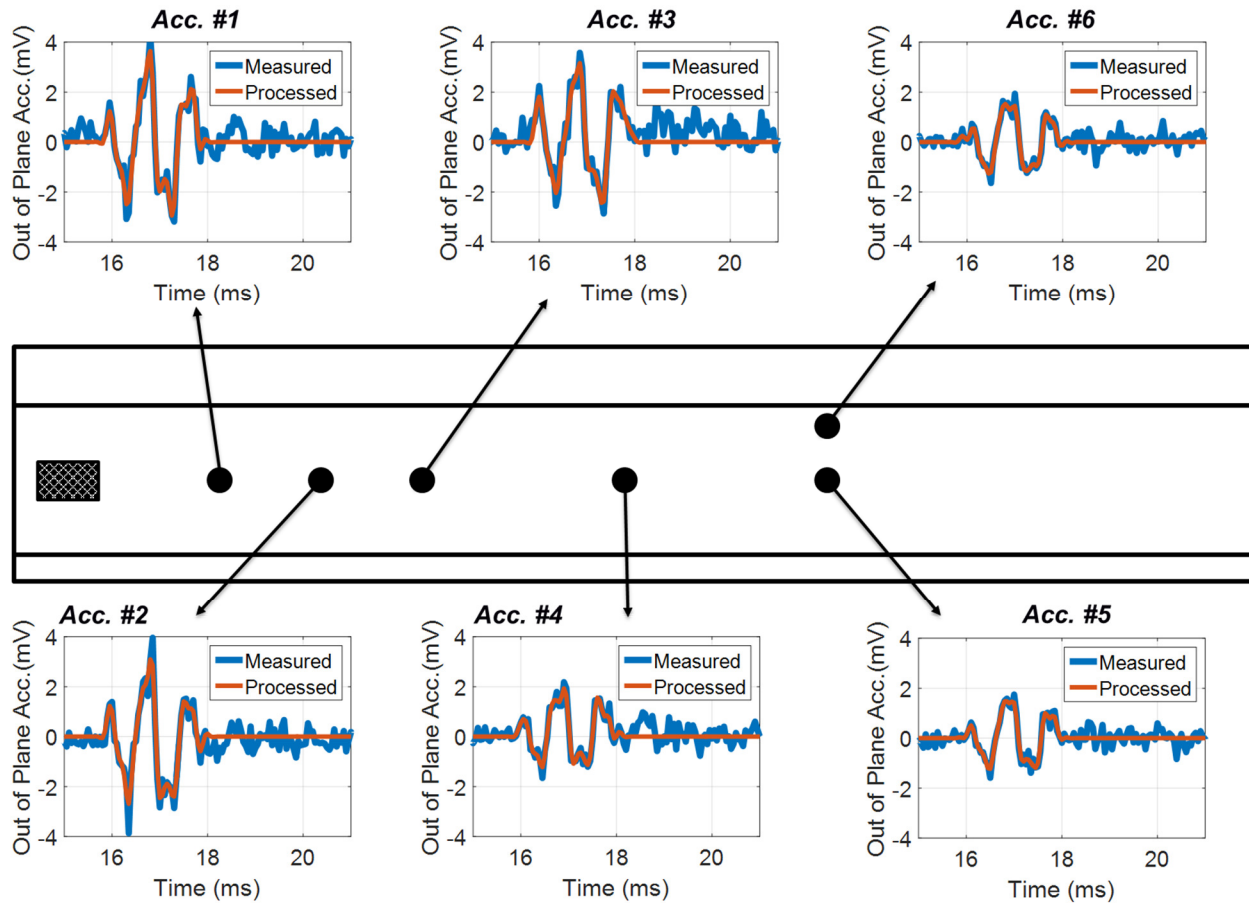
Figure 6.37. Measured and processed waveforms along the rail section for the 1 kHz excitation frequency. Measurements are carried out at 7:43 am.

This large error can be explained by examining dispersion curves of the rail section at different loading conditions, as shown in Figure 6.39. At 1 kHz, longitudinal state-of-stress has a minimal effect on wave speed. For the rail section under consideration, a 1 kHz frequency is equivalent to 230 kHz.mm. Therefore, uncertainties related to measurement location, material properties and geometric characteristics of the rail being tested result in significant errors in the estimated state-of-stress, as suggested by the sensitivity analysis presented in Section 5.5. For successful stress measurements, incident waves of center frequency in the range of 50-100 Hz are required. Such low-frequency requires a very large separation distance between the measurement locations and structure's boundaries, which can be easily accommodated by the railroad track. However, such low-frequency excitations cannot be achieved using MFC transducers. Thus, alternative excitation solutions are required. This will be investigated in future research efforts.
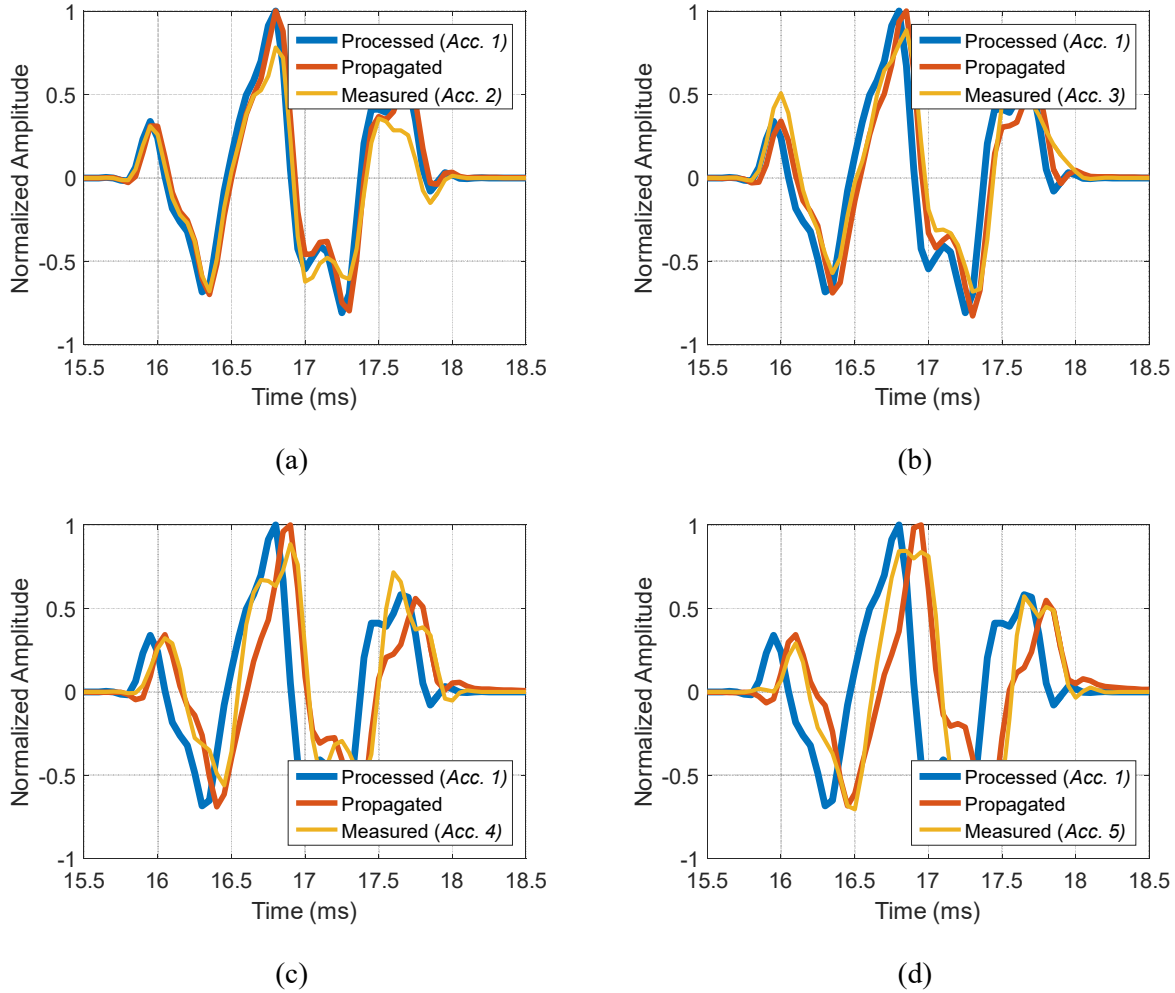
Figure 6.38. Incident, propagated and measured waveforms at (a) accelerometer 2, *x = 49.2 mm*, (b) accelerometer 3, *x = 98 mm*, (c) accelerometer 4, *x = 198.9 mm*, and (d) accelerometer 5, *x = 301.6 mm,* for the 1 kHz excitation signal and 760 MPa rail stress.

6.4   Conclusions

In this chapter, the applicability of impedance-based SHM and acoustoelastic-based stress measurement techniques to the railroad industry has been experimentally investigated. The feasibility of impedance-based SHM of insulated rail joints has first been studied with the aid of a representative lab-scale joint. Four types of joint related damage types have been identified, these are rail damage, torque loss, insulation failure, and
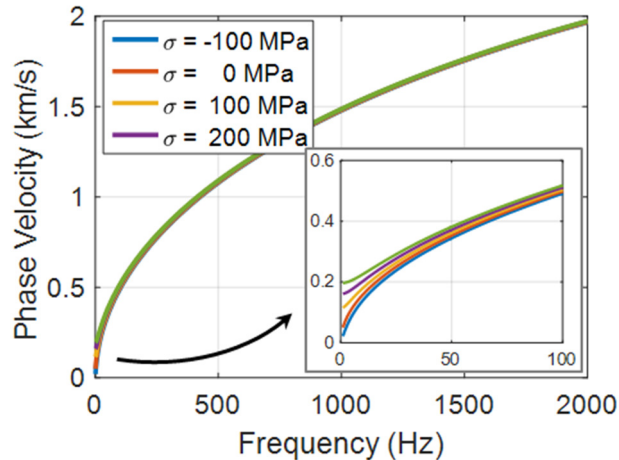
Figure 6.39. Phase velocity for the first anti-symmetric wave mode propagating along a 136 A.R.E.A. rail at several levels of longitudinal stress.

joint bar failure. All four damage types are successfully detected with impedance-based SHM. The lab-scale insulated joint has been used to investigate several sensor placement configurations, taking into consideration measurements sensitivity to different types of defects and sensors survivability. It is found that an MFC transducer attached to the inner surface of the joint bar is sensitive to torque loss, joint bar damage, and insulation failure, whereas a one attached to the rail side is only sensitive to rail damage.

Motivated by the success of the lab-scale joint health monitoring, the focus has been shifted to testing full-scale insulated joint components. A 136 A.R.E.A. rail section along with compatible Koppers joint bars have been tested for this purpose. Sensitive frequency ranges for different damage types have first been identified by measuring the impedance signatures of pristine and damaged states over the frequency range of 10-100 kHz and calculating damage metrics over 5-kHz-wide frequency bands. As far as rail defects are of concern, the frequency range of 20-30 kHz is the most sensitive, while the range of 50-85 kHz is the most sensitive to torque loss in the bolted joint. Joint bar defects, on the other hand, have not been successfully detected with standard impedance measurements due to the high damping introduced by the insulation layer being attached to the joint bar's surface. Therefore, high-voltage impedance setup has been developed and utilized to interrogate joint bars. It is found that impedance signatures measured with a 40-volt excitation signal are capable of detecting joint bar defects.

To further investigate the performance of impedance-based SHM under real life operating and environmental conditions, a full-scale insulated joint has been instrumented in collaboration with Norfolk

Southern and tested at TTCi FAST track. It is found that joint bar and rail impedance signatures are mostly dominated by the dielectric characteristics of the piezoelectric transducers, with minimal contributions from the dynamic response of host structures. This can be ascribed to the significant damping introduced to the joint bar upon assembly and to the rail section approximating an infinite beam when welded to the adjacent track. Torque loss, on the other hand, has been successfully detected in the field. Furthermore, damage sensitive features in the impedance signature have been successfully utilized to distinguish between torque loss effects and temperature-induced impedance variations.

The reference-free, acoustoelastic-based stress measurement technique developed in Chapter 5 has been utilized for rail neutral temperature measurement. Elastic waves are induced in the rail via an MFC transducer, while the response is measured using six accelerometers attached to the rail's web. Two cycle, amplitude modulated, sine wave tone bursts of 500 Hz, 1 kHz and 2 kHz central frequency have been utilized to excite the rail. Propagating waveforms have been measured at different times during the day corresponding to different rail temperature and longitudinal stress values. The stress measurement algorithm successfully propagates the excitation wave to different measurement locations. However, the high frequency of the excitation signals, along with noise contamination and material and geometric uncertainties, adversely affected the quality of stress estimates. Successful rail stress measurements require incident waves of center frequency in the range of 50-100 Hz. However, such low-frequency excitations cannot be achieved using MFC transducers and alternative excitation solutions need to be investigated.

CHAPTER SEVEN

CONCLUSIONS AND FUTURE WORK

7.1 Conclusions

Motivated by the growing need for structural health and loading monitoring solutions, this work has developed theoretical, numerical and experimental tools to advance the current state-of-the-art of impedance-based SHM and acoustoelastic-based stress measurement techniques. Impedance-based SHM lends itself as a non-intrusive technique that is highly sensitive to incipient damages and suitable for autonomous applications. However, the utilization of electromechanical impedance measurements for more than damage detection imposes several challenges stemming from the high-frequency nature of the technique. Current acoustoelastic-based stress measurement techniques, on the other hand, are hindered by their poor sensitivity and their need for calibration at a known state-of-stress. This limits the applicability of such techniques, especially for in-service structures, where a known reference state-of-stress is unattainable. These challenges have been tackled by this research effort. The main findings, conclusions, and contributions of this work are stated below.

High-frequency piezoelectric-structure interaction model: A new three-layer spectral element for piezoelectric augmented structures has been developed in this work, where the adhesive bonding layer has been explicitly modeled. The formulation of this new element takes into account axial and shear deformations in addition to rotary inertia effects in all three layers, which have been found to be significant for high-frequency dynamic responses. With its high-frequency capabilities, and by accounting for the

presence of the adhesive bonding layer, the proposed model represents an important addition to the piezoelectric-structure interaction models currently available in the literature.

The model has been validated against the commercial FE package, Abaqus. FEM predictions have been found to converge to the model's upon FE mesh refinement. The superiority of the SEM over the FEM is evident, especially at high-frequency ranges. The frequency range within which the developed model retains its accuracy has also been investigated. For this purpose, the underlying fundamental theories that were adopted for model development have been gauged against the Pochhammer-Chree exact solution. It has been found that the Elementary rod theory and the Timoshenko beam theory accurately describe the longitudinal and lateral deflections of beams, along with the first symmetric and anti-symmetric wave modes, up to the cut-off frequency of the second anti-symmetric mode, given by $(GA\overline{K}/\rho I)^{1/2}$.

Impedance-based characterization of piezoelectric transducers: The dynamic response of free piezoelectric transducers has been studied by non-dimensionalizing the electro-elastodynamic equations of motion. Three non-dimensional parameters have been defined to describe the coupled electromechanical behavior of the system. These non-dimensional parameters describe the geometry of the piezoelectric wafer, the ratio between driving electric force and restoring elastic force, and the ratio between dielectric charge and that induced by electromechanical coupling. The effects of each non-dimensional parameter on the frequency response functions and the electromechanical impedance of the free piezoelectric transducer have been studied thoroughly. Guided by the findings of this study, a procedure for piezoelectric material characterization utilizing its free electromechanical impedance signature has been developed.

Understanding the effects of the bonding layer on the dynamic behavior of piezoelectric augmented structures: The effects of bonding layer characteristics, namely its thickness, stiffness, and density, have been investigated using the developed piezoelectric structure interaction model. While the dynamic response of smart structures is mostly determined by the host structure itself, the presence of the piezoelectric wafer and bonding layer perturbs this initial state. To quantify these effects, resonance frequency shifts and actuation amplitude variations have been tracked as the characteristics of the bonding layer and piezoelectric wafer are varied. These features have been selected as they are essential for SHM, energy harvesting and control applications.

In general, the effects of bonding layer characteristics are strongly frequency-dependent. Changes in resonance frequencies due to variations in piezoelectric wafer and bonding layer characteristics are found to be negligible at low-frequency ranges. These effects become more profound as the frequency range of

interest increases. Actuation amplitude, on the other hand, is found to be strongly dependent on the bonding layer stiffness and thickness. At low frequency, a thin rigid bonding layer has been found to enhance the actuation authority of the piezoelectric transducer. Similar effects have also been observed at higher frequencies, however, there exists an optimal stiffness-thickness combination beyond which an increase in adhesive stiffness or a decrease in bonding layer thickness adversely affects the response. Numerical simulations are required to determine the optimal stiffness-thickness combination for the frequency range of interest.

The results highlight the need to include the effects of bonding layer characteristics, bonding stiffness degradation in particular, in damage detection and identification efforts. This is especially important for impedance-based damage characterization, where the high-frequency impedance measurements can be strongly affected by bonding layer characteristics. The thickness and rigidity of the bonding layer can also be optimized to enhance actuation authority, which is of interest for control and energy harvesting applications.

Impedance-based damage characterization: A novel optimization-based damage characterization approach that utilizes high-frequency impedance measurements has been developed in this work. For this approach, length-varying spectral elements have been introduced to minimize the number of damage characterization parameters. This adaptive discretization also allows for more accurate damage characterization, where the accuracy to which the damage can be identified is not limited by the resolution of the spectral element mesh.

The behavior of the optimization problem has been found to be strongly dependent on objective function definition. Among the objective functions considered in this work, the peak-shifts-based definition has been found to have a superior convex behavior, with respect to damage width and severity parameters, with clear search directions. This definition has been found to have an underlying periodic nature with respect to damage location. This underlying periodicity has been capitalized to develop the sine-fit localization method (SLM), which is a computationally efficient method capable of solving the ill-posed problem of damage localization with a minimal number of objective function evaluations. Based on the findings of this work, a two-stage optimization algorithm for damage characterization has been developed, where SLM is combined with the gradient descent method to solve for damage location, width, and severity. The algorithm has been tested with several damage scenarios, and it has been found to be capable of identifying damage parameters accurately and in a computationally efficient manner.

Reference-free acoustoelastic-based stress measurement: A novel acoustoelastic-optimization-based stress measurement technique has been developed in this work. The technique is model-based in nature and is capable of analyzing dispersive waves and calculating the state-of-stress in the structure under test. Depending on the structure, the effects of pre-loading on dispersion relations can be described by approximate beam theories or the semi-analytical finite element method. By mitigating the limitations imposed by conventional time-of-flight-based measurements, this technique allows the utilization of low-frequency, highly stress-sensitive, first anti-symmetric wave mode for stress measurements.

A criterion for optimal selection of excitation waveforms has been also proposed in this work. This criterion takes into consideration the sensitivity to the state-of-stress, the robustness against material and geometric uncertainties, and the ability to obtain a reflection-free response at desired measurement locations. For the problem at hand, a two-cycle, amplitude modulated sine wave tone burst has been found to be the optimal excitation waveform. The center frequency of the excitation signal is determined based on the dimensions of the structure under test.

In order to evaluate the impact of material- and geometry-related uncertainties on the performance of the stress measurement algorithm, a thorough sensitivity analysis has been conducted. Five parameters have been investigated in this study including material's modulus of elasticity, material's density, structure's width and thickness, and measurement locations. Sensitivity functions quantifying the error in the estimated state-of-stress due to the uncertainty in each of the five parameters have been determined as a function of frequency. Among the different parameters investigated in this work, uncertainties in beam's thickness have been found to be the most critical. The robustness of the stress measurement technique against different sources of uncertainties has been found to improve with low-frequency excitations. This gained robustness comes at the cost of increased separation requirements between measurement locations and structure's boundaries in order to obtain reflection-free responses.

The developed technique has also been experimentally validated. True reference-free, uncalibrated acoustoelastic-based stress measurements have been successfully conducted. Nominal material and geometric characteristics of the beam under test have been fed to the stress measurement algorithm. Accurate stress estimates have been obtained with 500 - 1000 Hz excitation frequency. The developed technique is ideal for in-service structures where calibration experiments cannot be conducted. Furthermore, by utilizing low-frequency anti-symmetric waves, the sensitivity of this technique is unprecedented in the field of ultrasonic testing.

Structural health and loading monitoring of railroad track components: The capabilities and limitations of impedance-based SHM for detecting structural defects in insulated rail joints have been investigated in this work. Extensive in-lab experiments have been conducted to evaluate the performance of the technique on lab-scale and full-scale rail joints, identify the types of structural defects that can be detected, and determine the most sensitive frequency ranges for each type. Optimal sensor placement configurations have also been identified taking into consideration measurements sensitivity and sensors survivability.

Motivated by the successful in-lab implementation of the technique on both lab-scale and full-scale insulated joints, in-field experiments have been conducted to further investigate the performance of impedance-based SHM under real life operating and environmental conditions. For this purpose, a full-scale insulated joint has been instrumented in collaboration with Norfolk Southern and tested at TTCi FAST track. Joint bar and rail impedance signatures have been found to be unaffected by structural damage. Torque loss, on the other hand, has been successfully detected in the field. Damage sensitive features have also been identified to distinguish between the effects of torque loss and temperature changes on the measured impedance signature.

The feasibility of utilizing the reference-free acoustoelastic-based stress measurement technique, that has been developed in this work, for rail neutral temperature measurement has also been investigated. Propagating waveforms measured at different times during the day, corresponding to different rail temperature and thus different levels of thermal stresses, have been analyzed for that purpose. The stress measurement algorithm successfully propagates the incident wave to different measurement locations. However, the high frequency of the excitation signals used in the experiments, along with noise contamination and material and geometric uncertainties, adversely affected the quality of stress estimates. Although non-conclusive, the results obtained with this initial in-filed testing of the reference-free stress measurement technique are in fact promising. Several aspects pertaining the practical implementation of this technique have been identified and will be further investigated in the future.

7.2   Future Work

While the research effort presented in this dissertation addressed several challenges facing the advancement of impedance-based SHM and acoustoelastic-based stress measurement techniques, it has motivated a number of research directions that need to be pursued in the future.

High-frequency piezoelectric-structure interaction model: At high-frequency excitations, the one-dimensional approximation of slender structures is no longer valid, and such structures are better approximated as plates. Therefore, extending the capabilities of the three-layer piezoelectric-structure interaction model to include two-dimensional structures is needed. This allows for more accurate high-frequency impedance simulations and expands the range of applications where the model can be utilized.

Impedance-based piezoelectric characterization: For in-field implementation of impedance-based SHM, temperature variations are considered as a major source of uncertainty. This can be ascribed to the temperature-induced variations of piezoelectric material characteristics. The impedance-based piezoelectric characterization approach developed in this work can be utilized to study such effects. The resulting empirical relations describing the effect of temperature on piezoelectric material characteristics can then be utilized for temperature compensation studies.

Impedance-based damage characterization: While the sine-fit localization method developed in this work has been successfully implemented to solve the ill-posed problem of damage localization, several aspects pertaining the performance of this algorithm, such as convergence and solution uniqueness, need to be further investigated. Additionally, the algorithm in its current version can only handle a single crack. Cases of multiple cracks are yet to be studied. Furthermore, extending the capabilities of this algorithm to include two-dimensional structures will be an important addition to the current damage characterization techniques with a wide spectrum of potential applications.

High-voltage Impedance-based damage characterization: Standard, low-voltage electromechanical impedance measurements live in the linear regime. However, several structural defects, such as cracks, bolt loosening, and delamination are nonlinear in nature. Tracking the evolution of such nonlinearities can help detecting the existence of damage, identifying it, and track its progression. The high-voltage impedance analyzer described in this work can be utilized for this purpose, where the amplitude of the excitation signal can be introduced as an additional variable. Both frequency and amplitude sweeps can be performed to track damage-induced nonlinearities. Ultimately, this work will establish the basis for reference-free impedance-based damage detection and identification.

Reference-free acoustoelastic-based stress measurement: Two major challenges facing the utilization of the low-frequency, anti-symmetric waves for stress measurement purposes have been identified in this work; these are dispersion effects and reflections form structures' boundaries. While the stress measurement algorithm developed in this work has successfully tackled dispersion effects, reflections have been avoided

by constraining the minimum allowable excitation frequency. Relaxing these constraints allows the utilization of lower frequency excitations, which in turn enhances the technique's sensitivity and robustness. For this purpose, two research directions will be pursued in future studies. The focus of the first direction is to account for reflected waves in the analysis, which in turn requires the boundaries of the structure under test to be identified. The second direction will investigate reflections cancellation solutions including active control and steady-state traveling waves.

Structural health and loading monitoring of railroad track components: Impedance-based SHM has been successfully utilized to detect torque loss in rail insulated joints under real-life operating conditions. Damage sensitive features have also been identified to distinguish between torque-loss-induced impedance changes and those induced by temperature variations. Machine learning algorithms, such as neural networks, support vector machine, and clustering networks, can be utilized to further enhance damage detection reliability under varying environmental and operating conditions. Spectral element method, along with ensemble modeling techniques, can also be utilized to study the high-frequency dynamic response of the joint. This will provide a better understanding of the dynamic behavior of such complicated structures and generate the data required for training different machine learning algorithms in order to perform damage identification.

The proposed reference-free, self-calibrating rail neutral temperature measurement approach needs to be further investigated in the future. Reflection cancellation solutions can be implemented to facilitate the utilization of the normal-to-loading propagation direction. Practical aspects pertaining the in-field implementation of the technique also need to be further investigated to enhance the technique's sensitivity and robustness.

BIBLIOGRAPHY

Abaqus 6.12, 2012. Abaqus Example Problems Manual (6.12).

Adams, R.D., Cawley, P., Pye, C.J., Stone, B.J., 1978. A vibration technique for non-destructively assessing the integrity of structures. J. Mech. Eng. Sci. 20, 93–100.

Agrahari, J.K., Kapuria, S., 2016. Effects of adhesive, host plate, transducer and excitation parameters on time reversibility of ultrasonic Lamb waves. Ultrasonics 70, 147–157.

Albakri, M.I., Tarazaga, P.A., 2016. A novel acoustoelastic-based technique for stress measurement in structural components, in: Pakzad, S., Juan, C. (Eds.), Dynamics of Civil Structures, Volume 2, Conference Proceedings of the Society for Experimental Mechanics Series. Springer International Publishing, pp. 49–56.

Albakri, M.I., Tarazaga, P.A., 2014. Spectral element based optimization scheme for damage identification, in: Wicks, A. (Ed.), Structural Health Monitoring, Volume 5, Conference Proceedings of the Society for Experimental Mechanics Series. Springer International Publishing, pp. 19–27.

Andrew Kish, Gopal Samavedam, Leith Al-Nazer, 2013. Track buckling prevention: theory, safety concepts, and applications, Track Systems Safety. Federal Railroad Administration, Washington, DC.

Annamdas, V., Radhika, M.A., 2013. Electromechanical impedance of piezoelectric transducers for monitoring metallic and non-metallic structures: A review of wired, wireless and energy-harvesting methods. J. Intell. Mater. Syst. Struct. 24, 1021–1042.

Annamdas, V., Soh, C.K., 2010. Application of electromechanical impedance technique for engineering structures: review and future issues. J. Intell. Mater. Syst. Struct. 21, 41–59.

Annamdas, V., Soh, C.K., 2007. Three-dimensional electromechanical impedance model. I: Formulation of directional sum impedance. J. Aerosp. Eng. 20, 53–62.

Benjeddou, A., 2000. Advances in piezoelectric finite element modeling of adaptive structural elements: a survey. Comput. Struct. 76, 347–363.

Bhalla, S., Naidu, A., Ong, C., Soh, C.K., 2002. Practical issues in the implementation of electro-mechanical impedance technique for NDE. pp. 484–494.

Bhalla, S., Soh, C.K., 2004a. Structural health monitoring by piezo-impedance transducers. I: Modeling. J. Aerosp. Eng. 17, 154–165.

Bhalla, S., Soh, C.K., 2004b. Electromechanical impedance modeling for adhesively bonded piezo-transducers. J. Intell. Mater. Syst. Struct. 15, 955–972.

Biot, M.A., 1965. Mechanics of incremental deformations: Theory of elasticity and viscoelasticity of initially stressed solids and fluids, including thermodynamic foundations and applications to finite strain, John Wiley & Sons.

Blitz, J., Simpson, G., 1996. Ultrasonic methods of non-destructive testing. Springer Science & Business Media.

Bouteiller, F., Grisso, B.L., Peairs, D.M., Inman, D.J., 2006. Broken rail track detection using smart materials. pp. 617809-617809–11.

Brownjohn, J.M.W., 2007. Structural health monitoring of civil infrastructure. Philos. Trans. Math. Phys. Eng. Sci. 365, 589–622.

Capron, M.D., Williams, F.W., 1988. Exact dynamic stiffnesses for an axially loaded uniform Timoshenko member embedded in an elastic medium. J. Sound Vib. 124, 453–466.

Carden, E.P., Fanning, P., 2004. Vibration based condition monitoring: a review. Struct. Health Monit. 3, 355–377.

Cerri, M.N., Vestroni, F., 2000. Detection of damage in beams subjected to diffused cracking. J. Sound Vib. 234, 259–276.

Chaki, S., Bourse, G., 2009. Guided ultrasonic waves for non-destructive monitoring of the stress levels in prestressed steel strands. Ultrasonics 49, 162–171.

Chee, C.Y.K., Tong, L., Steven, G.P., 1998. A Review on the modelling of piezoelectric sensors and actuators incorporated in intelligent structures. J. Intell. Mater. Syst. Struct. 9, 3–19.

Chen, F., Wilcox, P.D., 2007a. The effect of load on guided wave propagation. Ultrasonics 47, 111–122.

Chen, F., Wilcox, P.D., 2007b. The effect of load on guided wave propagation. Ultrasonics 47, 111–122.

Chinchalkar, S., 2001. Determiation of crack location in beams using natural frequencies. J. Sound Vib. 247, 417–429.

Crawley, E.F., De Luis, J., 1987. Use of piezoelectric actuators as elements of intelligent structures. AIAA J. 25, 1373–1385.

Crawley, E.F., Luis, J. de, 1987. Use of piezoelectric actuators as elements of intelligent structures. AIAA J. 25, 1373–1385. doi:10.2514/3.9792

De Marchi, L., Marzani, A., Caporale, S., Speciale, N., 2009. Ultrasonic guided-waves characterization with warped frequency transforms. IEEE Trans. Ultrason. Ferroelectr. Freq. Control 56, 2232–2240.

De Marchi, L., Ruzzene, M., Xu, B., Baravelli, E., Speciale, N., 2010. Warped basis pursuit for damage detection using lamb waves. IEEE Trans. Ultrason. Ferroelectr. Freq. Control 57, 2734–2741.

Doebling, S.W., Farrar, C.R., Prime, M.B., Shevitz, D.W., 1996. Damage identification and health monitoring of structural and mechanical systems from changes in their vibration characteristics: a literature review. Los Alamos National Lab., NM, United States.

Doyle, J.F., 1997. Wave Propagation in Structures: Spectral Analysis Using Fast Discrete Fourier Transforms, 2nd edition. Springer, New York, United States.

Dugnani, R., 2009. Dynamic behavior of structure-mounted disk-shape piezoelectric sensors including the adhesive layer. J. Intell. Mater. Syst. Struct. 20, 1553–1564.

Duquennoy, M., Ouaftouh, M., Ourak, M., 1999. Ultrasonic evaluation of stresses in orthotropic materials using Rayleigh waves. NDT E Int. 32, 189–199.

Fan, W., Qiao, P., 2011. Vibration-based damage identification methods: a review and comparative study. Struct. Health Monit. 10, 83–111.

Farrar, C.R., Doebling, S.W., Nix, D.A., 2001. Vibration-based structural damage identification. Philos. Trans. Math. Phys. Eng. Sci. 359, 131–149.

Farrar, C.R., Worden, K., 2007. An introduction to structural health monitoring. Philos. Trans. Math. Phys. Eng. Sci. 365, 303–315.

Figliola, R.S., Beasley, D.E., 2010. Theory and design for mechanical measurements, 5th edition. ed. John Wiley and Sons, Hoboken, NJ, United States.

Frikha, A., Treyssède, F., Cartraud, P., 2011. Effect of axial load on the propagation of elastic waves in helical beams. Wave Motion 48, 83–92.

Fromme, P., Wilcox, P.D., Lowe, M.J.S., Cawley, P., 2006. On the development and testing of a guided ultrasonic wave array for structural integrity monitoring. IEEE Trans. Ultrason. Ferroelectr. Freq. Control 53, 777–785.

Gandhi, N., Michaels, J.E., Lee, S.J., 2012. Acoustoelastic Lamb wave propagation in biaxially stressed plates. J. Acoust. Soc. Am. 132, 1284–1293.

Giurgiutiu, V., Zagrai, A.N., 2000. Characterization of piezoelectric wafer active sensors. J. Intell. Mater. Syst. Struct. 11, 959–976.

Graff, K.F., 1975. Wave Motion in Elastic Solids. Ohio State University Press, United States.

Green, A.E., Rivlin, R.S., Shield, R.T., 1952. General theory of small elastic deformations superposed on finite elastic deformations. Proc. R. Soc. Lond. Math. Phys. Eng. Sci. 211, 128–154.

Gudmundson, P., 1982. Eigenfrequency changes of structures due to cracks, notches or other geometrical changes. J. Mech. Phys. Solids 30, 339–353.

Guo, Z., Sun, Z., 2011. Spectral element modeling based structure piezoelectric impedance computation and damage identification. Front. Archit. Civ. Eng. China 5, 458–464.

Ha, S., Chang, F.-K., 2010a. Optimizing a spectral element for modeling PZT-induced Lamb wave propagation in thin plates. Smart Mater. Struct. 19, 015015.

Ha, S., Chang, F.-K., 2010b. Adhesive interface layer effects in PZT-induced Lamb wave propagation. Smart Mater. Struct. 19, 025006.

Han, B., Wang, Y., Dong, S., Zhang, L., Ding, S., Yu, X., Ou, J., 2015. Smart concretes and structures: a review. J. Intell. Mater. Syst. Struct. 26, 1303–1345.

Han, L., Wang, X.D., Sun, Y., 2008a. The effect of bonding layer properties on the dynamic behavior of surface-bonded piezoelectric sensors. Int. J. Solids Struct. 45, 5599–5612.

Han, L., Wang, X.D., Sun, Y., 2008b. The effect of bonding layer properties on the dynamic behavior of surface-bonded piezoelectric sensors. Int. J. Solids Struct. 45, 5599–5612.

Hauk, V., 1997. Structural and residual stress analysis by nondestructive methods: evaluation-application-assessment. Elsevier.

Hayes, M., Rivlin, R.S., 1961. Surface waves in deformed elastic materials. Arch. Ration. Mech. Anal. 8, 358–380.

Hirao, M., Fukuoka, H., Hori, K., 1981. Acoustoelastic effect of Rayleigh surface wave in isotropic material. J. Appl. Mech. 48, 119–124.

Hsu, N.N., 1974. Acoustical birefringence and the use of ultrasonic waves for experimental stress analysis. Exp. Mech. 14, 169–176.

Hughes, D.S., Kelly, J.L., 1953. Second-order elastic deformation of solids. Phys. Rev. 92, 1145–1149.

Husson, D., 1985. A perturbation theory for the acoustoelastic effect of surface waves. J. Appl. Phys. 57, 1562–1568.

Hutchings, M.T., Withers, P.J., Holden, T.M., Lorentzen, T., 2005. Introduction to the characterization of residual stress by neutron diffraction. CRC Press.

Islam, M.M., Huang, H., 2016. Effects of adhesive thickness on the Lamb wave pitch-catch signal using bonded piezoelectric wafer transducers. Smart Mater. Struct. 25, 085014.

Islam, M.M., Huang, H., 2014. Understanding the effects of adhesive layer on the electromechanical impedance (EMI) of bonded piezoelectric wafer transducer. Smart Mater. Struct. 23, 125037.

Jang, I., Park, I., Lee, U., 2014. Spectral element modeling and analysis of the dynamics and guided waves in a smart beam with a surface-bonded PZT layer. J. Mech. Sci. Technol. 28, 1229–1239.

Jiang, J.P., Li, D.X., 2007. A new finite element model for piezothermoelastic composite beam. J. Sound Vib. 306, 849–864.

Kamminga, J.-D., Keijser, T.H. de, Mittemeijer, E.J., Delhez, R., 2000. New methods for diffraction stress measurement: a critical evaluation of new and existing methods. J. Appl. Crystallogr. 33, 1059–1066.

Kish, A., Samavedam, G., 2005. Improved destressing of continuous welded rail for better management of rail neutral temperature. Transp. Res. Rec. J. Transp. Res. Board 1916, 56–65.

Ko, J.M., Ni, Y.Q., 2005. Technology developments in structural health monitoring of large-scale bridges. Eng. Struct., SEMC 2004 Structural Health Monitoring, Damage Detection and Long-Term Performance Second International Conference on Structural Engineering, Mechanics and Computation 27, 1715–1725.

Krawczuk, M., Palacz, M., Ostachowicz, W., 2004. Wave propagation in plate structures for crack detection. Finite Elem. Anal. Des. 40, 991–1004.

Lee, U., 2009. Spectral element method in structural dynamics, 1st edition. ed. Wiley, Singapore; Hoboken, NJ.

Lee, U., Kim, D., Park, I., 2013. Dynamic modeling and analysis of the PZT-bonded composite Timoshenko beams: Spectral element method. J. Sound Vib. 332, 1585–1609.

Lee, U., Kim, J., 2001. Spectral element modeling for the beams treated with active constrained layer damping. Int. J. Solids Struct. 38, 5679–5702.

Lee, U., Kim, J., 2000. Dynamics of elastic-piezoelectric two-layer beams using spectral element method. Int. J. Solids Struct. 37, 4403–4417.

Lee, U., Kim, J., Leung, A.Y., 2000. The spectral element method in structural dynamics. Shock Vib. Dig. 32, 451–465.

Lee, U., Shin, J., 2002. A frequency response function-based structural damage identification method. Comput. Struct. 80, 117–132.

Lee, Y.-S., Chung, M.-J., 2000. A study on crack detection using eigenfrequency test data. Comput. Struct. 77, 327–342.

Leo, D.J., 2007. Engineering analysis of smart material systems, 1st edition. ed. Wiley, Hoboken, N.J.

Liang, C., Sun, F.P., Rogers, C.A., 1994a. Coupled electro-mechanical analysis of adaptive material systems- determination of the actuator power consumption and system energy transfer. J. Intell. Mater. Syst. Struct. 5, 12–20.

Liang, C., Sun, F.P., Rogers, C.A., 1994b. An impedance method for dynamic analysis of active material systems. J. Vib. Acoust. 116, 120–128.

Loveday, P.W., Wilcox, P.D., 2010. Guided wave propagation as a measure of axial loads in rails. Proc. SPIE 7650, 1–8.

Mazzotti, M., Marzani, A., Bartoli, I., Viola, E., 2012. Guided waves dispersion analysis for prestressed viscoelastic waveguides by means of the SAFE method. Int. J. Solids Struct. 49, 2359–2372.

Nokes, J.P., Cloud, G.L., 1993. The application of interferometric techniques to the nondestructive inspection of fiber-reinforced materials. Exp. Mech. 33, 314–319.

Park, G., Cudney, H.H., Inman, D.J., 2000a. Impedance-based health monitoring of civil structural components. J. Infrastruct. Syst. 6, 153–160.

Park, G., Cudney, H.H., Inman, D.J., 2000b. An integrated health monitoring technique using structural impedance sensors. J. Intell. Mater. Syst. Struct. 11, 448–455.

Park, G., Inman, D.J., 2007. Structural health monitoring using piezoelectric impedance measurements. Philos. Trans. R. Soc. Lond. Math. Phys. Eng. Sci. 365, 373–392.

Park, G., Sohn, H., Farrar, C.R., Inman, D.J., 2003. Overview of piezoelectric impedance-based health monitoring and path forward. Shock Vib. Dig. 35, 451–464.

Park, H.W., Kim, E.J., Lim, K.L., Sohn, H., 2010a. Spectral element formulation for dynamic analysis of a coupled piezoelectric wafer and beam system. Comput. Struct. 88, 567–580.

Park, H.W., Kim, E.J., Lim, K.L., Sohn, H., 2010b. Spectral element formulation for dynamic analysis of a coupled piezoelectric wafer and beam system. Comput. Struct. 88, 567–580.

Park, I., Kim, S., Lee, U., 2013. Dynamics and guided waves in a smart Timoshenko beam with lateral contraction. Smart Mater. Struct. 22, 075034.

Park, S., Inman, D.J., Yun, C.-B., 2008. An outlier analysis of MFC-based impedance sensing data for wireless structural health monitoring of railroad tracks. Eng. Struct. 30, 2792–2799.

Park, S., Yun, C.-B., Roh, Y., Lee, J.-J., 2006. PZT-based active damage detection techniques for steel bridge components. Smart Mater. Struct. 15, 957.

Peairs, D.M., Tarazaga, P.A., Inman, D.J., 2007. Frequency range selection for impedance-based structural health monitoring. J. Vib. Acoust. 129, 701–709.

Perelli, A., De Marchi, L., Marzani, A., Speciale, N., 2012. Acoustic emission localization in plates with dispersion and reverberations using sparse PZT sensors in passive mode. Smart Mater. Struct. 21, 025010.

Pitchford, C., Grisso, B.L., Inman, D.J., 2007. Impedance-based structural health monitoring of wind turbine blades. p. 65321I–65321I–11.

Qing, X.P., Chan, H.-L., Beard, S.J., Ooi, T.K., Marotta, S.A., 2006. Effect of adhesive on the performance of piezoelectric elements used to monitor structural health. Int. J. Adhes. Adhes. 26, 622–628.

Raghavan, A., Cesnik, C.E., 2007. Review of guided-wave structural health monitoring. Shock Vib. Dig. 39, 91–116.

Reaves, M., Horta, L., n.d. Test cases for modeling and validation of structures with piezoelectric actuators, in: 19th AIAA Applied Aerodynamics Conference. American Institute of Aeronautics and Astronautics.

Ritdumrongkul, S., Abe, M., Fujino, Y., Miyashita, T., 2004. Quantitative health monitoring of bolted joints using a piezoceramic actuator–sensor. Smart Mater. Struct. 13, 20.

Rizzo, P., Lanza di Scalea, F., 2003. Effect of frequency on the acoustoelastic response of steel bars. Exp. Tech. 27, 40–43.

Rossini, N.S., Dassisti, M., Benyounis, K.Y., Olabi, A.G., 2012. Methods of measuring residual stresses in components. Mater. Des., New Rubber Materials, Test Methods and Processes 35, 572–588.

Salawu, O.S., 1997. Detection of structural damage through changes in frequency: a review. Eng. Struct. 19, 718–723.

Saravanos, D.A., Heyliger, P.R., 1995. Coupled layerwise analysis of composite beams with embedded piezoelectric sensors and actuators. J. Intell. Mater. Syst. Struct. 6, 350–363.

Seco, F., Jiménez, A.R., 2012. Modelling the generation and propagation of ultrasonic signals in cylindrical waveguides. INTECH Open Access Publisher.

Shi, F., Michaels, J.E., Lee, S.J., 2013. In situ estimation of applied biaxial loads with Lamb waves. J. Acoust. Soc. Am. 133, 677–687.

Silva, L.F.M. da, Adams, R.D., 2005. Measurement of the mechanical properties of structural adhesives in tension and shear over a wide range of temperatures. J. Adhes. Sci. Technol. 19, 109–141.

Sirohi, J., Chopra, I., 2000. Fundamental understanding of piezoelectric strain sensors. J. Intell. Mater. Syst. Struct. 11, 246–257.

Skrzypek, S.J., Baczmański, A., Ratuszek, W., Kusior, E., 2001. New approach to stress analysis based on grazing-incidence X-ray diffraction. J. Appl. Crystallogr. 34, 427–435.

Sohn, H., Farrar, C.R., Hemez, F.M., Shunk, D.D., Stinemates, D.W., Nadler, B.R., Czarnecki, J.J., 2004. A review of structural health monitoring literature: 1996-2001. Los Alamos National Laboratory Los Alamos, NM.

Sun, F.P., Chaudhry, Z., Liang, C., Rogers, C.A., 1995. Truss structure integrity identification using PZT sensor-actuator. J. Intell. Mater. Syst. Struct. 6, 134–139.

Talakokula, V., Bhalla, S., 2014. Reinforcement corrosion assessment capability of surface bonded and embedded piezo sensors for reinforced concrete structures. J. Intell. Mater. Syst. Struct.

Taylor, S.G., Farinholt, K., Choi, M., Jeong, H., Jang, J., Park, G., Lee, J.-R., Todd, M.D., 2014. Incipient crack detection in a composite wind turbine rotor blade. J. Intell. Mater. Syst. Struct. 25, 613–620.

Thyagarajan, S.K., Schulz, M.J., Pai, P.F., Chung, J., 1998. Detecting structural damage using frequency response functions. J. Sound Vib. 210, 162–170.

Vangi, D., 2001. Stress evaluation by pulse-echo ultrasonic longitudinal wave. Exp. Mech. 41, 277–281.

Wang, H., Zou, L., 2013. Interfacial effect on the electromechanical behaviors of piezoelectric/elastic composite smart beams. J. Intell. Mater. Syst. Struct. 24, 421–430.

Wilcox, P.D., 2003. A rapid signal processing technique to remove the effect of dispersion from guided wave signals. IEEE Trans. Ultrason. Ferroelectr. Freq. Control 50, 419–427.

Willberg, C., 2016. Analysis of the dynamical behavior of piezoceramic actuators using piezoelectric isogeometric finite elements. Adv. Comput. Des. 1, 37–60.

Willson, A.J., 1977. Wave propagation in thin pre-stressed elastic plates. Int. J. Eng. Sci. 15, 245–251.

Wilson, J.W., Tian, G.Y., Barrans, S., 2007. Residual magnetic field sensing for stress measurement. Sens. Actuators Phys. 135, 381–387.

Withers, P.J., Bhadeshia, H.K.D.H., 2001. Residual stress. Part 1- measurement techniques. Mater. Sci. Technol. 17, 355–365.

Worden, K., Farrar, C.R., Manson, G., Park, G., 2007. The fundamental axioms of structural health monitoring. Proc. R. Soc. Lond. Math. Phys. Eng. Sci. 463, 1639–1664.

Xu, Y.G., Liu, G.R., 2002a. A Modified electro-mechanical impedance model of piezoelectric actuator-sensors for debonding detection of composite patches. J. Intell. Mater. Syst. Struct. 13, 389–396.

Yan, Y.J., Cheng, L., Wu, Z.Y., Yam, L.H., 2007. Development in vibration-based structural damage detection technique. Mech. Syst. Signal Process. 21, 2198–2211.

Yang, Z., Wang, L., 2010. Structural damage detection by changes in natural frequencies. J. Intell. Mater. Syst. Struct. 21, 309–319.

Zagrai, A., Doyle, D., Gigineishvili, V., Brown, J., Gardenier, H., Arritt, B., 2010. Piezoelectric wafer active sensor structural health monitoring of space structures. J. Intell. Mater. Syst. Struct. 21, 921–940.

Zhai, G., Jiang, T., Kang, L., Wang, S., 2010. Minimizing influence of multi-modes and dispersion of electromagnetic ultrasonic lamb waves. IEEE Trans. Ultrason. Ferroelectr. Freq. Control 57, 2725–2733.

Zou, D., Liu, T., Liang, C., Huang, Y., Zhang, F., Du, C., 2015. An experimental investigation on the health monitoring of concrete structures using piezoelectric transducers at various environmental temperatures. J. Intell. Mater. Syst. Struct. 26, 1028–1034.

Zou, Y., Tong, L., STEVEN, G.P., 2000. Vibration-based model-dependent damage (delamination) identification and health monitoring for composite structures - a review. J. Sound Vib. 230, 357–378.

Żurek, Z.H., 2005. Magnetic contactless detection of stress distribution and assembly defects in constructional steel element. NDT E Int. 38, 589–595.

APPENDIX A

Spectral Element Method

With the spectral element method, all response variables and external forces appearing in the governing equations and boundary conditions are first transformed to the frequency domain. This is done by applying discrete Fourier transform as follows

$$\boldsymbol{u}(x,t) = \frac{1}{N}\sum_{n=0}^{N-1}\boldsymbol{U_n}(x,\omega_n)e^{i\omega_n t} \tag{A.1}$$

where: $\boldsymbol{u}(x,t)$ is the response variables vector in time domain, $\boldsymbol{U_n}(x,\omega_n)$ is the vector of the corresponding Fourier coefficients at the nth angular frequency ω_n, N is the number of spectral components considered in the discrete Fourier transform, with $N/2$ being the Nyquist frequency.

The Fourier coefficients are assumed to have a general solution of the form

$$\boldsymbol{U_n}(x,\omega_n) = \sum_m \boldsymbol{r}_m A_m\, e^{-ik_{mn}x} \tag{A.2}$$

where k_{mn} is the wave number corresponding to the mth mode at the nth angular frequency, $\boldsymbol{r} \in \mathbb{C}^{d\times m}$ and $\boldsymbol{A} \in \mathbb{C}^{1\times m}$ are the scaling matrix and amplitude vector for the Fourier coefficients in the frequency domain, respectively, with d being the number of components in the displacement field vector, i.e. the number of degrees of freedom. Fourier coefficients can be scaled relative to any one of them. In this work, the first element in the Fourier coefficients vector, normally corresponding to the axial displacement at the neutral axis, is selected to be the scaling coefficient. Hence, $r_{1m} = 1\ \forall\ m$, and all other coefficients are calculated with respect to it. Substituting the spectral solution in the governing equations yields

$$\boldsymbol{Q}\boldsymbol{r}\boldsymbol{A} = 0 \tag{A.3}$$

where the elements of $\boldsymbol{Q}$ are functions of material and geometric characteristics of the structure, as they appear in the governing equations, wavenumber, and frequency. To get a nontrivial solution, the matrix $\boldsymbol{Q}$ should be singular, which leads to the characteristic equation

$$det(\boldsymbol{Q}) = 0 \tag{A.4}$$

This results in a $2d$ order polynomial in k, with only even-order terms appearing in the characteristic equation. Therefore, d wave modes exist at each frequency, corresponding to propagating waves along with evanescent modes. In general, there is no closed form solution for this high-order polynomial, therefore, the characteristic equation is solved numerically. Once wavenumbers are calculated, the components of the scaling matrix $\boldsymbol{r}$, appearing in Equation A.3, are calculated.

At this stage, Fourier coefficients can be determined in terms of the unknown vector $\boldsymbol{A}$. These unknowns are found by applying force and moment boundary conditions at each node of the spectral element. For a given spectral element, spectral nodal degrees of freedom are defined as follows

$$\boldsymbol{d} = \boldsymbol{H}(\omega)\boldsymbol{A} \tag{A.5}$$

where $\boldsymbol{d}$ is the nodal degrees of freedom vector and $\boldsymbol{H}(\omega)$ is the shape functions matrix, constructed after the definition in Equation A.2.

Nodal forces and moments vector, $\boldsymbol{F}$, is obtained by substituting the spectral solution of response variables into boundary conditions equations

$$\boldsymbol{F} = \boldsymbol{G}(\omega)\boldsymbol{A} \tag{A.6}$$

where $\boldsymbol{G}(\omega)$ is the boundary conditions matrix. Substituting Eq. A.5 into Eq. A.6, the dynamic stiffness matrix relating nodal forces and nodal displacement vectors in frequency domain is calculated

$$\boldsymbol{F} = \boldsymbol{K}(\omega)\boldsymbol{d} \tag{A.7}$$

where the dynamic stiffness matrix, $\boldsymbol{K}(\omega)$, is defined in terms of the shape functions matrix and the boundary conditions matrix as follows

$$\boldsymbol{K}(\omega) = \boldsymbol{G}(\omega)\boldsymbol{H}^{-1}(\omega) \tag{A.8}$$

APPENDIX B

Spectral Element Formulation for Fundamental Beam Theories

For Timoshenko beam, Elementary rod element, nodal degrees of freedom, shown in Figure B.1.a, are defined as follows

$$d = \begin{Bmatrix} U(0) \\ W(0) \\ \phi(0) \\ U(L) \\ W(L) \\ \phi(L) \end{Bmatrix} = \underbrace{\begin{bmatrix} 1 & 1 & 0 & 0 & 0 & 0 \\ 0 & 0 & 1 & 1 & 1 & 1 \\ 0 & 0 & r_{23} & r_{24} & r_{25} & r_{26} \\ e^{-ik_1L} & e^{-ik_2L} & 0 & 0 & 0 & 0 \\ 0 & 0 & e^{-ik_3L} & e^{-ik_4L} & e^{-ik_5L} & e^{-ik_6L} \\ 0 & 0 & r_{23}e^{-ik_3L} & r_{24}e^{-ik_4L} & r_{25}e^{-ik_5L} & r_{26}e^{-ik_6L} \end{bmatrix}}_{H(\omega)} A$$

Figure B.1.b shows nodal forces and moments for this element. Based on the directions shown in the figure, and the boundary conditions defined by Eq. 2.13, the element force vector, F, is defined as follows

$$F = \begin{Bmatrix} F_x(0) \\ F_z(0) \\ M(0) \\ F_x(L) \\ F_z(L) \\ M(L) \end{Bmatrix}$$

$$= \underbrace{\begin{bmatrix} ik_1EA & ik_2EA & 0 & 0 \\ 0 & 0 & GA\bar{K}(ik_3 + r_{23}) & GA\bar{K}(ik_6 + r_{26}) \\ 0 & 0 & iEIk_3r_{23} & iEIk_6r_{26} \\ -ik_1EAe^{-ik_1L} & -ik_2EAe^{-ik_2L} & 0 & 0 \\ 0 & 0 & -GA\bar{K}(ik_3 + r_{23})e^{-ik_3L} & -GA\bar{K}(ik_6 + r_{26})e^{-ik_6L} \\ 0 & 0 & -iEIk_3r_{23}e^{-ik_3L} & -iEIk_6r_{26}e^{-ik_6L} \end{bmatrix}}_{G(\omega)} A$$
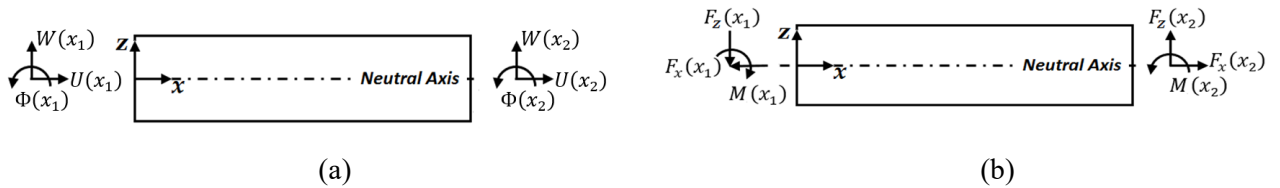

(a)   (b)

Figure B.1 Timoshenko beam, Elementary rod element, (a) nodal degrees of freedom, and (b) nodal forces and moments.

For Timoshenko beam Mindlin-Herrmann rod element, nodal degrees of freedom, shown in Figure B.2.a are defined as follows

$$
d = \begin{Bmatrix} U(0) \\ \Psi(0) \\ W(0) \\ \phi(0) \\ U(L) \\ \Psi(L) \\ W(L) \\ \phi(L) \end{Bmatrix} = \underbrace{\begin{bmatrix} 1 & 1 & 0 & 0 \\ r_{11} & r_{14} & 0 & 0 \\ 0 & 0 & 1 & 1 \\ 0 & 0 & r_{25} & r_{28} \\ e^{-ik_1 L} & e^{-ik_4 L} & 0 & 0 \\ r_{11}e^{-ik_4 L} & r_{14}e^{-ik_4 L} & 0 & 0 \\ 0 & 0 & e^{-ik_5 L} & e^{-ik_8 L} \\ 0 & 0 & r_{25}e^{-ik_5 L} & r_{28}e^{-ik_8 L} \end{bmatrix}}_{H(\omega)} A
$$

The elements of the boundary conditions matrix, G, are defined as follows

$$G_{1m} = ik_m Q_{11} A + Q_{13} A r_{1m}$$

$$G_{2m} = ik_m Q_{11} I r_{1m}$$

$$G_{3n} = (-ik_n - r_{2n}) Q_{55} A \bar{K}$$

$$G_{4n} = -ik_n Q_{11} I r_{2n}$$

where m takes the values of 1 to 4, n takes the values of 5 to 8, and all other elements are zeros. The other half of the matrix follows the same definitions, taking into consideration the convention shown in Figure B.2.b, and evaluated at $x = L$.
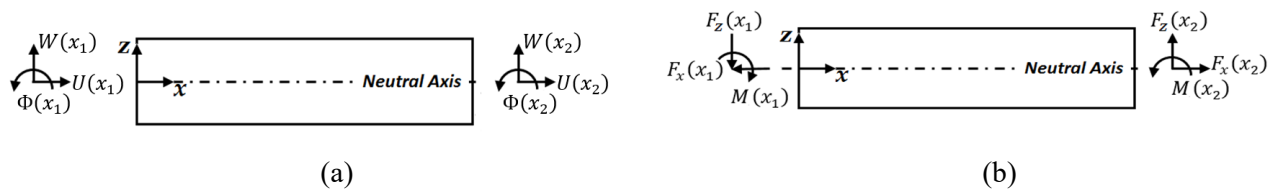
Figure B.2 Timoshenko beam, Mindlin-Herrmann rod element, (a) nodal degrees of freedom, and (b) nodal forces and moments.

APPENDIX C

Constitutive Relations for Piezoelectric Materials

Constitutive relations for linear piezoelectric materials, with strain and electric field as independent variables, can be expressed as (Donald J. Leo, 2007)

$$\sigma_i = \bar{c}_{ij}^E \varepsilon_j - e_{ik} E_k$$
$$D_k = e_{ik} \varepsilon_i - \bar{\epsilon}_{km}^S E_m \tag{C.1}$$

where ε_i denotes the components of Green strain tenor in Voigt notation, σ_i denotes the components of the Cauchy stress tensor in Voigt notation, D is the electric displacement vector, E is the electric field vector, e is the piezoelectric coupling coefficients matrix, $\bar{c}_{ij}^E = c_{ij}^E(1 - i\eta)$ are the components of the complex mechanical stiffness of the material measured at zero electric field, $\bar{\epsilon}_{km}^S = \epsilon_{km}^S(1 - i\gamma)$ are the components of the complex permittivity measured at zero strain, η and γ are the mechanical and dielectric loss factors, respectively.

For beam-like structures, the assumption of plane-stress is adopted. The mechanical behavior of the material is described as follows

$$\begin{Bmatrix} \sigma_1 \\ \sigma_2 \\ \tau_{12} \end{Bmatrix} = \begin{bmatrix} \frac{E}{1-\nu^2} & \frac{\nu E}{1-\nu^2} & 0 \\ \frac{\nu E}{1-\nu^2} & \frac{E}{1-\nu^2} & 0 \\ 0 & 0 & \frac{E}{2(1+\nu)} \end{bmatrix} \begin{Bmatrix} \varepsilon_1 \\ \varepsilon_2 \\ \gamma_{12} \end{Bmatrix} \tag{C.2}$$

For a surface bonded piezoelectric wafer with no transverse loads acting on its surface, the normal stress along the thickness direction is zero. Thus, stress-strain relations are reduced to

$$\begin{Bmatrix} \sigma_1 \\ \tau_{12} \end{Bmatrix} = \begin{bmatrix} E & 0 \\ 0 & \frac{E}{2(1+\nu)} \end{bmatrix} \begin{Bmatrix} \varepsilon_1 \\ \gamma_{12} \end{Bmatrix} \tag{C.3}$$

For a piezoelectric wafer operating at 31-mode, and following the aforementioned assumptions, the constitutive relations are defined as follows

$$\begin{Bmatrix} \sigma_1 \\ \tau_{12} \\ E_3 \end{Bmatrix} = \begin{bmatrix} E(1-i\eta) & 0 & -e_{31} \\ 0 & \frac{E(1-i\eta)}{2(1+v)} & 0 \\ e_{31} & 0 & \epsilon_{33}^S(1-i\gamma) \end{bmatrix} \begin{Bmatrix} \varepsilon_1 \\ \gamma_{12} \\ D_3 \end{Bmatrix} \qquad (C.4)$$

With strain and electric field being the independent variables in the constitutive relations, Electric Gibbs energy expression can be used for the piezoelectric material. The change in Electric Gibbs energy is given by (Donald J. Leo, 2007)

$$dG_2 = \sigma_i d\varepsilon_i - D_k dE_k \qquad (C.5)$$

Which implies that

$$\sigma_i = \frac{\partial G_2}{\partial \varepsilon_i} \qquad (C.6)$$

Substituting constitutive relations, Eq. C.1 and integrating the resulting form yields

$$G_2 = \frac{1}{2}\bar{c}_{ij}^E \varepsilon_i \varepsilon_j - e_{ik}\varepsilon_i E_k + f(E_k) \qquad (C.7)$$

where the function $f(E_k)$ represents the integration constant. Taking the derivative of the above equation with respect to E_k, and recognizing that $D_k = -\partial G_2/\partial E_k$, the function $f(E_k)$ is evaluated. The Electric Gibbs energy is then expressed as

$$G_2 = \frac{1}{2}\bar{c}_{ij}^E \varepsilon_i \varepsilon_j - e_{ik}\varepsilon_i E_k - \frac{1}{2}\bar{\epsilon}_{lm}^S E_l E_m \qquad (C.8)$$

For the piezoelectric-structure interaction model, strain and electric displacement are selected as the independent variables in the constitutive relations, as follows

$$\sigma_i = \bar{c}_{ij}^D \varepsilon_j - h_{ik}D_k$$
$$E_k = -h_{ik}\varepsilon_i - \bar{\beta}_{km}^S D_m \qquad (C.9)$$

where h_{31} is the piezoelectric coupling coefficient, $\bar{c}_{ij}^D = c_{ij}^D(1-i\eta)$ is the complex mechanical stiffness of the material measured at zero electric displacement, $\bar{\beta}_{km}^S = \beta_{km}^S(1-i\gamma)$ is the complex inverse permittivity measured at zero strain. All other symbols are as defined in Eq. C.1.

For this case, Helmholtz energy expression is used for the piezoelectric material, the change in which is defined as

$$dA = \sigma_i d\varepsilon_i + E_k dD_k \tag{C.10}$$

Following the procedure outlined by equations C.6-C.8, Helmholtz energy is expressed as

$$A = \frac{1}{2}\bar{c}^D_{ij}\varepsilon_i\varepsilon_j - h_{ik}\varepsilon_i D_k + \frac{1}{2}\bar{\beta}^S_{kl}D_k D_l \tag{C.11}$$

The conversion between the constitutive relations defined by Eq. C.1 to those given by Eq. C.9 can be achieved as follows

$$\bar{c}^D_{ij} = \bar{c}^E_{ij} + e_{ik}\left(\bar{\epsilon}^S_{km}\right)^{-1}e_{jm}$$

$$h_{ik} = e_{im}\left(\bar{\epsilon}^S_{mk}\right)^{-1} \tag{C.12}$$

$$\bar{\beta}^S_{km} = \left(\bar{\epsilon}^S_{km}\right)^{-1}$$

APPENDIX D

Piezoelectric-structure Interaction Model

List of the symbols used in Eq. 2.58 and 2.59

$I_b = A_b h_b^2/12$

$I_a = A_a h_a^2/3$

$I_p = A_p h_p^2/3$

$\bar{\beta} = A_p \dfrac{h_{31}^2}{\beta_{33}}$

$\bar{\alpha} = A_p \dfrac{h_{31}}{h_p \beta_{33}}$

$\rho A_1 = \rho_b A_b + \rho_a A_a + \rho_p A_p$

$\rho A_2 = (\rho_a A_a + \rho_p A_p)\dfrac{h_b}{2}$

$\rho A_3 = (\rho_a A_a + 2\rho_p A_p)\dfrac{h_a}{2}$

$\rho A_4 = \rho_p A_p \dfrac{h_p}{2}$

$\rho I_1 = \rho_b I_b + (\rho_a A_a + \rho_p A_p)\dfrac{h_b^2}{4}$

$\rho I_2 = (\rho_a A_a + 2\rho_p A_p)\dfrac{h_a h_b}{4}$

$\rho I_3 = \rho_p A_p \dfrac{h_p h_b}{4}$

$\rho I_4 = \rho_a I_a + \rho_p A_p h_a^2$

$\rho I_5 = \rho_p A_p \dfrac{h_p h_a}{2}$

$\rho I_6 = \rho_p I_p$

$EA_1 = c_{11}^b A_b + c_{11}^a A_a + c_{11}^p A_p - \bar{\beta}$

$EA_2 = (c_{11}^a A_a + c_{11}^p A_p - \bar{\beta})\dfrac{h_b}{2}$

$EA_3 = \left(\dfrac{1}{2}c_{11}^a A_a + c_{11}^p A_p - \bar{\beta}\right)h_a$

$EA_4 = (c_{11}^p A_p - \bar{\beta})\dfrac{h_p}{2}$

$EI_1 = c_{11}^b I_b + (c_{11}^a A_a + c_{11}^p A_p - \bar{\beta})\dfrac{h_b^2}{4}$

$EI_2 = \left(\dfrac{1}{2}c_{11}^a A_a + c_{11}^p A_p - \bar{\beta}\right)\dfrac{h_a h_b}{2}$

$EI_3 = (c_{11}^p A_p - \bar{\beta})\dfrac{h_p h_b}{4}$

$EI_4 = c_{11}^a I_a + (c_{11}^p A_p - \bar{\beta})h_a^2$

$EI_5 = (c_{11}^p A_p - \bar{\beta})\dfrac{h_a h_b}{2}$

$EI_6 = c_{11}^p I_p - \bar{\beta}\dfrac{h_p^2}{4}$

$GA_1 = \dfrac{1}{4}c_{66}^b A_b + \dfrac{1}{4}c_{66}^a A_a + \dfrac{1}{4}c_{66}^p A_p$

$GA_2 = \dfrac{1}{4}c_{66}^b A_b$

$GA_3 = \dfrac{1}{4}c_{66}^a A_a$

$GA_4 = \dfrac{1}{4}c_{66}^p A_p$

Elements Q_{ij} of the symmetric matrix $\boldsymbol{Q}$ in Eq. 2.64, where $i,j = 1,\dots,5$

$Q_{11} = -\rho A_1 \omega^2 + EA_1 k^2$

$Q_{12} = 0$

$Q_{25} = -iGA_4 k$

$Q_{33} = -\rho I_1 \omega^2 + EI_1 k^2 + GA_2$

$$Q_{13} = \rho A_2 \omega^2 - EA_2 k^2$$
$$Q_{14} = \rho A_3 \omega^2 - EA_3 k^2$$
$$Q_{15} = \rho A_4 \omega^2 - EA_4 k^2$$
$$Q_{22} = -\rho A_1 \omega^2 + GA_1 k^2$$
$$Q_{23} = -iGA_2 k$$
$$Q_{24} = -iGA_3 k$$

$$Q_{34} = -\rho I_2 \omega^2 + EI_2 k^2$$
$$Q_{35} = -\rho I_3 \omega^2 + EI_3 k^2$$
$$Q_{44} = -\rho I_4 \omega^2 + EI_4 k^2 + GA_3$$
$$Q_{45} = -\rho I_5 \omega^2 + EI_5 k^2$$
$$Q_{55} = -\rho I_6 \omega^2 + EI_6 k^2 + GA_4$$

The characteristic equation can be solved as a quadratic eigenvalue problem by rearranging the matrix $\boldsymbol{Q}$ as follows

$$\boldsymbol{Q} = \boldsymbol{Q_1}\omega^2 + \boldsymbol{Q_2} + \boldsymbol{Q_3}k + \boldsymbol{Q_4}k^2$$

where

$$\boldsymbol{Q_1} = \begin{bmatrix} -\rho A_1 & 0 & \rho A_2 & \rho A_3 & \rho A_4 \\ & -\rho A_1 & 0 & 0 & 0 \\ & & -\rho I_1 & -\rho I_2 & -\rho I_3 \\ & Sym. & & -\rho I_4 & -\rho I_5 \\ & & & & -\rho I_6 \end{bmatrix}$$

$$\boldsymbol{Q_2} = \begin{bmatrix} 0 & 0 & 0 & 0 & 0 \\ & 0 & 0 & 0 & 0 \\ & & GA_2 & 0 & 0 \\ & Sym. & & GA_3 & 0 \\ & & & & GA_4 \end{bmatrix}$$

$$\boldsymbol{Q_3} = -i \begin{bmatrix} 0 & 0 & 0 & 0 & 0 \\ 0 & 0 & GA_2 & GA_3 & GA_4 \\ 0 & -GA_2 & 0 & 0 & 0 \\ 0 & -GA_3 & 0 & 0 & 0 \\ 0 & -GA_4 & 0 & 0 & 0 \end{bmatrix}$$

$$\boldsymbol{Q_4} = \begin{bmatrix} EA_1 & 0 & -EA_2 & -EA_3 & -EA_4 \\ & GA_1 & 0 & 0 & 0 \\ & & EI_1 & EI_2 & EI_3 \\ & Sym. & & EI_4 & EI_5 \\ & & & & EI_6 \end{bmatrix}$$

Boundary conditions matrix, $\boldsymbol{G}(\omega)$, appearing in Eq. 2.70

$$
\boldsymbol{G}(\omega) = \begin{bmatrix}
\sum_{s=1}^{5} -G_{1s}r_{s1}\xi_1(x_1) & \cdots & \sum_{s=1}^{5} -G_{1s}r_{s10}\xi_{10}(x_1) \\
\vdots & \ddots & \vdots \\
\sum_{s=1}^{5} -G_{5s}r_{s1}\xi_1(x_1) & \cdots & \sum_{s=1}^{5} -G_{5s}r_{s10}\xi_{10}(x_1) \\
\sum_{s=1}^{5} G_{1s}r_{s1}\xi_1(x_2) & \cdots & \sum_{s=1}^{5} G_{1s}r_{s10}\xi_{10}(x_2) \\
\vdots & \ddots & \vdots \\
\sum_{s=1}^{5} G_{5s}r_{s1}\xi_1(x_2) & \cdots & \sum_{s=1}^{5} G_{5s}r_{s10}\xi_{10}(x_2)
\end{bmatrix}
$$

where the elements $G_{ij}, i, j = 1, \ldots, 5$ are defined as follows

$G_{11} = -ikEA_1$

$G_{12} = 0$

$G_{13} = ikEA_2$

$G_{14} = ikEA_3$

$G_{15} = ikEA_4$

$G_{21} = 0$

$G_{22} = -ikGA_1$

$G_{23} = -GA_2$

$G_{24} = -GA_3$

$G_{25} = -GA_4$

$G_{31} = ikEA_2$

$G_{32} = 0$

$G_{33} = -ikEI_1$

$G_{34} = -ikEI_2$

$G_{35} = -ikEI_3$

$G_{41} = ikEA_3$

$G_{42} = 0$

$G_{43} = -ikEI_2$

$G_{44} = -ikEI_4$

$G_{45} = -ikEI_5$

$G_{51} = ikEA_4$

$G_{52} = 0$

$G_{53} = -ikEI_3$

$G_{54} = -ikEI_5$

$G_{55} = -ikEI_6$

For a piezoelectric wafer operating as a sensor, the vector $\boldsymbol{\gamma} \in \mathbb{R}^{1 \times 10}$ appearing in Eq. 2.75 is defined as follows

$$
\boldsymbol{\gamma} = \begin{bmatrix} -1 & 0 & \frac{h_b}{2} & h_a & \frac{h_p}{2} & 1 & 0 & \frac{-h_b}{2} & -h_a & \frac{-h_p}{2} \end{bmatrix}
$$

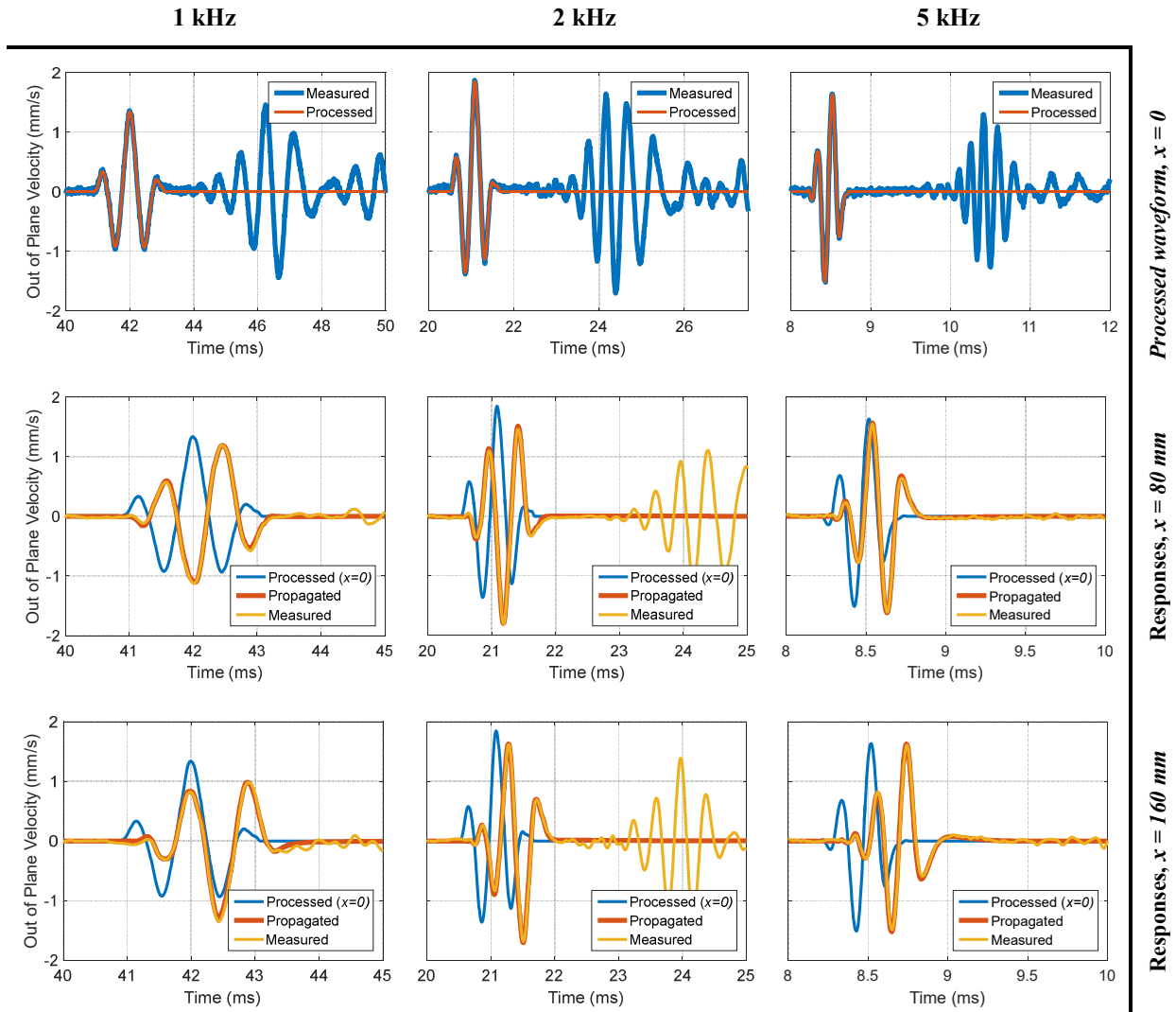## Waveforms for Reference-free Stress Measurements

Figure E.1. Incident, measured and propagated waveforms obtained with 1, 2 and 5 kHz excitation signals for the stress-free case.
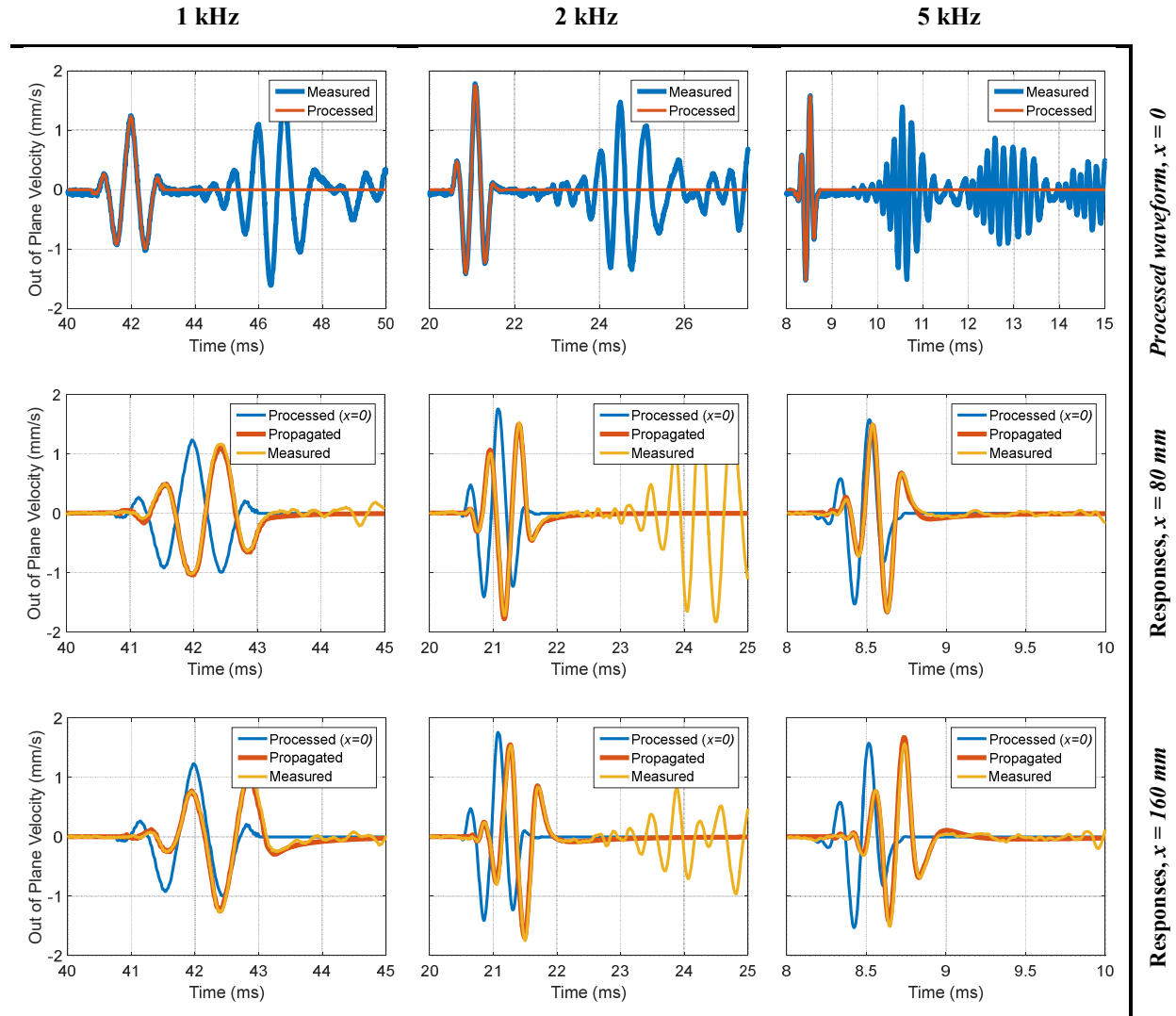
Figure E.2. Incident, measured and propagated waveforms obtained with 1, 2 and 5 kHz excitation signals for the 10 MPa loading state.
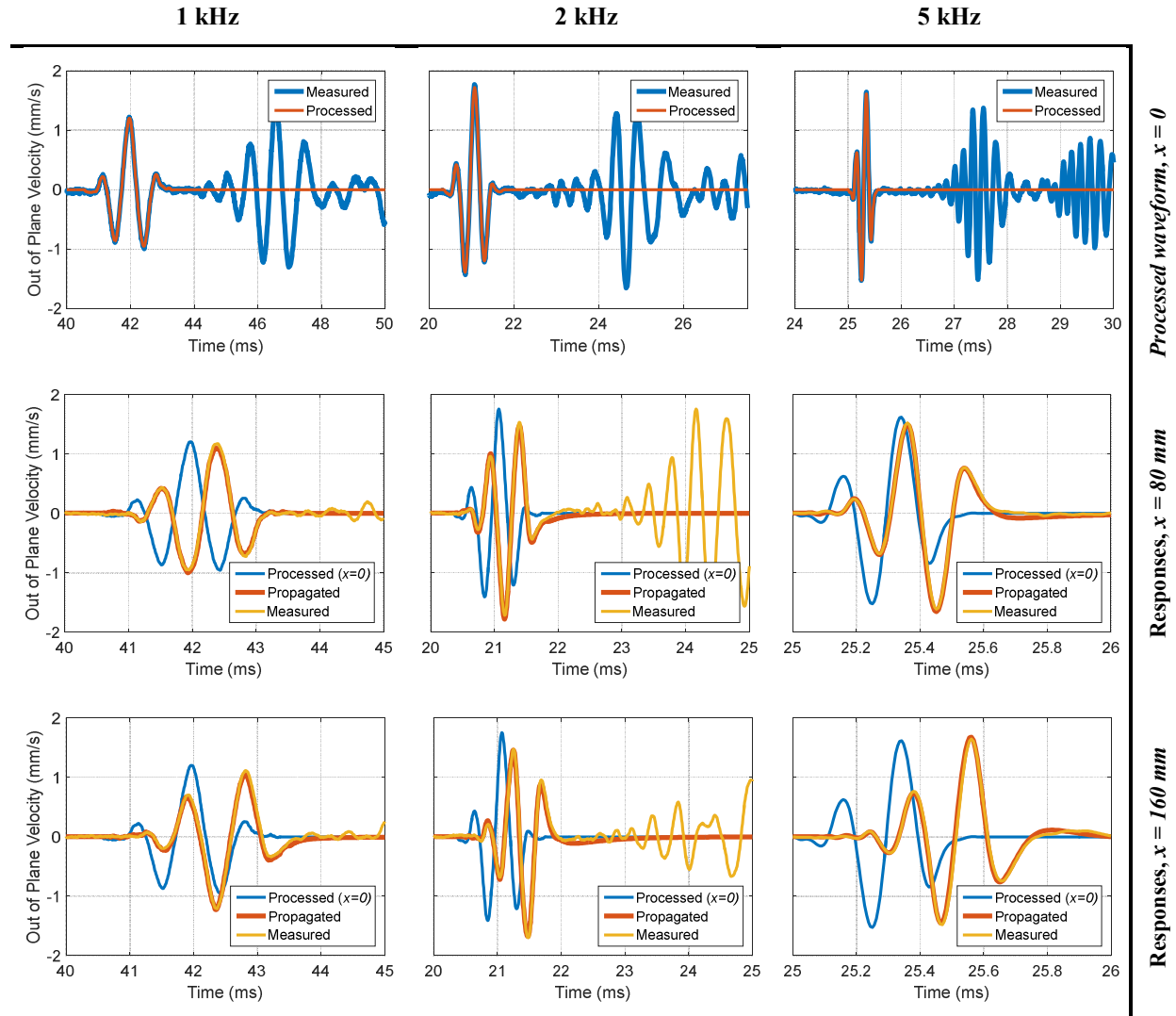
Figure E.3. Incident, measured and propagated waveforms obtained with 1, 2 and 5 kHz excitation signals for the 20 MPa loading state.
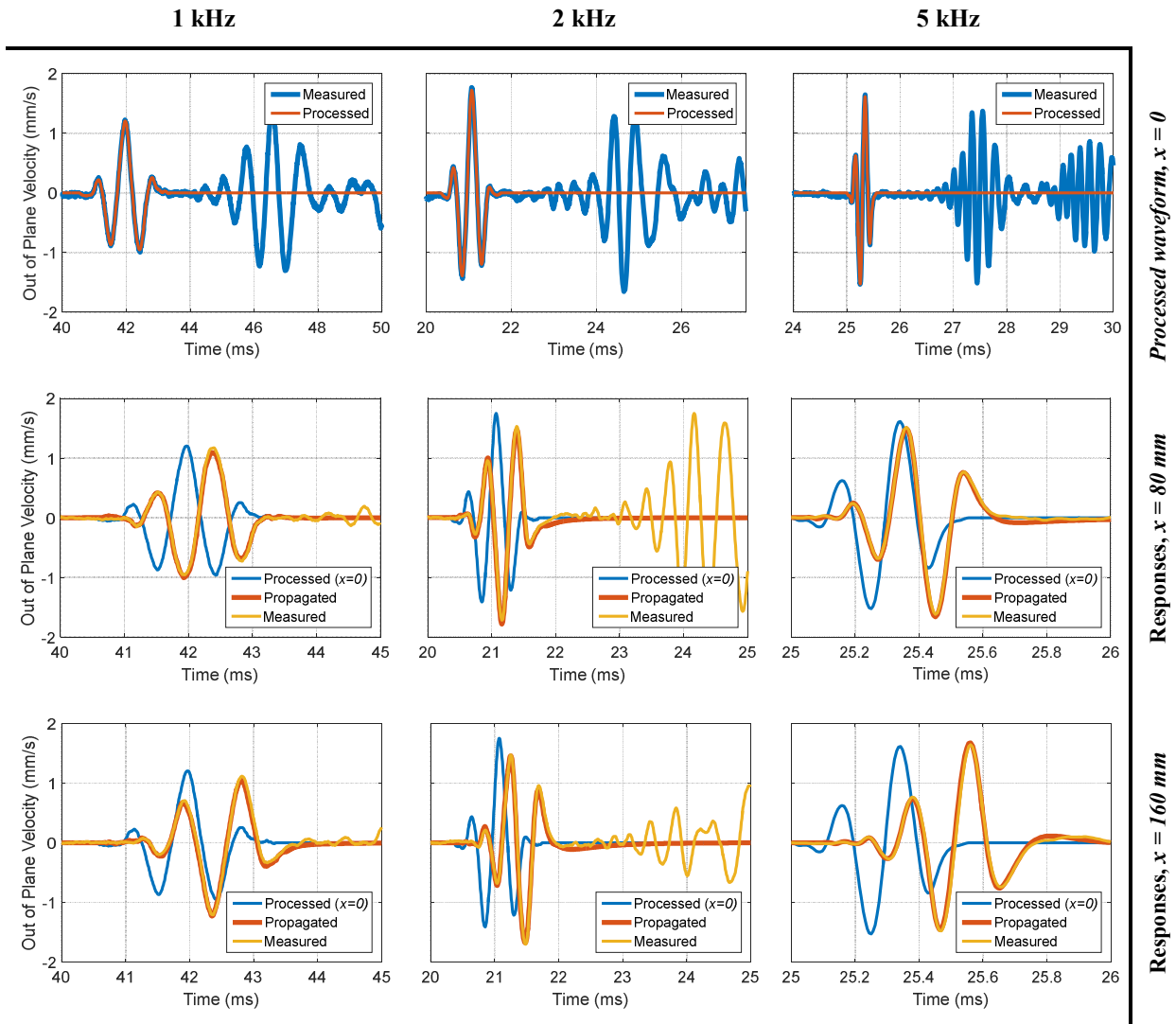
Figure E.4. Incident, measured and propagated waveforms obtained with 1, 2 and 5 kHz excitation signals for the 40 MPa loading state.